A Study of Slow Modes in Keplerian Discs

A Thesis
Submitted For the Degree of
Doctor of Philosophy
in the Faculty of Science

by

Mamta Gulati

Under the Supervision of

Dr. S. Sridhar
Raman Research Institute
&
Dr. Tarun Deep Saini
Indian Institute of Science

Astronomy & Astrophysics
Indian Institute of Science
BANGALORE – 560 012

April 2014

©Mamta Gulati

April 2014

All rights reserved

Declaration

I hereby declare that the work presented in this thesis is entirely original and has been carried out by me at the Raman Research Institute under the auspices of the Joint Astronomy Programme of the Department of Physics, Indian Institute of Science. I further declare that this has not formed the basis for the award of any degree, diploma, membership, associateship or similar title of any University or Institution.

Mamta Gulati
Date:
Department of Physics
Indian Institute of Science
Bangalore, 560012
INDIA

Acknowledgements

It is a pleasure to thank people for their support and encouragement during my Ph.D., though, I can not thank some of them enough for being by side all through good and bad times.

Working with both my supervisors, Sridhar and Tarun, has been an experience of lifetime. I joined my Ph.D. without having much idea of what research means and all the credit of my understanding how to pursue a research problem goes to both of them. Thanking both of them is no less difficult than the problems done in this thesis. I thank Sridhar from the bottom of my heart for teaching me the depths of the subjects, like dynamics and fluids. I thank Tarun for teaching me the insights of various topics, in particular numerical analysis and programming. Both of them have always been available for discussions and offered all the support required. I am grateful to both of them for believing in me and giving me enough confidence to pursue the research problems we have worked on. Not only science but they have also taught me a lot about having the right attitude in life for which I can never thank them enough.

I thank Prof. Biman Nath, Prof. Dwarkanath and Prof. Yashodhan for the support and encouragement during my PhD as a part of my advisory committee at RRI.

I thank all my JAP instructors for their excellent courses. I thank the instructors at ICTP school for offering some of the great courses on Dynamos. I wish to thank Bishwajit, Ravi, Uday, Naintara, Ramesh, Laxmi, Sam, and Suparna for the scientific and non-scientific discussions we've had from time-to-time. Due thanks to Subhash for his continuous enthusiasm which he showers on many of us.

I wish to thank Prof Jasjeet Bagla for his interest in my work and supporting my visit to IISER, Mohali.

Special thanks to Desh for all his support as a friend and as a mentor. His crisp suggestions on scientific and non-scientific matter have always been of great value and help. The evening 'Chai' discussions with him which would extend all the way up to dinner were always fun. I thank Ranjana for some of the great food and late night sittings at their place.

I am grateful to Shiv for all the formal and informal discussions we've had during my stay at RRI. All thanks to him for my knowledge of (world) politics. I thank Bhargavi for being such a good friend and inviting some of us for good fun dinner and tea sessions at her place.

I have used the computational facilities at RRI for some of the works in this thesis and I thank all the staff member of the computer department at RRI, especially Krishnamurthy and Jacob for being so helpful. I wish to thank the library staff at RRI for their prompt help during my stay at RRI.

I am grateful to Krishna for his encouragement and support during my stay in RRI, specially in the issues concerning my maternity leave. He has always tried to do more than what he could do to help me regarding the administrative issues. I would like to thank the administration of RRI and IISc for their help and support at various stages during my Phd.

Vidya can never be thanked enough for her motherly care she has given to all of us. Special thanks to her for asking me almost everyday if I had lunch or not, and sometimes even scolding for skipping lunch.

I wish to thank all my teachers all through my student life for believing in me and helping me throughout.

I would like to thank RRI shuttle drivers and security for making my stay in RRI smooth. Thanks to our canteen staff at RRI and hostel cooks. Thanks to Lakshmamma and Hanumantha for maintaining the pantry on astro-floor and making the 3.00 pm tea.

Now comes the turn of friends (some of them would be reading this just to see their names). It is difficult to imagine my life at RRI without friends like Nishant, Chandra, Harsha and Giri. These creatures have left no stone unturned to bug me throughout my Phd and I see no hopes of any relief in future (which I wish should never happen). Apart from this these are the friends whom I have always relied on since I came to Bangalore. Harsha deserves a special thanks for fulfilling all my demands of having good south-indian food.

Wasim, a friend-cum-brother, who might go into loops of thinking after reading this, if thanked would get offended. He deserves a special acknowledgement for his care and help. Salute to the girl power of astro-floor: Chandreyee, Nazma, Nipanjana, Karamveer, Priyanka, Arpita, Nafisa, Gayatri, along with Habiba, Renu and Amrita (non-astro girl power). Thanks to Yogesh, Chaitra, Mahavir, Jagdish, Jayantha, Kanhaiya, Naveen J, Kartik, Kshitj, Varun and Harsh, specially for the fun chats during the sessions at all times at the coffee lounge.

I would also like to thank my childhood friends Meenu, Megha, Isha and my M.Sc. friends Suru and Naveen G for there care and support.

Finally my family, who has been my biggest support during all my life. My parents & brother who have been there for me in good and bad all my life. My husband Abhinay who supports me unconditionally. My mother and father-in-law for their love, care and support. Last but not the least my daughter Navya for being my strength.

Abbreviations

AGN : Active Galactic Nuclei
BH : Black Hole
CBE : Collisionless Boltzmann Equation
CR : Co–rotation Resonance
DF : Distribution Function
HST : Hubble Space Telescope
ILR : Inner Lindblad Radius
LHS : Left Hand Side
LR : Lindblad Resonance
RHS : Right Hand Side
WKB : Wentzel-Kramers-Brillouin
w.r.t. : with respect to

Synopsis

A rich variety of discs are found orbiting massive bodies in the universe. These could be accretion discs composed of gas around stellar mass compact objects fueling micro-quasar activity; protoplanetary discs, mainly composed of dust and gas, are the progenitors for planet formation; accretion discs composed of stars and gas around super-massive black holes at the centers of galaxies fueling the active galactic nuclei activity; discs in spiral galaxies; and many more. Structural and kinematic properties of these discs in several astrophysical systems are correlated to the global properties; for example, over a sample of thousands of galaxies, a correlation has been found between lopsidedness, black hole growth, and the presence of young stellar populations in the centers of galaxies. Galaxy formation and evolution of the central BH are some of the contexts in which such correlations become important. Studying the dynamics of these discs helps to explain their structural properties and is thus of paramount importance.

In most astrophysical discs (a notable exception being the stellar discs in spiral galaxies), the dynamics are usually dominated by the gravity of the central object, and is thus nearly Keplerian. However, there is a small contribution to the total force experienced by the disc due to the disc material. Discs mentioned above differ from each other due to different underlying force that dominates the non-Keplerian dynamics of these discs. Two important numbers which are useful in describing physical properties of any disc structure in astrophysics are: (1) Mach number $\mathscr{M}$, and (2) Toomre Q parameter. If thermal pressure gradient and/or random motion dominate the non-Keplerian forces, then $\mathscr{M} \ll Q$, and in the case when the self-gravity of the disc is more important then $Q \ll \mathscr{M}$.

Particles constituting the disc orbit under Keplerian potential due to central object, plus the small contribution from the non-Keplerian potential due to disc self-gravity, or the thermal pressure gradient. For a Keplerian potential, the radial and azimuthal frequencies are in 1 : 1 ratio w.r.t. each other and hence there is no precession in the orbits. In case of nearly Keplerian potential (when non-Keplerian contributions are small), the orbits precess at a rate proportional to the non-Keplerian forces. It is this non-zero but small precession that allows the existence of modes whose frequencies are proportional to the precession rate. These modes are referred to as *slow modes* (Tremaine 2001). Such modes are likely to be the only large-scale or long-wavelength modes. The damping they suffer due to viscosity, collisions, Landau damping, or other dissipative processes is also relatively less. Hence, these modes can dominate the overall appearance of discs. In this thesis we intend to study *slow modes* for nearly Keplerian discs. Slow modes in near-Keplerian discs can to be the reason for various non-axisymmetric features observed in many systems:

1. *Galactic discs*: Of the few galaxies for which the observations of galactic nuclei exist, two galaxies: NGC4486B (an elliptical galaxy) and M31 (spiral galaxy), show an unusual double-peak distribution of stars at their centers. In order to explain such distributions, Tremaine in 1995 proposed an eccentric disc model for M31; this model was then further explored by many authors. In addition, lopsidedness is observed in many galaxies on larger scales, and such asymmetries need to be explained via robust modeling of galactic discs.

2. *Debris disc*: Many of the observed discs show non-axisymmetric structures, such as lopsided distribution in brightness of scattered light, warp, and clumps in the disc around β Pictoris; spiral structure in HD 141569A, etc. Most of these features have been attributed to the presence of planets, and in some cases planets have also been detected. However, Jalali & Tremaine (2012) proposed that most of these structures can be formed also due to *slow* ($m = 1$ or 2) modes.

3. *Accretion Discs* around stellar mass binaries have also been found to be asymmetric. One plausible reason for this asymmetry can be $m = 1$ slow modes in these systems.

Slow modes are studied in detail in this thesis. The main approaches that we have used, and the major conclusions from this work are as follows:

- **Slow pressure modes in thin accretion disc**

Earlier work on slow modes assumed that the self-gravity of the disc dominates the pressure gradient in the discs. However, this assumption is not valid for thin and hot accretion discs around stellar mass compact objects. We begin our study of slow modes with the analysis of modes in thin accretion discs around stellar mass compact objects. First, the WKB analysis is used to prove the existence of these modes. Next, we formulate the eigenvalue equation for the slow modes, which turns out to be in the Sturm-Liouville form; thus all the eigenvalues are real. Real eigenvalues imply that the disc is stable to these perturbations. We also discuss the possible excitation mechanisms for these modes; for instance, excitation due to the stream of matter from the secondary star that feeds the accretion disc, or through the action of viscous forces.

- **Slow modes in self-gravitating, zero-pressure fluid disc**

We next generalize the study of slow $m = 1$ modes for a single self-gravitating disc of Tremaine (2001) to a system of two self-gravitating counter–rotating, zero-pressure fluid discs, where the disc particles interact via softened-gravity. Counter–rotating streams of matter are susceptible to various instabilities. In particular, Touma (2002) found unstable modes in counter–rotating, nearly Keplerian systems. These modes were calculated analytically for a two-ring system, and numerically for discs modeled assuming a multiple–ring system. Motivated by this, the corresponding problem for continuous discs was studied by Sridhar & Saini (2010), who proposed a simple model, with dynamics that could be studied largely analytically in the local WKB approximation. Their work, however, had certain limitations; they could construct eigenmodes only for $\eta = 0$ & $1/2$, where η is the mass fraction in the retrograde disc. They could only calculate eigenvalues but not the eigenfunctions. To overcome the above mentioned limitations, we formulate and analyze the full eigenvalue problem to understand the systematic behaviour of such systems. Our general conclusions are as follows

1. The system is stable for $m = 1$ perturbations in the case of no-counter rotation.
2. For other values of mass fraction η, the eigenvalues are generally complex,

and the discs are unstable. For $\eta = 1/2$, the eigenvalues are imaginary, giving purely growing modes.

3. The pattern speed appears to be non-negative for all values of η, with the growth (or damping) rate being larger for larger values of pattern speed.
4. Perturbed surface density profile is generally lopsided, with an overall rotation of the patterns as they evolve in time, with the pattern speed given by the real part of the eigenvalue.

- **Local WKB analysis for Keplerian stellar disc**

We next turn to stellar discs, whose dynamics is richer than softened gravity discs. Jalali & Tremaine (2012) derived the dispersion relation for short wavelength slow modes for a single disc with Schwarzschild distribution function. In contrast to the softened gravity discs (which have slow modes only for $m = 1$), stellar discs permit slow modes for $m \geq 1$. The dispersion relation derived by Jalali & Tremaine makes it evident that all $m \geq 1$ slow modes are neutrally stable. We study slow modes for the case of two counter–rotating discs, each described by Schwarzschild distribution function, and derive the dispersion relation for slow $m \geq 1$ modes in the local WKB limit and study the nature of the instabilities.

One of the important applications of the dispersion relation derived in this chapter is the stability analysis of the modes. For fluid discs, it is well known that the stability of $m = 0$ modes guarantees the stability of higher m modes; and the stability criterion for such discs is the well known Toomre stability criterion. However, this is not the case for collisionless discs. Even if the discs are stable for axisymmetric modes, they can still be unstable for non-axisymmetric modes. The stability of axisymmetric modes is governed by the Toomre stability criterion The non-axisymmetric perturbations were found to be unstable if the mass in the retrograde component of the disc is non-zero.

We next solve the dispersion relation using the Bohr-Sommerfeld quantization condition to obtain the eigen-spectrum for a given unperturbed surface density profile and velocity dispersion. We could obtain only the eigenvalues for no counter–rotation $\eta = 0$, where η is the mass fraction in the retrograde disc and equal counter–rotation ($\eta = 1/2$). All the eigenvalues obtained were real for no counter–rotation, and purely growing/damping for equal counter–rotation. The eigenvalue trends that we get favour detection of high ω and low m modes observationally. We also make a detailed comparison between the eigenvalues for $m = 1$ modes that we obtain with those obtained after solving the integral eigenvalue problem for the softened gravity discs for no counter–rotation and equal counter–rotation. The match between the eigenvalues are quite good, confirming the assertion that softened gravity discs can be reasonable surrogates for collisionless disc for $m = 1$ modes.

- **Non-local WKB theory for eigenmodes**

One major limitation of the above method is that eigenfunctions cannot be obtained as directly as in quantum mechanics because the dispersion relation is transcendental in radial wavenumber k. We overcome this difficulty by dropping the assumption of locality of the relationship between perturbed self-gravity and surface density. Using the standard WKB analysis and epicyclic theory, together with the logarithmic-spiral decomposition of surface density and gravitational potential, we formulate an integral equation for determining both WKB eigenvalues and eigenfunctions. The application of integral equation derived is not only restricted to Keplerian disc; it could be used to study eigenmodes in galactic discs where the motion of stars is not dominated by the potential due to a central black hole (however we have not pursued the potential application in this thesis).

We first verify that the integral equation derived reduces to the well known WKB dispersion relation under the local approximation. We next specialize to slow modes in Keplerian discs. The following are some of the general conclusions of this work

1. We find that the integral equation for slow modes reduces to a symmetric eigenvalue problem, implying that the eigenvalues are all real, and hence the disc is stable.
2. All the non-singular eigenmodes we obtain are prograde, which implies that the density waves generated will have the same sense of rotation as the disc, albeit with a speed which is $O(\varepsilon)$ compared to the the rotation speed of the disc.

3. Eigenvalue ω decreases as we go from $m = 1$ to 2. In addition, for a given ω, the number of nodes for $m = 1$ are larger than those for $m = 2$.
4. The fastest pattern speed is a decreasing function of the heat in the disc.

Asymmetric features in various types of discs could be due to the presence of slow $m = 1$ or 2 modes. In the case of debris discs, these asymmetric features could also be due to the presence of planets. Features due to the presence of slow modes or due to planets can be distinguished from each other if the observations are made for a long enough time. The double peak nucleus observed in galaxies like M31 and NGC4486B differ from each other: stellar distribution in NGC4486B is symmetric w.r.t. its photocenter in contrast to a lopsided distribution seen in M31. It is more likely that the double peak nucleus in NGC4486B is due to $m = 2$ mode, rather than $m = 1$ mode as is the case for M31. NGC4486B being an elliptical galaxy, it is possible that the excitation probability for $m = 2$ mode is higher.

Publications based on this Thesis

1. Slow pressure modes in thin accretion discs.
   Tarun Deep Saini, Mamta Gulati and S. Sridhar (2009), MNRAS, Vol. 400, Page 2090-2097.

2. Unstable $m = 1$ modes of counter-rotating Keplerian discs.
   Mamta Gulati, Tarun Deep Saini and S. Sridhar (2012), MNRAS, Vol. 424, Page 348-360.

3. Non-Local WKB Theory for Eigenmodes of Axisymmetric Stellar Discs in the Epicyclic Approximation.
   Mamta Gulati, S. Sridhar, Tarun Deep Saini,
   manuscript under preparation

Contents

List of Tables

List of Figures

Chapter 1

Introduction

1.1 Astrophysical discs

Discs orbiting massive bodies are found in many astrophysical systems:

- *Protoplanetry discs* were proposed by Kant and Laplace in the eighteenth century, as progenitors for planet formation. These are largely composed of dust and gas. Many such discs have been imaged using HST since 1995. These are understood to be an essential part of the star–formation process.

- *Accretion Discs* composed of gas around stellar mass compact objects in binary systems. In a sufficiently close binary system, when the more massive 'primary' star reaches the end of its life as a compact object, the low mass 'secondary' which is still on the main sequence, can at some stage fill its *Roche lobe* (the critical equipotential surface). It will then spill mass towards the compact object, which in turn forms a disc around the compact object, owing to the angular momentum carried by the infalling mass. Example: X-ray binaries, classical novae, dwarf novae etc.

- *Active Galactic Nuclei* (AGN): It is widely accepted that most galaxies contain a super-massive Black Hole (BH) at their center. Some of them are AGNs, whose standard model includes a Black Hole (BH) surrounded by an accretion disc composed of stars and gas. Such a disc provides the energy source, and allows the BH to grow. The Doppler shift in spectral line due to orbital motion of gas in the disc allows the measurement of mass of central BH. AGNs represent a temporary phase in the evolution history of a galaxy.

- *Spiral Galaxies* are disc galaxies containing a central BH, and a disc composed of gas and stars. Their dynamics is governed by self gravity of the disc as well as the Keplerian potential due to the BH, unlike accretion discs whose dynamics are largely dominated by the central BH. Examples: Milky way, Andromeda galaxy(M31) etc.
- *Other astrophysical discs* includes *Planetary rings*, equatorial rings around *Be stars* and progenitors discs in *Gamma Ray Bursts*.

In general the discs introduced above differ from each other because of different underlying force terms which dominate the non-Keplerian dynamics of the discs. Two important numbers which are useful in describing physical properties of any disc structure in astrophysics are:

- *Mach Number* $\mathscr{M}$ is a dimensionless quantity defined as the ratio of fluid velocity v to the sound speed in the medium c_s:

  $$\mathscr{M} = \frac{v}{c_s}. \tag{1.1}$$

  Mach number varies with the composition of the surrounding medium and also with local conditions, especially temperature and pressure. The Mach number can be used to determine if a flow can be treated as incompressible. If $\mathscr{M}$ is small, and the flow is quasi-steady and isothermal, compressibility effects will be small and a simplified incompressible flow model is applicable.

- *Toomre Q parameter* for a gas disc is defined as

  $$Q \equiv \frac{c_s \kappa}{\pi G \Sigma_{\rm d}}, \tag{1.2}$$

  where κ is the radial frequency of a non-circular orbit, and $\Sigma_{\rm d}$ is the surface density of unperturbed disc. The disc is stable to axisymmetric perturbations if and only if $Q > 1$, which was first derived by Toomre (1964). He also offered a simple physical interpretation of this criterion: If we perturb a patch on a uniformly rotating disc, patches of smaller radii are stable against inward gravitational pull by pressure forces acting outward, whereas larger patches are stable due to outward centrifugal forces. Instabilities for intermediate size perturbations can be suppressed if the perturbed disc follows the Toomre's stability criterion.

Discs for which self-gravity of the disc is more important than thermal pressure gradient and random motion, we have $\mathscr{M} \gg Q$ (a continuous disc), or $\mathscr{M} \gg 1$ (a collisionless disc) (Tremaine, 2001). However, for the case of accretion discs around stellar mass compact objects, for example accretion discs around white dwarfs, one estimates $\mathscr{M} \sim 50$ and $Q \sim 10^9$ which means $\mathscr{M} \ll Q$ (Frank et al., 2002). Therefore, for these discs the non-Keplerian motion results due to thermal pressure gradient.

Particles of the disc orbit under Keplerian potential due to central object plus small contribution from non-Keplerian potential due to disc self-gravity or the gradient of thermal pressure. For a Keplerian potential, the radial and azimuthal frequencies are in $1:1$ resonance w.r.t. each other and hence the orbits do not precess. In case of nearly Keplerian potential (with a small non-Keplerian contribution), the orbits precess at the rate proportional to the non-Keplerian component of the potential. It is this non-zero but small precession rate which allows the existence of modes whose frequencies are proportional to the precession rate itself. These modes are referred to as *slow modes* (Tremaine, 2001). These modes are likely to be the only large-scale or long-wavelength modes present in nearly Keplerian discs. They also suffer relatively less damping due to viscosity, collisions, Landau damping or other dissipative processes. Hence these can dominate the overall appearance of the disc. In this thesis we intend to study *slow modes* for various astrophysical discs

Structural and kinematic properties of many astrophysical systems are correlated to the global properties of the system. For example: over a sample of thousands of galaxies, a correlation has been found between the lopsidedness, BH growth, and the presence of young stellar populations in the center of a galaxy (Reichard et al., 2009). There is a tight correlation between the central BH mass and velocity dispersion in elliptical galaxies/spiral galaxy bulges (Gebhardt et al., 2000; Ferrarese & Merritt, 2000), BH mass and stellar mass of the surrounding spheroid or bulge (Häring & Rix, 2004). Luminous hot galaxies are found to have cuspy cores whose intensity profile can be explained as a steep outer power law and a shallow inner profiles in contrast to faint hot galaxies which shows steep single power law and lack cores. Core galaxies rotate slowly and tend to be boxy whereas power-law galaxies are disky and rotate fast (Gebhardt

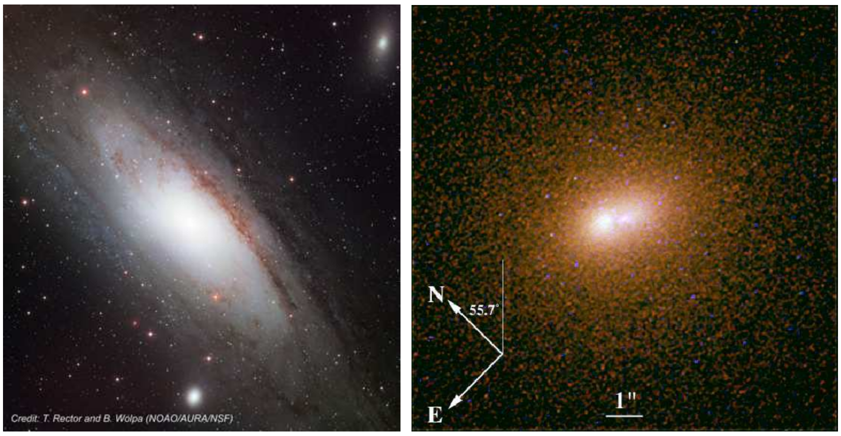

Figure 1.1: Two images of M31; left panel is full image of the spiral M31 (Credit: T. Rector and B. Wolpa (NOAO/AURO/NSF)) and the right one is image of central few arcsec with scale and directions mentioned on the image (Lauer et al., 1998). Double peak structure is clearly revealed in second image.

et al., 1996). Galaxy formation and evolution of central BH are some of the scenarios in which such correlations become important. Studying dynamics of such systems helps largely in explaining structural properties of discs. In the next section we shall give some observational features of discs which could possibly result due to these modes in near-Keplerian discs.

1.2 Non-axisymmetric features in discs:

- **Discs in Galactic Nuclei:** Observations of galactic nuclei are limited largely by the resolutions of present telescopes. Out of a few galaxies for which such observations are known, two galaxies: NGC4486B (in the Virgo cluster) and M31 (closest neighbour to our galaxy), show an unusual double peak distribution of stars in their nuclei as can be seen in Figure 1.1 and 1.2.

  Double nucleus observed in both the galaxies and their ambient galaxies have subtle differences. Both M31 and NGC4486B are different morphologically; M31 is a spiral galaxy whereas NGC4486B is an elliptical galaxy. Physical separation of peak in NGC4486B is $5-7$ times larger than that of M31. Both the peaks in NGC4486B are at similar distances from photocenter in contrast with M31 for which the fainter peak is within $0.05''$ of the photocenter. Central surface brightness and peaks are

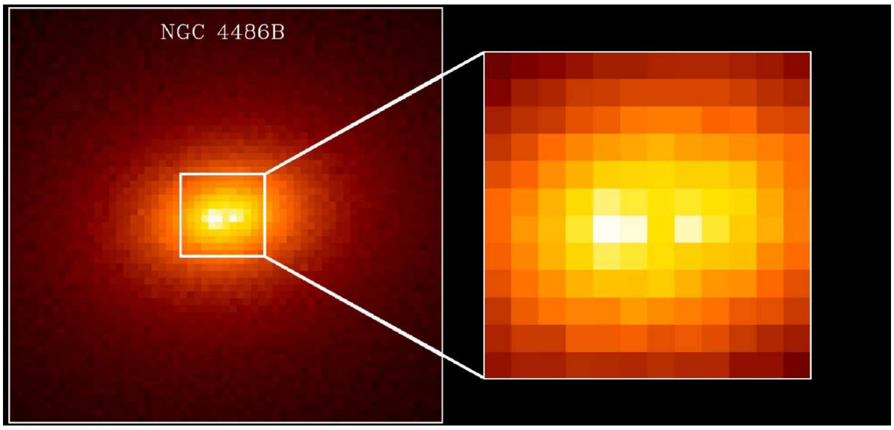

Figure 1.2: Image of NGC4486B (Credit: Karl Gebhardt (University of Michigan), Tod Lauer (NOAO), and NASA). Dimensions of left panel is 2.7 arcsec in sky and right panel is a blow-up of central 0.5 arcsec. Two brightness peaks comes out distinctively in the images.

more closely matched in NGC4486B as compared to M31. Bulge and nucleus in M31 are distinct components but surface brightness profile in NGC4486B shows no evidence of a distinct nucleus.

Observation of double peak nucleus in two morphologically different galaxies urges the need of a robust theoretical modeling for the nucleus in which this feature comes out naturally. Most promising model to explain such stellar distributions is an eccentric disc model proposed by Tremaine (1995), which is further explored in Bacon et al. (2001); Salow & Statler (2001); Sambhus & Sridhar (2002); Peiris & Tremaine (2003); Jalali & Tremaine (2012); Kazandjian & Touma (2013); Brown & Magorrian (2013) for M31. Also lopsidedness is observed in many galaxies at larger scales, and such asymmetries needs to be explained via robust modeling of galactic discs.

- **Debris discs:** Planetesimal discs detected through the thermal infrared emission or scattered star light by the dust component of the disc are called debris discs. Many of these discs are observed to be showing non-axisymmetric structures. For example: lopsided brightness distribution of scattered light, warp and clumps in the disc around β Pictoris, which is the second brightest star in the constellation Pictor (Heap et al., 2000; Telesco et al., 2000); spiral structure in HD 141569A (Clampin et al., 2003); clumpy rings in Vega (Marsh et al., 2006) and many more.

Most of these features are attributed to the presence of planets. In fact planets are also detected in some cases. However, Jalali & Tremaine (2012) proposed that most of these structures can also form due to *slow* $m = 1$ or 2 modes. Both these hypotheses can be distinguished from each other if motion of these features is followed for long time. For instance, features associated with slow modes will rotate with the disc at slower angular speeds whereas the ones due to presence of a planet will be rotating with the disc at same angular speed as that of the disc itself.

- **Other Discs:** Accretion discs in stellar mass binaries are also found to be asymmetric (for example see Mason et al. (2000)). One of the plausible reasons for such asymmetries can be $m = 1$ slow modes.

1.3 Motivation and plan of the thesis

- *Chapter 2*: Various types of discs present in astrophysical systems differ from each other in different ways, for instance; their composition, formation mechanism, etc. Dynamically these discs can be distinguished based on which force term dominates the non-Keplerian potential in the disc. The non-Keplerian potential is dominated by pressure gradient or self-gravity depending on if $\mathscr{M}/Q$ is less than or greater than unity respectively. Slow modes are studied in detail in Tremaine (2001) for a gas disc. In this paper he assumes that the self-gravity of the disc dominates pressure gradient (i.e, $\mathscr{M}/Q \gg 1$). However his analysis is not valid for thin accretion discs around stellar mass compact objects like white dwarfs and neutron stars, for which the pressure gradient is more important (i.e., $\mathscr{M}/Q \ll 1$). In Chapter 2 we study large scale $m = 1$ slow modes in thin accretion discs, where $Q \gg \mathscr{M} \gg 1$.
- *Chapter 3*: We next study the cases where the disc self-gravity dominates. In Chapter 3, we study slow $m = 1$ modes in counter-rotating discs, where the disc particles interact via softened-gravity. Of particular interest to this work is the model of Sambhus & Sridhar (2002), which included a few per cent of stars on retrograde (i.e. counter–rotating) orbits in a prograde disc orbiting a central BH to explain the lopsided stellar distribution in the nuclei of M31. Such retrograde orbits could be a result of infall of debris into the center of the galaxies. They proposed that these stars could have been accreted to the center of M31 in the form

of a globular cluster that spiraled-in due to the dynamical friction. For the infalling mass in galactic nuclei, the sense of rotation will be uncorrelated with respect to the pre-existing material. Thus in the course of evolution of a galaxy, it is probable that counter–rotating systems are generic. Recent simulations by Nixon et al. (2012) show breaking of disc in the vicinity of rapidly rotating central massive object, and hence generically forming counter–rotating discs. Such counter–rotating streams of matter are also thought to be helpful in feeding massive BHs at center of many galaxies.

Counter–rotating streams of matter in a self–gravitating disc are known to be unstable (Zang & Hohl, 1978; Araki, 1987; Sawamura, 1988; Merritt & Stiavelli, 1990; Palmer & Papaloizou, 1990; Sellwood & Merritt, 1994; Lovelace et al., 1997). The dynamics of galactic nuclei involve nearly Keplerian systems of stars or other collisionless matter (Rauch & Tremaine, 1996; Sridhar & Touma, 1999; Sridhar et al., 1999; Tremaine, 2001; Touma et al., 2009), and these are susceptible to various instabilities (Touma, 2002; Tremaine, 2005; Polyachenko et al., 2008; Sridhar & Saini, 2010). In particular Touma (2002) considered the linearized secular dynamics of particles orbiting a point mass, where particle orbits may be thought of as slowly deforming elliptical rings of small eccentricities. Pertinent to his work is the work of Tremaine (2001), who used softened gravity to understand slow modes of Keplerian discs. It is proposed by Tremaine (1995) that these eccentric modes are responsible for the lopsidedness of the nucleus of M31. Touma (2002) constructed unstable modes in counter–rotating nearly Keplerian systems. Modes are constructed analytically for a two-ring system and numerically for discs modeled via multiple–ring system. He demonstrated that a Keplerian axisymmetric disc is susceptible to a linear lopsided instability, even when only a small fraction of disc mass is in retrograde motion. Although he was able to handle counter–rotating hot Keplerian discs, he emphasized the need of considering a more accurate model of the disc.

Motivated by this, the corresponding problem for continuous discs was studied by Sridhar & Saini (2010), who proposed a simple model, with dynamics that could be studied largely analytically in the Wentzel–Kramers–Brillouin (WKB) approximation (see § 1.5). Their model consisted of a two–component zero pressure fluid disc where the disc particles interact via *softened* gravity[1] (explained in § 1.6), orbiting a massive central black hole. They used a short–wavelength (WKB) approximation, derived an analytical expression for the dispersion relation, and showed that the eigenfrequency ω is smaller than the Keplerian orbital frequency by a factor proportional to $\varepsilon = M_{\rm d}/M \ll 1$ (which is the ratio of the disc mass to mass of the central object); in other words, the modes are *slow*. The WKB dispersion relation was used to argue that equal mass counter–rotating discs with the same surface density profiles (i.e. when there is no net rotation) could have unstable modes. It was also argued that for an arbitrary mass ratio, the discs must be unrealistically hot to avoid an instability. Further, they used Bohr–Sommerfeld quantization to construct global modes within the WKB approximation. Some of the limitations of Sridhar & Saini (2010) were:

- ⊛ Wavelengths of modes could be the same order as the scale length of the discs; therefore the WKB approximation may only be marginally valid.
- ⊛ They could construct (WKB) global modes only for equal mass counter–rotating discs.
- ⊛ Their analysis gives only the growth rate of the modes and the could not infer the nature of wavefunctions due to the transcendental nature of the dispersion relation.
- ⊛ Softened gravity discs can only support $m = 1$ modes (where m is the azimuthal wavenumber).
- ⊛ Although softened gravity discs serve as a substitute for hot collisionless stellar discs, it is still a debatable approximation as far as robust modeling of stellar discs is concerned.

Therefore it is necessary to address the full eigenvalue problem to understand the systematic behaviour of such systems. We formulate and numerically solve the integral eigenvalue problem for slow $m = 1$ modes in a nearly Keplerian, softened gravity, counter–rotating, zero pressure fluid discs in Chapter 3. With this we still could not address the following issues:

---

[1] In rest of the thesis we refer these discs as softened gravity discs

- ⊛ We restricted ourself to softened-gravity discs, which support only $m = 1$ modes.
- ⊛ We treated the random motions in the discs by simplistic approach of softened–gravity potential in this chapter.

Both these approximations were a part of our analysis, and while having limitations, we shall see in later chapters that it is in fact not a bad approximation, and gives us a good picture of the physics of the problem that compares well with a more accurate but more involved treatment of the problem. In this chapter we aim to:

- √ Formulate and solve a coupled integral eigenvalue equation and use the WKB–approximation to compare the nature of solutions qualitatively.
- √ Construct global modes for an arbitrary mass fraction in counter–rotating discs.
- √ Calculate both the eigenvalues and the eigenfunctions.

- *Chapter 4—6*: Although (as will be explained in Chapter 3) the above model gives a reasonable realization of expected features in galactic nuclei of M31, it seems necessary to formulate the problem for a more realistic disc to overcome its limitations. Rather than softened-gravity disc, we next consider a collisionless disc. Motivation behind considering collisionless discs are: (1) Softened gravity disc considered in Ch. 3 only supports slow $m = 1$ modes. It was urgued by Jalali & Tremaine (2012) using the WKB-analysis that collisionless discs support modes with azimuthal wavenumber other than unity. However they focus largely on the properties of $m = 1$ modes. Higher m modes form an important new class of slow modes. For instance, $m = 2$ perturbations give rise to bar instabilities, which is an intrinsic feature of several spiral galaxies. (2) Softened–gravity prescription for potential, after all, gives an approximate behaviour of a realistic collisionless disc, which needs to be tested against this more accurate formulation. To this end, we formulate and study the above problem for collisionless discs, in which stellar orbits follows epicycles— which we describe in § 1.7—in Chapters 4—6:
  - In Ch. 4 we derive and analyze the WKB–dispersion relation for a collisionless self gravitating system of counter–rotating discs.
  - In Ch. 5 we derive an integral equation for collisionless system for non-local tightly-wound eigenmodes. We shall also give the local WKB-solution of the

integral equation derived.

  - In Ch. 6 we begin with reducing the integral equation derived in Ch. 5 to an integral eigenvalue problem for slow modes. Then we solve the eigenvalue equation numerically for a given unperturbed surface density profile and discuss the results obtained.

  Analysis done in these chapters overcomes most of the limitations of earlier works, and improves it by:

  - ✓ We use collisionless discs whose dynamics is governed by the potential of the central object (BH or star) and self–gravity of the disc, which is a more accurate description of galactic nuclei/debris discs.
  - ✓ We construct slow modes for all values of m.
  - ✓ We formulate and solve of both the WKB–dispersion relation and integral equation.
  - ✓ We can obtain both eigenvalues and eigenfunctions.

  Simulations involving linear perturbations in near Keplerian collisionless discs have been performed by Jalali & Tremaine (2012) using finite element method. We shall make a comparison with it in the relevant chapters.

- *Chapter 7*: Lastly, in Chapter 7, we offer some conclusions and discussions of the results obtained in this thesis, along with some of the unanswered questions and future directions.

Before we begin with the detailed study of problems that we aim to address in this thesis, we would like to discuss some basic equations and techniques/concepts which will be used in the due course of this thesis. We shall first describe basic equations used in this thesis in § 1.4 and then in § 1.5 we explain WKB–approximation. We explain the basis of a softened–gravity potential in § 1.6. An account of epicyclic orbits is given in § 1.7.

1.4 Basic equations

Ideally all systems can be regarded as a collection of particles, however small (like atoms or molecules of air in a room) or large (as stars in a galaxy) be the size of a particle. For such systems we can define a Distribution Function (DF) $f(\mathbf{x}, \mathbf{v}, t)$ in the phase-space, which gives the particle number density in six-dimensional space $(\mathbf{x}, \mathbf{v})$ at time t. For an electrically neutral medium, the time evolution of the DF is given by the *Boltzmann Equation.* In this thesis, we are interested in studying accretion discs around stellar mass compact objects (Chapter 2) and galactic/debris discs around a supermassive BH/stars (Chapter 3–6). In general, Boltzmann equation is applicable to both the systems, however using this would lead to tedious mathematics, which can be avoided if we use fluid equations which are valid for continuous medium (gas in our case).

Collisionless Boltzmann Equation:

It is a well established fact that collisions play an important role in attaining thermodynamic equilibrium in any physical system. But in certain systems like stellar component of galaxies, collisions are not important as can be seen from the following estimates. In case of stars in a galaxy, two body *relaxation time* $t_{\rm 2body}$ is the measure of time for collisional relaxation of star due to gravitational perturbations from other stars, which can be estimated as:

$$t_{\rm 2body} = n_{\rm 2body}\, t_{\rm cross},$$

where $n_{\rm 2body} \sim 0.1\,\mathcal{N}/\ln\mathcal{N}$ are the number of crossings required for stellar velocity to change by order of itself, $t_{\rm cross}$ is the stellar crossing time and $\mathcal{N}$ is the number of stars in a galaxy (Binney & Tremaine, 2008). Galaxies typically have $\mathcal{N} \simeq 10^{11}$, and are few crossing times old, implying that the relaxation time is several orders of magnitude larger than the age of the universe. Although, for stellar systems around massive BH in galactic nuclei, $t_{\rm 2body}$ can be longer than the age of the universe, but resonant relaxation times (Binney & Tremaine, 2008) can be shorter and relevant for the long-term evolution of the system. For times shorter than these, the stellar system can be assumed to be collisionless. Thus the DF obeys the *collisionless Boltzmann equation* (CBE):

$$\frac{{\rm d}f}{{\rm d}t} = 0, \tag{1.3}$$

where ${\rm d}/{\rm d}t$ is the Lagrangian or convective derivative.

Hydrodynamics:

We give the basic equations which determines the dynamical behaviour of non-viscous fluid (Ideal fluid):

Continuity equation: In a nutshell continuity equation is a mathematical representation of conservation of mass and can be stated as

$$\frac{\partial \rho}{\partial t} + \nabla.(\rho \mathbf{v}) = 0, \tag{1.4}$$

here ρ is mass density, and $\mathbf{v}$ is the velocity field.

Euler equation: is an equation for momentum conservation for non-viscous fluid;

$$\frac{\partial \mathbf{v}}{\partial t} + (\mathbf{v}.\nabla)\mathbf{v} = -\frac{1}{\rho}\nabla p + \mathbf{F}, \tag{1.5}$$

where p is the fluid pressure, and $\mathbf{F}$ is the external force per unit mass. Pressure is isotropic since we are only dealing with ideal fluids. The corresponding equation for viscid fluids is known as Navier–stokes equation. We do not intend to discuss it here, since we only deal with non–viscous fluids in this thesis.

These form a set of four equations, however we have five variables (ρ, three components of velocity $\mathbf{v}$, and p) and hence we need one more evolution equation to close the loop, which is the *energy conservation*, giving how temperature evolves with time. However, for a certain class of fluids such as *Barotropic fluids* the equation of state takes the form

$$p = p(\rho). \tag{1.6}$$

which gives the fifth equation and we need not consider the full energy conservation equation. These five equations with appropriate boundary conditions form a complete set of equations for ideal fluids. We shall be using this in our analysis in Chapter 2. Another example of such fluids under which energy conservation renders unimportant are incompressible fluids.

In accretion discs around stellar mass compact objects accreting matter, like most of the material in the universe, are in gaseous form. Thus the constituent particles interact directly via collisions, and thermodynamic equilibrium can be attained by means of collisional relaxation. Also, number densities and the length scales associated with them are large enough. Hence continuum model described above applies very well to accretion discs around stellar mass compact objects (Frank et al., 2002), which we discuss in Chapter 2.

Poisson equation:

For a self–gravitating system Poisson equation relates mass density of the system to the gravitational potential of the mass distribution. If the force $\mathbf{F}$ on a particle is due to the gravitational pull of the rest of the system with mass density ρ then $\mathbf{F}$ can be written as $-\nabla\Phi$, where Φ denotes the gravitational potential. Poisson equation relates the gravitational potential with density through

$$\nabla^2\Phi = 4\pi G\rho. \tag{1.7}$$

The above equation can also be written in integral form called the Poisson integral given by

$$\Phi(\mathbf{x}) = -G\int \mathrm{d}^3\mathbf{x}'\frac{\rho(\mathbf{x}')}{|\mathbf{x}'-\mathbf{x}|}. \tag{1.8}$$

For this section refer to: Choudhuri (1998); Binney & Tremaine (2008); Feynman et al. (1964-66)

1.5 WKB–approximation

Wentzel-Kramers-Brillouim(WKB)/Short wavelength/tight-winding or Quasi–classical (as it is commonly known in quantum mechanics) approximation is an indispensable tool for studying the properties of differentially rotating discs. We take a slightly different route to explain WKB-approximation. We first discuss it for quantum systems and then apply it to disc dynamics. Consider the one dimensional (x say) Schrodinger equation for a single particle of mass m,

$$\frac{\hbar^2}{2m}\frac{\mathrm{d}^2\Psi}{\mathrm{d}x^2} + (E - U(x))\Psi = 0. \tag{1.9}$$

Here E is the energy eigenvalue and $U(x)$ is the potential. Substitute in this equation the wave function of the form $\Psi = \exp(\mathrm{i}\Lambda(x)/\hbar)$, where $\Lambda(x)$ is in general a complex quantity. Then expand Λ as a series $\Lambda = \Lambda_0 + (\hbar/\mathrm{i})\Lambda_1 + (\hbar/\mathrm{i})^2\Lambda_2 + \ldots$, in powers of $\hbar$. Keeping terms to lowest order in $\hbar$, we get $\Lambda = \Lambda_0 = \pm\int p\,dx$, where $p = \sqrt{2m(E-U)}$

is the classical momentum. The approximation made here is legitimate if $|\hbar\Lambda''/\Lambda'^2| \ll 1$ which implies,

$$\left|\frac{\mathrm{d}}{\mathrm{d}x}\left(\lambda/2\pi\right)\right| \ll 1, \tag{1.10}$$

where the de-Broglie wavelength $\lambda = 2\pi\hbar/p$. In words this condition implies that wavelength of the particle must vary only slightly over distances of the order itself which is termed as the *Quasi-classical* approximation.

Let us now move from here to discuss tight-winding/short-wavelength/WKB approximation for density waves in differentially rotating discs which will lead us to a similar condition as Eq. (1.10) . If we perturb a gravitating disc, perturbations in all parts of the disc are coupled because gravity is a long range force, and the wave pattern must be determined numerically. In early 1960s, authors like Kalnajs, Lin and Toomre noted that for tightly wound density waves the coupling is negligible and such systems can be studied locally using analytical techniques. Reason for this can be understood using the following argument. Imagine a differentially rotating disc for which angular velocity depends explicitly on radius, R, and paint a stripe on it radially outward from center at time $t = 0$. As disc rotates the stripe tends to wind up and form a spiral pattern. After sufficiently long time, the pattern is quite tightly wound. At this stage this pattern can also be viewed as a rapidly oscillating wave as a function of radius R. In such a case the contribution from the perturbed surface density to its corresponding potential from far away regions cancel and only the local disturbances contribute.

The angle between the tangent to the spiral arm and circle '$R =$ *constant*' is called **Pitch angle**, and is given by

$$\cot(i) = \left|\frac{kR}{m}\right|, \tag{1.11}$$

where k is radial wavenumber and m is azimuthal wavenumber. Tight-winding approximation would imply that pitch angle is small, i.e. $\cot(i) \gg 1$ or $|kR| \gg m$. In other words, wavelength, which is proportional to $1/k$, is much smaller than the radius itself. This condition is same as the one derived in Eq. (1.10) . The one-to-one correspondence derived here supports the analogy drawn with the quasi-classical approximation used in quantum mechanics, and using the analogy the well known Bohr-Sommerfeld quantization condition is used to quantize the wavemodes.

To get an idea of how well the approximation holds in spiral galaxies, typical pitch angle for a spiral galaxy is between $10^\circ - 15^\circ$, which for two-armed spiral gives $|kR| \simeq$

$7 - 11$. Thus WKB approximation is valid for most of the galaxies but only marginally. For axisymmetric waves ($m = 0$) pitch angle is always zero that is $\cot(i) \gg 1$ and hence these are always tightly wound but wavelength may not be small. In such case approximation is valid if $|kR| \gg 1$. Thus, interchanging terms "tightly-wound" and "short-wavelength" should be done with caution. Also, for large values of azimuthal wavenumber, even though wavelength might not be small, but still $|kR| \sim m$ can be much greater than unity. In such cases this approximation is not valid. Having said that we point out that the results obtained using WKB approximation give reasonable match with exact solutions (as we shall also see in our calculations later in this thesis), therefore, it is reasonable to view it as a qualitative tool to understand the behaviour of waves in discs.
References for this section: Binney & Tremaine (2008), Landau & Lifshitz (1994)

1.6 Softened–gravity

Simplest description for gravitational potential between two gravitating bodies is the Newtonian potential, which goes as R^{-1}, where R is the distance between two masses. While modeling such systems numerically, in situations of close encounters, potentials would blow up. To avoid such computational glitches from such close encounters (i.e. $R \to 0$), Miller (1971) introduced a modified prescription for gravitational potential which goes as $(R^2 + b^2)^{-1/2}$, where b is called the softening length. Convenient way to think about such potential is to imagine it in 3-dimension. Consider a particle moving in $z = 0$ plane, then in this approximation the force on a test particle is measured b distance above the plane, that is in the plane $z = b$.

In the context of waves in discs, it is well known that the softening length mimics the epicyclic radius (epicyclic orbits are explained in § 1.7). Thus softened gravity discs can serve as an analog to collisionless stellar discs, and are much easier handle analytically and numerically as compared to stellar disc (Binney & Tremaine, 2008). Softening length should be chosen to be sufficiently small so that potential tends to R^{-1} for values of its argument larger than the softening length, but large enough to avoid singularities. Some limits on softening length appropriate for our calculation will be discussed later in Chapter 3 where we shall use softened gravitational potential. This shortcut has been happily adopted by the galactic dynamics community, which uses it to smoothen its way out of costly close encounters, on one hand, and to better represent the collisionless dynamics of their systems, on the other hand. However, as is evident from Tremaine (2001); Jalali & Tremaine (2012), softened gravity can be a surrogate for collisionless discs only for $m = 1$ slow modes. Softened gravity discs do not support $m > 1$ slow modes, whereas collisionless discs do. This is investigated in more detail in Ch. 4 – 6 of this thesis. References for this section: Miller (1971); Binney & Tremaine (2008)

1.7 The Schwarzschild distribution function

Consider an axisymmetric potential with z-axis as the axis of symmetry. It can be shown that for such a potential, particle at any radial location R in the disc oscillates around a mean radius as it revolves around the center (Binney & Tremaine, 2008). For most of the astrophysical discs this mean radius is the radius of circular orbit for a given angular momentum. Such near circular orbits are called *Epicyclic orbits*. Restricting the motion in the the disc plane ($z = 0$), the phase-space coordinates (R, ϕ, v_R, v_ϕ) under the epicyclic approximation are given by

$$\begin{aligned}
&R = R_g + X\cos(\kappa_g t + \psi),\\
&\phi = \phi_0 \,+\, \Omega_g t - \frac{\gamma(R)}{R} X\sin(\kappa_g t + \psi),\\
&v_R(R) = -\kappa_g X\sin(\kappa_g t + \psi),\\
&v_\phi(R) = v_c(R) - \frac{\kappa(R)}{\gamma(R)} X\cos(\kappa_g t + \psi),
\end{aligned} \tag{1.12}$$

where $\gamma(R) = 2\Omega(R)/\kappa(R)$; $v_c(R) = R\Omega(R)$ is the circular velocity; R_g is the mean radius of the orbit for a given angular momentum; X, ψ and ϕ_0 are epicyclic amplitude, the initial phase, and the initial azimuthal angle, respectively; $\kappa_g = \kappa(R_g)$ and $\Omega_g = \Omega(R_g)$. We can calculate the values of R_g, X, ψ and ϕ_0 using the boundary/initial conditions for the problem as we shall discuss later in this thesis.

DFs that are appropriate for cold discs for which the velocity dispersions are much smaller than the circular velocity are very important in understanding galactic nuclei or debris discs. Orbits in these discs are nearly-circular. As discussed above, epicyclic approximation is adequate to describe such orbits.

For motion of particles in a given potential, a function $I(\mathbf{x}(t), \mathbf{v}(t))$ is called an integral of motion if and only if satisfies

$$\frac{\mathrm{d}}{\mathrm{d}t} I(\mathbf{x}(t), \mathbf{v}(t)) = 0. \tag{1.13}$$

According to *Jeans Theorem*, any function of phase space coordinates is a steady-state solution of CBE if and only if it depends on the phase space coordinates through integrals of motion. For an axisymmetric potential, the integrals of motion are the Hamiltonian (or total energy) H and the z-component of angular momentum L_z. Hence the solution of CBE can be written as a function of both these integrals of motion, that is $f(H, L_z)$. Using the theory of epicyclic orbit, of which a brief account is given above, the solution of CBE for a razor thin disc with nearly circular orbits can be written as:

$$f(H(v_R, \tilde{v}_\phi), L_z) \equiv f(v_R, \tilde{v}_\phi, L_z) = \mathscr{S}(L_z) \exp\left(-\frac{v_R^2 + \gamma^2 \tilde{v}_\phi^2}{2\sigma_R^2(L_z)}\right), \tag{1.14}$$

where $L_z = R v_\phi(R)$ is the angular momentum of the orbit. σ_R is the radial component of the velocity dispersion, $\tilde{v}_\phi(R) = v_\phi(R) - v_c(R)$ is the difference between azimuthal & circular velocity at radius R, $v_R(R)$ is radial velocity at the current location. This DF is called the Schwarzschild distribution function. Note that for circular orbits, $\tilde{v}_\phi = 0$ and $v_R(R) = 0$. Also $f(v_R, \tilde{v}_\phi, L_z)$ is the mass density DF in the phase-space, unlike the probability density DF defined commonly.

Chapter 2

Slow Pressure Modes in Thin Accretion Discs

2.1 Introduction

Most of the stars are formed in binary systems. If one of the star in the binary is more massive than the other, the more massive star evolves more rapidly and reaches the end state of its life as a compact object: white dwarf, neutron star, or black hole, depending on its mass. However, the companion star may still be a main sequence star. At this stage the binary separation may shrink to a point such that the gravitational pull of compact object can remove the outer layer of the main sequence star which flows towards the compact star. Such an outflow is called Roche lobe overflow. Since the inflowing matter has angular momentum, it can not fall radially inward. Angular momentum is lost due to viscous torques and the infalling material spirals in to form a disc, such discs are called accretion disc. As the matter falls in, the gas releases energy and the disc becomes luminous. These discs form important sources of energy in the universe.

Disc around a stellar mass compact object have angular semi-thickness $\sim 0.01 - 0.05$ and hence can be considered as thin. For thin discs, Mach number $\mathscr{M}$ and Toomre Q parameter are defined in § 1.1. We here evaluate these numbers for accretion discs around various stellar mass compact objects. In Table 2.1 we give a comparison of some of the parameters for compact objects like white dwarf, neutron star, and stellar mass black hole. First column is the mass of the star $M_\star$ and second and third columns give the radius of the star $R_\star$ and mass accretion rate $\dot{M}$ on the star, respectively.

	$M_\star$	$R_\star$	$\dot{M}$	$\mathscr{M}$	Q
White dwarf	$0.5M_\odot$	10^9 cm	10^{16}g s^{-1}	50	10^9
Neutron star	$1.4M_\odot$	10^6 cm	10^{18}g s^{-1}	60	10^7
Black hole	$10M_\odot$	10^6 cm	10^{18}g s^{-1}	160	2×10^7

Table 2.1: Table of some of the parameters for stellar mass compact objects and accretion disc around them. First column gives the mass of star $M_\star$, second column is radius of star $R_\star$. $\dot{M}$ given in third column is the mass accretion rate. Fourth and fifth column gives mach number $\mathscr{M}$ & Toomre Q parameter for the accretion disc around the compact objects.

Next two columns are $\mathscr{M}$ and Q values for the respective accretion disc formed around them. To calculate these we require mass of the disc $M_{\rm d}$. Mass in the accretion discs is approximately equal to accretion rate times the diffusion time scale of the inflowing matter. If v_R is the radial velocity of the gas and L is the typical extend of the disc, L/v_R gives an estimate of the diffusion time scales. Typically, $v_R \sim 0.3 \times 10^5$ cm s^{-1} and $L \sim 5 \times 10^{10}$ cm for accretion discs around stellar mass compact objects. We use these numbers to calculate $M_{\rm d}$. Also the sound speed c_s, for thin accretion discs, is $\sim 10^6$ cm s^{-1}. All the numbers quoted here are typical estimates of these quantities as given in Frank et al. (2002). Substituting these in Eq. (1.1) & Eq. (1.2), we get an order of magnitude estimate of $\mathscr{M}$ and Q. On comparing fifth and sixth column, we get $Q \gg \mathscr{M} \gg 1$ for disc around these stars. In other words the dominant contribution to the non-Keplerian potential in the disc is due to pressure gradient. However, earlier studies of slow modes focused mainly on the effect of the self-gravity of the disc, where $Q \ll \mathscr{M}$ (Kato, 1983; Sridhar et al., 1999; Lee & Goodman, 1999; Sridhar & Touma, 1999; Tremaine, 2001). The goal of this chapter is to study large-scale $m = 1$ slow modes in thin accretion discs where $Q \gg \mathscr{M} \gg 1$. Asymmetric features observed in accretion discs (Mason et al., 2000), may possibly be due to these modes.

In § 2.2 we use the WKB approximation to establish that pressure gradient, in the absence of self-gravity, can enable slow $m = 1$ modes in thin accretion discs. The linear eigenvalue problem for slow pressure modes (or "p-modes") is formulated in § 2.3 for a flat barotropic disc, which is axisymmetric in its unperturbed state. When appropriate boundary conditions are chosen, the eigenvalue equation reduces to a Sturm-Liouville problem. Since the differential operator is self-adjoint, the eigenfrequencies are real:

therefore all p-modes are stable, and the eigenfunctions form a complete set of orthogonal functions. We also map the eigenvalue equation into a Schrodinger-like equation, which is useful in the interpretation of our numerical results. In § 2.4 we present numerical results for a variety of discs, namely (i) an approximation to the Shakura-Sunyaev thin disc, (ii) the Kuzmin disc which is more centrally concentrated, (iii) power-law discs. Of particular interest is the nature of the eigenfrequency: whether it is positive or negative. This has bearing on the excitation of these modes, because they are stable and will not grow spontaneously through a non-viscous instability. Comparison with earlier work, summary and conclusions follow in § 2.5.

2.2 Slow pressure modes

We start by considering a flat thin disc of ideal fluid orbiting a central mass M. The fluid is assumed to be barotropic and the disc is described by a surface density profile Σ. Although viscous forces are responsible for the accretion flows, in our analysis we ignore viscous forces, assuming that they adjust to maintain a quasi-stationary flow with a small radial velocity, and have little effect on the perturbed flow. Thus, we start with the continuity and Euler equations in cylindrical polar coordinates

$$\begin{aligned}
&\frac{\partial\Sigma}{\partial t} + \frac{1}{R}\frac{\partial}{\partial R}(R\Sigma v_R) + \frac{1}{R}\frac{\partial}{\partial\phi}(\Sigma v_\phi) = 0\,,\\
&\frac{\partial v_R}{\partial t} + v_R\frac{\partial v_R}{\partial R} + \frac{v_\phi}{R}\frac{\partial v_R}{\partial\phi} - \frac{{v_\phi}^2}{R} = -\frac{GM}{R^2} - \frac{\partial}{\partial R}(\Phi + h)\,,\\
&\frac{\partial v_\phi}{\partial t} + v_R\frac{\partial v_\phi}{\partial R} + \frac{v_\phi}{R}\frac{\partial v_\phi}{\partial\phi} + \frac{v_R v_\phi}{R} = -\frac{1}{R}\frac{\partial}{\partial\phi}(\Phi + h)\,,
\end{aligned} \tag{2.1}$$

where v_R and v_ϕ are the radial and azimuthal components of the fluid velocity, h is the enthalpy per unit mass, and Φ is the gravitational potential due to the disc. In writing the above equation we have taken our disc in $z = 0$ plane. For a barotropic fluid with an equation of state given by $p = D\Sigma^\Gamma$ (where $D > 0$ is a constant and Γ is the barotropic index), the isentropic sound speed and enthalpy are given by

$$c_s^2 = \Gamma\, D\, \Sigma^{\Gamma-1}\,, \tag{2.2}$$

$$h = \frac{\Gamma D}{\Gamma - 1}\Sigma^{\Gamma-1} = \frac{c_s^2}{\Gamma - 1}\,. \tag{2.3}$$

2.2.1 Precession rate in the unperturbed disc

We assume that the radial velocity of the unperturbed flow is much smaller than the azimuthal velocity and set it identically equal to zero; this assumption is justified below at the end of § 2.2.2. The unperturbed disc is assumed to be axisymmetric, therefore all ϕ derivatives are set to zero. Gas flows along circular orbits, with centrifugal balance maintained largely by the gravitational attraction of the central mass (with small but non trivial contributions from gas pressure gradient and disc self-gravity). The azimuthal and radial frequencies, $\Omega(R) > 0$ and $\kappa(R) > 0$, respectively, associated with nearly circular orbits are given by

$$\begin{aligned} \Omega^2(R) &= \frac{GM}{R^3} + \frac{1}{R}\frac{\mathrm{d}}{\mathrm{d}R}(\Phi_\mathrm{d} + h_\mathrm{d})\,, \\ \kappa^2(R) &= \frac{GM}{R^3} + \frac{\mathrm{d}^2}{\mathrm{d}R^2}(\Phi_\mathrm{d} + h_\mathrm{d}) + \frac{3}{R}\frac{\mathrm{d}}{\mathrm{d}R}(\Phi_\mathrm{d} + h_\mathrm{d})\,, \end{aligned} \tag{2.4}$$

where the subscript ‘d’ indicates unperturbed quantities. Note that the Mach number of the unperturbed flow $\mathscr{M}(R) = R\Omega(R)/c_s(R) \gg 1$. The dominant contribution to both $\Omega(R)$ and $\kappa(R)$ is due to the central mass, with small corrections coming from the disc self-gravity Φ_d, and enthalpy h_d. Let us define $\epsilon \ll 1$ as the larger of $(\Sigma_\mathrm{d} R^2/M)$ and $(h_\mathrm{d} R/GM)$. The apsides of a nearly circular orbit of a fluid element precess at a rate given by,

$$\begin{aligned} \dot{\varpi}(R) &= \Omega(R) - \kappa(R) \\ &= -\frac{1}{2\,\Omega(R)}\left(\frac{\mathrm{d}^2}{\mathrm{d}R^2} + \frac{2}{R}\frac{\mathrm{d}}{\mathrm{d}R}\right)(\Phi_\mathrm{d} + h_\mathrm{d}) + O(\epsilon^2)\,. \end{aligned} \tag{2.5}$$

Note that, in contrast to Tremaine (2001) we have retained the contribution from gradient of gas pressure (i.e. enthalpy) here. In fact, in thin accretion discs around compact stars, disc self-gravity is negligible and the contribution to $\dot{\varpi}$ is almost entirely from the gradient of gas pressure. The goal of this section is to establish that these discs have large-scale slow modes driven only by pressure gradient. In the WKB analysis of linear modes given below we follow the presentation due to Tremaine (2001).

2.2.2 The WKB approximation

We consider linear perturbations (of the velocity, surface density etc) of the form

$$A(R)\exp\left[\mathrm{i}\left(\int^{R} k(R)dR + m\phi - \omega t\right)\right], \tag{2.6}$$

where $k(R)$ and m are the radial and azimuthal wavenumbers, respectively, and ω is the angular frequency of the mode. In the tight-winding limit where $|k(R)R| \gg m$, a dispersion relation between ω and $k(R)$ can be derived (Safronov, 1960; Binney & Tremaine, 2008):

$$(\omega - m\Omega)^2 = \kappa^2 - 2\pi G\Sigma_{\mathrm{d}}|k| + c_s^2 k^2 \,. \tag{2.7}$$

As stated in § 1.1, the disc is stable to axisymmetric ($m = 0$) perturbations if and only if

$$Q \equiv \frac{c_s \kappa}{\pi G \Sigma_{\mathrm{d}}} > 1 \,. \tag{2.8}$$

This is readily satisfied in thin accretion discs around compact stars as shown in Table 2.1 . Tremaine (2001) showed that the dispersion relation for $m = 1$ modes can be written as

$$\omega = \dot{\varpi} + \frac{\pi G \Sigma_{\mathrm{d}}|k|}{\Omega} - \frac{c_s^2 k^2}{2\Omega} + \frac{1}{\Omega} O(\dot{\varpi}^2, \omega^2) \,. \tag{2.9}$$

In Tremaine (2001) it is argued that, when the pressure gradient is negligible compared to disc self-gravity (i.e. $c_s \approx 0$), the WKB dispersion relation of Eq. (2.9) admits large-scale ($|k(R)R| \sim 1$) modes with frequencies $\omega \sim \dot{\varpi} \sim (\Sigma_{\mathrm{d}} R^2/M)\Omega$. This implies that Mach number $\mathscr{M} \gg Q$. However, as we have argued in the introduction, this inequality is violated for thin accretion discs around compact stars where the opposite is true, i.e. $Q \gg \mathscr{M} \gg 1$. Hence we need to consider a situation that is complementary to the analysis of Tremaine (2001). Disc self-gravity being negligible in accretion discs, the precession rate is determined entirely by the gradient of gas pressure. Then equation (2.5) can be written as

$$\dot{\varpi} = -\frac{1}{2\,\Omega}\left[\frac{\mathrm{d}^2 h_{\mathrm{d}}}{\mathrm{d}R^2} + \frac{2}{R}\frac{\mathrm{d}h_{\mathrm{d}}}{\mathrm{d}R}\right] + O(1/\mathscr{M}^4) \sim \frac{\Omega}{\mathscr{M}^2} \,, \tag{2.10}$$

(see Kato (1983)) and we can approximate equation (2.9) as

$$\omega = \dot{\varpi} - \frac{c_s^2 k^2}{2\Omega} + \frac{1}{\Omega} O(\dot{\varpi}^2, \omega^2) \,. \tag{2.11}$$

For a disc with a non zero inner radius, eigenmodes must satisfy the Bohr-Sommerfeld quantization condition, given by

$$\oint k(R)\, dR = \left(n + \frac{3}{4}\right) 2\pi\,, \qquad n = 0, 1, 2, \ldots \tag{2.12}$$

Thus, there exists a *prima facie* case for modes with frequencies $\omega \sim \dot{\varpi}$, with radial wavenumbers,

$$k(R) \sim \left|\frac{\Omega\dot{\varpi}}{c_s^2}\right|^{1/2} \sim \frac{1}{R}\,, \tag{2.13}$$

comparable to the radial scale of the disc. However, this tentative conclusion is based on a WKB analysis which may not be valid for modes with $k(R)R \sim 1$. This is the motivation for our studies of the eigenvalue problem for slow modes given below. Henceforth we ignore disc self-gravity altogether and consider only the effect of gradient in gas pressure.

We now justify the assumption made at the beginning of § 2.2.1, that the radial velocity in the unperturbed disc is small, and may be ignored when studying slow modes. The time scale of radial spreading of the disc is, $t_{vis} \sim R^2/\nu \sim \mathscr{M}^2/(\alpha\Omega)$, where $\alpha \ll 1$ is the Shakura–Sunyaev viscosity parameter. The frequency of a slow mode is $\omega \sim \dot{\varpi} \sim \Omega\mathscr{M}^{-2}$. Therefore $\omega t_{vis} \sim \alpha^{-1} \gg 1$ implies that the radial spreading occurs over many slow mode periods.

2.3 Formulation of the eigenvalue problem

2.3.1 Eigenvalue equation

The linearized Euler, continuity and enthalpy equations that govern the perturbed flow are

$$\frac{\partial u_1}{\partial t} + \Omega(R)\frac{\partial u_1}{\partial \phi} - 2\Omega(R) v_1 = -\frac{\partial h_1}{\partial R}\,, \tag{2.14}$$

$$\frac{\partial v_1}{\partial t} + \Omega(R)\frac{\partial v_1}{\partial \phi} - 2B(R) u_1 = -\frac{1}{R}\frac{\partial h_1}{\partial \phi}\,, \tag{2.15}$$

$$\frac{\partial \Sigma_1}{\partial t} + \Omega(R)\frac{\partial \Sigma_1}{\partial \phi} + \frac{\Sigma_d}{R}\frac{\partial v_1}{\partial \phi} + \frac{1}{R}\frac{\partial}{\partial R}(R\Sigma_d u_1) = 0, \tag{2.16}$$

$$h_1 = c_s^2 \frac{\Sigma_1}{\Sigma_{\rm d}}, \tag{2.17}$$

where the subscript ‘d’ stands for the unperturbed quantities and ‘1’ stands for the first order perturbed quantities. u_1 and v_1 are the perturbed radial and azimuthal velocity components and c_s is the unperturbed sound speed. The Oort’s parameter $B(R)$ is related to the radial frequency through $\kappa^2(R) = -4\Omega(R)B(R)$.

We consider non-axisymmetric perturbations with azimuthal wave number $m = 1$, of the form $T_1 = T_a(R)\exp[\mathrm{i}(\phi - \omega t)]$, where T_1 stands for any perturbed quantity. Substituting this form in equations (2.14), (2.15), (2.16) and (2.17) yields

$$\mathrm{i}(\Omega-\omega)u_a - 2\Omega(R)v_a + \frac{\mathrm{d}h_a}{\mathrm{d}R} = 0\ , \tag{2.18}$$

$$\mathrm{i}(\Omega-\omega)v_a - 2B(R)u_a + \frac{\mathrm{i}h_a}{R} = 0\ , \tag{2.19}$$

$$\mathrm{i}(\Omega-\omega)\Sigma_a + \frac{\mathrm{i}\Sigma_\mathrm{d}v_a}{R} + \frac{1}{R}\frac{\mathrm{d}}{\mathrm{d}R}(R\Sigma_\mathrm{d}u_a) = 0\,, \tag{2.20}$$

$$h_a = c_s^2\frac{\Sigma_a}{\Sigma_\mathrm{d}}\,. \tag{2.21}$$

Solving equations (2.18) and (2.19) for the velocity amplitudes we obtain

$$u_a = -\frac{\mathrm{i}}{\Delta}\left[(\Omega-\omega)\frac{\mathrm{d}h_a}{\mathrm{d}R} + \frac{2\Omega}{R}h_a\right]\,, \tag{2.22}$$

$$v_a = \frac{1}{\Delta}\left[-2B\frac{\mathrm{d}h_a}{\mathrm{d}R} + \frac{\Omega-\omega}{R}h_a\right]\,, \tag{2.23}$$

where $\Delta = \kappa^2 - (\Omega-\omega)^2$. These equations, along with Eq. (2.21), when substituted in (2.20) yields

$$\left[\frac{\mathrm{d}^2}{\mathrm{d}R^2} + \left\{\frac{\mathrm{d}}{\mathrm{d}R}\ln\left(\frac{R\Sigma_\mathrm{d}}{\Delta}\right)\right\}\frac{\mathrm{d}}{\mathrm{d}R} + \frac{2\Omega}{R(\Omega-\omega)}\left\{\frac{\mathrm{d}}{\mathrm{d}R}\ln\left(\frac{\Sigma_\mathrm{d}\Omega}{\Delta}\right)\right\} - \frac{1}{R^2}\right]h_a = \frac{h_a\Delta}{c_s^2}, \tag{2.24}$$

which is the eigenvalue problem for *undriven modes*, with eigenvalue ω and eigenfunction h_a. This equation is a special case of equation (13) of Goldreich & Tremaine (1979); Tsang & Lai (2009), where $m = 1$, and the external and self gravity perturbations are set equal to zero. It can be noted that this equation becomes singular at $\Omega = \omega$ and $\Delta = 0$. The former corresponds to the Co–rotation Resonance (CR) and the latter corresponds to the Lindblad Resonance (LR). Below we discuss the validity of Eq. (2.24) at LR; a similar analysis holds for the singularity at co–rotation radius but we do not discuss it in this chapter since, as is argued later, for the slow modes the co–rotation radius has to lie outside the disc.

The system of equations (2.18)—(2.21) describe an undriven, autonomous system. At the LR the algebraic equations (2.18) and (2.19), become indeterminate if no conditions are imposed on the enthalpy perturbations h_a. It is easily seen that these equations become consistent if

$$-\frac{\mathrm{i}(\Omega-\omega)}{2B} = \frac{2\mathrm{i}\Omega}{(\Omega-\omega)} = \frac{\mathrm{d}h_a/\mathrm{d}R}{\mathrm{i}h_a/R}\,. \tag{2.25}$$

The first equality follows from $\Delta = 0$. Rearranging the second equality yields

$$\left[\frac{\mathrm{d}}{\mathrm{d}R}(R^2 h_a) - \frac{\omega}{\Omega}\left(R^2\frac{\mathrm{d}h_a}{\mathrm{d}R}\right)\right]\Bigg|_{\mathrm{LR}} = 0. \tag{2.26}$$

This condition must be satisfied at the LR's for all undriven modes. However, equation (2.26) may not be satisfied if the disc is driven by external forcing and may lead to more complicated dynamics around the LR and transport of angular momentum away from the LR due to external torquing (Goldreich & Tremaine, 1979). In this work we confine our investigations to modes of an undriven disc.

2.3.2 Slow mode approximation

We now make the ansatz that the perturbed flow supports frequencies that are small in comparison to the circular frequency, i.e., $|\omega| \ll \Omega$. Therefore, when $\omega \neq 0$, the disc must be finite, with outer radius such that the orbital frequency at the outer edge is much greater than $|\omega|$. Applying the slow mode approximation to equation (2.24) we obtain

$$\frac{c_s^2 R^{3/2}}{\Sigma_d\Omega}\frac{\mathrm{d}}{\mathrm{d}R}\left(\frac{\Sigma_d\Omega}{R^{3/2}\,\Delta}\frac{\mathrm{d}}{\mathrm{d}R}(R^2 h_a)\right) = R^2 h_a\,. \tag{2.27}$$

Similar to equation (2.24), equation (2.27) too is singular at the LRs. However the singularity at the co–rotation radius has gone away since this equation has been derived under the slow mode condition, $|\omega| \ll \Omega$. The condition $\Delta = 0$ implies that at some radius, either $\omega = \Omega - \kappa$ or $\omega = \Omega + \kappa$. The first one corresponds to the inner LR where as the second corresponds to the outer LR. Since $\kappa \simeq \Omega + O(\epsilon^2)$, we see that the second equality cannot be satisfied under the slow mode approximation. It is straightforward to see that the radius where this would be satisfied would be larger than the co-rotation radius due to the fact that the Keplerian circular frequency falls off monotonically with radius. Therefore, there are no outer LR singularities for slow modes. However, the Inner

Lindblad Radius (ILR), where $\omega = \dot{\varpi}(R)$, could very well lie inside the disc. Due to the fact that the disc surface density is completely arbitrary, there could in general be more than one ILRs. To make the problem well posed under the slow mode approximation, at the ILRs, the condition (2.26) reduces to

$$\frac{\mathrm{d}}{\mathrm{d}R}(R^2 h_a)\bigg|_{\mathrm{ILR}} = 0\,. \tag{2.28}$$

We shall see later that the numerical solutions of equation (2.30) satisfy this condition and the velocity amplitude at the ILR remains finite; thus the linear approximation remains valid and nothing special happens at the ILR.

From equation (2.10), $\dot{\varpi}/\Omega \simeq O(\mathscr{M}^{-2})$. This allows us to approximate $\kappa^2 \simeq \Omega^2$, leading to $B(R) \simeq -\Omega(R)/4$. Using these in equation (2.23) we obtain

$$\begin{aligned} v_a &= \frac{\Omega}{2\Delta}\left[\frac{\mathrm{d}h_a}{\mathrm{d}R} + \frac{2h_a}{R}\right], \\ &= \frac{\Omega}{2\Delta}\frac{1}{R^2}\frac{\mathrm{d}}{\mathrm{d}R}\left(R^2 h_a\right)\,. \end{aligned} \tag{2.29}$$

Differentiating equation (2.27) and using equation (2.29) we obtain,

$$\frac{\mathrm{d}}{\mathrm{d}R}\left[\left(\frac{c_s^2 R^{3/2}}{\Sigma_d \Omega}\right)\frac{\mathrm{d}\Theta}{\mathrm{d}R}\right] + \frac{2R^{3/2}}{\Sigma_d}(\dot{\varpi} - \omega)\Theta = 0\,, \tag{2.30}$$

where we have used the variable $\Theta = R^{1/2}\Sigma_{\mathrm{d}}\, v_a$ and $\Delta \simeq 2\Omega(\omega - \dot{\varpi})$, which is valid under the slow mode approximation.

2.3.3 Slow modes as a Sturm-Liouville problem

Before we proceed to specific examples, we have to choose the boundary conditions that we impose to solve equation (2.30) . We first cast the equation in a dimensionless form by choosing a radius $R_\star$, at which we evaluate various quantities, $\Sigma_\star, c_{s\star}, \dot{\varpi}_\star$ and $\Omega_\star$. We introduce the parameter $x = R/R_\star$, and similarly for a quantity H, we use $H' = H/H_\star$, leading to the Sturm-Liouville form of the eigenvalue equation

$$\frac{\mathrm{d}}{\mathrm{d}x}\left(\mathrm{P}(x)\frac{\mathrm{d}\Theta}{\mathrm{d}x}\right) + \left[\mathrm{Q}(x) + \lambda \mathrm{W}(x)\right]\Theta = 0\,, \tag{2.31}$$

where

$$\begin{aligned} \mathrm{P}(x) &= \frac{{c'_s}^2 x^{3/2}}{\Sigma'_{\mathrm{d}}\Omega'}, \quad \mathrm{W}(x) = \frac{2x^{3/2}}{\Sigma'_{\mathrm{d}}}, \\ \mathrm{Q}(x) &= \frac{2x^{3/2}\dot{\varpi}'}{\Sigma'_{\mathrm{d}}}, \quad \Theta = x^{1/2} v_a^1 \Sigma'_{\mathrm{d}}, \quad \lambda = -\frac{\omega {\mathscr{M}_\star}^2}{\Omega_\star}. \end{aligned} \tag{2.32}$$

In equation (2.31), λ is defined with a negative sign to make an explicit correspondence with the Schrödinger's equation, to be introduced in § 2.3.4. Henceforth in this chapter we reserve the term "eigenvalue" for λ, and use either "frequency" or "eigenfrequency" for ω.

We consider discs with an inner edge at R_{inner}, and an outer edge at R_{outer}, and we choose $R_\star = R_{\mathrm{inner}}$. We now argue that the parameters of the disc and the central mass for astrophysically interesting discs are such that the slow mode condition can be easily satisfied everywhere inside the disc. In a Keplerian disc the slow mode condition $|\omega| \ll \Omega$ is satisfied everywhere in the disc if it is satisfied at the disc outer radius, that is, $|\omega| \ll \Omega(R_{\mathrm{outer}})$, this leads to

$$\left(\frac{R_{\mathrm{outer}}}{R_\star}\right)^{3/2} \ll \frac{{\mathscr{M}_\star}^2}{|\lambda|}, \tag{2.33}$$

where we have used $\Omega(R_{\mathrm{outer}}) = \Omega_\star (R_\star/R_{\mathrm{outer}})^{3/2}$. Typical expected values for $\mathscr{M}_\star$, for the case of accretion discs around stellar mass compact objects, are in the range 10^4–10^6 (Frank et al., 2002). Most examples we consider have surface densities that decline by $R_{\mathrm{outer}}/R_\star \simeq 30$–$50$, therefore we see that for an eigenmode to be slow through out the disc, $|\lambda|$ has to be much smaller than $\sim 10^5$–10^9. We shall see in the examples that this condition is comfortably satisfied.

We integrate the eigen equation in the range $1 < x < x_{\mathrm{outer}}$, assuming that the perturbations obey the boundary conditions,

$$\Theta(1) = \Theta(x_{\mathrm{outer}}) = 0. \tag{2.34}$$

We note that these boundary conditions make the differential operator in equation (2.31) self-adjoint: *therefore the eigenvalues λ are real, and all slow p-modes are stable.* The complete set of eigenfunctions also form a complete basis; however, we note that not all eigenvalues are slow, and thus we do not expect this set to describe the evolution of arbitrary perturbations, but only the ones that obey the slow mode condition, $|\omega| \ll \Omega$.

2.3.4 Effective potential and WKB approximation

In the usual WKB approximation we substitute the trial solution

$$\Theta(x) = A(x)\exp\left[\frac{\mathrm{i}}{\mu}\int^{x}\tilde{k}\mathrm{d}x\right] , \tag{2.35}$$

in the following equation:

$$\mu^2\frac{\mathrm{d}}{\mathrm{d}x}\left(\mathrm{P}(x)\frac{\mathrm{d}\Theta}{\mathrm{d}x}\right) + \left(\mathrm{Q}(x) + \lambda\mathrm{W}(x)\right)\Theta = 0\,. \tag{2.36}$$

Here μ is an ordering parameter which is finally set equal to unity. $A(x)$ and $\tilde{k}(x)$ are the amplitude and the wavevector, respectively. Collecting terms of zeroth order in μ leads to the dispersion relation

$$\tilde{k}^2 = \frac{\mathrm{Q}(x) + \lambda\mathrm{W}(x)}{\mathrm{P}(x)} = \frac{2\Omega}{c_s^2}\left(\dot{\varpi} + \lambda\right) , \tag{2.37}$$

which is identical to Eq. (2.11). However we find that this dispersion relation, together with the Bohr-Sommerfeld quantization condition of Equation (2.12) predicts eigenvalues that compare poorly with those obtained from numerical integration of the Sturm-Liouville equation. Hence we have reformulated equation (2.31), using new variables $\vartheta(x) = \sqrt{\mathrm{P}(x)}$ and $\Psi = \sqrt{\mathrm{P}(x)}\Theta$. Then equation (2.31) takes the Schrödinger-like form

$$\Psi'' + K^2(x)\Psi = 0\,, \tag{2.38}$$

where

$$K^2(x) = \frac{1}{\vartheta^2(x)}\left[\mathrm{Q}(x) + \lambda\mathrm{W}(x) - \vartheta(x)\vartheta''(x)\right] , \tag{2.39}$$

which on defining $\mathrm{V}(x) = (-\mathrm{Q}(x) + \vartheta(x)\vartheta''(x))/\mathrm{W}(x)$ can be written as

$$K^2(x) = \frac{\mathrm{W}(x)}{\vartheta^2(x)}\left[\lambda - \mathrm{V}(x)\right] . \tag{2.40}$$

This dispersion relation differs from Eq. (2.11) and seems to better describe the numerical solutions, giving a match with the numerically obtained eigenvalues up to a few percent, as can be seen in Table 2.2.

Note that $K^2(x)$ in Eq. (2.40) differs from the standard form for the Schrödinger equation by the factor $\mathrm{W}(x)/\vartheta^2(x)$. However, it is very useful for discussions of the turning points, where $K^2(x) = 0$, separating classically accessible regions from the forbidden ones. The solution is oscillatory where $K^2 > 0$, implying $\lambda > \mathrm{V}(x)$, and damped otherwise. Since the disc is finite the eigen spectrum is always discrete and there are two distinct types of spectra:

Type I: This occurs when there is at least one turning point within the disc. In the case of a single turning point we can have oscillatory solution on either side of the turning point, depending on the form of $K^2(x)$. If there are more than one turning point then we could either have oscillatory behaviour confined between the turning points or outside, such as the case of the Shakura-Sunyaev disc discussed in § 2.4.

Type II: This occurs when there are no turning points within the disc and the discreteness of the spectra depends entirely on the size of the disc.

To obtain real eigenvalues we need to consider the possibility of satisfying $K^2 > 0$ in a bounded region, which could either be bounded by one or both of the disc boundaries or by turning points. Thus a useful first step is to plot this potential for the problem at hand. If the potential allows regions that can support bound states, we search for solutions numerically, and to verify our results we use the WKB approximation.

Let us consider the case of the Shakura-Sunyaev disc shown in Fig 2.1. On the negative side the potential blows up at the inner edge at $x = 1$, where the perturbations are assumed to vanish. If $\lambda < 0$ is to be a valid eigenvalue, then it must satisfy the quantization condition

$$\int_1^a K(x)\,dx = \left(n + \frac{3}{4}\right)\pi\,, \qquad n = 0, 1, 2, \ldots \tag{2.41}$$

where, $x = a > 1$ is a turning point which separates a classically accessible region (I) on the left from a forbidden region (II) on the right. The case of positive eigenvalues, $\lambda > 0$, is more interesting. If the eigenvalue is positive and smaller than the maximum value of $\mathrm{V}(x)$, then there are two turning points (say, $x = a, b$ with $b > a$) separating three distinct regions. The classically forbidden region lies between $x = a$ and $x = b$, separating the two classically accessible regions $(1, a)$ and (b, x_{outer}). If λ is greater then

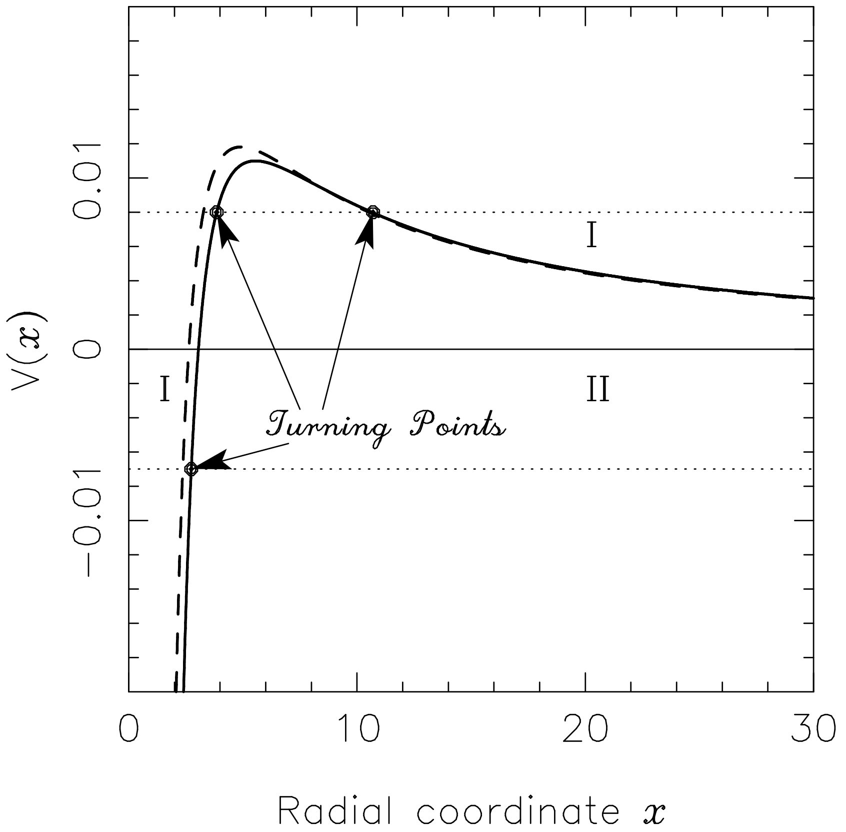

Figure 2.1: The effective potentials for our barotropic approximations to the Shakura-Sunyaev disc. The solid line corresponds to $\mathrm{V}_1(x)$ and the dashed line to $\mathrm{V}_2(x)$, described in § 2.4.1. The positive values of λ can provide both Type I and Type II eigenvalues as described in the § 2.3.4. The negative values, although seemingly allowing eigenstates lead to no such solution. Note that positive values of λ correspond to the negative frequency modes.

the maximum of $\mathrm{V}(x)$, then whole disc is classically allowed. Below we present numerical results on eigenvalues and eigenfunctions, and use WKB approximation to understand them. It turns out that WKB approximation is very useful even for the case of small quantum numbers.

2.4 Numerical results

As discussed in the last section, we consider a finite disc and we expect the spectra of Eq (2.31) to be discrete. These modes would have observational consequences since they would rotate at a fixed pattern speed. The perturbations in the enthalpy would lead to azimuthal variations in the temperature and density across the disc, which might be observable depending on the amplitude of perturbations.

Since very little is known about the surface density profiles of the discs we carry out calculations based on certain standard forms of the disc as test cases. We also consider the generic power law profile. Some of the profiles considered below are formally infinite in size, however as noted above, we need to keep the disc finite. This would imply that the surface density would abruptly fall to zero at the outer disc radius. This is unphysical and we expect that there would be a thin transition region that would deviate from the density profile being considered near $x_{\rm outer}$. If the eigenvalues and eigenmodes are not very sensitive to $x_{\rm outer}$, then this is not an issue and in our numerical investigation we indeed find this to be true.

2.4.1 Shakura-Sunyaev discs

We first consider the standard model of an accretion disc proposed by Shakura and Sunyaev and is associated by their names (Shakura & Sunyaev, 1973). This model is the simplest solution of steady state equations for accretion discs with turbulent viscosity, which is proportional to the product of the size of the largest turbulent cell and velocity of the turbulence cell relative to the mean gas flow. Typical size of the largest turbulent cell cannot exceed the disc scale height, H. Second, it is unlikely that the turbulent velocity is supersonic, as in this case, the turbulent motions would probably be thermalized by shocks. Hence viscosity, $\nu \simeq \alpha c_s H$, where $\alpha \lesssim 1$ is a dimensionless parameter. Though in our analysis we assume viscous forces to adjust to balance small quasi–stationary radial flow and neglect them but still use Shakura-Sunyaev (SS) disc model as one of the test model because this is most widely used model for accretion discs around stellar mass compact objects. SS disc is also called as standard disc.

The surface density and temperature of this disc are given by (see Frank et al. (2002)):

$$\Sigma_{\rm SS} = 5.2\,\alpha^{-4/5}\dot{M}_{16}^{7/10}{m_1}^{1/4}{R_{10}}^{-3/4}f^{14/5}\ {\rm g\ cm^{-2}}\,, \tag{2.42}$$

$$T_{\rm SS} = 1.4\times10^{4}\alpha^{-1/5}\dot{M}_{16}^{3/10}{m_1}^{1/4}{R_{10}}^{-3/4}f^{6/5}\,{\rm K}\,, \tag{2.43}$$

where

$$f = \left[1 - \left(\frac{R_*}{R_{10}}\right)^{1/2}\right]^{1/4} . \tag{2.44}$$

$\dot{M}_{16}$ is the mass accretion rate in the units of 10^{16}g s^{-1}, m_1 is the mass of disc in solar mass units, R_{10} is radius in the units of 10^{10}cm, R_* is the radius of the central object in the units of 10^{10}cm, and α is the Shakura-Sunyaev viscosity parameter.

Although the SS disc is not based on a barotropic model, we find that a barotropic disc with index $\Gamma = 2$ serves as a reasonable approximation. We have considered two cases:

1. Choosing $\Sigma_{\rm d} = \Sigma_{\rm SS}$ of equation (2.42), and deriving the temperature profile for $\Gamma = 2$, we find that the temperature and effective potential are

$$\begin{aligned} T_d(x) &= x^{-3/4} f^{14/5}(x), \\ \mathrm{V}_1(x) &= \frac{344 - 590\sqrt{x} + 225x}{800\, x^{9/4}\,(1 - \sqrt{1/x})^{13/10}}\,, \end{aligned} \tag{2.45}$$

2. Choosing $T_{\rm d} = T_{\rm SS}$ of equation (2.43), and deriving the surface density profile for $\Gamma = 2$, we find that the effective potential is

$$\mathrm{V}_2(x) = \frac{12 - 22\sqrt{x} + 9x}{32\, x^{9/4}\,(1 - \sqrt{1/x})^{3/2}}\,, \tag{2.46}$$

where we have used the natural length scale given by the inner disc radius, which we have adopted for conversion of our eigen equation into a dimensionless form. For comparison between SS disc and barotropic assumption of standard disc with index $\Gamma = 2$ and to see the validity of our assumption we plot in Fig 2.2 both $T_{\rm d}(x)$ (defined in Eq. (2.45)) marked as *Barotropic Disc*, and $T_{\rm SS}(x)$ marked as *Standard Disc*. Comparison of two gives us a reasonable confidence in our assumption. Figure 2.1 shows, $\mathrm{V}_1(x)$ and $\mathrm{V}_2(x)$ are also quite similar to each other. The effective potential blows up at the inner edge of the disc and steadily climbs up above zero and then decreases asymptotically. In the immediate vicinity of the inner edge a negative λ gives an oscillatory solution, and to the right of it is a classical turning point. Beyond the turning point the solution is exponentially decaying. This suggests that discrete, Type I, negative eigenvalues might exist, however, both the numerical search and the WKB quantization condition

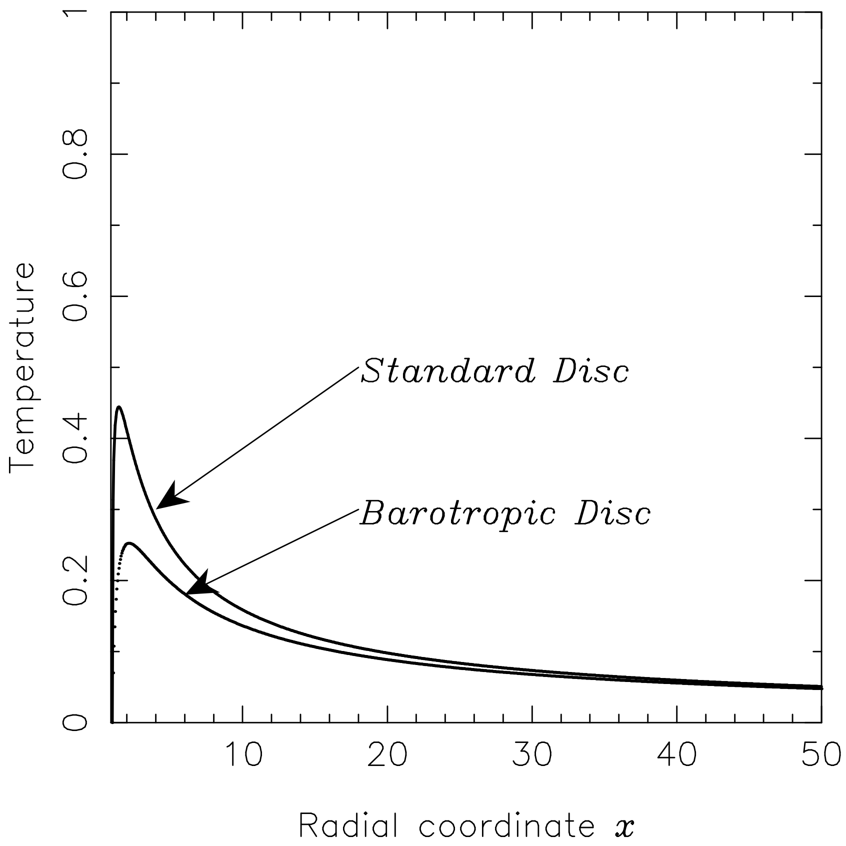

Figure 2.2: Normalized Temperature profile for standard Disc, $T_{\rm SS}$, and barotropic assumption of standard Disc, $T_{\rm d}$ are displayed. Both $T_{\rm SS}$ and $T_{\rm d}$ are defined in § 2.4.1. Plots are labeled appropriately. Nearly similar profiles justify appproximating standard disc as barotropic disc with $\Gamma = 2$.

(2.41), fail to find such discrete eigenvalues. For $0 < \lambda \lesssim 0.01$, we find discrete, Type I eigenvalues for which the oscillatory behaviour is outside the region bounded by two turning points. For $\lambda \gtrsim 0.01$, we find discrete eigenvalues of Type II, where the separation between neighbouring eigenvalues decreases with increasing values of the outer radius of the disc.

2.4.2 The Kuzmin disc

In contrast to the SS discs, the Kuzmin disc has a centrally concentrated surface density, and hence offers a distinct case to study slow modes. For comparison see Fig. 2.3 where we have plotted surface density normalized to unity for both Kuzmin disc (with dotted line) and Standard disc ($\Sigma_{\rm SS}$, with solid line). The surface density profile in this case is given by

$$\Sigma_{\rm d}(R) = \frac{aM_{\rm d}}{2\pi\,(R^2+a^2)^{3/2}}\,, \tag{2.47}$$

where $M_{\rm d}$ is the mass in the disc and a is the core radius. The surface density extends all the way to $R = 0$. If we take a as the size of the inner radius of the disc then we can rescale our equation by choosing $R_\star = a$, leading to;

$$\begin{aligned}
\mathrm{P}(x) &= \frac{x^3}{(1+x^2)^{(3\Gamma-6)/2}},\\
\mathrm{Q}(x) &= \frac{3x^3(x^2(4-3\Gamma)+3)}{(1+x^2)^{(3\Gamma-2)/2}},\\
\mathrm{W}(x) &= x^{3/2}(1+x^2)^{3/2},\\
\mathrm{V}(x) &= \frac{3(x^4(5-4\Gamma+3\Gamma^2)+x^2(6-8\Gamma)+1)}{8x^{1/2}(1+x^2)^{(3\Gamma+1)/2}}.
\end{aligned} \tag{2.48}$$

- **Γ value**: Before we do any further analysis we need to look for a suitable value of gamma. For slow modes to be valid, Ω should be much greater than the precession frequency, $\dot\varpi$, that is,

  $$\frac{\Omega}{\dot\varpi} \gg 1.$$

  Since Ω for nearly Keplerian discs decreases as we go towards larger radii, and $\dot\varpi$ is equal to $\mathrm{Q}(x)/\mathrm{W}(x)$, we see that for large value of x, $\Omega/\dot\varpi$ goes as $x^{3\Gamma-4}$. This is clearly much greater than 1 for large x if and only if $\Gamma \geq 4/3$. Here onwards we take gamma equals $4/3$.

In Fig. 2.4 we have plotted this potential for $\Gamma = 4/3$. As may be seen, this case qualitatively resembles Fig. 2.1, and the discussion in § 2.3.4 carries through. For negative values of λ, we can infer from Fig. 2.4 that $K^2(x) < 0$, so wave like solutions are not possible. For positive values of λ in the range $0 < \lambda \lesssim 0.3$, we can have Type I eigenvalues, but this region of λ is further divided into two parts: for $0 < \lambda \leq \mathrm{V}(1)$, there is only one turning point and oscillatory behaviour is possible for radius greater than the turning point, and for $\mathrm{V}(1) < \lambda \lesssim 0.3$ there are two turning points and oscillatory behaviour is possible outside the region bounded by the two turning points. For $\lambda \gtrsim 0.3$ the eigenvalues are of Type II. This behaviour is confirmed by numerical integration of the eigenvalue equation. We can also admit values of Γ other than 4/3. However, the effective potential in Eq. (2.48) retains the general shape of Fig. 2.4, and the conclusions stated above remain valid.

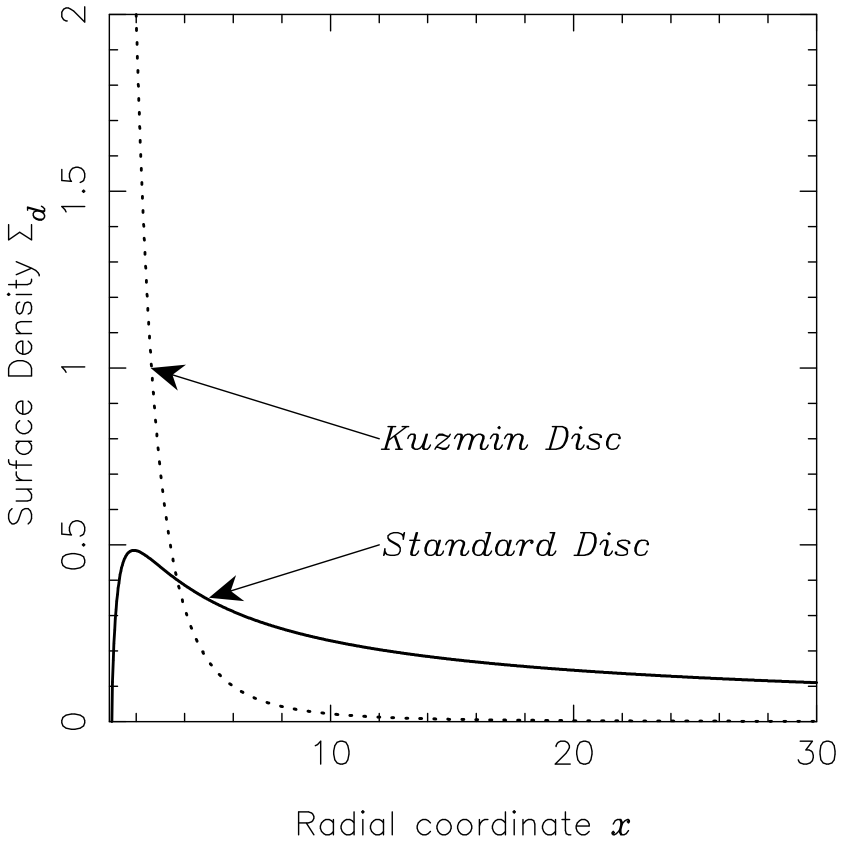

Figure 2.3: Comparison of surface density profile for Kuzmin disc and standard disc. Dotted curve is for Kuzmin disc and solid line is for standard disc model.

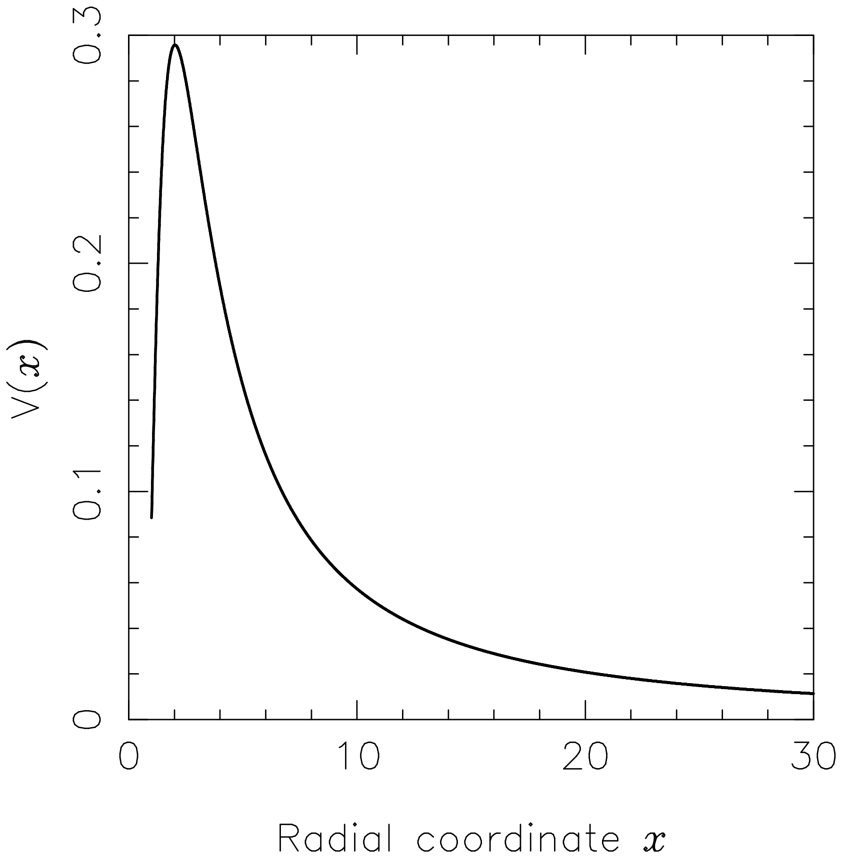

Figure 2.4: The effective potential for the Kuzmin disc is displayed here. Positive values of λ lead to a discrete spectrum of both Type I and Type II eigenvalues. There are no negative eigenvalues.

2.4.3 Power law discs

Certain physical models (e.g. Narayan & Yi (1994)) naturally lead to scale invariant discs that follow a power law profile. Although in these models there are no associated length scales, we choose to truncate the disc at the inner disc radius thus leading to the form

$$\Sigma_0 = \Sigma_\star \, x^{\beta} \,, \tag{2.49}$$

where, $\Sigma_\star = \Sigma(R_\star)$ and β is the power law index. The potential is given by

$$\mathrm{V}(x) = C(\beta,\Gamma) x^{\nu(\beta,\Gamma)} \,, \tag{2.50}$$

where

$$\begin{aligned} C(\beta,\Gamma) &= \frac{1}{8}\left(3 + \beta\left(-4 + \Gamma(4 + \beta\Gamma)\right)\right) \,, & (2.51) \\ \nu(\beta,\Gamma) &= \beta\Gamma - \beta - 1/2 \,. & (2.52) \end{aligned}$$

There are four distinct possibilities:

1. $C(\beta,\Gamma) < 0$, $\nu(\beta,\Gamma) < 0$: The region in $\beta - \Gamma$ space satisfying these conditions is plotted in Fig. 2.5 . The regions where these conditions are satisfied are those with (1) β positive and Γ negative or (2) very small negative β and very large Γ. Both these cases are unphysical. Note that there is a region with large, positive β, and small, positive Γ, and these are also physically uninteresting.

2. $C(\beta,\Gamma) < 0$, $\nu(\beta,\Gamma) > 0$: It can be verified that $\nu(\beta,\Gamma) > 0 \Leftrightarrow \beta\Gamma > \beta + 1/2$, for which $C(\beta,\Gamma)$ is always positive and hence it is impossible to satisfy these conditions.

3. $C(\beta,\Gamma) > 0$, $\nu(\beta,\Gamma) > 0$: These two constraints give us a region in the $\beta - \Gamma$ space, displayed in Fig. 2.6, that admits physically reasonable values. We display effective potential for $\beta = \Gamma = 2$ in Fig. 2.7. For $\mathrm{V}(x_{\mathrm{inner}}) < \lambda < \mathrm{V}(x_{\mathrm{outer}})$, we have one turning point admitting Type I eigenvalues. In Fig. 2.8 we plot two examples of eigenmodes for the same case. The eigenfunctions for small quantum numbers are found to be centrally concentrated while they extend to larger radii for larger quantum numbers. It should be noted that our solutions are regular at turning point (approximately close to ILR), which is the point where the solution changes

from an oscillatory behaviour to an exponentially decaying one. The first few eigenvalues for this case are tabulated in Table 2.2, where we find an excellent match with the WKB eigenvalues. In Table 2.2, we also display the numerical eigenvalues corresponding to $x_{\text{outer}} = 50$ and 200 in third and fourth column respectively. Close match between the eigenvalues in third and forth column shows that eigenvalues are not very sensitive to precise value of x_{outer}. Outside this range of positive λ (that is for $\lambda > \mathrm{V}(x_{\text{outer}})$) there are no turning points and hence only Type II eigenvalues are possible. Similar conclusions hold for other allowed values of β and Γ.

4. $C(\beta, \Gamma) > 0$, $\nu(\beta, \Gamma) < 0$: The region in β–Γ space satisfying these constraints is plotted in Fig. 2.9. Effective potential for this case for $\beta = -2, \Gamma = 2$ is plotted in Fig. 2.10. For $0 < \lambda < \mathrm{V}(1)$, we have one turning point admitting Type I eigenvalues. Here the classically accessible region is bounded by the turning point on left and x_{outer} on right. Numerical solution for $\beta = -2$ and $\Gamma = 2$ are plotted in Fig. 2.11. Comparison with Fig. 2.8 shows that the solutions are more radially extended, with well separated peaks. For $\lambda > \mathrm{V}(1)$ there is no turning point and the eigenvalues are of Type II. Rest all values of allowed β and Γ show similar trends.

2.5 Discussion and conclusions

We have presented a theory of slow $m = 1$ linear pressure modes (or “p-modes”) in thin accretion discs around massive compact objects, such as white dwarfs and neutron star, in this chapter. These modes are enabled by the small deviation from a purely Keplerian flow, due to gradient in fluid pressure rather than disc self-gravity. For simplicity we have taken the fluid to be barotropic. Our formulation largely follows that of Tremaine (2001), although there is a key difference: using the WKB approximation, Tremaine (2001) argued that fluid discs for which disc self-gravity dominates fluid pressure gradient can support slow modes, if the Mach number $\mathscr{M}$ is much larger than the Toomre Q parameter. This condition may be satisfied in relatively cool discs, but not for thin accretion discs around white dwarfs or neutron stars. In these discs $Q \gg \mathscr{M} \gg 1$, and the analysis in Tremaine (2001) does not apply, because disc self-gravity is negligible when compared with fluid pressure gradient in thin accretion discs. This implies that

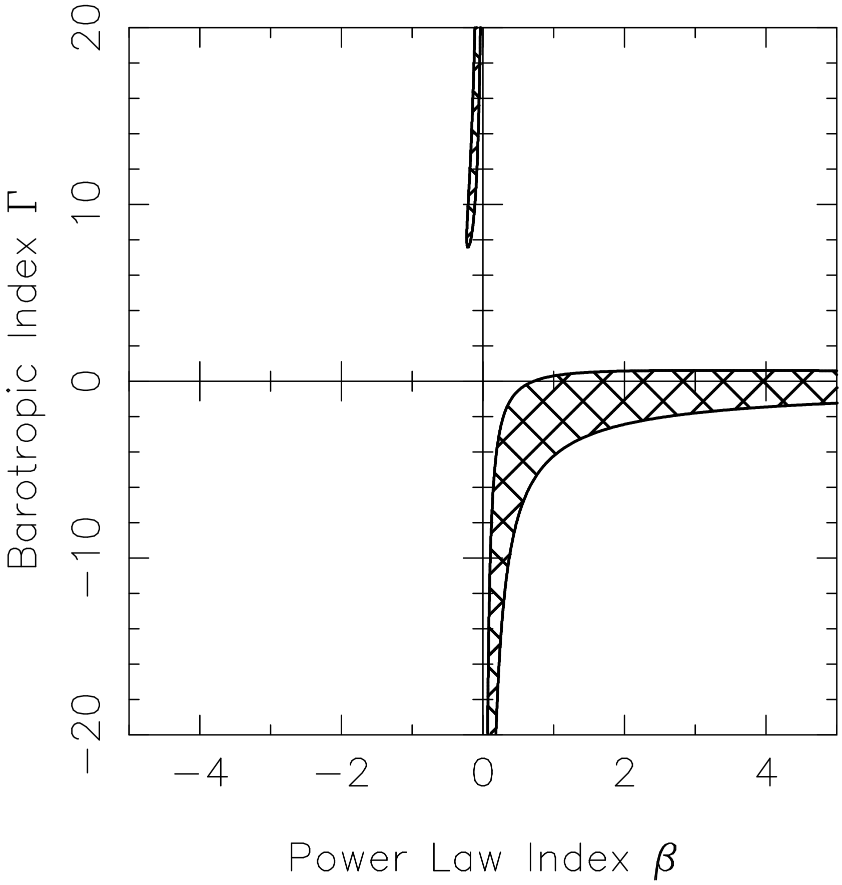

Figure 2.5: The allowed region (cross-hatched) in the β - Γ space to obtain Type I negative eigenvalues (corresponding to the positive frequency modes) for the power law discs (case (1), discussed in § 2.4.3). Most of the region is either unphysical or uninteresting.

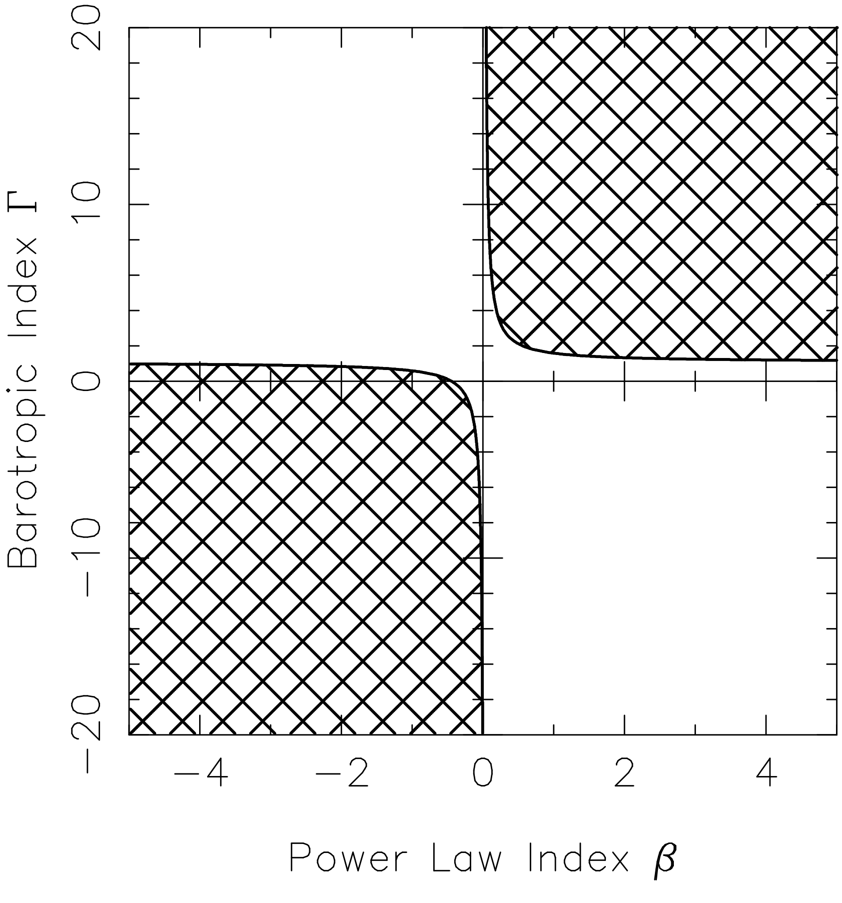

Figure 2.6: The allowed region (cross-hatched) in the β - Γ space to obtain discrete positive eigenvalues (corresponding to the negative frequency modes), corresponding to Type I eigenvalues for case (3), for the power law discs.

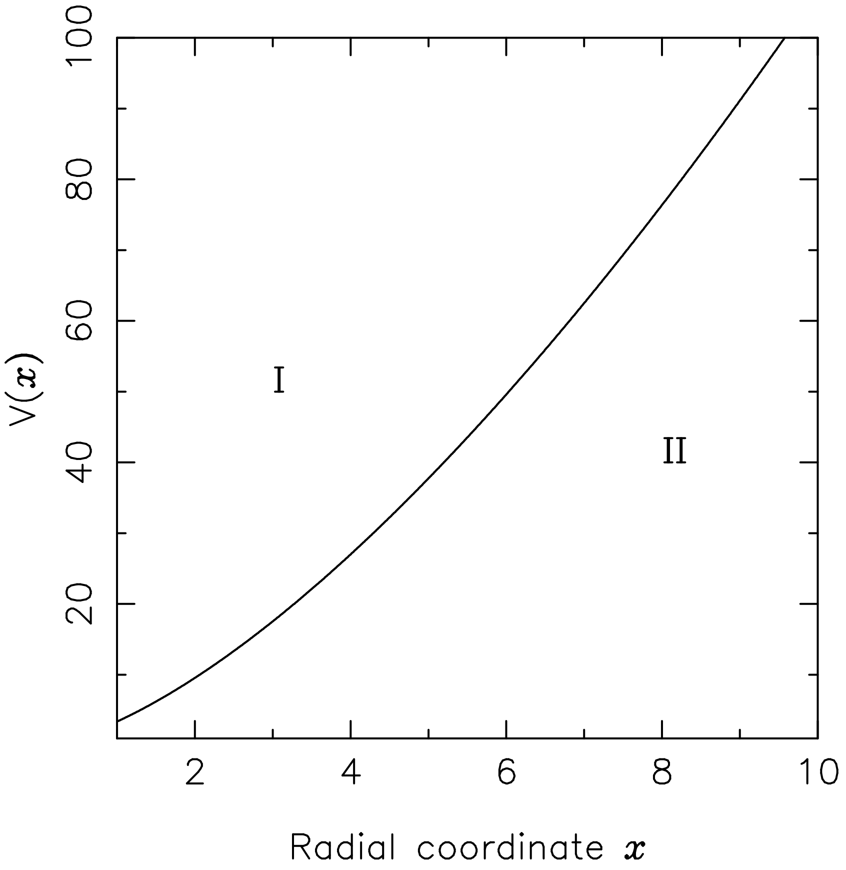

Figure 2.7: Effective potential for power law disc for $\beta = \Gamma = 2$. Region marked ‘I’ is classically accessible whereas the one marked with ‘II’ is forbidden region.

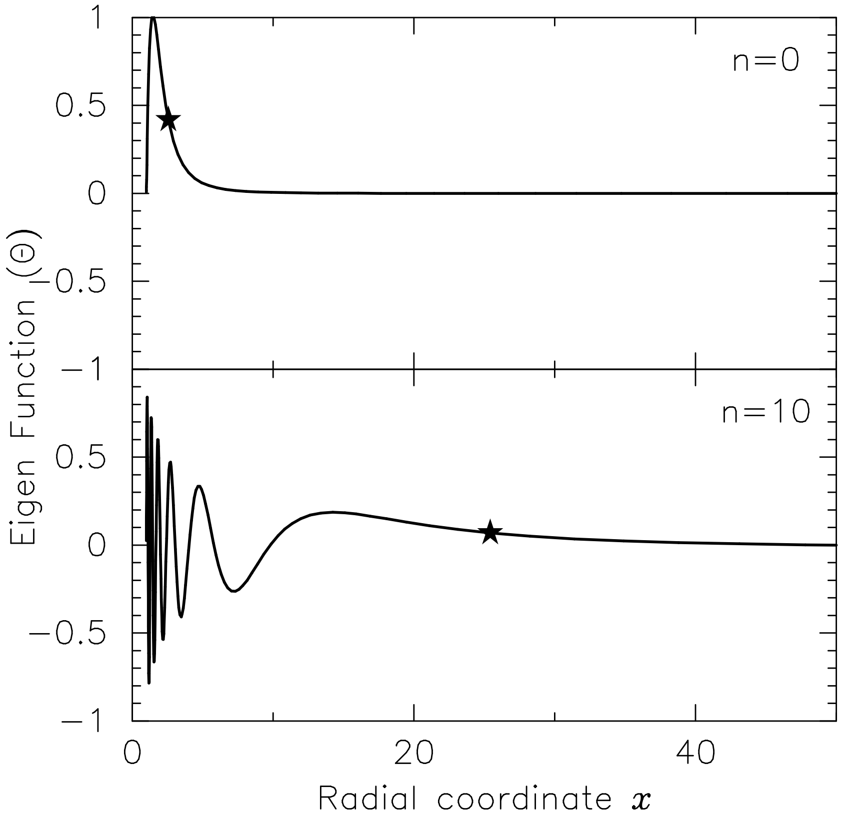

Figure 2.8: Two eigenfunctions (Type-I eigenvalue) obtained for the power law case (case (3)) with $\beta = \Gamma = 2$. The higher quantum number leads to a more radially extended eigenmode. Star marks the position of the turning point.

n	WKB λ	Numerical λ_{50}	Numerical λ_{200}
0	13.42	13.86	13.86
1	30.15	30.73	30.73
2	52.31	53.06	53.06
3	79.99	80.92	80.91
4	113.22	114.32	114.31
5	151.99	153.29	153.26
6	196.31	197.83	197.75
7	246.18	247.96	247.80
8	301.60	303.72	303.40
9	362.57	365.16	364.54
10	429.09	432.31	431.24

Table 2.2: The eigenvalues for the power law model with $\beta = \Gamma = 2$ are tabulated here for comparison between those obtained numerically and those obtained using the WKB approximation. The values in columns λ_{50} and λ_{200} are the eigenvalues corresponding to $x_{\text{outer}} = 50$ and 200, respectively. The match between numerical and WKB eigenvalues is within a few per cent, and remains good even for small quantum numbers. Eigenvalues are not very sensitive to precise value of x_{outer}.

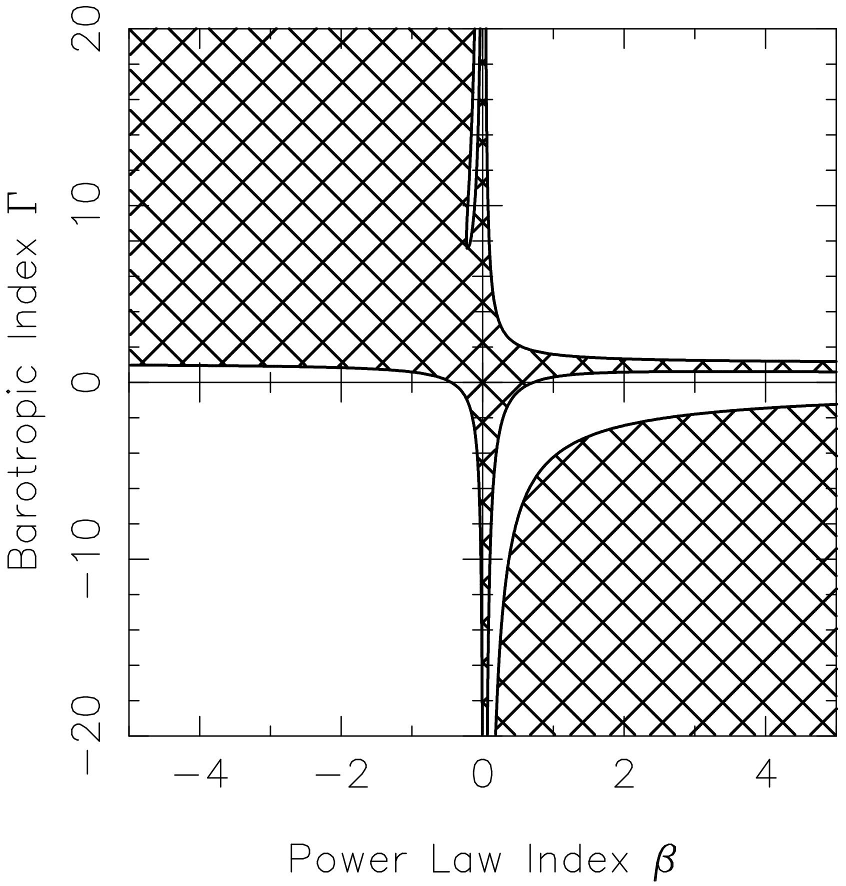

Figure 2.9: The allowed region (cross-hatched) in the β - Γ space for the positive Type I eigenvalues (corresponding to negative frequency eigenmodes), for case (4) for the power law discs.

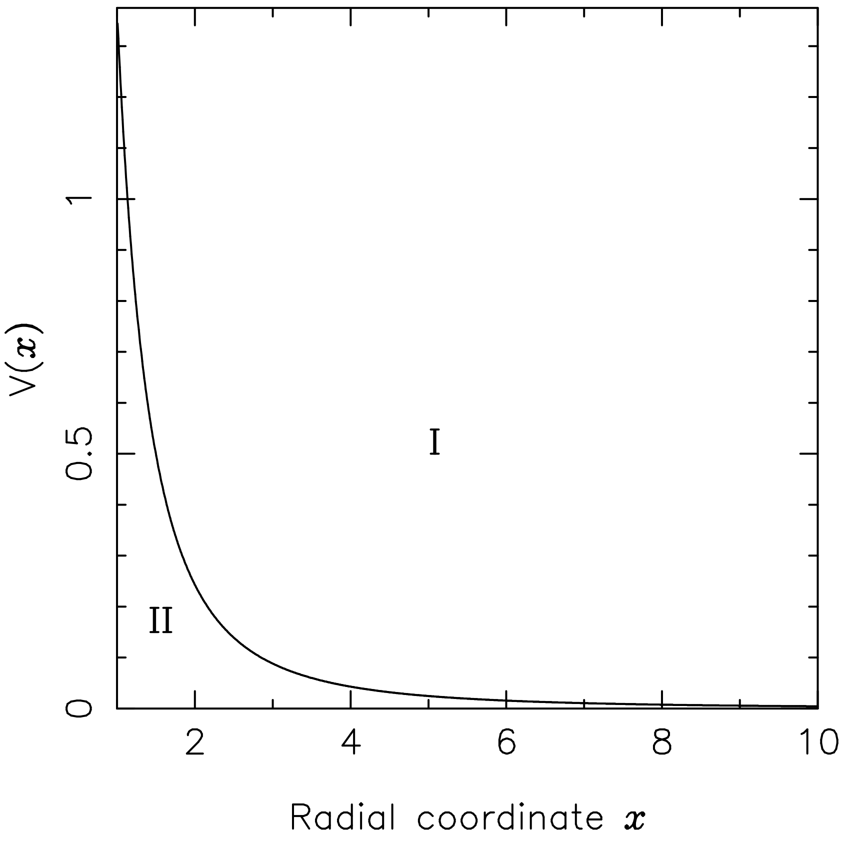

Figure 2.10: Effective potential for power law disc with $\beta = -2, \Gamma = 2$, with classically allowed region marked as ' I ' and forbidden region marked with ' II '.

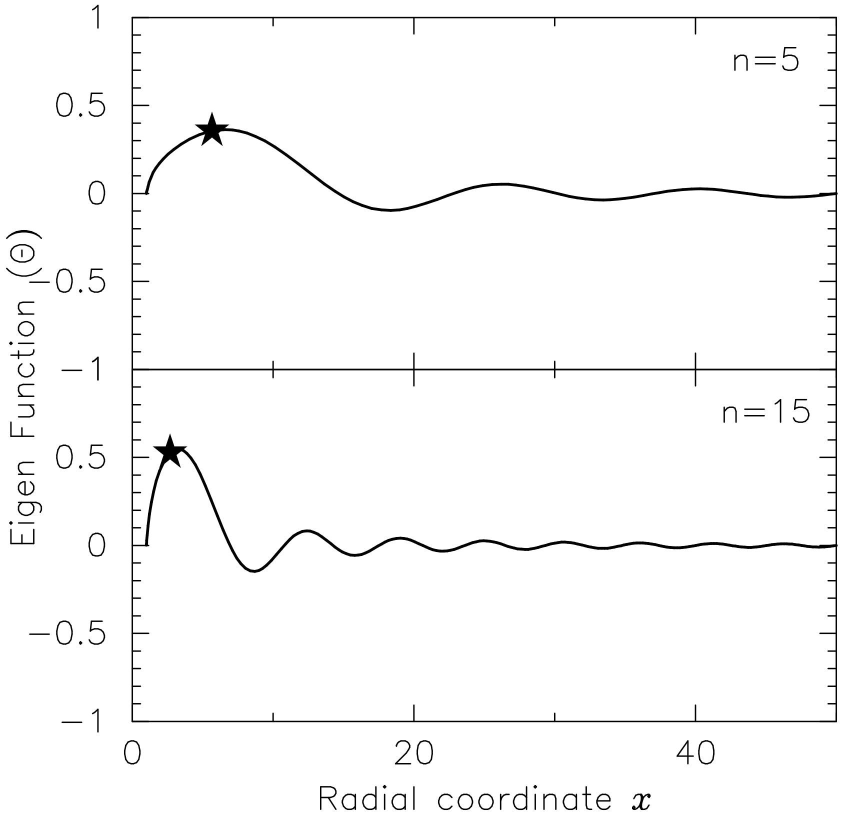

Figure 2.11: Two eigenfunctions (Type-I eigenvalue) obtained for the power law case (case (4)) with $\beta = -2$, $\Gamma = 2$. Star marks the position of the turning point.

the precession rate of the apsides ($\dot{\varpi}$) of a fluid element in a nearly circular orbit is determined by the fluid pressure gradient; to order of magnitude, $\dot{\varpi} \sim (\Omega/\mathscr{M}^2)$.

A WKB analysis was used first to argue that thin accretion discs can support large-scale ($k(R)R \sim 1$), $m = 1$ p-modes with small angular frequencies, $\omega \sim \dot{\varpi} \sim (\Omega/\mathscr{M}^2)$. These long wavelength modes may dominate the appearance of the disc, and are not expected to be damped by viscosity. We derived an eigen equation for slow linear modes and showed that it is identical to a Sturm-Liouville problem. The differential operator being self-adjoint implies that the eigenvalues are all real, so that all slow p-modes are stable. This corresponds to the result in Tremaine (2001) that all slow modes of the softened gravity disc. We solved the Sturm-Liouville problem numerically for a variety of unperturbed discs, and summarize our results below.

1. The first result corresponds to two different kinds of barotropic approximations to the Shakura-Sunyaev thin disc, which have modes with negative eigenfrequencies.
2. The second is the Kuzmin disc, which is more centrally concentrated. As earlier, this too supports only negative eigenfrequencies.
3. Power-law discs can support modes with negative eigenfrequencies for reasonable values of β and Γ. For certain combinations of these parameters power law discs can support positive eigenfrequencies as well; however the range of parameters turn out to be physically uninteresting.

If slow modes are stable, it is necessary to consider how they could be excited. Since they have azimuthal wavenumber $m = 1$, we need look for excitation mechanisms which possess the same symmetry, at least in the linear limit. One possibility is from the stream of matter from the secondary star that feeds the accretion disc. When viewed in the rest frame of the primary, the region where the stream meets the outer edge of the disc rotates in a prograde sense with angular frequency equal to the orbital frequency of the binary system. Since the orbital frequency of the binary can be much smaller than the orbital frequency of the gas in the accretion disc, there is the possibility of the resonant excitation of a slow mode if it has positive frequency. In the cases we have considered, we find only negative frequencies belonging to a discrete spectrum, allowing only for non–resonant driving.

There is, however, another alternative that does not rely on external sources of excitation. Zhang & Lovelace (2005) have studied linear waves in thin accretion discs and applied their theory to slow $m = 1$ modes around black holes. They used the pseudo-Newtonian gravitational potential of Paczyńsky & Wiita (1980) to model the general relativistic effects due to a Schwarzschild black hole. In this case $\dot{\varpi}$ is due to the deviation of the pseudo-Newtonian potential from a Kepler potential, so their slow modes are not driven by pressure gradient, in contrast to all the cases we have considered; hence more detailed comparison with our work is not possible. What is interesting is that they find that their slow modes to have negative energy and angular momentum, and suggest that slow modes may be excited spontaneously through the action of viscous forces. This possibility should be examined in the context of the p-modes we have studied. However, this would require reformulating the eigenvalue problem taking into account viscous effects.

Chapter 3

Unstable $m = 1$ Modes of Counter–Rotating Keplerian Discs

3.1 Introduction

We next turn to discs for which the self-gravity dominates the non-Keplerian potential in the discs. As already pointed in Chapter 1, the nuclei of two nearby galaxies, M31 and NGC4486B, show an unusual double peak in the stellar distribution. Tremaine (1995) proposed an eccentric disc model for the stars orbiting a massive BH in the nucleus of M31. After Tremaine's work this model was explored by many authors (Bacon et al., 2001; Salow & Statler, 2001; Sambhus & Sridhar, 2002; Peiris & Tremaine, 2003). One of the most interesting question concerns the origin of the high eccentric orbits. A possible origin of such high eccentricity orbits, as suggested by Touma (2002), is through an instability of counter–rotating streams of stars. This could occur when a globular cluster is tidally disrupted and added to the stellar system. Linear–lopsided unstable modes are constructed in Touma (2002), analytically considering two coplanar rings, and numerically via many–ring system, for nearly Keplerian axisymmetric systems. Eccentric mode are known to be unstable to counter–rotating streams of matter in self–gravitating discs (Zang & Hohl, 1978; Araki, 1987; Sawamura, 1988; Merritt & Stiavelli, 1990; Palmer & Papaloizou, 1990; Sellwood & Merritt, 1994; Lovelace et al., 1997). Sridhar & Saini (2010) studied these instabilities analytically in the WKB limit for softened gravity disc. However, their analysis had certain limitations, for instance; (1) they could calculate only the eigenvalues but not the eigenfunctions, (2) their analysis could only be used to calculate eigenvalues for equal counter-rotation.

In this chapter we formulate and numerically solve the eigenvalue problem for the linear slow, $m = 1$ modes in a two–component, softened gravity, counter–rotating disc. We model our discs to be softened gravity zero pressure fluid discs following Sridhar & Saini (2010). Due to the long–range nature of gravitational interactions, we have to deal with a pair of coupled integral equations defining the eigenvalue problem. We draw some general conclusions and then proceed to solve the equations numerically for eigenvalues and eigenfunctions. In formulating the integral eigenvalue problem, we have largely followed Tremaine (2001), but with differences in the way softening is treated; this is discussed in detail later in this chapter. We construct global modes for arbitrary mass fraction in retrograde component of disc and obtained both eigenspectra and wavefunctions by solving coupled integral equations.

We start with unperturbed counter–rotating discs in Section 3.2, with an account of perturbed discs and its potential theory in Section 3.3 . The § 3.4 contains details of derivation and stability of WKB–dispersion relation for slow $m = 1$ modes. Then we go-on to derive coupled integral equation for slow modes in Section 3.5, specialize to a case of constant mass fraction in Section 3.6 and give some comments on the nature of the solutions. In Section 3.7 we apply our model to Kuzmin disc and solve WKB–dispersion relation by quantizing the wavefunctions using Bohr–Sommerfeld quantization condition in Section 3.8. We explain the method used to solve integral equation in Section 3.9 and discuss results of our numerical exploration of modes in Section 3.10 for different values of mass fraction in retrograde disc. Concluding remarks for this chapter are offered in Section 3.11. Two appendices related to this chapter are:

- Appendix A contains derivation of perturbed potential for softened gravity two component disc (to be used in § 3.3).
- Appendix B gives relation between softened Laplace coefficients and usual (unsoftened) Laplace coefficients defined in § 3.3.

3.2 Unperturbed two component disc

We consider linear non–axisymmetric perturbations in two counter–rotating discs orbiting a central point mass M. The discs are assumed to be coplanar and consist of cold collisionless particles which attract each other through softened gravity. However, the central mass and the disc particles interact via the usual (unsoftened) Newtonian gravity. We assume that the total mass in the discs, $M_{\rm d}$, is small in comparison to the central mass, M. Since $\varepsilon \equiv M_{\rm d}/M \ll 1$, the dynamics is dominated by the Keplerian attraction of the central mass, and the self–gravity of the discs is a small perturbation which enables slow modes.

We use polar-coordinates $\mathbf{r} \equiv (R\,,\phi)$ in the plane of the discs, with the origin at the location of the central mass. Throughout this and next chapter the superscripts '+' and '−' refer to the prograde and retrograde components, respectively. The unperturbed discs are assumed to be axisymmetric with surface densities, $\Sigma_{\rm d}^{\pm}(R)$. The disc particles orbit in circles with velocities, $\mathbf{v}_{\rm d}^{\pm} = \pm\, R\Omega(R)\mathbf{e}_\phi$, where $\Omega(R) > 0$, is the angular speed determined by the unperturbed gravitational potential,

$$\Phi(R) \;=\; -\,\frac{GM}{R} \;+\; \Phi_{\rm d}(R)\,. \tag{3.1}$$

The first term on the right side is the Keplerian potential due to the central mass, and $\Phi_{\rm d}(R)$ is the softened gravitational potential due to the combined self-gravities of both the discs:

$$\Phi_{\rm d}(\mathbf{r}) \;=\; -\,G\int \frac{\Sigma_{\rm d}^{+}(\mathbf{r}') + \Sigma_{\rm d}^{-}(\mathbf{r}')}{\sqrt{\left|\mathbf{r} \,-\, \mathbf{r}'\right|^2 + b^2}}\,{\rm d}^2 r'\,, \tag{3.2}$$

where b is the Miller softening length. Note that the potential $\Phi_{\rm d}(R)$ is $O(\varepsilon)$ compared to GM/R. Test particles for nearly circular prograde orbits have azimuthal and radial frequencies, Ω and κ, given by

$$\Omega^2(R) \;=\; \frac{GM}{R^3} \;+\; \frac{1}{R}\frac{{\rm d}\Phi_{\rm d}}{{\rm d}R}, \tag{3.3}$$

$$\kappa^2(R) \;=\; \frac{GM}{R^3} \;+\; \frac{3}{R}\frac{{\rm d}\Phi_{\rm d}}{{\rm d}R} \;+\; \frac{{\rm d}^{\,2}\Phi_{\rm d}}{{\rm d}R^2}\,. \tag{3.4}$$

The line of apsides of a nearly circular eccentric particle orbit of angular frequency $\pm\,\Omega(R)$, subjected only to gravity, precesses at a rate given by $\pm\,\dot{\varpi}(R)$, where

$$\begin{aligned}\dot{\varpi}(R) &= \Omega(R) \;-\; \kappa(R)\\ &= -\frac{1}{2\Omega(R)}\left(\frac{2}{R}\frac{\mathrm{d}}{\mathrm{d}R} + \frac{\mathrm{d}^{\,2}}{\mathrm{d}R^2}\right)\Phi_{\mathrm{d}}(R) \;+\; O(\varepsilon^2)\,. \end{aligned}\tag{3.5}$$

The cancellation of the $O(1)$ term (GM/R^3) which is common to both Ω^2 and κ^2 makes $\dot{\varpi} \sim O(\varepsilon)$. This is the special feature of nearly Keplerian discs which is responsible for the existence of (slow) modes whose eigenfrequencies are $\sim O(\varepsilon)$ when compared with orbital frequencies.

3.3 Perturbed disc and potential theory

Let $\mathbf{v}_a^{\pm}(\mathbf{r},t) = u_a^{\pm}(\mathbf{r},t)\mathbf{e}_R + v_a^{\pm}(\mathbf{r},t)\mathbf{e}_\phi$ and $\Sigma_a^{\pm}(\mathbf{r},t)$ be infinitesimal perturbations to the velocity fields and surface densities of the ± discs, respectively. These satisfy the following linearized Euler and continuity equations (defined in § 1.4):

$$\frac{\partial \mathbf{v}_a^{\pm}}{\partial t} + (\mathbf{v}_{\mathrm{d}}^{\pm}\cdot\nabla)\mathbf{v}_a^{\pm} \;+\; (\mathbf{v}_a^{\pm}\cdot\nabla)\mathbf{v}_{\mathrm{d}}^{\pm} \;=\; -\nabla\Phi_a\,, \tag{3.6}$$

$$\frac{\partial \Sigma_a^{\pm}}{\partial t} + \nabla\cdot(\Sigma_{\mathrm{d}}^{\pm}\mathbf{v}_a^{\pm} \;+\; \Sigma_a^{\pm}\mathbf{v}_{\mathrm{d}}^{\pm}) \;=\; 0, \tag{3.7}$$

where $\Phi_a(\mathbf{r},t)$ is the perturbing potential. Fourier analyzing the perturbations in ϕ and t, we seek solutions of the form $X_a(\mathbf{r},t) = \sum_m X_a^m(R)\exp[\mathrm{i}(m\phi-\omega t)]$. Then

$$u_a^{m\pm} \;=\; -\,\frac{\mathrm{i}}{D_m^{\pm}}\left[(\pm m\Omega-\omega)\frac{\mathrm{d}}{\mathrm{d}R} \;\pm\; \frac{2m\Omega}{R}\right]\Phi_a^m\,, \tag{3.8}$$

$$v_a^{m\pm} \;=\frac{1}{D_m^{\pm}}\left[\pm\frac{\kappa^2}{2\Omega}\frac{\mathrm{d}}{\mathrm{d}R} \;+\; \frac{m}{R}(\pm m\Omega-\omega)\right]\Phi_a^m\,, \tag{3.9}$$

$$\mathrm{i}(\pm m\Omega{-}\omega)\Sigma_a^{m\pm} \;+\; \frac{1}{R}\frac{\mathrm{d}}{\mathrm{d}R}(R\Sigma_{\mathrm{d}}^{\pm}u_a^{m\pm}) \;+\; \frac{\mathrm{i}m}{R}\Sigma_{\mathrm{d}}^{\pm}v_a^{m\pm} = 0\,, \tag{3.10}$$

where

$$D_m^{\pm} = \kappa^2 - (\pm m\Omega - \omega)^2 . \tag{3.11}$$

The above equations determine $u_a^{m^\pm}$, $v_a^{m^\pm}$ and $\Sigma_a^{m^\pm}$ in terms of the perturbing potential Φ_a^m ; this would be the solution were Φ_a^m due to an external source. We are interested in modes for which Φ_a^m arises from self gravity of the discs. In this case it depends on the total perturbed surface density, $\Sigma_a^{m^+}(R) + \Sigma_a^{m^-}(R)$. Manipulating the Poisson integral given in Eq. (3.2), we obtain

$$\Phi_a^m(R) = \int_0^\infty R'\mathrm{dR}'\, P_m(R, R')\, [\Sigma_a^{m^+}(R') + \Sigma_a^{m^-}(R')] , \tag{3.12}$$

where the kernel

$$P_m(R, R') = -\frac{\pi G}{R_>} B_1^{(m)}(\alpha, \beta) + \frac{\pi G R}{R'^2}(\delta_{m,1} + \delta_{m,-1}) . \tag{3.13}$$

Derivation of $\Phi_a^m(R)$ is given in Appendix A. The second term on the right side of Eq. (3.13) is the indirect term arising from the fact that our coordinate system is a non–inertial frame because its origin is located on the central mass, which reacts to the gravitational field of the perturbations in the disc and therefore accelerates. The first term is the direct term coming from the perturbed self–gravity. In Eq. (3.13), $R_< = \min(R, R')$, $R_> = \max(R, R')$, $\alpha = R_</R_>$ and $\beta = b/R_>$. The functions,

$$B_s^{(m)}(\alpha, \beta) = \frac{2}{\pi} \int_0^\pi \mathrm{d}\theta \, \frac{\cos m\theta}{(1 - 2\alpha\cos\theta + \alpha^2 + \beta^2)^{s/2}} , \tag{3.14}$$

are “softened Laplace coefficients”, introduced in Touma (2002). They can be expressed in terms of the usual (unsoftened) Laplace coefficients, Eq. (B.6), as shown in Appendix B. We note that the unperturbed disc potential Φ_d can be obtained from the unperturbed disc density, $\Sigma_\mathrm{d}^+(R) + \Sigma_\mathrm{d}^-(R)$, by using Eq. (3.12) with $m = 0$.

Our basic aim here is to solve the set of Eqs. (3.8)-(3.14) for slow modes, which can be done by two methods:

1. Following Sridhar & Saini (2010) we use the WKB approximation, which has its limitations as discussed in the introduction.
2. We solve the coupled integral equation numerically.

3.4 WKB dispersion relation

Before going into formulation and analysis of coupled integral equation, we shall infer how these modes would behave under local approximation. Dispersion relation derived in this section was first calculated and analyzed by Sridhar & Saini (2010). They calculate global modes for the case of equal counter rotation and found two separate branches in the spectrum, corresponding to short and long–wavelengths for each value of b. However while comparing WKB–solutions found by them and solutions of integral equation (derived in § 3.5) obtained by us, we get a poor correspondence. Upon revisiting WKB calculation in Sridhar & Saini (2010), we discovered an error in their solution to dispersion relation. We shall discuss the formulation and offer some some general comments regarding the nature of the modes in this section. We give the corrected solutions in § 3.8 and their match with our integral equation solution in § 3.10.

If radial wave number k is larger ($|kR| \gg m$), then for tightly–wound density waves, perturbed density is of the form, $\Sigma_a^{m\pm}(R) = \left|\Sigma_a^{m\pm}(R)\right| \exp\left[\mathrm{i}\int^R \mathrm{d}R\; k(R)\right]$. WKB solution of the Poisson equation for a single softened gravity disc is given in Problem (6.3) of Binney & Tremaine (2008). For counter–rotating discs, total perturbed surface density is $\Sigma_a^m = \Sigma_a^{m^+} + \Sigma_a^{m^-}$, which gives,

$$\Phi_a^m = -2\pi G \frac{\exp\left(-|k|b\right)}{|k|} (\Sigma_a^{m^+} + \Sigma_a^{m^-}). \tag{3.15}$$

The factor $\exp(\mathrm{i}\int^R \mathrm{d}R\; k(R))$ is shared by Φ_a^m with $\Sigma_a^{m\pm}$. Thus the term with $\mathrm{d}/\mathrm{d}R$ in right hand side of Eqs (3.8)–(3.10) is $O(|kR|/m)$ larger than the others. Hence neglecting the latter we get:

$$u_a^{m\pm}(R) \;=\; \frac{(\pm m\Omega - \omega)}{D_m^{\pm}}\, k\Phi_a^m\,, \tag{3.16}$$

$$v_a^{m\pm}(R) \;=\; \pm i\,\frac{\kappa^2}{2\Omega D_m^{\pm}}\, k\Phi_a^m\,, \tag{3.17}$$

$$\Sigma_a^{m\pm}(R) \;=\; -\,\frac{\Sigma_{\rm d}^{\pm}}{D_m^{\pm}}\, k^2\Phi_a^m\,. \tag{3.18}$$

The responses are singular at radii where $D_m^{\pm} = 0$ (commonly known as LRs; Binney & Tremaine (2008)). Set of Eqs. (3.15)–(3.18) form a self–consistent linear response theory under WKB approximation. Substituting for $\Sigma_a^{m\pm}$ from Eq (3.18) and eliminating Φ_a^m in Eq. 3.15 gives the WKB dispersion relation,

$$D_m^+\, D_m^- \;=\; 2\pi G\,|k|\exp\left(-|k|b\,\right)\left[D_m^-\Sigma_{\rm d}^+ \;+\; D_m^+\Sigma_{\rm d}^-\right]\,, \tag{3.19}$$

which is a quadratic equation in ω. Coefficients of various powers of ω are real, which implies that if ω is a solution, so is its complex conjugate, ω^*. It should be noted that no assumptions about the Keplerian nature of the disc is being made. Therefore the dispersion relation of Eq. (3.19) is valid for a non Keplerian disc as well, with or without the central mass. The dispersion relation is not restricted to *slow* perturbations yet. When the counter–rotating component is absent (i.e. $\Sigma_{\rm d}^- = 0$), Eq (3.19) reduces to the WKB dispersion relation, familiar from Problem (6.3) of Binney & Tremaine (2008).

m = 0 perturbations:

When $m = 0$, we have $D_0^+ = D_0^- = \kappa^2 - \omega^2$, and Eq (3.19) becomes,

$$\omega^2 \;=\; \kappa^2 \;-\; 2\pi G\Sigma_{\rm d}|k|\exp\left(-|k|b\,\right), \tag{3.20}$$

which is identical to the dispersion relation for a disc without counter–rotating components. It is straightforward to prove (as Problem (6.5) of Binney & Tremaine (2008) invites the reader to do) that the disc is stable to short–wavelength axisymmetric perturbations if

$$b \;>\; b_0 \;\equiv\; \frac{2\pi G\Sigma_{\rm d}}{\kappa^2 {\rm e}}\,. \tag{3.21}$$

3.4.1 $m = 1$, Slow mode ansatz

At this point it is convenient to define,

$$\Sigma_{\rm d}^{+}(R) \;=\; (1-\eta(R))\Sigma_{\rm d}(R)\,, \qquad \text{and} \qquad \Sigma_{\rm d}^{-}(R) \;=\; \eta(R)\Sigma_{\rm d}(R)\,, \tag{3.22}$$

where $0 \leq \eta(R) \leq 1$ is the local mass fraction in the counter–rotating component. When $m = 1$, the near equality of Ω and κ enables slow modes for which $|\omega/\Omega| = O(\varepsilon) \ll 1$. Applying slow mode condition to simplify $D_m^{\pm}$ defined in Eq. 3.11 and using definition of $\dot{\varpi}$ from Eqn. 3.5 we get,

$$D_1^{\pm} = \pm 2\Omega\,(\omega \mp \dot{\varpi}) + O(\varepsilon^2). \tag{3.23}$$

Substituting these in Eq. 3.19 and rearranging terms provides dispersion relation for slow $m = 1$ modes:

$$\omega^2 \;-\; \mathcal{S}\,(1\,-\,2\eta)\,\omega \;-\; \dot{\varpi}\,(\dot{\varpi}\,+\,\mathcal{S}) \;=\; 0\,, \tag{3.24}$$

where $\mathcal{S}$ is defined as

$$\mathcal{S}(R, |k|) \;=\; \frac{\pi G \Sigma_{\rm d}(R)}{\Omega(R)}\,|k|\exp\left(-|k|b\,\right). \tag{3.25}$$

Solutions of the quadratic Eq. 3.24 is given by

$$\omega \;=\; \frac{\mathcal{S}}{2}\,(1\,-\,2\eta) \;\pm\; \frac{1}{2}\sqrt{\mathcal{S}^2\,(1\,-\,2\eta)^2 \,+\, 4\dot{\varpi}\,(\dot{\varpi}\,+\,\mathcal{S})}\,. \tag{3.26}$$

Note that Eqs. (3.24) and (3.26) are invariant under simultaneous transformation $(\eta, \omega) \rightarrow (1-\eta, -\omega)$, because this operation is equivalent to interchanging the meaning of "prograde" and "retrograde".

Stability and nature of the modes

We first discuss the stability criterion for WKB modes already noted by Sridhar & Saini (2010). $m = 1$ modes are stable/unstable if ω is real/imaginary which is in turn determined by the sign of discriminant of quadratic Eq. (3.24). Discriminant is given by,

$$\mathcal{D} \;=\; \mathcal{S}^2\,(1\,-\,2\eta)^2 \,+\, 4\dot{\varpi}\,(\dot{\varpi}\,+\,\mathcal{S})\;. \tag{3.27}$$

If $\dot{\varpi} > 0$, then $\mathcal{D} > 0$, hence ω is real. However, precession rate $\dot{\varpi} < 0$ for most continuous discs, which leaves $\mathcal{D} < 0$, if $\mathcal{S}$ lies in the range of values, $0 < \mathcal{S}_- < \mathcal{S} < \mathcal{S}_+$, where

$$\mathcal{S}_\pm \;=\; \frac{2|\dot{\varpi}|}{(1-2\eta)^2}\left[1 \pm 2\sqrt{\eta\,(1-\eta)}\right] . \tag{3.28}$$

It is straightforward to calculate that maxima of the function $x\exp(-x)$ is '1/e', which is attained at $x = 1$. Thus the maximum value of $\mathcal{S}$ at any R is

$$\mathcal{S}_{\rm max}(R) \;=\; \frac{\pi G\Sigma_{\rm d}}{{\rm e}b\Omega} \;=\; \frac{\kappa^2\, b_0}{2\Omega b} \;\simeq\; \frac{\Omega b_0}{2b}\,, \tag{3.29}$$

which is attained for $|k| = 1/b$. Here b_0 is the minimum softening length, defined in Eq. (3.21), that ensures local stability to axisymmetric perturbations. So for a given R, $\mathcal{D}$ is positive for all k if $\mathcal{S}_- > \mathcal{S}_{\rm max}$. Therefore, the disc is stable to all short–wavelength $m = 1$ slow perturbations if

$$\begin{aligned} b \;\;>\;\; b_1 \;&\equiv\; \frac{\pi G\Sigma_{\rm d}}{e\Omega|\dot{\varpi}|}\left[\frac{(1-2\eta)^2}{2 \,-\, 4\sqrt{\eta\,(1-\eta)}}\right] \\ &\simeq\; b_0\left(\frac{\Omega}{2|\dot{\varpi}|}\right)\left[\frac{(1-2\eta)^2}{2 \,-\, 4\sqrt{\eta\,(1-\eta)}}\right] . \end{aligned} \tag{3.30}$$

Factor dependent on η is non-zero always, specifically it approaches unity for $\eta = 1/2$, and is equal to 0.5 for $\eta = 0$. Since $(\Omega/|\dot{\varpi}|) = O(1/\varepsilon) \gg 1$, the b value required for local stability of non-axisymmetric perturbations, according to Eq. (3.30), equals b_0 (which is the minimum softening required for local axisymmetric stability) multiplied by a large factor of $O(1/\varepsilon)$, implying that even though the disc might be stable to axisymmetric perturbations, the non-axisymmetric $m = 1$ mode can be unstable. Since softening mimics "heat" (more precisely, the epicyclic radius) in collisionless discs, this criterion suggests that a Keplerian disc would have to be very hot indeed to be able to avoid a local instability to $m = 1$ perturbations. Hence one is led to consider overstable perturbations which we discuss later in the chapter.

We here make few comments regarding the nature of modes for different values of η:

- *No counter–rotation:* For $\eta = 0$, discriminant $\mathcal{D} = (\mathcal{S} + 2\dot{\varpi})^2 > 0$, giving all real roots, which is consistent with results of Tremaine (2001). He studied similar eigenvalue problem for a single disc; we present the results for single disc as a special case to our calculation and make a comparison with results of Tremaine

(2001) in § 3.10.1.

- *Equal counter–rotation:* If the mass fraction is equal for both ± discs, that is $\eta = 1/2$, then Eq. (3.26) implies that $\omega = \pm\sqrt{\dot{\varpi}(\dot{\varpi} + \mathcal{S})}$. Roots are always real if $\dot{\varpi}$ is positive or $|\dot{\varpi}| > \mathcal{S}$, whereas purely imaginary otherwise.
- *Other values of η:* For values of η other than zero or half, ω is in general a complex number with non–zero real and imaginary part if $\mathcal{D} < 0$, and hence we have over–stable modes.

Solutions of WKB–dispersion relation correcting for errors in Sridhar & Saini (2010) are presented in § 3.8. Comparison with integral equation solutions are presented in § 3.10.2. We take the opportunity to present a complete formulation of coupled integral equation for slow $m = 1$ modes, before calculating numerically the WKB eigen spectrum.

3.5 Coupled integral equation: slow $m = 1$ modes

Without loss of generality we may choose $m = 1$. In the slow mode approximation (Tremaine, 2001), we use the fact that $\Omega \gg \omega$ in Eqs. (3.8)–(3.11), and write

$$u_a^{1\pm} \;=\; \mp\,\frac{\mathrm{i}}{D_1^{\pm}}\left[\Omega\frac{\mathrm{d}}{\mathrm{d}R} \;+\; \frac{2\Omega}{R}\right]\Phi_a^1\,, \tag{3.31}$$

$$v_a^{1\pm} \;=\; \pm\,\frac{1}{D_1^{\pm}}\left[\frac{\Omega}{2}\frac{\mathrm{d}}{\mathrm{d}R} \;+\; \frac{\Omega}{R}\right]\Phi_a^1\,, \tag{3.32}$$

$$\pm\,\mathrm{i}\,\Omega\Sigma_a^{1\pm} \;+\; \frac{1}{R}\frac{\mathrm{d}}{\mathrm{d}R}(R\Sigma_{\mathrm{d}}^{\pm}u_a^{1\pm}) \;+\; \frac{\mathrm{i}}{R}\Sigma_{\mathrm{d}}^{\pm}v_a^{1\pm} \;=\; 0\,, \tag{3.33}$$

where

$$D_1^{\pm} \;=\; \pm\,2\Omega(\omega \;\mp\; \dot{\varpi}). \tag{3.34}$$

Eqs. (3.31) and (3.32) imply the following relations between the perturbed velocity amplitudes:

$$\begin{aligned} u_a^{1^\pm} &= -\,2\mathrm{i}v_a^{1^\pm}\,, \\ D_1^- u_a^{1^-} &= -\,D_1^+ u_a^{1^+}\,, \\ D_1^- v_a^{1^-} &= -\,D_1^+ v_a^{1^+}\,. \end{aligned} \tag{3.35}$$

We use Eqs. (3.35) in the continuity equation (3.33) to eliminate $u_a^{1^\pm}$ and write,

$$\pm\,\Omega\Sigma_a^{1^\pm} = \frac{2}{R^{1/2}}\frac{\mathrm{d}}{\mathrm{d}R}(R^{1/2}\Sigma_\mathrm{d}^\pm v_a^{1^\pm})\,. \tag{3.36}$$

Combining Eqs. (3.12), (3.32) and (3.34)—(3.36) we obtain

$$\begin{aligned} [\omega\,\mp\,\dot{\varpi}(R)]\,v_a^{1^\pm}(R) &= \int_0^\infty \frac{\mathrm{d}R'\,R'^{1/2}}{2R^2\Omega(R')}\left\{\frac{\partial}{\partial R}\left[R^2P_1(R,R')\right]\right\}\times \\ &\quad\times\left\{\frac{\mathrm{d}}{\mathrm{d}R'}\left[R'^{1/2}\Sigma_\mathrm{d}^+(R')v_a^{1^+}(R')\;-\;R'^{1/2}\Sigma_\mathrm{d}^-(R')v_a^{1^-}(R')\right]\right\}\,. \end{aligned} \tag{3.37}$$

We rewrite this by defining

$$z^\pm(R) = \left[\frac{R^2\Sigma_\mathrm{d}^\pm(R)}{\Omega(R)}\right]^{1/2} v_a^{1^\pm}\,, \tag{3.38}$$

using the fact that $\Omega(R) \propto R^{-3/2}$ for a Keplerian flow, and integrating by parts to obtain,

$$\begin{aligned} [\omega\,\mp\,\dot{\varpi}(R)]\,z^\pm(R) &= -\int_0^\infty \frac{\mathrm{d}R'}{R'}\,2\mathcal{F}(R,R')\left[\frac{\Sigma_\mathrm{d}^+(R')\Sigma_\mathrm{d}^\pm(R)}{\Omega(R')\Omega(R)}\right]^{1/2} z^+(R') \\ &\quad+\int_0^\infty \frac{\mathrm{d}R'}{R'}\,2\mathcal{F}(R,R')\left[\frac{\Sigma_\mathrm{d}^-(R')\Sigma_\mathrm{d}^\pm(R)}{\Omega(R')\Omega(R)}\right]^{1/2} z^-(R')\,, \end{aligned} \tag{3.39}$$

where

$$\mathcal{F}(R,R') = \left(1+\frac{1}{2}\frac{\partial}{\partial\ln R'}\right)\left(1+\frac{1}{2}\frac{\partial}{\partial\ln R}\right)P_1(R,R')\,. \tag{3.40}$$

As before $\Sigma_{\rm d}^{-}(R) = \eta(R)\Sigma_{\rm d}(R)$ and $\Sigma_{\rm d}^{+}(R) = (1-\eta(R))\Sigma_{\rm d}(R)$, where $\eta(R)$ is the local mass fraction in the unperturbed retrograde component; by definition, $0 \leq \eta(R) \leq 1$. Then, Eq. (3.39) can be recast as

$$\begin{aligned}
\omega z^{+}(R) &= +\dot{\varpi} z^{+}(R) + \int_{0}^{\infty}\frac{{\rm d}R'}{R'}[(1-\eta(R'))(1-\eta(R))]^{1/2}\mathcal{K}(R,R')z^{+}(R') \\
&\quad - \int_{0}^{\infty}\frac{{\rm d}R'}{R'}[\eta(R')(1-\eta(R))]^{1/2}\mathcal{K}(R,R')z^{-}(R')\,, \\
\omega z^{-}(R) &= -\dot{\varpi} z^{-}(R) + \int_{0}^{\infty}\frac{{\rm d}R'}{R'}[(1-\eta(R'))\eta(R)]^{1/2}\mathcal{K}(R,R')z^{+}(R') \\
&\quad - \int_{0}^{\infty}\frac{{\rm d}R'}{R'}[\eta(R')\eta(R)]^{1/2}\mathcal{K}(R,R')z^{-}(R'), \qquad (3.41)
\end{aligned}$$

where the kernel

$$\begin{aligned}
\mathcal{K}(R,R') &= -\,2\left[\frac{\Sigma_{\rm d}(R')\Sigma_{\rm d}(R)}{\Omega(R')\Omega(R)}\right]^{1/2}\mathcal{F}(R,R') \\
&= -\,2\left[\frac{\Sigma_{\rm d}(R')\Sigma_{\rm d}(R)}{\Omega(R')\Omega(R)}\right]^{1/2}\left(1+\frac{1}{2}\frac{\partial}{\partial\ln R'}\right)\left(1+\frac{1}{2}\frac{\partial}{\partial\ln R}\right)P_{1}(R,R') \\
&= 2\pi G\left[\frac{\Sigma_{\rm d}(R')\Sigma_{\rm d}(R)}{\Omega(R')\Omega(R)}\right]^{1/2}\left(1+\frac{1}{2}\frac{\partial}{\partial\ln R'}\right)\left(1+\frac{1}{2}\frac{\partial}{\partial\ln R}\right)\frac{B_{1}^{(1)}(\alpha,\beta)}{R_{>}}\,. \qquad (3.42)
\end{aligned}$$

The contribution from the indirect term in $P_1(R,R')$ goes as R'^{-2} which vanishes, because $(2+\partial/\partial\,\ln R')\,R'^{-2} = 0$. Therefore the kernel $\mathcal{K}(R,R')$ is a real symmetric function of R and R'.

Using Eqs. (3.35) and (3.38), we can relate the eigenfunctions $z^{+}(R)$ and $z^{-}(R)$ to each other:

$$\sqrt{\eta(R)}\,[\omega-\dot{\varpi}(R)]\,z^{+}(R) \;=\; \sqrt{(1-\eta(R))}\,[\omega+\dot{\varpi}(R)]\,z^{-}(R)\,. \qquad (3.43)$$

This relation can, in principle, be used to eliminate one of $z^{+}(R)$ or $z^{-}(R)$ from the coupled Eqs. (3.41), in which case the eigenvalue problem can be formulated in terms of a single function (which can be either $z^+(R)$ or $z^-(R)$). However, such a procedure results in a further complication: the eigenvalue, ω, will then occur inside the R' integral in the combination, $(\omega \pm \dot{\varpi})/(\omega \mp \dot{\varpi})$, and this makes further analysis difficult. Eqs. (3.41) are symmetric under the (simultaneous) transformations, $\{`+' \,, \eta(R) \,, \omega\} \to \{`-' \,, (1-\eta(R)) \;, -\omega\}$, which interchange the meaning of the terms prograde and retrograde. It seems difficult to obtain general results when $\Sigma^+_{\rm d}(R)$ and $\Sigma^-_{\rm d}(R)$ have different functional forms. Below we consider the case when the mass fraction, η, is a constant, i.e. when both $\Sigma^+_{\rm d}(R)$ and $\Sigma^-_{\rm d}(R)$ have the same radial profile.[1]

3.6 The eigenvalue problem for constant η discs

When the counter–rotating discs have the same unperturbed surface density profiles, i.e. $\Sigma^+_{\rm d}(R) \propto \Sigma^-_{\rm d}(R)$, some general results can be obtained. This case corresponds to the choice $\eta =$ constant, so that $\Sigma^-_{\rm d}(R) = \eta\Sigma_{\rm d}(R)$ and $\Sigma^+_{\rm d}(R) = (1-\eta)\Sigma_{\rm d}(R)$. Then the eigenfunctions, $z^+(R)$ and $z^-(R)$, are related to each other by,

$$[\omega - \dot{\varpi}(R)]\,\sqrt{\eta}\,z^+(R) \;=\; [\omega + \dot{\varpi}(R)]\,\sqrt{(1-\eta)}\,z^-(R)\,. \tag{3.44}$$

Let us define a new function, $Z(R)$, which is a linear combination of $z^+(R)$ and $z^-(R)$:

$$Z(R) \;=\; \sqrt{1-\eta}\,z^+(R) \;-\; \sqrt{\eta}\,z^-(R)\,. \tag{3.45}$$

Then equations (3.41) can be manipulated to derive a closed equation for $Z(R)$:

$$\left[\frac{\omega^2 - \dot{\varpi}^2}{(1-2\eta)\omega + \dot{\varpi}}\right] Z(R) \;=\; \int_0^\infty \frac{{\rm d}R'}{R'}\,\mathcal{K}(R,R')\,Z(R')\,, \tag{3.46}$$

We note that in this integral eigenvalue problem for the single unknown function $Z(R)$, the (as yet undetermined) eigenvalue ω occurs outside the integral. Once the problem is solved and $Z(R)$ has been determined, we can use Eq. (3.44) and (3.45) to recover $z^\pm(R)$:

---

[1] However problem for different functional forms for $\Sigma^\pm_{\rm d}(R)$ can be studied numerically with same machinery as we develop to solve the eigenvalue problem for constant η here.

$$z^{+}(R) \;=\; \sqrt{1-\eta}\,\frac{\omega+\dot{\varpi}(R)}{(1-2\eta)\omega+\dot{\varpi}}\,Z(R)\,, \qquad z^{-}(R) \;=\; \sqrt{\eta}\,\frac{\omega-\dot{\varpi}(R)}{(1-2\eta)\omega+\dot{\varpi}}\,Z(R)\,. \tag{3.47}$$

Some general conclusions can be drawn here:

1. In Eq. (3.46), kernel $\mathcal{K}(R,R')$ is real symmetric. Therefore the eigenvalue ω are either real or exist in complex conjugate pairs.

2. When $\eta=0$, the counter–rotating component is absent, which is the case studied by Tremaine (2001); then the left side of Eq. (3.46) becomes $(\omega-\dot{\varpi})\,Z$. Since the kernel $\mathcal{K}(R,R')$ is real symmetric, the eigenvalues ω are real, so the slow modes are stable and oscillatory in time. Then the eigenfunctions $Z(R)$ may be taken to be real. Therefore $z^{+}(R)=Z(R)$ is a real function, and $z^{-}(R)=0$ [2].

3. When $\eta=1/2$, there is equal mass in the counter–rotating component, and the surface densities of the '±' discs are identical to each other. This case may also be thought of as one in which there is no net rotation at any radius. Then Eq. (3.46) becomes

   $$\dot{\varpi}^{-1}(R)\left(\omega^{2}-\dot{\varpi}^{2}(R)\right)Z(R) \;=\; \int_{0}^{\infty}\frac{\mathrm{d}R'}{R'}\,\mathcal{K}(R,R')\,Z(R')\,, \tag{3.48}$$

   Since the kernel $\mathcal{K}(R,R')$ is real symmetric, ω^{2} must be real. There are two cases to consider, when the eigenvalues ω are either real ($\omega^{2}>0$) or purely imaginary ($\omega^{2}<0$).

   - When ω is real, the slow modes are stable and oscillatory in time. The eigenfunctions $z^{\pm}(R)$ can be taken to be real functions.

   - When ω is imaginary, the eigenvalues come in pairs that are complex conjugates of each other, corresponding to non–oscillatory growing/damped modes. Let us set $\eta=1/2$ and $\omega=\mathrm{i}\gamma_{\mathrm{I}}$ (where γ_{I} is real) in Eq. (3.47):

   $$z^{+}(R) \;=\; \frac{\mathrm{i}\gamma_{\mathrm{I}}+\dot{\varpi}(\mathrm{R})}{2^{1/2}\dot{\varpi}(R)}\,Z(R)\,, \qquad z^{-}(R) \;=\; \frac{\mathrm{i}\gamma_{\mathrm{I}}-\dot{\varpi}(\mathrm{R})}{2^{1/2}\dot{\varpi}(R)}\,Z(R) \tag{3.49}$$

---

[2] When $\eta=1$, the eigenvalues, ω, are again real, with $z^{-}(R)=Z(R)$ a real function, and $z^{+}(R)=0$.

> The function $Z(R)$, which is a solution of Eq. (3.48), can be taken to be a real function multiplied by an arbitrary complex constant. It is useful to note two special cases: (i) when $Z(R)$ is purely imaginary, then $z^{+}(R)$ and $z^{-}(R)$ are complex conjugates of each other; (ii) when $Z(R)$ is real, $z^{+}(R)$ is equal to minus one times the complex conjugate of $z^{-}(R)$.

To make progress for other values of η, it seems necessary to address the eigenvalue problem numerically; the rest of this chapter is devoted to this.

3.7 Application to Kuzmin disc

For numerical explorations of the eigenvalue problem, we consider the case when both the unperturbed $\pm$ discs are Kuzmin discs, with similar surface density profiles: $\Sigma_{\rm d}^{-}(R) = \eta\Sigma_{\rm d}(R)$ and $\Sigma_{\rm d}^{+}(R) = (1-\eta)\Sigma_{\rm d}(R)$, where

$$\Sigma_{\rm d}(R) \;=\; \frac{aM_{\rm d}}{2\pi(R^2+a^2)^{3/2}} \tag{3.50}$$

is the total surface density, $M_{\rm d}$ is the total disc mass and a is the disc scale length. Kuzmin discs, being centrally concentrated, are reasonable candidates for unperturbed discs. Moreover, earlier investigations of slow modes (Tremaine, 2001; Sridhar & Saini, 2010) have explored modes in Kuzmin discs, so we find this choice useful for comparisons with earlier work. The precession rate in the limit of zero softening length (i.e. $b = 0$) is

$$\dot{\varpi}_0(R) \;=\; -\,\frac{3GM_{\rm d}\,a^2}{2\Omega(R)(R^2+a^2)^{5/2}} \tag{3.51}$$

Radial dependence of the precession rate is displayed in Fig. 3.1, where we also give for future reference, the radial dependence of the precession rate for softening length $b = 0.1$. Solid line is for $b = 0$ and dashed is for $b = 0.1$. Dots on the dashed curve mark the location of ILR radius as explained in § 3.10.3. For other values of b, difference between precession rate decreases with decreasing b.The difference is close to zero for $b \lesssim 10^{-2}$, which is typical lower limit of b used in our calculations, as will be discussed in § 3.9 .

The characteristic values of orbital frequency and surface density are given by $\Omega^{\star} = \sqrt{GM/a^3}$, and $\Sigma_{\rm d}^{*} = M_{\rm d}/a^2$, respectively. All physical quantities can be cast in a dimensionless form in terms of these physical scales. When the coupled Eqs. (3.41) are

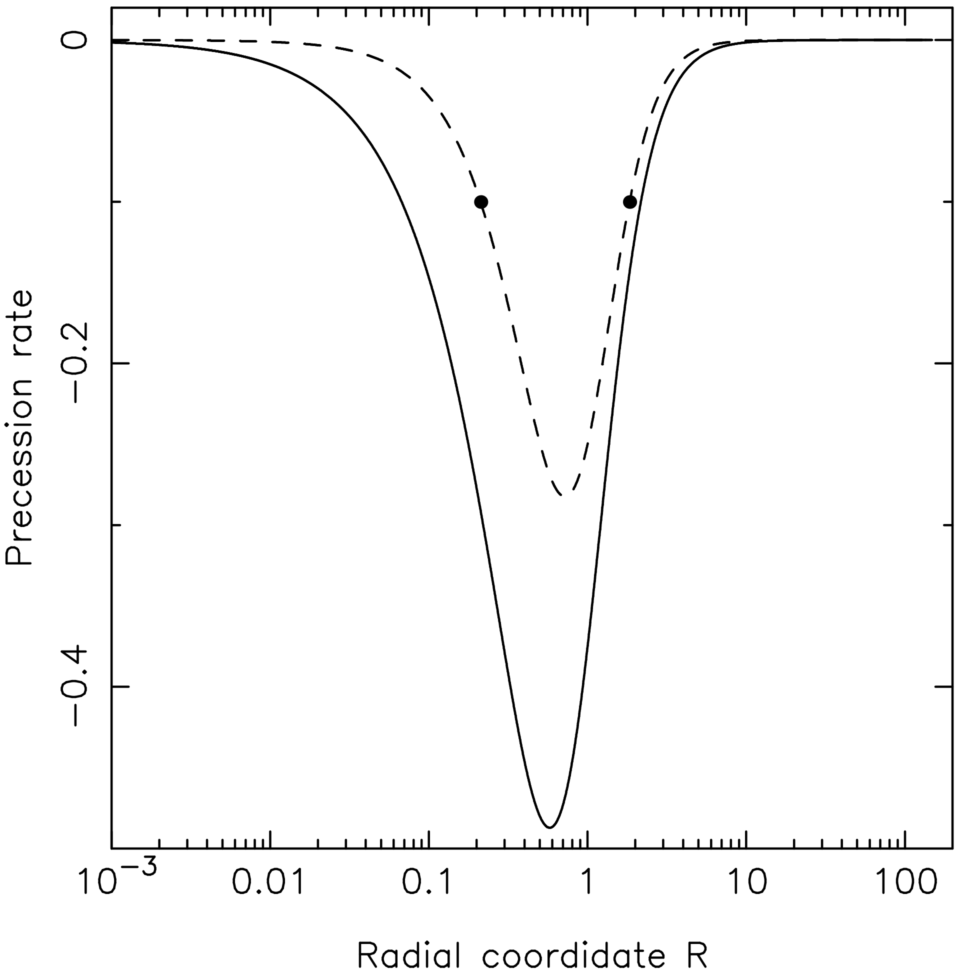

Figure 3.1: Precession rate for the Kuzmin disc: the solid line corresponds to the expression in Eq (3.51) for zero softening (i.e. $b = 0$), and the dashed line is for softening length $b = 0.1$. Dots mark the location of radius of ILR as explained in § 3.10.3

cast in dimensionless form, the net effect is to rescale the eigenvalue ω to σ, where

$$\sigma = \left(\frac{\Omega^{\star} a}{G\Sigma^{\star}}\right)\omega\,. \tag{3.52}$$

In the following section, all quantities are to be taken as dimensionless; however, with some abuse of notation, we shall continue to use the same symbols for them. Before solving coupled integral equation we would first solve WKB dispersion relation discussed in § 3.4 for equal counter–rotation for Kuzmin disc.

3.8 WKB–solutions

For constant mass fraction in retrograde disc, dispersion relation derived in Eq (3.24) reduces to

$$\frac{\omega^2 - \dot{\varpi}^2}{\omega(1-2\eta) + \dot{\varpi}} = \frac{\pi G \Sigma_{\mathrm{d}} |k| \mathrm{e}^{-|k|b}}{\Omega(R)}\,. \tag{3.53}$$

Substituting for Σ_{d} and $\dot{\varpi}$ defined in Eqs. (3.50) & (3.51) and for $\eta = 1/2$ converting to dimensionless form above equation reads as,

$$b|k|\exp(-b|k|) = \frac{\Gamma_g^2}{b}\frac{(1+R^2)^4}{R^3} + \frac{3b}{(1+R^2)}\,. \tag{3.54}$$

Since we are interested in comparing with the unstable global modes studied in Sridhar & Saini (2010), we have defined Γ_g (identical to Γ in Sridhar & Saini (2010)) above as

$$\mathrm{i}\Gamma_g = \sqrt{\frac{4}{3}}\,b\,\sigma\,. \tag{3.55}$$

Here we present results with precession rate for zero softening ($b = 0$), same as what is used by Sridhar & Saini (2010), which differs from one with non–zero softening. We also performed calculations with softened precession rate. We find that although results do change by few percent and match better the results obtained from the integral eigenvalue problem, they are qualitatively similar. So we still continue with $\dot{\varpi}$ for $b = 0$ because (1) it is more efficient in terms of computational time required (2) since we have an exact formulation, being an approximation the WKB–results are offered here only for qualitative comparison, therefore a few percent difference in magnitude of eigenvalues calculated here does not change our conclusions.

Sridhar & Saini (2010) divided their spectrum into two distinct branches namely short–wavelength and long–wavelength branches for which the transition takes place from long–wavelength to short–wavelength branch at $|k|b = 1$. Note that at $|k|b = 1$ left hand side of Eq. (3.54) attains maxima. But upon solving coupled integral equation we do not get any such branching. Upon a closer inspection we found that the distinction between the long and short wavelength branch turned out to be spurious one, moreover there was a sign error in a term in the code that was used to calculate the results in that paper. Therefore we revisit evaluation of WKB–eigenspectrum and plot contours of constant Γ_g^2 for dispersion relation Eq. (3.54) in phase–space, which are displayed in Fig. 3.2. Lighter shades are for positive values of Γ_g^2 (candidates for imaginary eigenvalue) whereas dark ones are for negative Γ_g^2 (candidates of real and oscillatory modes). We characterize contours as follows:[3]

1. ***Type I***: closed contours around $k = 0$.
2. ***Type II***: the closed contours on both sides of $k = 0$. If the disc rotates in the direction of increasing azimuthal angle, then $k > 0$ is for trailing waves whereas $k < 0$ is for leading waves.
3. ***Type III***: are the open contours (with dark shades) for both positive and negative k towards the highest value of $|k|$.

Values of Γ_g for which contours are closed are characterized as eigenvalues if they satisfy quantization condition, which we will discuss now. Modes are determined by solving numerically Eq. (3.54) for k for a given value of Γ_g & R and then using Bohr- Sommerfeld quantization condition to obtain the eigenvalue. LHS of Eq. (3.54) is bounded above by unity, whereas the RHS is bounded below but unbounded above as it blows up at $R = 0$ and $R \to \infty$. Hence, if the minimum of RHS is less than maximum of LHS then Equation (3.54) will admit real roots (k value for a given R and Γ_g value). Also for small and large R, right hand side of Eq. (3.54) is singular, so real roots exist only for a finite range of R, $R_1 < R < R_2$, where both R_1 and R_2 depends on Γ_g and $|k|$ in a complicated manner. These are points at which wave is reflected (turning points). To visualize it let us follow one of the type II closed contours, start at one point and move along the contour, position at which we would notice a change in direction from forward motion to backward and vice versa are the turning points. We therefore impose

---

[3] Classification of eigen spectrum in this chapter is different from the one used in previous chapter.

Bohr-Sommerfeld quantization condition;

$$\oint k\mathrm{d}R = (2n+1)\,\pi \quad ; \quad n = 0, 1, 2, \cdots , \tag{3.56}$$

where n is the number of nodes of the wavefunction and integration is to be done along closed contours for candidate Γ_g values.

Since we are interested in growing/damping modes we quantize type II contours. Growth rate as a function of number of nodes for two values of the softening parameter $b = 0.1$ & $b = 0.05$ [4] calculated numerically is displayed in Fig. 3.3 . From contour plots shown in Fig. 3.2, we see a trend that as Γ_g increases the area under each contour decreases. We obtain a similar trend in spectrum in Fig. 3.3, that is as Γ_g decreases n increases. The spectrum is seen to be close to a power law, is quite robust and persists for other values of b as well. Our conclusions are similar to that of Sridhar & Saini (2010), however there are two significant differences:

1. We do not get two different branches as them.
2. Slope of our spectrum does not match with any of their branches. Reason for this might be different ways of identifying eigenvalues.

Both these differences make our present result better match with the spectrum obtained from integral equation, as shown in § 3.10.2.

3.9 Numerical method used to solve integral equations

Our numerical method is broadly similar to Tremaine (2001). In order to calculate eigenvalues and eigenfunctions numerically, we approximate the integrals by a discrete sum using the Gauss–Legendre N–point quadrature rule (Press et al., 1992). The presence of the term dR/R in the integrals suggests a natural choice of variables as $u = \log(R)$ and $v = \log(R')$, where, as mentioned earlier, R stands for the dimensionless length R/a. The use of a logarithmic scale is numerically more efficient because it induces spacing

---

[4] Sridhar & Saini (2010) have used softening 0.1 & 0.01. We use different values because we want to compare spectra obtained by solving WKB-dispersion relation and by numerically solving coupled integral equation for which $b = 0.01$ is the limiting value.

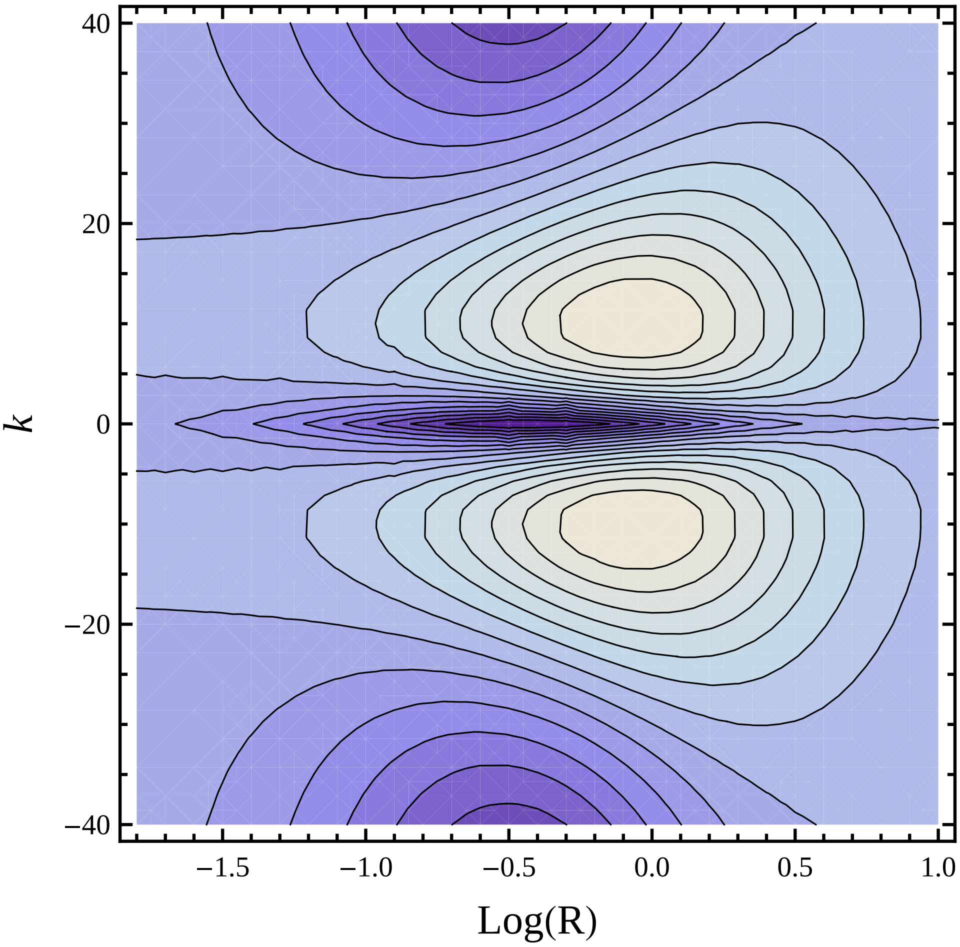

Figure 3.2: Contour plots for constant Γ_g^2 in phase–space. Lighter shades are positive Γ_g^2 (growing/decaying modes) whereas darker are for negative Γ_g^2 (real and oscillatory modes).

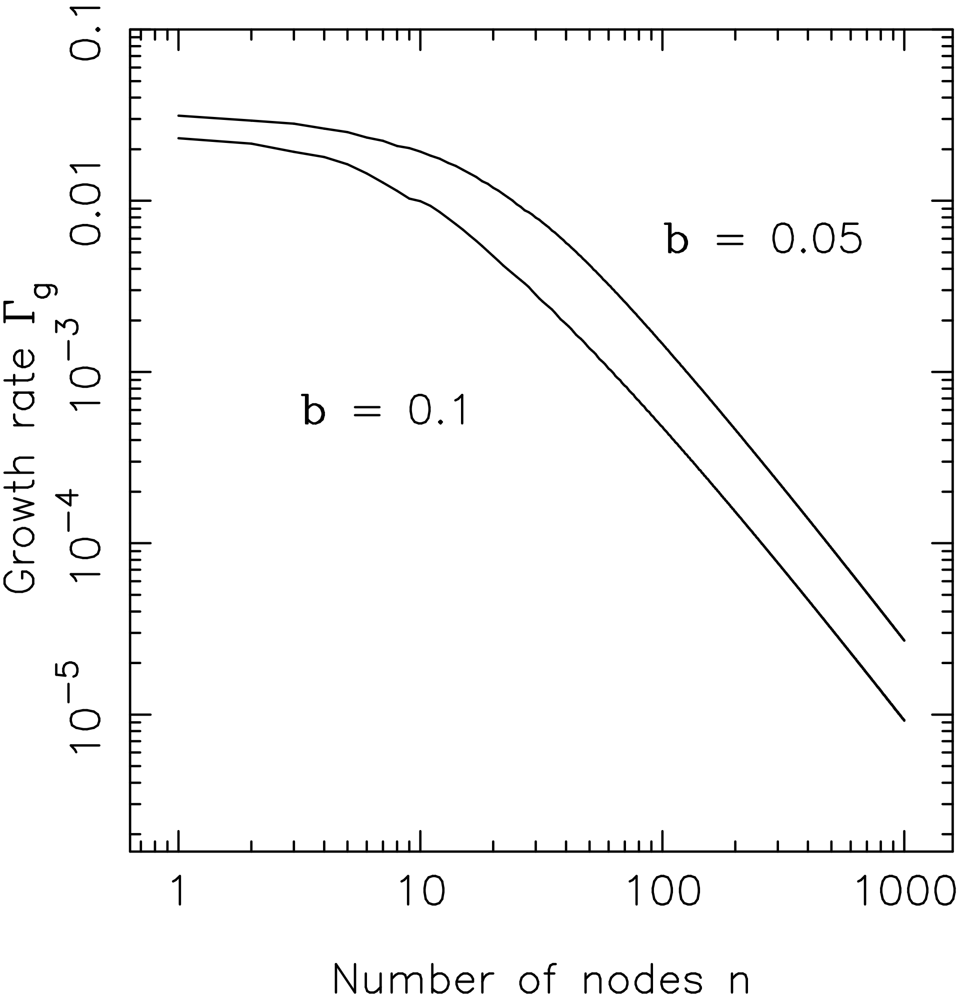

Figure 3.3: Plot of growth rate Γ_g vs number of nodes n calculated for equal mass fraction in the retrograde disc $\eta = 1/2$ for softening length $b = 0.1$ & $b = 0.05$, obtained by solving WKB dispersion relation coupled with Bohr-Sommerfeld quantization condition.

in the coordinate space that increases with the radius. This handles naturally a certain expected behaviour of the eigenfunctions: since the surface density in a Kuzmin disc is a rapidly decreasing function of the radial distance, we expect the eigenfunctions to also decrease rapidly with increasing radius. However, we have recast coupled integral equations defined in Eq. (3.41) by defining a new variable $Z(R)$, which is useful to infer general nature of the solutions. But solving numerically Eq. (3.46) is difficult as its left hand side does not allow us to write it in a simple matrix eigenvalue problem apart from the cases of $\eta = 0$ and $1/2$. This is not the case with integral equations written in terms of $z^{\pm}(R)$. Hence, we solve Eq. (3.41) numerically for $z^{\pm}(R)$ and σ and then calculate $Z(R)$ using relation given by Eq. (3.45)

Discretization of the coupled Eqs. (3.41) follows the schema:

$$\int_0^\infty \frac{\mathrm{d}R'}{R'}\,\mathcal{K}(R,R')\,z^+(R') \quad\longrightarrow\quad \sum_{i=1}^{N} w_i\,\mathcal{K}(e^u, e^{v_i})\,z^+(e^{v_i})\,, \tag{3.57}$$

where w_i are suitably chosen unequal weights. Then the discretized equations can be written as a matrix eigenvalue problem:

$$\mathbf{A}\,\zeta \;=\; \sigma\,\zeta\,, \tag{3.58}$$

where

$$\mathbf{A} \;=\; \begin{bmatrix} (1-\eta)w_j\mathcal{K}_{ij} + \dot{\varpi}_j\delta_{ij} & -\sqrt{\eta(1-\eta)}w_j\mathcal{K}_{ij} \\ \\ \sqrt{\eta(1-\eta)}w_j\mathcal{K}_{ij} & -\eta w_j\mathcal{K}_{ij} - \dot{\varpi}_j\delta_{ij} \end{bmatrix} \quad\text{and}\quad \zeta \;=\; \begin{pmatrix} z_i^+ \\ \\ z_i^- \end{pmatrix}. \tag{3.59}$$

The $2N \times 2N$ matrix $\mathbf{A}$ has been represented above in a 2×2 block form, where each of the 4 blocks is a $N \times N$ matrix, with row and column indices i and j. Note that δ_{ij} is the Kronecker delta symbol, and no summation is implied over the repeated j indices. Thus we have an eigenvalue problem for eigenvalues σ, and eigenvectors given by the $2N$ dimensional column vector ζ .

In our original problem kernal $\mathcal{K}$ is symmetric but use of unequal weights destroys the natural symmetry of the kernel. We would like to restore the symmetry in the problem as matrix eigenvalue problem is much easier to solve for symmetric matrices. And this is readily restored through a simple transformation given in § 18.1 of Press et al. (1992)

which is based on the fact that weights calculated using Gaussian quadrature rule are positive. We write $\tilde{\mathcal{K}} = \mathcal{K}\,\mathbf{D}$, where $\mathbf{D} = \mathrm{diag}(w_j)$. Now

$$\begin{aligned} \mathbf{D}^{1/2}\,\tilde{\mathcal{K}}\,\zeta &= \left(\mathbf{D}^{1/2}\,\mathcal{K}\,\mathbf{D}^{1/2}\right)\,\mathbf{D}^{1/2}\,\zeta, \\ &= \left(\mathbf{D}^{1/2}\,\mathcal{K}\,\mathbf{D}^{1/2}\right)\,\mathbf{h}, \end{aligned} \tag{3.60}$$

where $\mathbf{h} = \mathbf{D}^{1/2}\,\zeta$ and $\mathbf{D}^{1/2} = \mathrm{diag}(\sqrt{w_j})$. It can be easily seen that matrix in bracket in Eqn. (3.60) is symmetric. We use this as our input to calculate the eigenvalues and eigenfunctions (which now is $\mathbf{h}$) numerically rather than $\tilde{\mathcal{K}}$, which is originally there in matrix $\mathbf{A}$. And then restore ζ by using the transformation $\zeta = \mathbf{D^{-1/2}}\,\mathbf{h}$, where $\mathbf{D}^{-1/2} = \mathrm{diag}(1/\sqrt{w_j})$.

The grid for our numerical calculations covers the range $-7 \leq \log R \leq 5$, which is divided into $N = 4000$ points; larger values of N give similar results. Our method always yields $2N$ eigenvalues and eigenvectors. Just like in Tremaine (2001), many of these correspond to singular (van Kampen) modes; these are discussed later in § 3.10.3.

We note some differences with Tremaine (2001) concerning details of the numerical method and assumptions. The major difference is in the treatment of softening: In Tremaine (2001), a dimensionless softening parameter $\beta = b/R$ was introduced, and the eigenvalue problem for slow modes was solved by holding the parameter β constant, This renders the physical softening length b effectively dependent on radius, making it larger at larger radii, thereby not corresponding to any simple force law between two disc particles located at different radii. We have preferred to keep b constant, so that the force law between two disc particles is through the usual Miller prescription. Other minor differences in treatment are: (i) In Tremaine (2001), the disc interior to an inner cut-off radius was assumed to be frozen. In contrast we use a straightforward inner cut-off radius of 10^{-5}, as mentioned above; (ii) Tremaine (2001) uses a uniform grid in $\log R$, with four–point quadrature in the intervals between consecutive grid points; we also use a uniform grid in $\log R$ but instead employ a single N–point quadrature for integration.

If we were to deal with unsoftened gravity (i.e. the case when $b = 0$), the diagonal elements of the kernel would be singular. Hence, when the softening parameter b is much smaller than the grid size, accuracy is seriously compromised by the round-off errors. Typically, the usable lower limit for b is $\sim 10^{-2}$ [5].

---

[5] In Tremaine (2001), lower limit on dimensionless softening parameter, $\beta \sim 10^{-4}$ is used $\Rightarrow \beta =$

3.10 Numerical results & comparison with earlier works

We obtained the eigenvalues and eigenfunctions of equation (3.58) using the linear algebra package LAPACK (Anderson et al., 1999). We now present the results of our calculations for specific values of η. As noted earlier, interchanging the meaning of prograde and retrograde orbits leave the results invariant under the transformation $(\eta, \omega) \rightarrow (1 - \eta\,, -\omega)$; therefore, we present results below only for $0 \leq \eta \leq 1/2\,$.

3.10.1 No counter-rotation: $\eta = 0$

We are dealing with a single disc whose particles rotate in the prograde sense. The eigenvalue problem for this case was studied first by Tremaine (2001), who also showed that the eigenvalues are real; in other words, the disc supports stable slow modes. We consider this case first to benchmark our numerical method as well as assess the differences in results that may arise due to the manner in which softening is treated as compared to Tremaine (2001). To facilitate comparison we use the same nomenclature as Tremaine (2001). Briefly, modes corresponding to positive and negative eigenvalues are referred to as "p–modes" and "g-modes", respectively; we also introduce a parameter $\lambda = (1+c)^{-1}$, where c is a constant that mimics additional precession due to an external source of the form $\dot{\varpi}_e(R) = c\,\dot{\varpi}_{\rm d}(R)$; we define eccentricity e_K through

$$\mathrm{e}_K \;=\; 2\left(\frac{GM}{R}\right)^{-1/2} v_a^1\,, \tag{3.61}$$

and use the normalization,

$$\int \frac{\mathrm{dR}}{R}\,\mathrm{e}_K^2(R) \;=\; 1\,. \tag{3.62}$$

Our results corresponding to g–modes, for $\lambda = 0.1$ and $b = 10^{-2}$, are presented in Fig. 3.4, where we plot modes with three or fewer nodes and give their eigenvalues. These figures are to be compared with Fig. 3 of Tremaine (2001). We see that the eigenfunctions are of similar form, but that the eigenvalues differ substantially. The reason for this discrepancy is a typographical error in Fig. 3 of Tremaine (2001). The

---

$b/R \sim 10^{-4} \Rightarrow b \sim 10^{-2}$ for $R \sim 100$, (typical value of maximum radius used), which is same as ours.

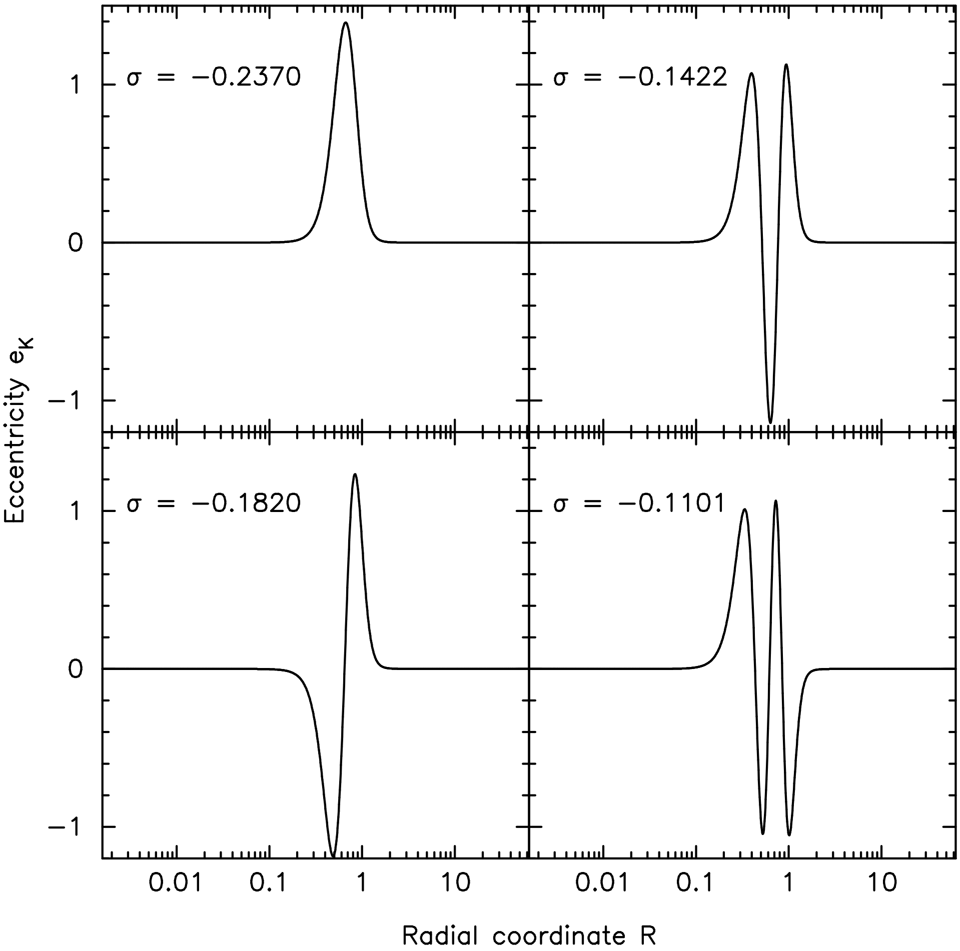

Figure 3.4: Slow g–modes in a single, prograde ($\eta = 0$) Kuzmin disc with $\lambda = 0.1$ and $b = 10^{-2}$. The panels are labeled by the scaled eigenvalue σ.

eigenvalues quoted there correspond to $\lambda = 0.05$ (not $\lambda = 0.1$ as stated), as can be verified by referring to Fig. 4 of Tremaine (2001). This was pointed out to us by Dr. Evgeny Polyachenko. Once this is taken into account, the eigenvalues quoted in our Fig. 3.4 are in good agreement with those corresponding to $\lambda = 0.1$ of Fig. 4 of Tremaine (2001). However, we would like to note that this agreement between our eigenvalues worsens somewhat for the higher eigenmodes: for instance, when $\lambda = 0.05$, we calculate an eigenvalue of -0.1219 for a eigenmode with 8 nodes, whereas we would infer a value of -0.0229 from Tremaine (2001). Results for p–modes for $\lambda = 1$ (no external source) and various values of softening parameter b, are displayed in Fig. 3.5; these are to be compared with Fig. 6 of Tremaine (2001), which matches reasonably.

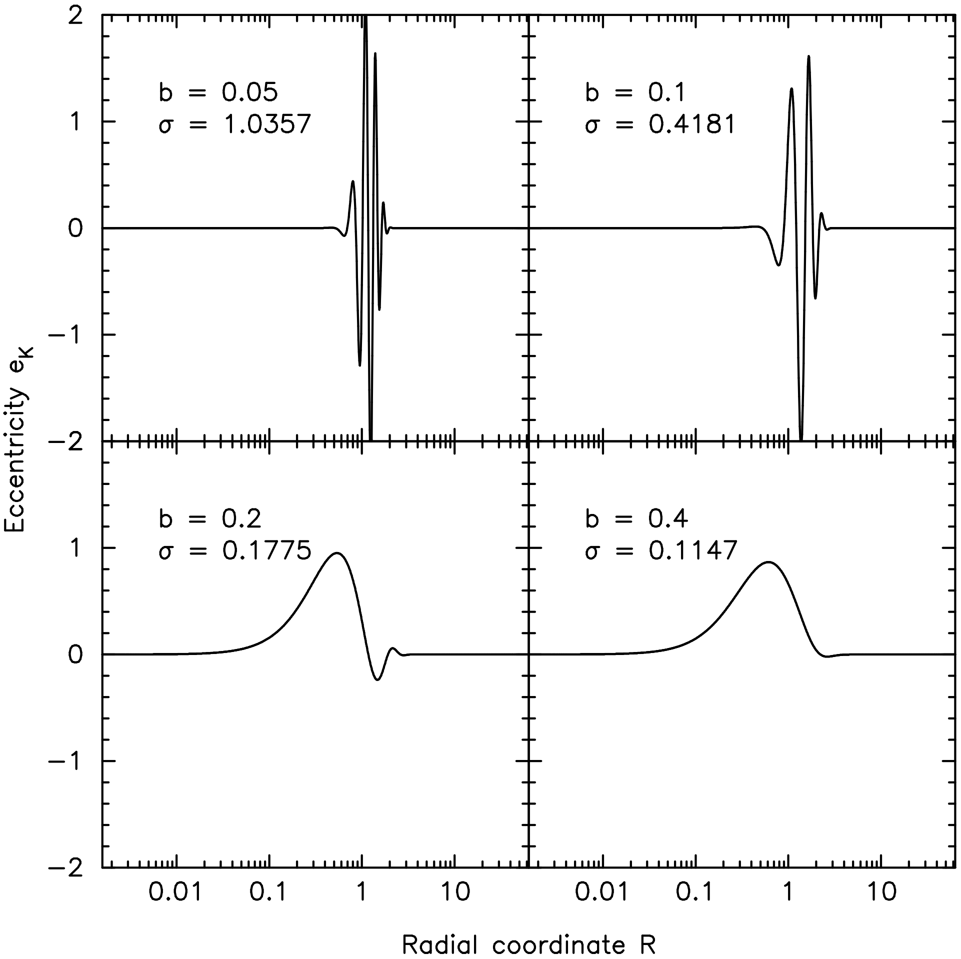

Figure 3.5: Slow p–modes in single, prograde ($\eta = 0$) Kuzmin disc with no external source (i.e $\lambda = 1$). The panels are labeled for the scaled eigenvalue σ, and the softening parameter b (which has been scaled with respect to a, the disc scale length).

3.10.2 Equal counter-rotation (or no net rotation): $\eta = 1/2$

This case was studied by Sridhar & Saini (2010), but due to reasons discussed earlier in § 3.8, we redo the evaluation of eigenspectrum using "WKB" dispersion relation given by Eq. (3.54) . From this expression it is concluded: if $\dot{\varpi}$ happens to be positive then ω is real (and the disc is stable), but $\dot{\varpi}$ is negative for most continuous discs which implies that ω can be either real or purely imaginary. We have calculated the conditions in § 3.4 for which eigenvalues are real (stable oscillatory modes), or purely imaginary (non–oscillatory growing/damped modes). Here we focus on the growing (unstable) modes; we use the *growth rate* of perturbations as defined in Eq. (3.55), in order to facilitate comparisons with solutions obtained by solving WKB–dispersion relation. In Fig. 3.6 we plot Γ_g versus the number of nodes of $Z(R)$, for b equal to 0.1 and 0.05. Solid line corresponds to numerical solution of integral equation whereas dashed ones to WKB eigenvalues (same as in Fig. 3.3). As Fig. 3.6 shows, there is good agreement between both, including the horizontal shift in the spectrum when the value of b is changed.

In Fig. 3.7 we plot a few of these eigenfunctions as a function of R for values of b equal to 0.1 and 0.05. Note that, from the discussion in § 3.6, $Z(R)$ can always be chosen to be a real function of R. The smallest number of nodes correspond to the largest value of the growth rate. The eigenfunctions with the fewest nodes have significant amplitudes in a small range of radii around $R \sim 1$, and this range increases with the number of nodes (and correspondingly, with decreasing the growth rate).

One direct application of relation between ± perturbations derived in Eq. (3.35) is that we can calculate phase difference between $z^{\pm}(R)$, which we do below for growing modes. As already pointed out, after Eq. (3.49) (which is derived from Eq. (3.35)), $z^{\pm}(R)$ are either complex conjugates or minus one times complex conjugate of each other. And hence, if ψ is the phase of $z^{+}(R)$ for a given value of R then phase difference between z^{+} & z^{-} is 2ψ, where

$$\psi = \arctan\left(\frac{\dot{\varpi}}{\gamma}\right) \tag{3.63}$$

is calculated using Eq. (3.49). Since we calculate $z^{\pm}(R)$ numerically, the phase difference between them is also calculated numerically, and compared with the analytical form above. Phase difference calculated by both these methods is displayed in Fig. 3.8 for $b = 0.1$, $\Gamma_g = 0.0355$ and 0.0283. Solid line corresponds to numerically calculated phase difference and dashed to the one obtained using Eq. (3.63). There is close match between them, which provides a check to the accuracy of our numerical method.

Fig. 3.9 is a gray–scale plot of the positive part of surface density perturbations in the ± discs, $\Sigma_a^{\pm}(R, \phi, t)$ at time $t = 0$. This basically displays the density enhancement regions. In Fig. 3.10 we display positive part of total surface density perturbations, $\Sigma_a^{+}(R, \phi, t = 0) + \Sigma_a^{-}(R, \phi, t = 0)$. Note the relative phase shift between the ± perturbations and lopsidedness in the brightness distribution. Since the modes are purely growing modes, pattern rotates rigidly with the disc, with amplitude growing exponentially. For other values of b shown in Fig. 3.7 we get similar patterns. As one more test for the robustness of our numerical method, all the results for this case ($\eta = 1.2$) are evaluated by solving for $z^{\pm}(R)$ (Eq. (3.41)) which gives $Z(R)$ using relation given in Eq. (3.45) and we already have $Z(R)$ by solving Eq. (3.46) separately. As expected we get one-to-one match.

3.10.3 Other values of η

We present results for values of η other than 0 and 1/2. These are particularly interesting, not only because they could not be explored by WKB, but because the eigenvalues can be truly complex, corresponding to growing and damped modes which precess with steady pattern speeds. We write the eigenvalues as $\sigma = \sigma_R + \mathrm{i}\sigma_I$, sum of real and imaginary parts. In Fig 3.11, we display the eigenvalues in the complex σ–plane, for softening parameter $b = 0.1$ and η equal to 0.1, 0.25 and 0.4.[6] The horizontal lines correspond to the real and continuous part of the spectrum, whereas the "wedge"–like distribution corresponds to the complex and discrete part of the spectrum. Panels on the left, labeled 'a', provide an overview, whereas the panels on the right, labeled 'b', provide a close–up view of the distribution of eigenvalues near the origin of the complex σ–plane; this distribution is similar to Fig. 3 of Touma (2002). We are able to provide much more detail, essentially because we are dealing with continuous discs rather than a finite number of rings.

The continuous spectrum corresponds to singular (van Kampen) modes which are concentrated at the ILR, which occur at radii where the pattern speed equals the precession rate as can be seen from the following discussion. Radius at which $D_1^{\pm} = 0$ is ILR radius, which implies $\pm\Omega(\sigma \mp \dot{\varpi}) = 0$ (dimensionless form of $D_1^{\pm}$ is used here). For prograde disc this means ILR occurs at $\sigma = \dot{\varpi}$ and for retrograde disc $\sigma = -\dot{\varpi}$ gives

---

[6] Because of symmetry of problem, values of $\eta > 1/2$ correspond to value of $(1 - \eta)$ discussed in this section, like patterns for $\eta = 0.6$ correspond to $1 - \eta = 0.4$.

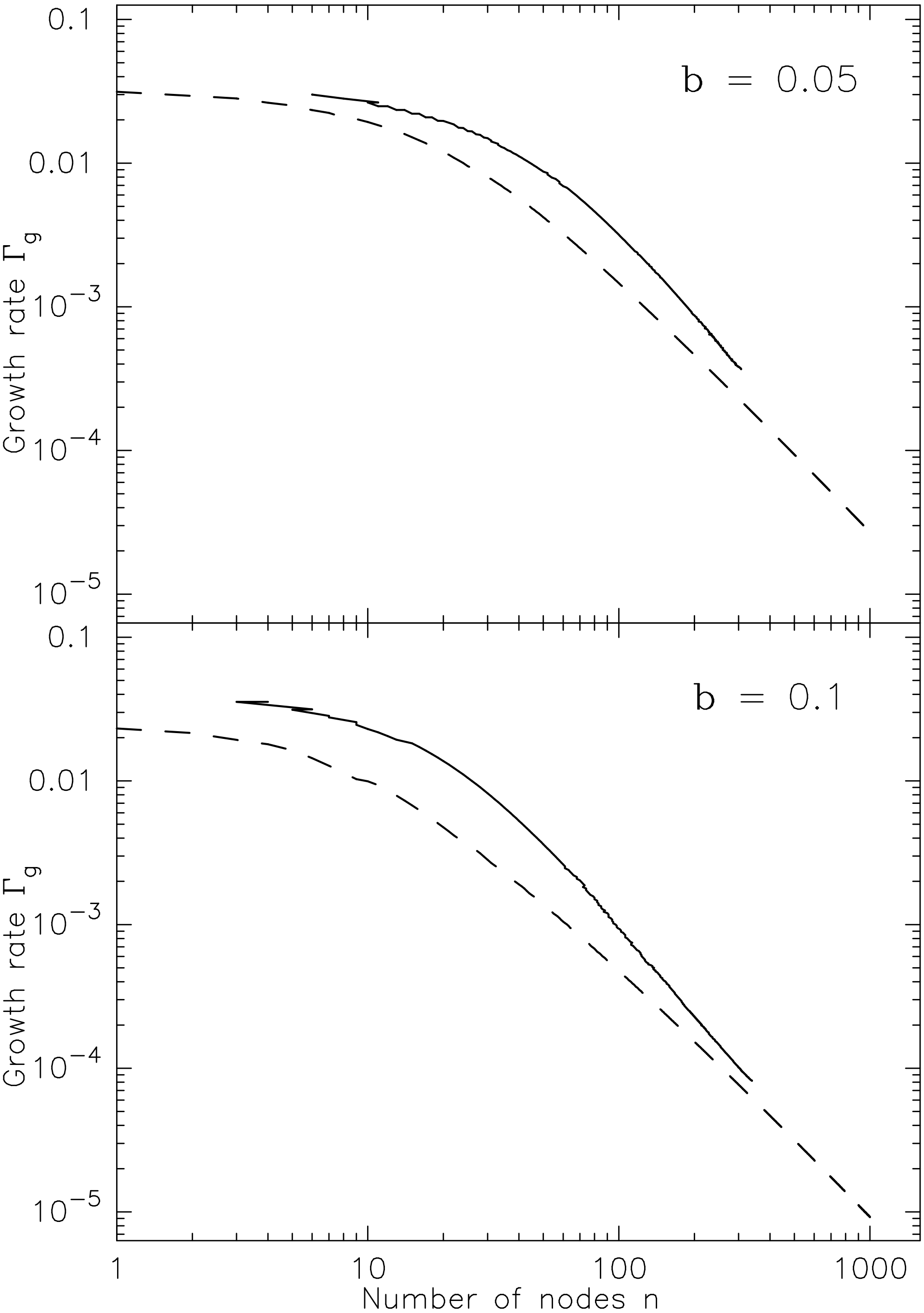

Figure 3.6: Growth rate versus number of nodes for $\eta = 0.5$. Pannels are marked for value of softening used. The solid lines are from the numerical solution of the eigenvalue problem, Eq (3.58) . The dashed lines are from a WKB calculation.

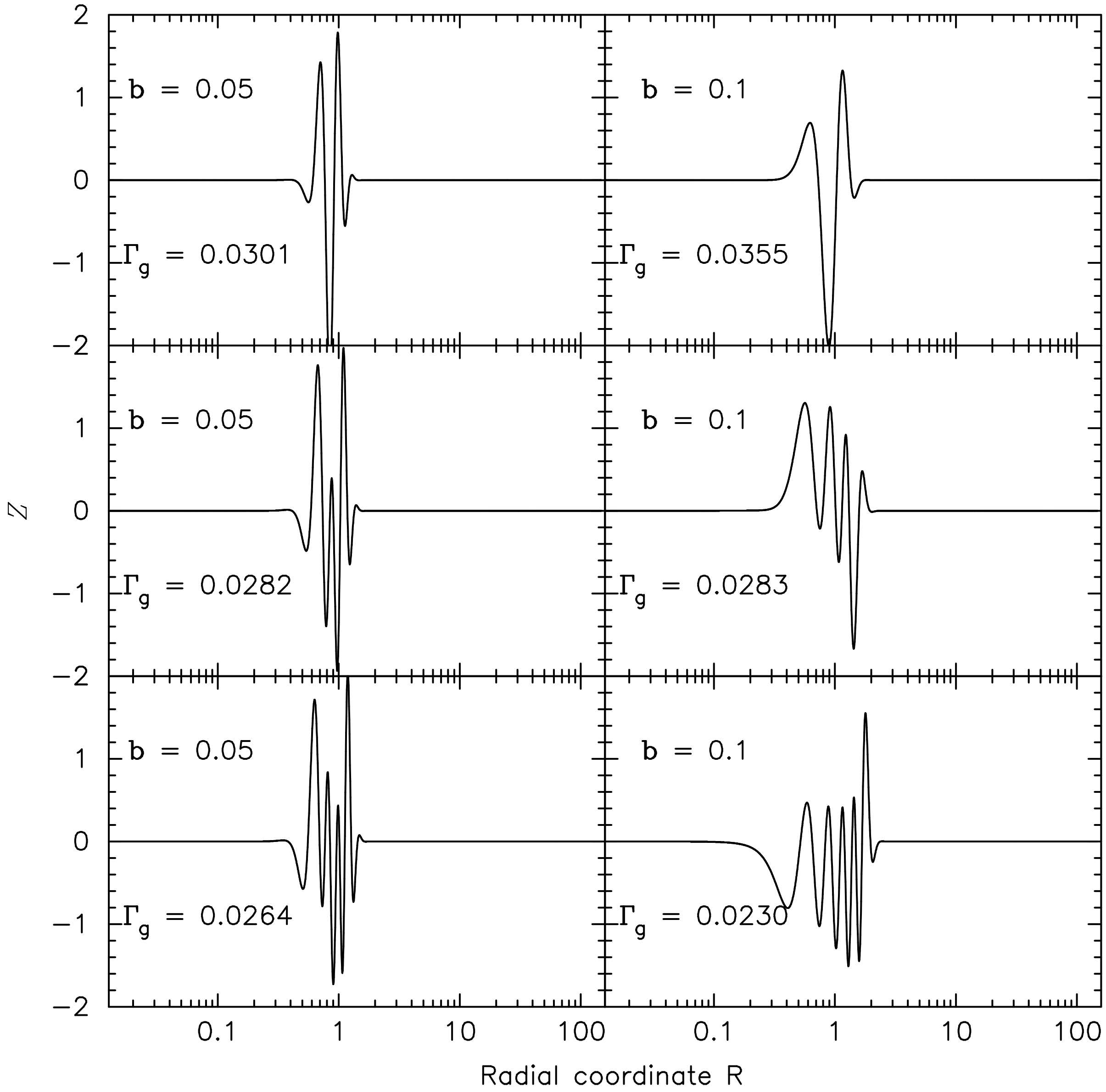

Figure 3.7: Eigenfunctions $Z(R)$ are plotted as a function of the radial coordinate R, for $\eta = 0.5$. The panels are labeled by the values of the growth rate Γ_g and softening length b.

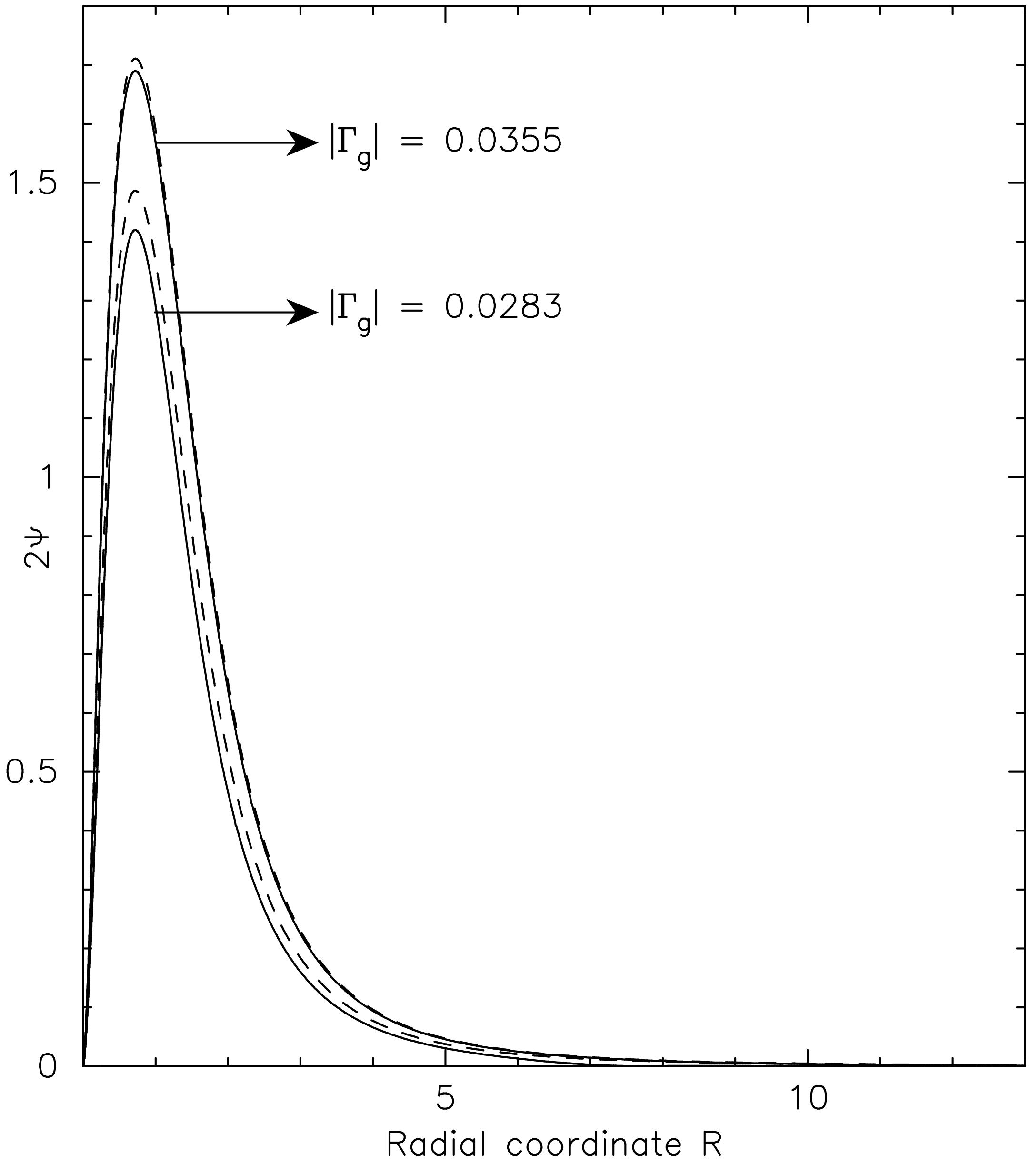

Figure 3.8: Phase difference between z^+ and z^- for $\eta = 1/2$ for growing/damping modes as a function of radial coordinate R. Curves are labeled for $|\Gamma_g|$ values. Phase difference calculated from numerically obtained eigenfunctions is given by solid lines whereas dashed ones are the expected phase difference calculated using Eq (3.63) .

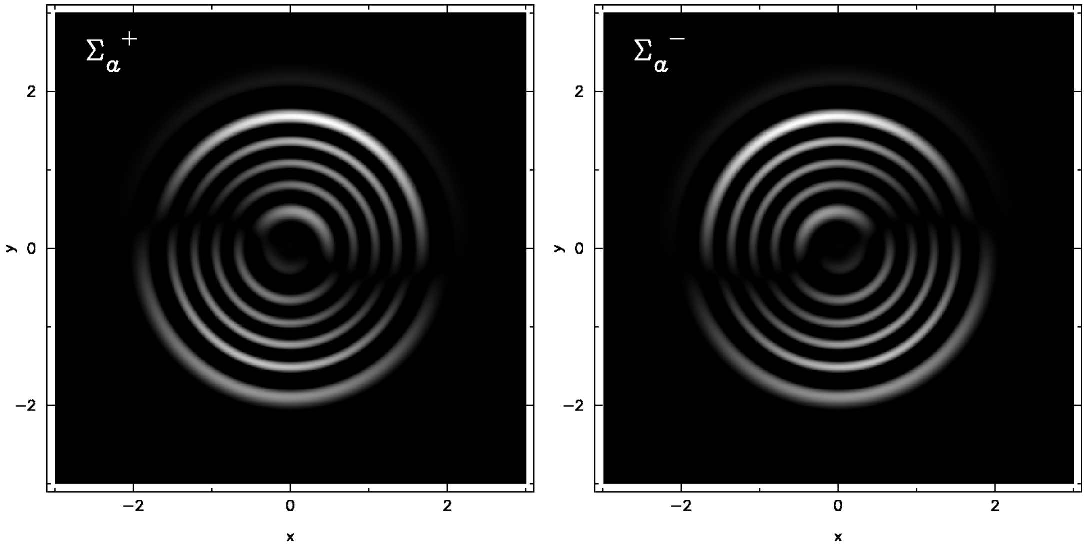

Figure 3.9: Gray–scale plots of positive part surface density perturbations, $\Sigma_a^{\pm}(R, \phi, t)$ at time $t = 0$ for the parameter values, $\eta = 0.5$, $b = 0.1$ and $\Gamma_g = 0.0230$. White/black correspond to the maximum positive/zero values of the perturbations.

the location of ILR. In Fig. 3.1 we have marked the location for $|\dot{\varpi}| = |\sigma|$ with dots, for $|\sigma| = 0.1001$. Same figure also tells us that nature of the radial dependence of the precession rate is such that the condition $|\sigma| = |\dot{\varpi}|$ has (generically) none or two solutions. The precession rate is negative for the "+" disc and positive for the "-" disc. So for $\sigma < 0$, perturbations are singular only in the "+" disc, at the radius corresponding to $\sigma = \dot{\varpi} < 0$ and perturbations in "-" disc are smooth. Similarly, for $\sigma > 0$, the singularity occurs only in "-" disc, at the radius corresponding to $\sigma = -\dot{\varpi} > 0$ and eigenfunction are smooth and oscillatory for "+" disc. Fig. 3.12 shows a typical case for $\eta = 0.25$, $b = 0.1$ and $|\sigma| = 0.1001$. It can be seen that for any value of σ, either negative or positive, there are two radial locations (in the "+" disc or "-" disc, respectively) where the singular perturbations are concentrated because of reason discussed above. Note that Co–Rotation (CR) and outer LR are not relevant for slow modes because: at CR and outer LR, Ω is equal to and less than ω, respectively, but for slow modes $\Omega > \omega$.

As η increases from 0, the eigenvalues belonging to the discrete part of the spectrum go from real to complex, a bifurcation that has been traced in Touma (2002) to a phenomenon identified by M. J. Krein due to the resonant crossing of stable modes. The complex eigenvalues come in complex conjugate pairs, so there are two branches to the distribution, distributed in the shape of a symmetrical "wedge" in the complex

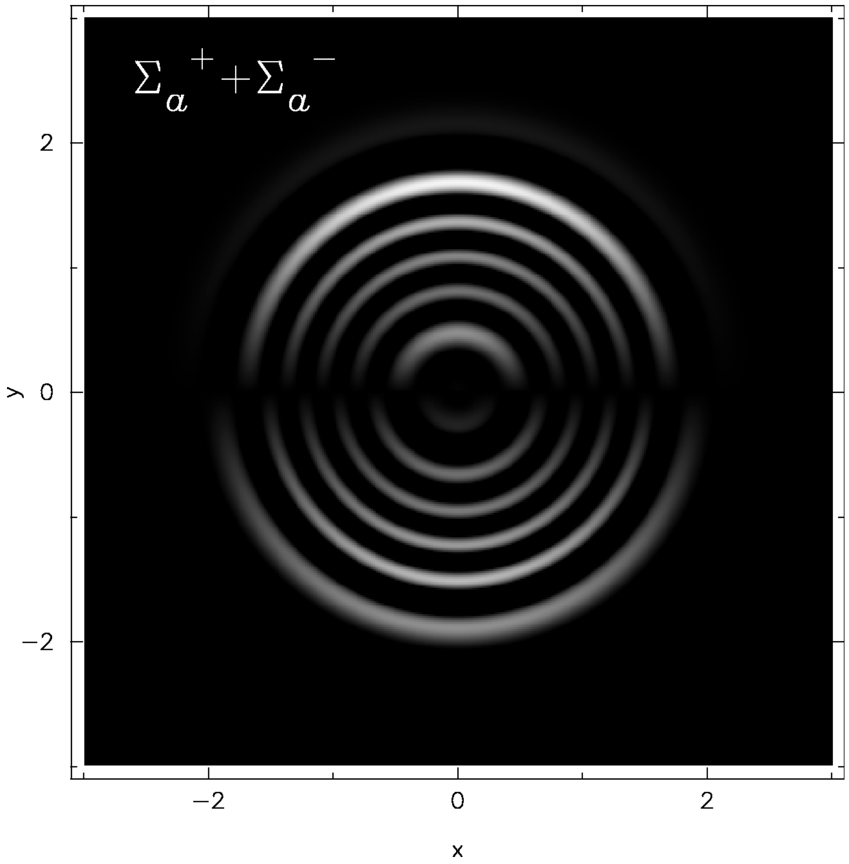

Figure 3.10: Gray–scale plots of positive component of surface density perturbations, $\Sigma_a^+(R,\phi,t)+\Sigma_a^-(R,\phi,t)$ at time $t = 0$ for the parameter values as of Fig 3.9 . White/black correspond to the maximum positive/zero values of the perturbations.

plane. As η increases, the branches progressively separate and, for $\eta = 1/2$, they must lie along the positive and negative imaginary axes. It is intriguing that each of these two branches consists of more than one arm. In the close–up views provided by the 'b' panels of Fig. 3.11, it appears as if each of the branch has two arms; however, more detailed investigations are required to determine if there are more arms. The arms of each of the branch are most widely separated when $\eta = 0.25$, which is the value of η exactly midway in its range $0 \leq \eta \leq 0.5$. The separations decrease as η approaches either 0 or 1/2; this is natural because, for $\eta = 0$ both branches must lie on the real axis and, for $\eta = 1/2$ both branches must lie on the imaginary axis.

The eigenfunctions are in general complex, and have a rich structure as functions of their eigenvalues. Since our interest is in the unstable modes, we now display in Fig 3.13 plots of the $Z_R = \Re[Z(R)]$ defined in Eq. (3.45), corresponding to the "most unstable" modes for softening parameter $b = 0.1$ and η equal to 0.1, 0.25 and 0.4. In other words, for some chosen value of σ_R, we display the real part of the eigenfunction corresponding to the largest value of σ_I. For a fixed value of η, the number of nodes of the eigenfunctions decreases with increasing pattern speed and growth rate. Fig 3.14 is a gray–scale plot of the positive part of surface density perturbations in the ± discs, $\Sigma_a^{\pm}(R, \phi, t = 0)$, for the parameter values $\eta = 0.25$, $b = 0.1$ and $\sigma = 0.1574 + \mathrm{i}\,0.2365$. Density contrast is clearly lopsided. We also display snapshots of evolution of positive part of total surface density perturbation, $\Sigma_a^{+}(R, \phi, t) + \Sigma_a^{-}(R, \phi, t)$, in Fig 3.15, where panels are labeled for $\varphi_p = \sigma_R\, t$, for same set of parameters as in Fig 3.14. White and black represent maximum positive and zero amplitudes respectively. Some of noticeable points in Fig 3.15 are: (i) Each snapshot shows certain amount of lopsidedness in the amplitude; (ii) Apart from an overall increase in the magnitude as the system evolves (exponential increase in magnitude because of factor of $\exp(\sigma_I\, t)$), the pattern also rotates at an angular speed given by σ_R.

It is also of interest to ask how eigenfunctions from two different arms of the same branch behave. To do this, we picked two eigenfunctions with nearly the same value of σ_R, but with values of σ_I corresponding to two different arms of one branch; Fig. 3.16 shows two such pairs of eigenfunctions for $\eta = 0.25$. We have looked at pairs of such eigenfunctions for other values of η, but do not display them, here we note what seems to be a general trend: (i) the two members of a pair are more similar to each other when the values of their σ_R are closer to each other; (ii) the member of a pair with the smaller value of σ_I is more displaced toward larger radii.

3.11 Conclusions

We study linear, *slow* $m = 1$ modes in softened gravity, counter–rotating Keplerian discs. The eigenvalue problem is formulated as (i) WKB–dispersion relation which is also solved by Sridhar & Saini (2010), but due to an error in their calculations we have reworked it here, (ii) a pair of coupled integral equations for the ± modes. We then specialize to the case when the two discs have similar surface density profiles but different ± disc masses. It is of great interest to study the properties of the modes as a function of η, which is the fraction of the total disc mass in the retrograde population. Recasting the coupled equations as a single equation in a new modal variable, we are able to demonstrate some general properties: for instance, when $\eta = 1/2$, the eigenvalues must be purely imaginary or, equivalently, the modes are purely unstable. In other words, when the ± discs have identical surface density profiles then there are growing $m = 1$ modes with zero pattern speed, a conclusion which is consistent with Araki (1987); Palmer & Papaloizou (1990); Sellwood & Merritt (1994); Lovelace et al. (1997); Touma (2002); Tremaine (2005). To study modes for general values of η, the eigenvalue problem needs to be solved numerically and also WKB has its limitation that modes can only be calculated for no– or equal–counter rotation. Our method for solving integral equation is broadly based on Tremaine (2001), but there are some differences whose details have been discussed earlier. The main point of departure is in the way that softening is treated. In Tremaine (2001), a dimensionless softening parameter $\beta = b/R$ was introduced, and the eigenvalue problem was solved by holding the parameter β constant. This procedure renders the physical softening length b effectively dependent on radius (making it larger at larger radii), thereby not corresponding to any simple force law between two disc particles located at different radii. We have preferred to keep b constant, so that the force law between two disc particles is through the usual Miller's prescription.

We calculate eigenvalues and eigenfunctions numerically for discs with surface density profiles of Kuzmin form. Kuzmin discs, being centrally concentrated, are reasonable candidates for unperturbed discs. Moreover, earlier investigations of slow modes (Tremaine, 2001; Sridhar & Saini, 2010) have explored modes in Kuzmin discs, so this choice is particularly useful for comparisons with earlier work. As noted earlier our equations are invariant under simultaneous transformation $(`+', \eta, \omega) \to (`-', 1-\eta, -\omega)$ and hence we choose values of η such that $0 \leq \eta \leq 1/2$. We first calculate global modes by quantizing the WKB–dispersion relation for the case of equal counter rotation and find a single

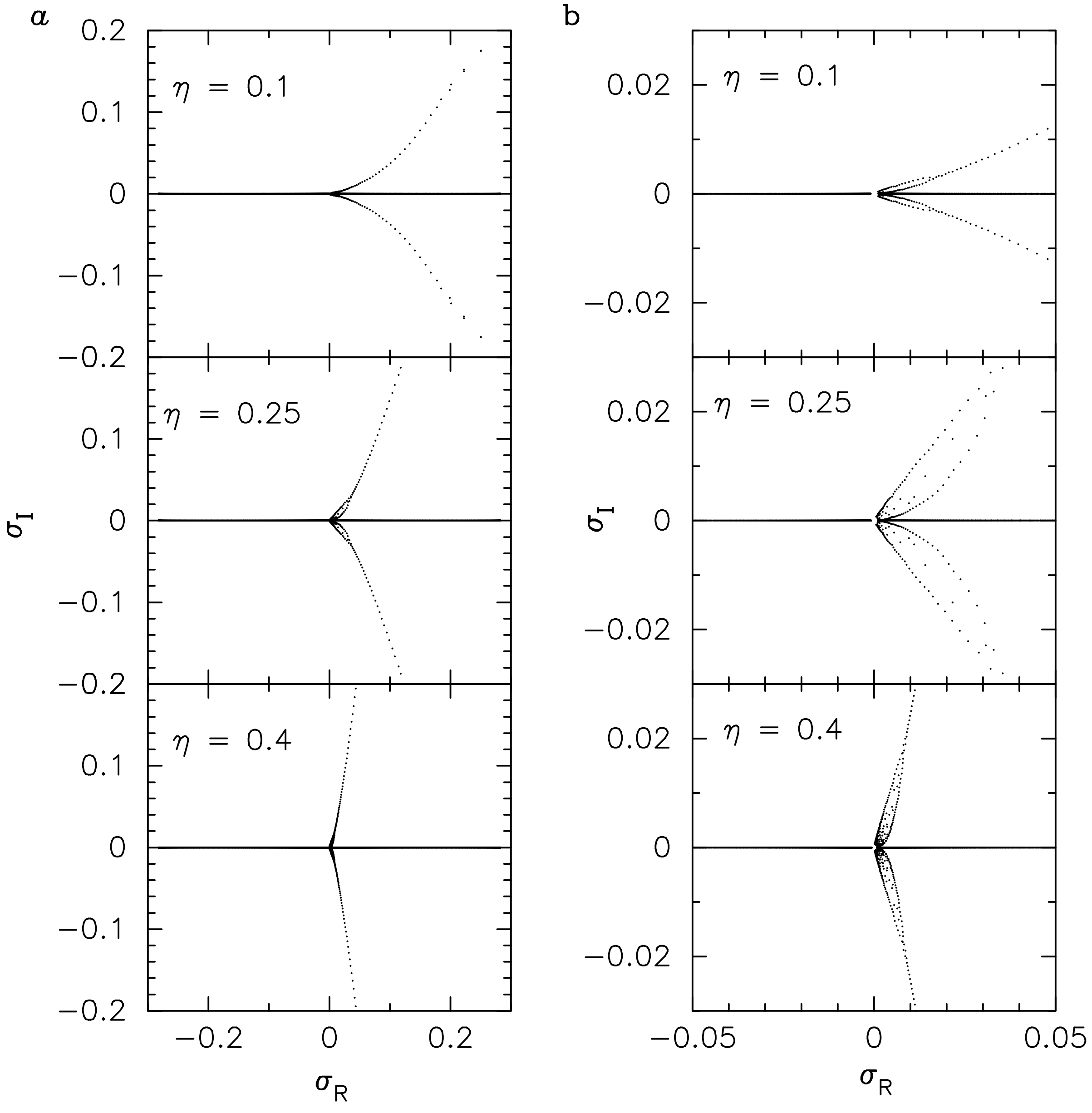

Figure 3.11: Distribution of eigenvalues in the complex σ plane, for $\eta = 0.1, 0.25$ and 0.4. Panels labeled 'a' give an overview, whereas the panels labeled 'b' provide a close–up view near the origin.

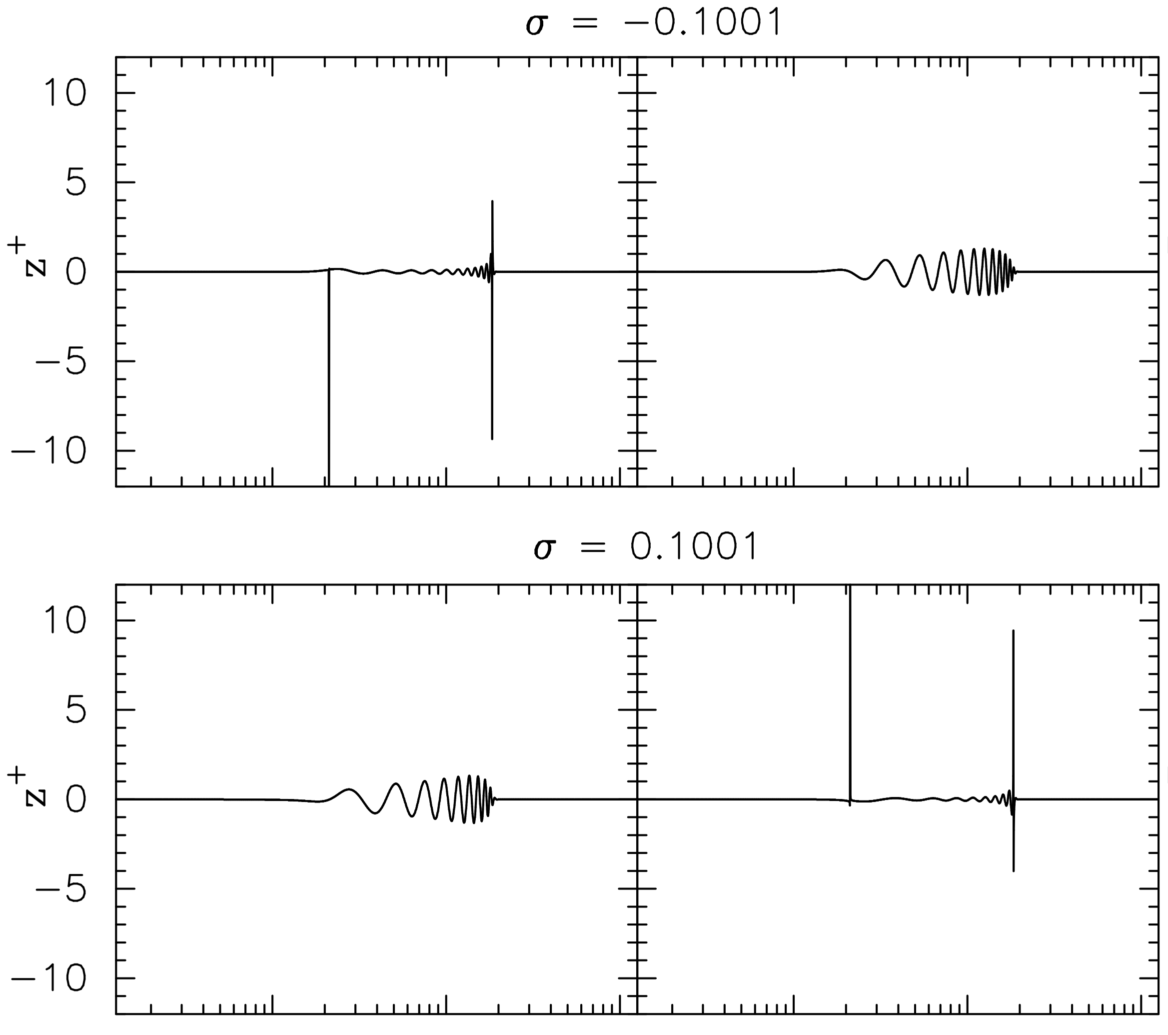

Figure 3.12: Singular modes on the ± discs corresponding to the continuous spectrum for $\eta = 0.25$ and $b = 0.1$. The modes are concentrated at the inner Lindblad resonances, which occur at $\sigma = \dot{\varpi} < 0$ for the "+" disc, and $\sigma = -\dot{\varpi} > 0$ for the "–" disc.

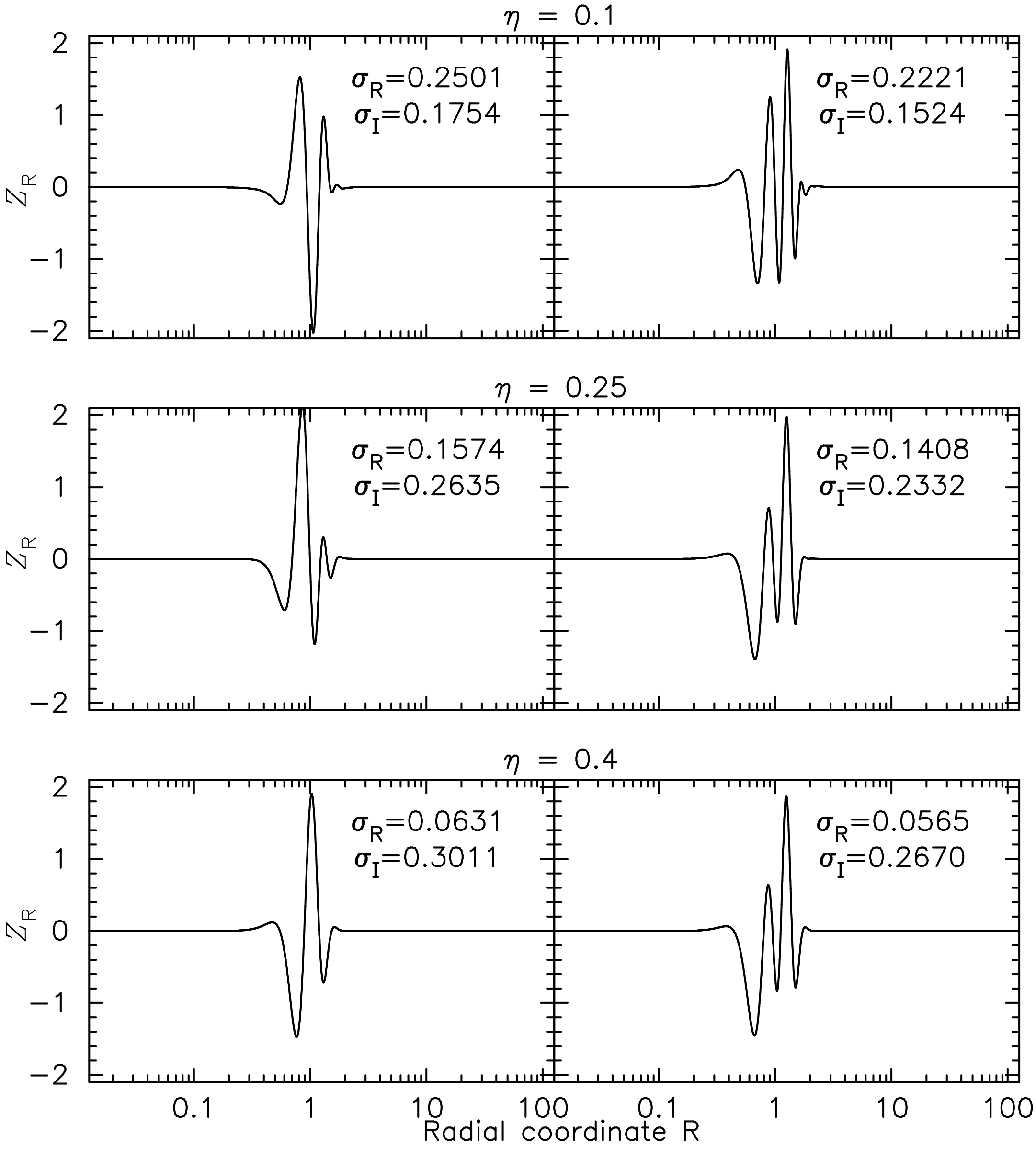

Figure 3.13: Real parts of the "most unstable" eigenfunctions $Z(R)$, plotted as a function of the radial coordinate, (R) for $b = 0.1$ and $\eta = 0.1, 0.25$ and 0.4. Panels are labeled by the real and imaginary parts of the eigenvalues.

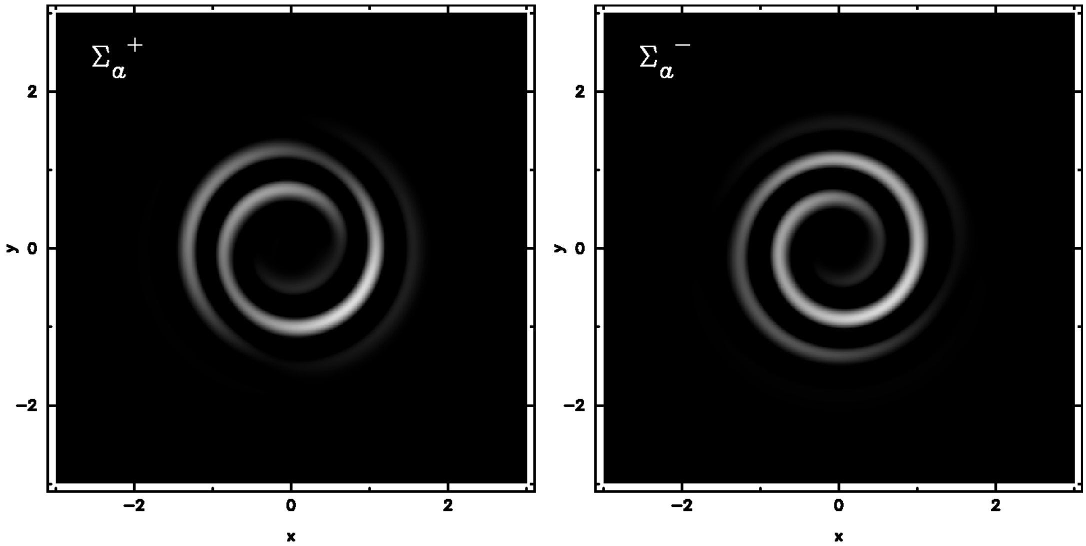

Figure 3.14: Gray–scale plots of positive part surface density perturbations, $\Sigma_a^{\pm}(R, \phi, t)$ at time $t = 0$ for the parameter values; $\eta = 0.25$, $b = 0.1$ and $\sigma = 0.1574 + \mathrm{i}0.2365$. White/black correspond to the maximum positive/zero values of the perturbations.

almost a power–law kind of spectrum in contrast with two branches found by Sridhar & Saini (2010), owing to an error in their numerical explorations of modes. Solving the integral equation and comparing our results with those of Tremaine (2001) for $\eta = 0$ (when the slow modes are stable), we find that the g–mode eigenfunctions are of similar form, but the eigenvalues differ substantially. The reason for this discrepancy can be traced to a typographical error in Tremaine (2001) as pointed to us by Dr. Evgeny Polyachenko; when this is taken into account there is good agreement for eigenmodes with a small number of nodes. For higher eigenmodes there is less agreement, which is probably due to different ways in which softening has been treated. We next compare our solutions to integral equation for $\eta = 1/2$ with the WKB results calculated earlier for the same case. As Fig. 3.6 shows, there is good agreement between WKB–spectrum and the growth rates calculated via solving coupled integral equation, including the horizontal shift in the spectrum when the value of b is changed.

We have also investigated eigenmodes for values of η other than 0 and 1/2. These cases are particularly interesting, not only because they were not explored by WKB–analysis, but because the eigenvalues can be truly complex, corresponding to growing (and damped) modes with non zero pattern speeds. We have presented results for $\eta = 0.1, 0.25$ and 0.4 in the previous sections. Based on these, we interpolate and offer

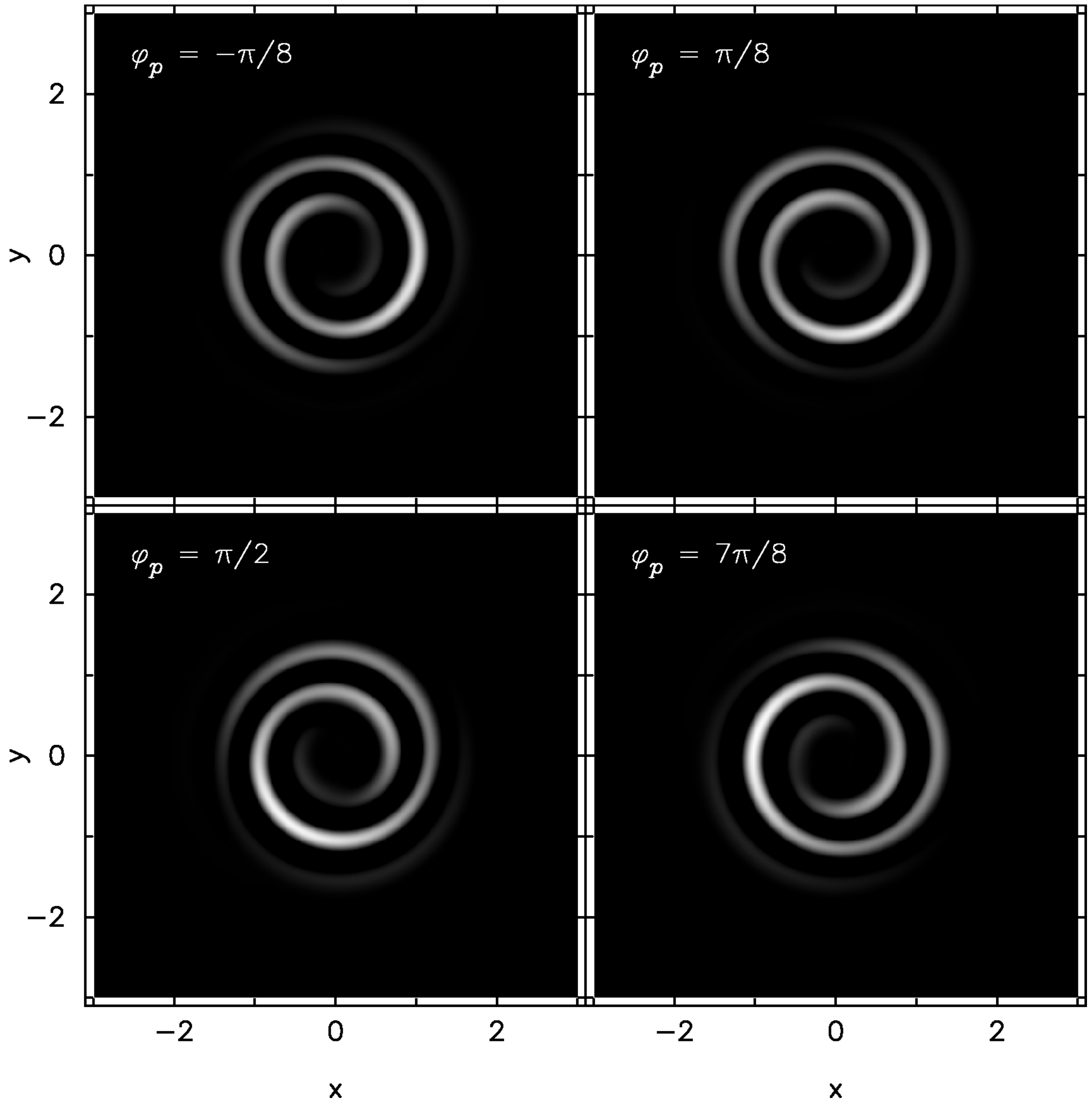

Figure 3.15: Gray–scale plots of positive part of total surface density perturbations, $\Sigma_a^+(R,\phi,t) + \Sigma_a^-(R,\phi,t)$, for same parameter values as in Fig 3.14. White/black correspond to the maximum positive/zero values of the perturbations. Panels are labeled for values of $\varphi_p = \sigma_R\, t$.

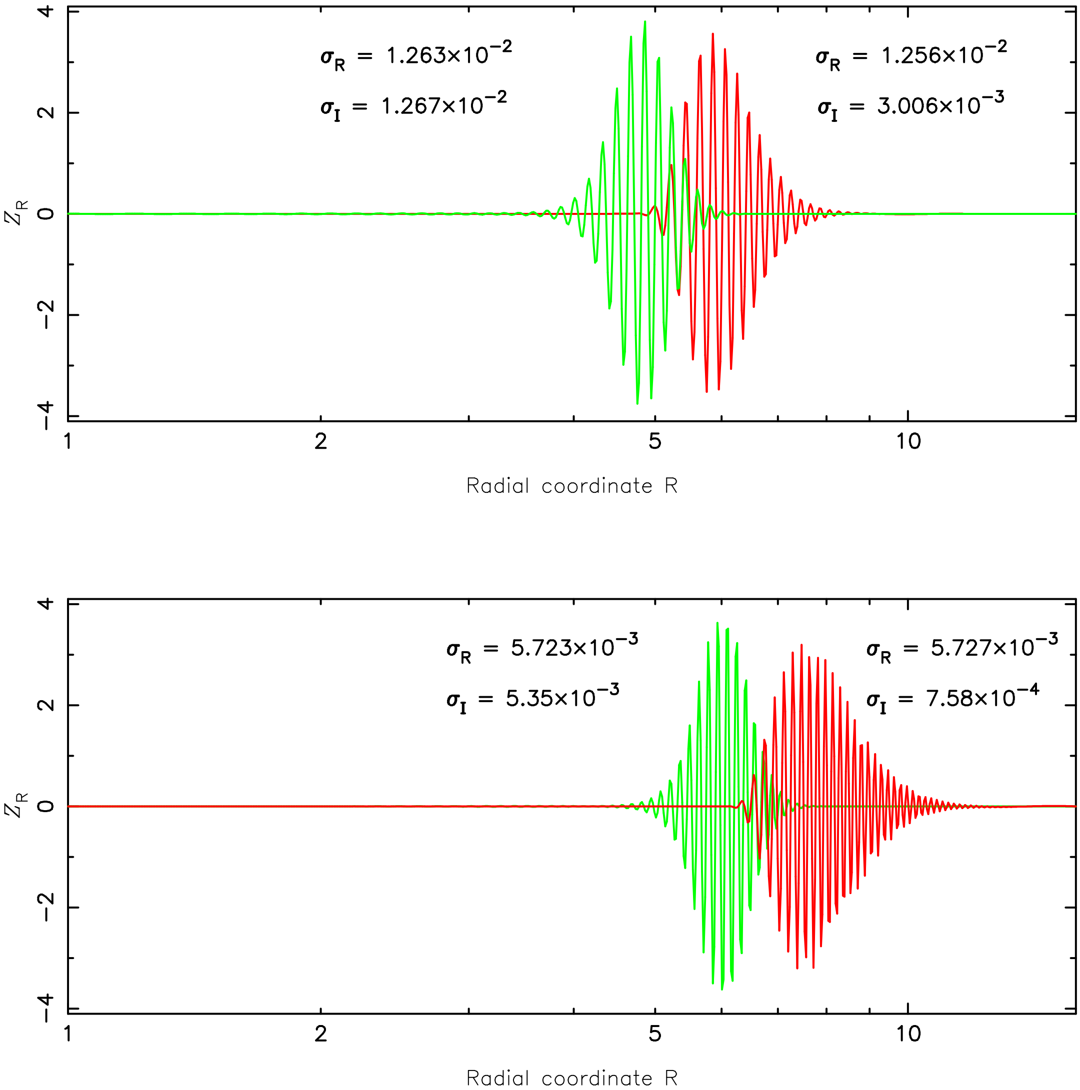

Figure 3.16: Real parts of two pairs of eigenfunctions $Z(R)$ (from two arms of a branch), plotted as a function of the radial coordinate R, for $b = 0.1$ and $\eta = 0.25$. Panels are labeled by the real and imaginary parts of the eigenvalues.

the following conclusions about the properties of the eigenmodes and their physical implications, for all values of η (which is the mass fraction in the retrograde population):

1. There are both continuous and discrete parts of the spectrum of eigenvalues. The former is real whereas the latter occupies a "wedge"–like distribution in the complex plane.

2. The eigenfunctions belonging to the continuous part of the spectrum are singular (van Kampen) modes, which are concentrated at the inner Lindblad resonances.

   The statements below are all concerned with the discrete part of the spectrum.

3. For a general value of η (between 0 and 1/2), the two branches of the wedge are symmetrically placed about the real axis, because the eigenvalues come in complex conjugate pairs.

4. The pattern speed appears to be non negative for all values of η, with the growth (or damping) rate being larger for larger values of the pattern speed.

5. For a fixed value of η, the number of nodes of the eigenfunctions decreases with increasing pattern speed and growth (or damping) rate.

6. Perturbed surface density profile is generally lopsided with an over all rotation of the pattern, as they evolve in time t with pattern speed given by real part of the eigenvalue.

7. For a value of pattern speed in a chosen narrow interval, the growth (or damping) rate increases as η increases from 0 to 1/2.

8. Each of the two branches in the complex (eigenvalue) plane has at least two arms. When $\eta = 0$, the eigenvalues are all real, so both branches lie on the real axis, with zero spacing between the arms. As η increases, the branches lift out of the real axis, and the arms separate. It appears as if the maximum separation between the arms happens when $\eta = 1/4$. As η increases further, branches continue to rise with greater slope, while the arm separation begins decreasing. Finally, when $\eta = 1/2$, the arm separation decreases to zero as the branches lie on the imaginary axis.

Observations of lopsided brightness distributions around massive black holes are somewhat more likely to favour the detection of modes with fewer nodes than modes with a large number of nodes, because the former suffer less cancellation due to finite angular resolution. From items (4) and (5) above, we note that the modes with a small number of nodes also happen to be those with larger values of the pattern speed and growth rate, both qualities that enable detection to a greater degree. We note that the softened gravity discs can be surrogates for collisionless stellar discs only for $m = 1$ slow modes. To study $m > 1$ slow modes, it is necessary to formulate the eigenvalue problem for truly collisionless stellar discs. Such an analysis is expected to have interesting physical implications as we would see in consecutive chapters. Our results here serve as a benchmark for further investigations of modes in these more realistic models.

Chapter 4

Counter–Rotating Keplerian Stellar Discs: Local WKB Analysis

4.1 Introduction

In this chapter we turn to stellar discs, whose dynamics is richer than softened gravity discs. Jalali & Tremaine (2012) derived the dispersion relation for short wavelength slow modes in a single disc with Schwarzschild DF. In contrast to softened gravity discs, which have slow modes only for $m = 1$, stellar discs permit slow modes for $m \geq 1$. Dispersion relation derived by Jalali & Tremaine (2012) makes it evident that all $m \geq 1$ slow modes are neutrally stable. In this chapter we generalize their work to the case of two counter–rotating discs each described by Schwarzschild DF. We derive the dispersion relation for slow $m \geq 1$ waves in the local WKB limit and study the nature of the instabilities.

Section 2 is an account of two–component unperturbed disc; unperturbed orbits, unperturbed mass distribution function given by Schwarzschild distribution function, Poissons integral, and Precession rate of orbits. In Section 3, we derive WKB dispersion relation for the system described in Section 2. Stability of modes is discussed in Section 4 for both axisymmetric and non-axisymmetric perturbations. In Section 5 we discuss in detail numerical calculation of the eigenmodes for various values of azimuthal wavenumber m and mass fraction in the retrograde component of disc. Some concluding remarks and discussions on the results obtained in this chapter are presented in Section 6.

4.2 Unperturbed two-component disc

Dynamics of disc around a massive compact object, like discs of stars orbiting the suppermassive BH found in the center of most galaxies, debris discs etc, are governed by the gravitational potential of the central mass and the self gravity of the disc. In such situations normally the ratio of disc mass $M_{\rm d}$ to central mass M (i.e. $\varepsilon \equiv M_{\rm d}/M$) is much less than unity. Orbits of disc particles are nearly Keplerian, since we neglect relativistic effects the discussion is applicable several Schwarzschild radius away from the central BH. Henceforth we proceed by approximating our discs to be razor-thin, i.e. we restrict ourselves to $z = 0$ plane and work in two spatial dimensions ($\mathbf{r} \equiv (R, \phi)$, cylindrical polar coordinates are used here) rather than three. We shall refer prograde and retrograde components of the discs by '+' and '−' respectively.

The potential $\Phi_0(R)$ for the unperturbed disc is given by,

$$\Phi_0(R) \;=\; -\frac{GM}{R} + \Phi_{\rm d}(R)\,, \tag{4.1}$$

which is a sum of the Keplerian potential due to central mass and gravitational potential due to self gravity of both '±' discs:

$$\Phi_{\rm d}(\mathbf{r}) \;=\; -G\int \frac{\Sigma^{+}_{\rm d}(\mathbf{r}') + \Sigma^{-}_{\rm d}(\mathbf{r}')}{|\mathbf{r} - \mathbf{r}'|}{\rm d}^2 r'\,. \tag{4.2}$$

Since disc masses are $O(\varepsilon)$ smaller compared to central mass, so is $\Phi_{\rm d}$ compared to Keplerian potential. Nearly circular orbits have radial frequency κ and azimuthal frequency Ω given by;

$$\Omega^2(R) \;=\; \frac{GM}{R^3} + \frac{1}{R}\frac{{\rm d}\Phi_{\rm d}}{{\rm d}R}\,, \tag{4.3}$$

$$\kappa^2(R) \;=\; \frac{GM}{R^3} + \frac{3}{R}\frac{{\rm d}\Phi_{\rm d}}{{\rm d}R} + \frac{{\rm d}^2\Phi_{\rm d}}{{\rm d}R^2}\,. \tag{4.4}$$

Such nearly circular orbit with azimuthal frequency $\pm\Omega(R)$ precess at a rate given by $\pm\dot{\varpi}$:

$$\begin{aligned}\dot{\varpi}(R) \;&=\; \Omega(R) - \kappa(R) \\ &=\; -\frac{1}{2\Omega(R)}\left(\frac{2}{R}\frac{\rm d}{{\rm d}R} + \frac{{\rm d}^2}{{\rm d}R^2}\right)\Phi_{\rm d}(R) + O(\varepsilon^2)\,.\end{aligned} \tag{4.5}$$

Note that $\dot{\varpi} \sim O(\varepsilon)$, which allows the existence of slow modes in nearly Keplerian discs for which complex eigenfrequencies are $O(\varepsilon)$ compared to the orbital frequency.

Orbits of the unperturbed disc particles are assumed to be following *Epicycles* (nearly circular orbits). Phase space coordinates (R, ϕ, v_R, v_ϕ) under epicyclic approximation, as given in Eq. (1.12), are;

$$\begin{aligned} R &= R_g + X\cos(\kappa_g t + \psi)\,, \\ \phi &= \phi_0 + \Omega_g t - \frac{\gamma(R)}{R} X \sin(\kappa_g t + \psi)\,, \\ v_R(R) &= -\kappa_g X \sin(\kappa_g t + \psi)\,, \\ v_\phi(R) &= v_c(R) - \frac{\kappa(R)}{\gamma(R)} X \cos(\kappa_g t + \psi)\,. \end{aligned} \tag{4.6}$$

where $\gamma(R) = 2\Omega(R)/\kappa(R)$; $v_c(R) = R\,\Omega(R)$ is the circular velocity; and R_g is the radius of circular orbit for a given angular momentum; X, ψ, and ϕ_0 are epicyclic amplitude, the initial phase and initial azimuthal angle, respectively; $\kappa_g = \kappa(R_g)$ and $\Omega_g = \Omega(R_g)$. We can calculate the values of R_g, X, ψ and ϕ_0 using the boundary/initial conditions for the problem which we shall discuss later.

Two body collisional time for discs such as stellar discs or debris discs are much larger, sometimes even several orders of magnitude larger than the age of the disc itself. However there are relaxation processes like resonant relaxation, time scales relevant for which can be shorter and important for long term evolution of the disc. For times shorter than these we can assume such systems to be collisionless and Collisionless Boltzmann Equation (CBE) is appropriate to describe their evolution. For discs where orbit of a disc particle is described in the *epicyclic approximation*, the solution of CBE is given by the Schwarzschild DF $f_0(v_R, \tilde{v}_\phi, L_z)$ as given in Eq. (1.14),

$$f_0(v_R, \tilde{v}_\phi, L_z) = \mathscr{S}(L_z)\exp\left(-\frac{v_R^2 + \gamma^2\tilde{v}_\phi^2}{2\sigma_R^2(L_z)}\right), \tag{4.7}$$

where L_z is the z-component of the angular momentum. $\tilde{v}_\phi(R) = v_\phi(R) - v_c(R)$ is the difference between azimuthal & circular velocity, $v_R(R)$ is radial velocity, and σ_R is the R component of velocity dispersion. Note that for circular orbits $\tilde{v}_\phi = 0$ and $v_R(R) = 0$. The integral of $f_0(v_R, \tilde{v}_\phi, L_z)$ over the velocity space gives the mass surface density $\Sigma_{\rm d}(R)$ of the unperturbed disc at a particular location in the disc. Integrating f_0 under the condition $\sigma_R \ll v_c$ gives

$$\mathscr{S}(L_z) \;=\; \frac{\gamma(L_z/v_c)\Sigma_{\rm d}(L_z/v_c)}{2\pi\sigma_R^2(L_z/v_c)}\,. \tag{4.8}$$

Hence

$$f_0(R, v_R, \tilde{v}_\phi) \;=\; \frac{\gamma\Sigma_{\rm d}(R)}{2\pi\sigma_R^2}\exp\left(-\,\frac{v_R^2+\gamma^2\tilde{v}_\phi^2}{2\sigma_R^2}\right)\,. \tag{4.9}$$

The prograde and the retrograde discs are assumed to follow Schwarzschild distribution function. Hence DFs for mass density in phase-space for razor-thin unperturbed '±' discs are given by,

$$f_0^{\pm}(R, v_R^{\pm}, \tilde{v}_\phi^{\pm}) \;=\; \frac{\gamma\Sigma_{\rm d}^{\pm}(R)}{2\pi{\sigma_R^{\pm}}^2}\exp\left(-\frac{{v_R^{\pm}}^2+\gamma^2{\tilde{v}_\phi^{\pm}}^2}{2{\sigma_R^{\pm}}^2}\right)\,. \tag{4.10}$$

We have already discussed all the terms in the expression earlier, here they are distinguished for ± discs appropriately. Integrating f_0^+ (f_0^-) over v_R^+ and $\tilde{v}_\phi^+$ (v_R^- and $\tilde{v}_\phi^-$) from $-\infty$ to $+\infty$ gives unperturbed mass surface density $\Sigma_{\rm d}^+(R)$ ($\Sigma_{\rm d}^-(R)$).

4.3 Perturbed disc: WKB dispersion relation

Accounting for the fact that gravity is a long range force, in general the perturbations in all parts of the disc are coupled. However, for tightly wound density waves or WKB approximation, i.e., the waves whose radial wave length is much less than the radius ($|kR| \gg |m|$), the long range interactions are negligible and the system can be studied locally (Lin & Shu, 1964; Toomre, 1964). In this section we shall calculate the dispersion relation for the counter–rotating streams of matter to study some of the global properties of the eigenmodes in the discs. We linearize CBE for the perturbed distribution function, use WKB solution of Poissons equation, and the equation of motion for *epicyclic approximation* for an unperturbed disc, given by equation (4.6), to get the dispersion relation. Before formulating WKB dispersion relation for counter–rotating discs, we first describe main steps involved in the calculation of WKB dispersion relation for a single disc.

4.3.1 Single disc: No counter–rotation

We give here a brief summary of results from Binney & Tremaine (2008); Jalali & Tremaine (2012). Unperturbed axisymmetric disc potential is perturbed adding a non-axisymmetric part to it, which in turn produces perturbation in the DF,

$$\begin{aligned}\Phi(R,\phi,t) &= \Phi_0(R) + \Phi_1(R,\phi,t)\,,\\ f(R,\phi,v_R,\tilde{v}_\phi,t) &= f_0(R,v_R,\tilde{v}_\phi) + f_1(R,\phi,v_R,\tilde{v}_\phi,t)\,.\end{aligned} \tag{4.11}$$

The perturbations are assumed to be infinitesimally small as compared to the unperturbed quantities. Substituting the above equations in CBE and keeping only linear order terms in the perturbed quantities, we get:

$$f_1(R,\phi,v_R,v_\phi,t) = -\int_{-\infty}^{t} \mathrm{d}t' \left(\frac{\partial f_0}{\partial \mathbf{v}} \cdot \nabla\Phi_1\right)_{\mathbf{r}',\mathbf{v}',t'}\,, \tag{4.12}$$

where the integration is done along the unperturbed orbits which follow *epicycles*. The phase-space coordinates $(\mathbf{r}',\mathbf{v}')$ are determined by equations of motion for *epicyclic* approximation given in Eq. (4.6) and the boundary conditions are: for time $t'=t$ phase-space coordinates $(\mathbf{r}',\mathbf{v}')=(\mathbf{r},\mathbf{v})$. Combining Eq. (4.6), the boundary conditions, and keeping only linear order terms in epicyclic amplitude X, we get

$$\begin{aligned}R' &= R + \frac{\gamma\tilde{v}_\phi}{\kappa}\left(1-\cos(\tau)\right) + \frac{v_R}{\kappa}\sin(\tau)\,,\\ \phi' &= \phi + \frac{\Omega\tau}{\kappa} + \frac{\gamma\gamma'}{2\kappa}\tilde{v}_\phi\tau + \frac{\gamma}{R\kappa}\left[\gamma\tilde{v}_\phi\sin(\tau) - v_R\left(1-\cos(\tau)\right)\right]\,,\end{aligned} \tag{4.13}$$

and

$$\begin{aligned}v_R' &= v_R\cos(\tau) + \gamma\tilde{v}_\phi\sin(\tau)\,,\\ \gamma\tilde{v}_\phi' &= \gamma\tilde{v}_\phi\cos(\tau) - v_R\sin(\tau)\,.\end{aligned} \tag{4.14}$$

We have defined $\tau = \kappa_g(t'-t)$ in writing the above, and γ' is the derivative of γ w.r.t. R.

The mean radial perturbed velocity up to first order in perturbations is given by

$$\bar{v}_{R1} = \frac{\int \mathrm{d}v_R\,\mathrm{d}\tilde{v}_\phi\, f_1\, v_R}{\Sigma_{\mathrm{d}}}\,. \tag{4.15}$$

We write the perturbed potential as

$$\Phi_1(R,\phi,t) \;=\; F(R)\exp\left[\mathrm{i}\left(\int^R k(R)\,\mathrm{d}R + m\phi - \omega t\right)\right]\,, \tag{4.16}$$

which essentially divides the radial variation of Φ_1 into a slowly varying function $F(R)$ and a fast varying oscillatory function $\exp\left[\mathrm{i}\left(\int^R k(R)\,\mathrm{d}R\right)\right]$. Only leading order terms in $|kR|$ (that is, WKB or tight winding approximation is applied) and linear order terms in small quantities like X (epicyclic amplitude) and ε (disc mass to central mass ratio) are retained. After carrying out the algebra, expression for $\bar{v}_{R1}$ reduces to

$$\bar{v}_{R1} \;=\; -\frac{k(\omega - m\Omega)}{D_m}\Phi_1\mathcal{F}(s,\chi)\,, \tag{4.17}$$

where $D_m \;=\; \kappa^2 \;-\; (\omega - m\Omega)^2$, $s \;=\; (\omega - m\Omega)/\kappa$, $\chi \;=\; (k\sigma_R/\kappa)^2$; and $\mathcal{F}(s,\chi)$ is defined as:

$$\mathcal{F}(s,\chi) \;=\; \frac{2}{\chi}\,(1-s^2)\,e^{-\chi}\sum_{n=1}^{\infty}\frac{I_n(\chi)}{1-s^2/n^2}\,, \tag{4.18}$$

$I_n(\chi)$ is the modified Bessel's function of order n. Next, Jeans equation (Binney & Tremaine, 2008) is linearized and combined with the solution of Poissons equation under the tight winding approximation, along with equation (4.17), to get WKB dispersion relation:

$$(\omega - m\Omega)^2 \;=\; \kappa^2 \;-\; 2\pi G|k|\Sigma_{\mathrm{d}}\mathcal{F}(s,\chi)\,. \tag{4.19}$$

Note that dispersion relation (4.19) is the same as derived in § 6.2, Eq. (6.61) & (6.63) of Binney & Tremaine (2008). For $m = 1, 2, \ldots$ there are slow modes with $\omega \;\sim\; O(\varepsilon)$ as shown by Jalali & Tremaine (2012). In this case $s^2 \sim m^2$, hence the dominating term in the summation in equation (4.18) corresponds to $n = m$. Using this and keeping only first order terms in ε we get dispersion relation for slow modes for a single disc, as given in appendix of Jalali & Tremaine (2012):

$$\omega \;=\; m\dot{\varpi} \;+\; \frac{m\pi G\Sigma_{\mathrm{d}}|k|}{\kappa}\mathcal{F}_m(\chi)\,, \tag{4.20}$$

where

$$\mathcal{F}_m(\chi) \;=\; \frac{2}{\chi}\,\mathrm{e}^{-\chi}\,I_m(\chi)\,. \tag{4.21}$$

For cold disc $\sigma_R \to 0$. In this case $m = 1$ slow modes behave differently from slow modes with $m > 1$. Using $\sigma_R \to 0$

$$\mathcal{F}_m = \frac{\mathrm{e}^{-\chi}}{m!}\left(\frac{\chi}{2}\right)^{m-1} . \tag{4.22}$$

For $m = 1$, substituting this in Eq. (4.20) we get,

$$\omega = \dot{\varpi} + \frac{\pi G|k|\Sigma_{\mathrm{d}}}{\Omega} , \tag{4.23}$$

which implies that non-singular eigenvalues for $m = 1$ exists even for cold discs. For $m > 1$, Eq. (4.20) & (4.22) implies $\omega = m\dot{\varpi}$. These are singular Van-Kampen modes similar to those discussed § 3.10.3. Note that this also explains why slow modes do not exist for $m > 1$ for zero pressure fluid discs.

4.3.2 Counter–rotating discs:

With the discussions in the previous subsection, background for the formulation of WKB dispersion for counter–rotating discs is complete. We derive the WKB dispersion for counter–rotating discs and make some general comments on the nature of modes supported by the counter–rotating discs in rest of this section. We shall keep all the notations same, but defined separately for '+' and '−' discs with '±' superscripts, respectively. Following the algebra done for a single component disc we can write mean radial velocity, Jeans equation and solution to Poissons equation for both prograde and retrograde discs as follows:

$$\begin{aligned} v_a^{m^\pm}(R) &= \frac{(\pm m\Omega - \omega)}{D_m^\pm} k\Phi_a^m \mathcal{F}(s^\pm, \chi^\pm), \\ \Sigma_a^{m^\pm}(\pm m\Omega - \omega) &= -k\Sigma_{\mathrm{d}}^\pm v_a^{m\pm}, \\ \Phi_a^m &= -\frac{2\pi G}{|k|}\Sigma_a^m, \\ \Sigma_a^m &= \Sigma_a^{m^+} + \Sigma_a^{m^-} , \end{aligned} \tag{4.24}$$

where

$$D_m^\pm = \kappa^2 - (\omega \mp m\Omega)^2, \qquad s^\pm = \frac{\omega \mp m\Omega}{\pm\kappa}, \quad \text{and} \quad \chi^\pm = \frac{k^2 {\sigma_R^\pm}^2}{\kappa^2} \tag{4.25}$$

There are 6 equations and 7 unknowns: the 5 perturbed quantities, the eigenvalue ω, and the radial wavenumber k. These can easily be rearranged to get one equation in terms of the Ω, $\Sigma_{\rm d}^{\pm}$, $\sigma_R^{\pm}$, κ, ω, and k, which is the WKB dispersion relation for counter–rotating discs:

$$2\pi G|k|\left(\frac{\mathcal{F}^{+}}{D_m^{+}}\Sigma_{\rm d}^{+}+\frac{\mathcal{F}^{-}}{D_m^{-}}\Sigma_{\rm d}^{-}\right)=1, \tag{4.26}$$

here $\mathcal{F}^{\pm}=\mathcal{F}(s^{\pm},\chi^{\pm})$. For no counter–rotation $\Sigma_{\rm d}^{-}=0$ and equation (4.26) reduces to the well known WKB dispersion relation derived in equation (4.19).

We now specialize to slow modes with $\omega\sim O(\varepsilon)$ for $m\geq 1$. In this case $s^2\to m^2$, and the dominant term in the summation in expression for $\mathcal{F}^{\pm}$ corresponds to $n=m$. Applying this and keeping terms up to linear order in small quantity ε we get

$$\begin{aligned}\frac{\mathcal{F}^{\pm}}{D_m^{\pm}}&=\frac{\pm m\mathcal{F}_m^{\pm}}{2\Omega(\omega\mp m\dot{\varpi})},\\ \mathcal{F}_m^{\pm}&=\frac{2}{\chi^{\pm}}{\rm e}^{-\chi^{\pm}}I_m(\chi^{\pm})\,.\end{aligned}\tag{4.27}$$

Using this in equation (4.26) and defining $\eta(R)=\Sigma_{\rm d}^{-}(R)/\Sigma_{\rm d}(R)$ to be the mass fractions in retrograde disc at a particular radius, this implies the mass fraction in the prograde disc is '$1-\eta(R)$', we get:

$$\omega^2+B_m\omega+C_m=0\,, \tag{4.28}$$

where

$$\begin{aligned}B_m&=\frac{-\pi mG|k|\Sigma_{\rm d}}{\Omega}\left[(1-\eta)\mathcal{F}_m^{+}-\eta\mathcal{F}_m^{-}\right],\\ C_m&=-m^2\dot{\varpi}^2-\frac{\pi m^2G|k|\Sigma_{\rm d}\dot{\varpi}}{\Omega}\left[(1-\eta)\mathcal{F}_m^{+}+\eta\mathcal{F}_m^{-}\right]\,.\end{aligned}\tag{4.29}$$

Solving the quadratic equation for ω we obtain the dispersion relation:

$$\omega=-\frac{B_m}{2}\pm\frac{\sqrt{B_m^2-4C_m}}{2}. \tag{4.30}$$

The eigenvalue ω is real or imaginary depending on if the discriminant '$B_m^2-4C_m$' is positive or negative respectively. Note that in the limit $\sigma_R^{\pm}\to 0$, as is the case of single disc, non-singular eigenvalues exists only for $m=1$ and for $m>1$, we only have singular van-Kampen modes given by $\omega=\pm m\dot{\varpi}$. We next discuss the stability of these modes.

4.4 Stability of WKB modes:

Stability analysis of the modes is one of the most important application of the dispersion relation derived in the previous section. A system is stable if eigenvalues are real and the modes are oscillatory, whereas a system is unstable or overstable and the modes are growing/damping if ω is complex. The coefficients B_m and C_m in equation (4.28) are all real. Therefore, either ω^2 is real or ω exists as complex conjugate pair. Although the velocity dispersion for '±' discs, σ_R^+ and σ_R^- need not be equal but for simplicity, hereafter, we assume that $\sigma_R^+ = \sigma_R^- = \sigma_R$.

In this case for $m = 0$, the dispersion relation (4.26) reduces to the well-known relation due to Toomre (1964). Therefore the counter–rotating discs are stable to axisymmetric perturbations if it satisfies the Tommre's stability criterion, i.e. $Q > 1$. We next study the stability of slow non-axisymmetric perturbations. The dispersion relation of Eq. 4.30 for $m \geq 1$ slow modes can be rewritten in more explicit form as:

$$\frac{\omega^2 - m^2\dot{\varpi}^2}{\omega[(1-\eta)\mathcal{F}_m^+ - \eta\mathcal{F}_m^-] + m\dot{\varpi}[(1-\eta)\mathcal{F}_m^+ + \eta\mathcal{F}_m^-]} = \frac{m\pi G|k|\Sigma_{\rm d}}{\Omega}\,. \tag{4.31}$$

For a single disc ($\eta = 0$), above equation reduces to equation (4.20), dispersion relation for stable $m \geq 1$ modes.

But for non-zero mass fraction in retrograde and prograde discs this is not the case. The eigenvalues can be in general complex numbers Using $\sigma_R^\pm = \sigma_R$, equation (4.31) reduces to,

$$\frac{\omega^2 - m^2\dot{\varpi}^2}{\omega(1-2\eta) + m\dot{\varpi}} = \frac{m\pi G\Sigma_{\rm d}|k|\mathcal{F}_m}{\Omega}\,, \tag{4.32}$$

where we have defined $\mathcal{F}_m^+ = \mathcal{F}_m^- = \mathcal{F}_m$, which is true when the velocity dispersion for both '±' discs are equal. The above equation is quadratic in ω and its discriminant D is;

$$D = m^2\left[\nu^2(1-2\eta)^2\mathcal{F}_m^2 + 4\dot{\varpi}\nu\mathcal{F}_m + 4\dot{\varpi}^2\right]\,, \tag{4.33}$$

where $\nu = \pi G|k|\Sigma_{\rm d}/\Omega$. Modes are stable if $D > 0$ and unstable if $D < 0$. For the case of single disc ($\eta = 0$), the discriminant $D = m^2\left(\nu\mathcal{F}_m + 2\dot{\varpi}\right)^2 \geq 0$, which implies the modes are all stable, as we know already from Jalali & Tremaine (2012). Note that, for two counter–rotating discs with arbitrary η, $D > 0$ when $\dot{\varpi} > 0$. This agrees with the result of Sridhar & Saini (2010) – see discussion in Sect. 3.4.1 of this thesis. However $\dot{\varpi} < 0$ for the mass precession in realistic discs. Here we briefly note some general conclusions for $\dot{\varpi} < 0$ discs:

1. For equal counter–rotation $\eta = 1/2$, equation (4.32) gives $\omega^2 = m^2\left(\dot{\varpi}^2 + \nu\dot{\varpi}\mathcal{F}_m\right)$ as a real quantity. Modes are stable and oscillatory if $|\dot{\varpi}| > \nu\mathcal{F}_m$, and purely growing/damping otherwise. Thus the stability condition is:

$$\frac{\sigma_R}{v_c} > \left|\frac{\sigma_{R0}}{R\dot{\varpi}}\right| \,, \tag{4.34}$$

   here v_c is the circular velocity and we have defined $\sigma_{R0} = \pi G\Sigma_{\rm d}/\Omega$. In writing the above we have used the fact that $2{\rm e}^{-\chi}I_m(\chi)/\sqrt{\chi} < 1$ for all values of χ and m.

2. Defining $\mathcal{S} = \nu\mathcal{F}_m$, solution for the relation $D = 0$ is given by

$$\mathcal{S}_{\pm} = 2|\dot{\varpi}|\left[\frac{1 \pm 2\sqrt{\eta(1-\eta)}}{(1-2\eta)^2}\right]. \tag{4.35}$$

   Note that $\mathcal{S}$ is always positive. It is straightforward to determine that for $0 < \mathcal{S}_{-} < \mathcal{S} < \mathcal{S}_{+}$, we have $D < 0$. Hence the system is stable if $S_{-} > S_{\rm max}$, where $S_{\rm max}$ is the maximum value of S in the disc which is calculated below. For Keplerian discs $\mathcal{S}$ can be written as:

$$\begin{aligned}\mathcal{S} =& \frac{\pi G\Sigma_{\rm d}\kappa}{\Omega\sigma_R}\frac{2}{\sqrt{\chi}}{\rm e}^{-\chi}I_m(\chi)\\ <& \frac{\Omega\sigma_{R0}}{\sigma_R} \equiv S_{\rm max}\,.\end{aligned} \tag{4.36}$$

   Using all this, the condition $\mathcal{S}_{-} > S_{\rm max}$ simplifies to

$$\frac{\sigma_R}{v_c} > \left|\frac{\sigma_{R0}}{R\dot{\varpi}}\right|\left[\frac{(1-2\eta)^2}{2 - 4\sqrt{\eta(1-\eta)}}\right], \tag{4.37}$$

   Terms on the RHS are of $O(1)$ whereas for the unperturbed distribution function assumed in the present formulation, that is Schwarzschild distribution function, it is assumed that $\sigma_R/v_c \ll 1$. So discs are largely unstable. Note that in deriving Eq. (4.37) we have not used any constraint on the value of η and it is applicable for all the values of $\eta \neq 0$. For example, when $\eta \to 1/2$, the term in $[\ldots]$ goes to unity and the condition (4.37) reduces to the one derived for $\eta = 1/2$ above.

Since we now know the general nature of eigenmodes, it will be good to construct these local WKB modes with some concrete model for discs surface density and velocity dispersion. In rest of the chapter, we shall consider specific models for $\Sigma_{\rm d}$ and σ_R, to solve dispersion relation coupled with an appropriate quantization condition numerically for ω, and to study characteristics of the eigenmodes quantitatively for a given value of η.

4.5 Numerical calculation of the eigenvalues

Stability of the eigenmodes depend on whether the disc satisfies the stability criterion discussed in the previous section. We have already seen that for no counter–rotation ($\eta = 0$), eigenmodes are oscillatory and for equal counter–rotation ($\eta = 1/2$) they are either oscillatory or purely growing/damping. Below we calculate eigenvalues numerically for $\eta = 0$ & $\eta = 1/2$.

We assume the surface density of the unperturbed disc to be of the Kuzmin form:

$$\Sigma_{\rm d}(R) = \frac{aM_{\rm d}}{2\pi(R^2 + a^2)^{3/2}}\,, \tag{4.38}$$

where a is the central concentration parameter. The precession rate $\dot{\varpi}$ for the Kuzmin disc is given by

$$\dot{\varpi}(R) = -\frac{3GM_{\rm d}a^2}{2\Omega(R)(R^2 + a^2)^{5/2}}\,. \tag{4.39}$$

The Keplerian frequency $\Omega(R) = \sqrt{GM/R^3}$. Both the ± discs are assumed to have identical surface density profiles, that is η is a constant. We consider two models for σ_R:

- ***Model I:*** The only assumption that goes into the derivation of Schwarzschild distribution function is that $\sigma_R \ll v_c$. As a first case we take $\sigma_R(R) = Av_c(R) = AR\,\Omega(R) \simeq AR\,\kappa(R)$, with $A \ll 1$, clearly it satisfies the above mentioned criterion.
- ***Model II:*** Epicyclic amplitude for nearly Keplerian orbits is $\cong \sigma_R/\kappa$. Considering it to be a constant, we assume $\sigma_R = b\kappa(R) \simeq b\Omega(R)$. For $b \ll R$, we have $\sigma_R \ll v_c$, consistent with the assumption used for Schwarzschild DF

Normalizing the radius R as R/a, we can recast equation (4.32) into a dimensionless form

$$\frac{\Omega}{m\pi|k|\Sigma_{\rm d}}\left(\frac{\omega^2 - m^2\dot{\varpi}^2}{\omega(1-2\eta) + m\dot{\varpi}}\right) = \mathcal{F}_m\,, \tag{4.40}$$

where we rescale the eigenvalue ω and precession rate $\dot{\varpi}$ with $a^3\Omega(a)/GM_{\rm d}$ to make it a dimensionless quantity. Ω and $\Sigma_{\rm d}$ are recasted into dimensionless form by rescaling them with $\sqrt{GM/a^3}$ and $M_{\rm d}/a^2$ respectively. Modes are determined by solving equation (4.40) for k numerically for a given value of ω & R, and then using Bohr-Sommerfeld quantization condition to obtain the eigenvalues. For $m \neq 0$, RHS of the above equation is bounded and has a maxima less than unity, whereas the LHS is bounded below but unbounded above as it blows up at $R = 0$ and $R \to \infty$. Hence, if the minimum of LHS is less than maximum of RHS then the equation will admit real roots (giving k value for a given R and ω). Also, for small and large R, LHS of (4.40) is singular. So real roots exist only for a finite range of R, $R_1 < R < R_2$ where both R_1 and R_2 are the classical turning points. Following Jalali & Tremaine (2012) we determine the eigenvalues through the Bohr-Sommerfeld quantization condition;

$$\oint k dR = (2n-1)\,\pi \qquad ; n = 1, 2, ... \tag{4.41}$$

n being the quantum number or the number of nodes. In Fig 4.1 we plot contours of constant ω^2 in phase-space for $\eta = 1/2$ and $m = 1$. These contours are of three types. We characterize them as *Type I, II* and *III* exactly the same way as defined in § 3.8, as given below for reference

1. ***Type I***, closed loops around $k = 0$.
2. ***Type II***, the closed contours on both sides of $k = 0$.
3. ***Type III***, are the open contours (with dark shades) for both k positive and negative towards the highest value of $|k|$.

Values of ω for which contours are closed are characterized as eigenvalues if they satisfy the quantization condition (4.41). Above characterization of the contours also holds for other values of m and $\eta = 0$ as well (though their shapes might differ a bit but then our distinction does not depend on the shapes). Next, we solve dispersion relation coupled with quantization condition numerically. Before specializing to specific values of η and m, we mention a mathematical trick that we have used to calculate the reduction factor $\mathcal{F}_m(\chi)$: since the modified Bessel function $I_m(\chi)$ increases exponentially for large values of its argument [1], this makes it difficult to numerically calculate it. Instead, we

---

[1] Asymptotic form of $I_m(x) = {\rm e}^x/\sqrt{2\pi x}$ for large x

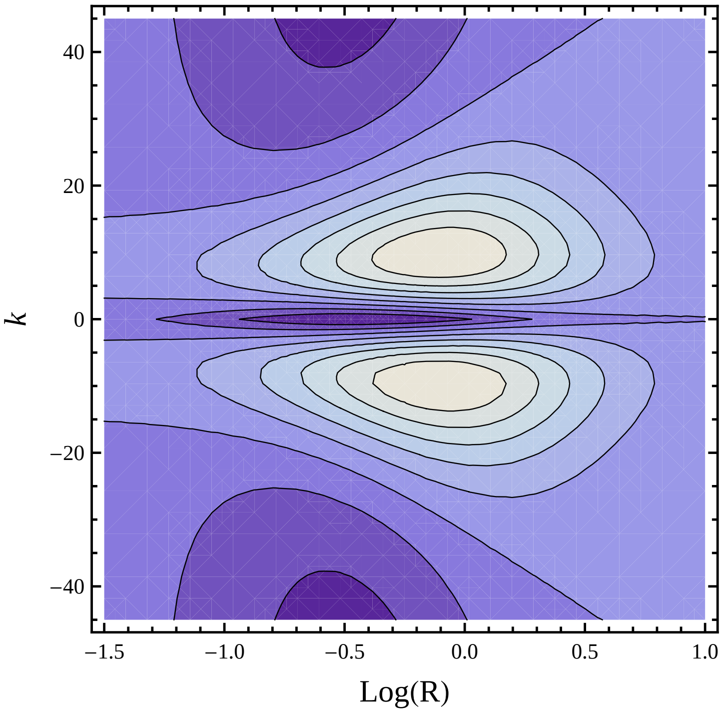

Figure 4.1: Contours of constant ω^2, for $m = 1$ and $\eta = 1/2$ in phase space.

evaluate $e^{-\chi} I_m(\chi)$, which decreases monotonically as $1/\sqrt{\chi}$. Note that this combination exists in the functional form of $\mathcal{F}_m(\chi)$. Next, for a specific value of η, we solve for $m \in (1, 2)$ (in rest of the text by $m \neq 0$ we shall mean $m \in (1, 2)$).

1. $\boldsymbol{\eta = 0}$: For this case equation (4.40) reduces to;

$$\omega = m\dot{\varpi} + \frac{m\pi\Sigma_{\rm d}|k|\mathcal{F}_m}{\Omega}.$$

Clearly eigenvalues are all real and the modes are all oscillatory, as noted by Jalali & Tremaine (2012). For both the models of σ_R discussed earlier, Type I & III contours for $\eta = 0$ and $m \neq 0$ are for $\omega < 0$ whereas ω is positive for type II contours. We give some comments regarding the nature of eigenfrequencies for cold discs (or low velocity dispersion in other words) here. For low σ_R such that $\chi \ll 1$, the factor

$$\mathcal{F}_m = \frac{1}{m!}\left(\frac{\chi}{2}\right)^{m-1}. \tag{4.42}$$

We have used asymptotic from of $I_m(\chi) = \chi^2/m!2^m$ in writing the above expression.

Note that for $m = 1$, $\mathcal{F}_m = 1$ and therefore the eigenvalue ω does not depend on the heat in the system so long as $\chi \ll 1$. But in case of $m \geq 2$, eigenvalues vary with σ_R. For the values of A and b used in this chapter $\chi \ll 1$ for only Type I contours, and hence this conclusion holds only for them.

Area under the curve for Type I closed contours is quite small in this case for both models of σ_R for $m = 1$ and we get eigenvalue for $n = 1$ only. Spectrum for $m = 2$ is shown in Fig. 4.2 with σ_R given by model I for $A = 0.1, 0.05$ & 0.01. Spectrum shifts towards the right as the value of A is decreased. Contours of $\omega = -0.5$ for the same model parameters as in Fig. 4.2 for all values A are plotted in Figure 4.3. The innermost contour, has the lowest area is for $A = 0.1$, next one is for $A = 0.05$ and the largest area is for $A = 0.01$. Larger the area, larger is the n value, as can be seen from equation (4.41), and hence the shift towards right for lower values of A in Fig 4.2.

Spectrum for positive eigenvalues for $m \neq 0$ and model I of σ_R is given in Fig. 4.4. Left panel in Fig. 4.4 displays the spectrum for $m = 1$ & 2 and $A = 0.1$. Right panel displays the spectrum for $m = 1$ and $A = 0.1$ & 0.05. Spectrum shifts towards right with decreasing value of A. Figure 4.5 gives similar plots for model II of velocity dispersion. The trends with varying b & m remain same. All these trends are as expected from the contour plots of constant ω in phase-space.

2. $\boldsymbol{\eta = 1/2}$: For this case Eq. (4.40) becomes

$$\frac{\omega^2 - m^2\dot{\varpi}^2}{m\dot{\varpi}} = \frac{m\pi\Sigma_{\mathrm{d}}|k|\mathcal{F}_m}{\Omega}. \tag{4.43}$$

ω^2 is always real but can be positive or negative, which implies that ω is either purely real (oscillatory modes) or purely imaginary (growing/damping modes), respectively. Referring back to Fig. 4.1, contours around $k = 0$ (Type I) are for positive values of ω^2 and hence real eigenvalues. Type II contours are for $\omega^2 < 0$ (growing/damping modes). Type III contours are for $\omega^2 > 0$ but are not closed. We quantize the closed contours to get the respective eigenvalues. Fig. 4.6 shows the growth rate ($\sqrt{-\omega^2}$) for Type II contours vs number of nodes with σ_R given by model II. Left panel is for $b = 0.1$ and right panel is for $b = 0.05$. Curves for both $m = 1\,\&\,2$ are plotted. Spectrum is quite independent of m. Fig. 4.7 gives the comparison of spectrum for $m = 1$ for both values of b as in Fig. 4.6. Shift in

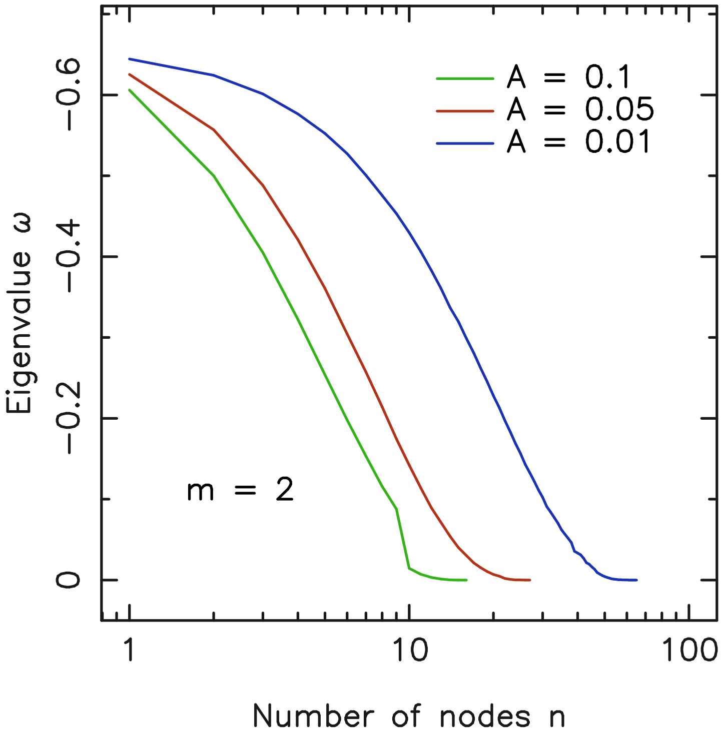

Figure 4.2: ω vs number of nodes for $\eta = 0$ for Type I contours. We discuss the types of contours in § 4.5. $\sigma_R = AR\kappa(R)$, model I. A and m values are mentioned in the plot.

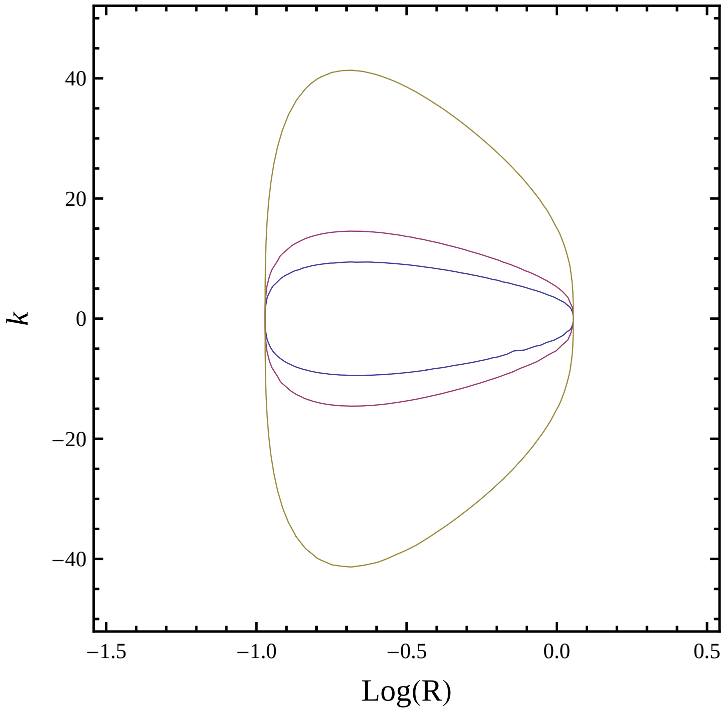

Figure 4.3: Closed (Type I) contours of $\omega = -0.5$ for $\eta = 0$, $m = 2$ and model I for different values of A. Innermost contour is for $A = 0.1$ then for 0.05 and 0.01, respectively.

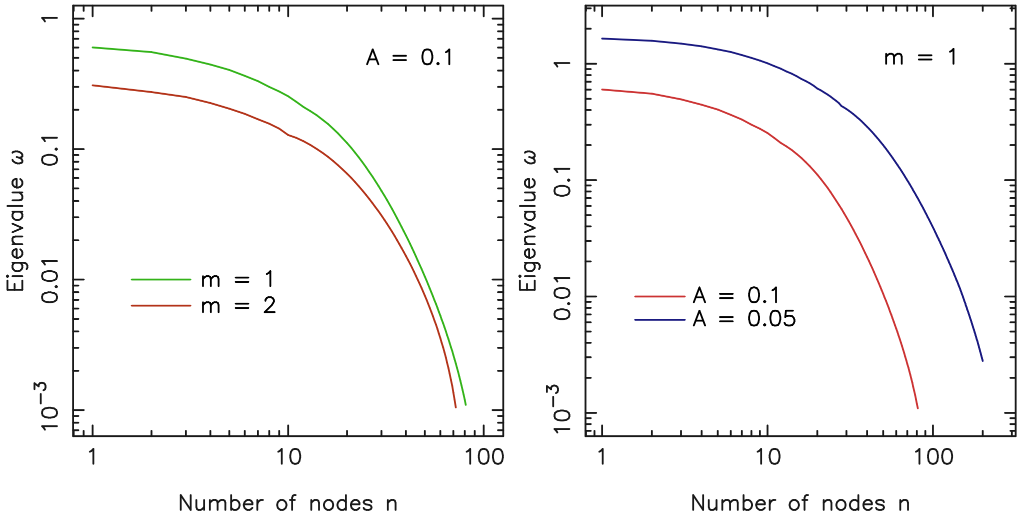

Figure 4.4: ω vs number of nodes for $\eta = 0$ for type II contours. Model I for Velocity dispersion is used. Figure is labeled for values of A and m. Left panel is eigenspectra plot for a fixed value of A and $m \neq 0$. Right panel shows the variation with different values of A, for a given value of m.

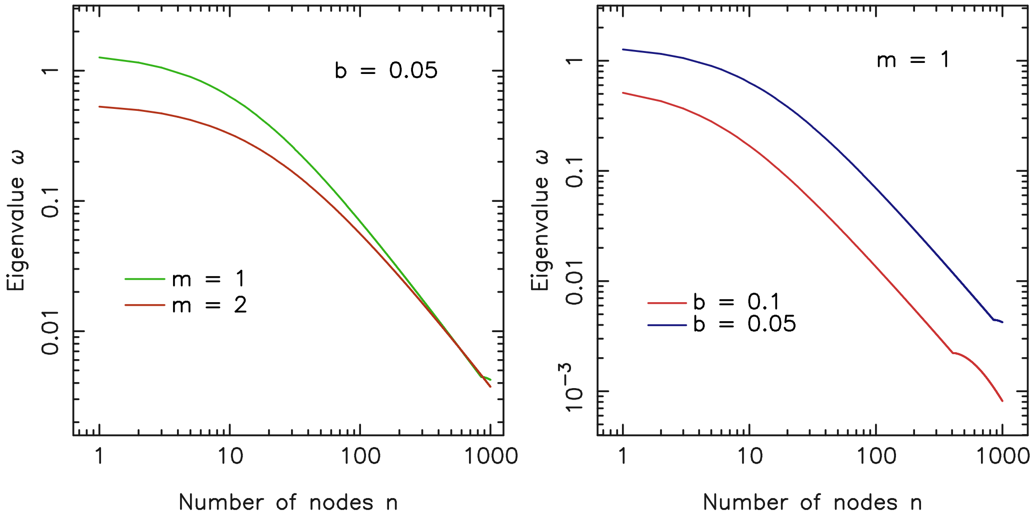

Figure 4.5: ω vs number of nodes for $\eta = 0$ with $\sigma_R = b\kappa(R)$, model II. Plots are labeled for the values of b and m. Left and right panel show the variation in the eigenspectra for a fixed value of b & different m's and fixed value value of m & varying b, respectively.

the eigenvalue curve towards right as we go from $b = 0.1$ to $b = 0.05$ is seen and is consistent with the expected trend from the contour plots. All these conclusions are consistent with Sridhar & Saini (2010) and Gulati et al. (2012).

Similar plots for model I for σ_R are given in Figs. 4.8 and 4.9. Left panel in Fig. 4.8 is the spectrum for $m = 1\,\&\,2$ with $A = 0.1$, and right panel gives the plots with $A = 0.05$. Spectrum is almost independent of m for $A = 0.05$ whereas for $A = 0.1$ there is a shift towards left as we go from $m = 1$ to 2. Reason for the differences can not be attributed to the area enclosed by respective contours as nothing definite can be claimed regarding it from visual inspection of the contours.

Area enclosed in the closed contours for Type I (real eigenvalues) contours is so small in most of the cases that we do not get eigenvalues for nodes greater then $1\,\mathrm{or}\,2$. We plot spectrum for this case in Fig. 4.10 using model II for velocity dispersion, for $b = 0.05\,\&\,0.01$ and $m = 2\,\&\,3$. Left panel of the figure is a plot for $m = 2$ for both the values of b. Abrupt cutoff in both the plots is because the contours are not closed for values of ω lesser than '0.1 for $b = 0.05$' and '0.01 for $b = 0.01$'. Shift towards the right for lower value of b is consistent with the trends in earlier cases. Right panel is the eigenvalue plot for $b = 0.01$ and $m = 2\,\&\,3$. Note that for same value of ω, number of nodes for $m = 2$ are smaller then $m = 3$ whereas the trend was opposite for all the earlier cases displayed. Reason for this can be understood by plotting the contours in phase-space as earlier. We have plotted such contours in Fig. 4.11 for same parameters as of Fig. 4.10 for $\omega = 0.3$. Blue curve is for $m = 2$ and the pink one is for $m = 3$. Area under the curve for $m = 2$ is less than the one for $m = 3$ and hence we expect that for same value of ω, $m = 2$ will have smaller n value than $m = 3$, which is what is observed in Fig. 4.10. The trend is opposite for all the earlier cases.

4.5.1 Comparison with softened-gravity disc

We have already discussed earlier in the previous chapter and this chapter, that softened-gravity provides close analog of a more complex stellar disc for $m = 1$ modes, and can be easily handled numerically. Softened gravity is thought of as a surrogate to stellar disc where softening length mimics heat or velocity dispersion. Here we take the opportunity

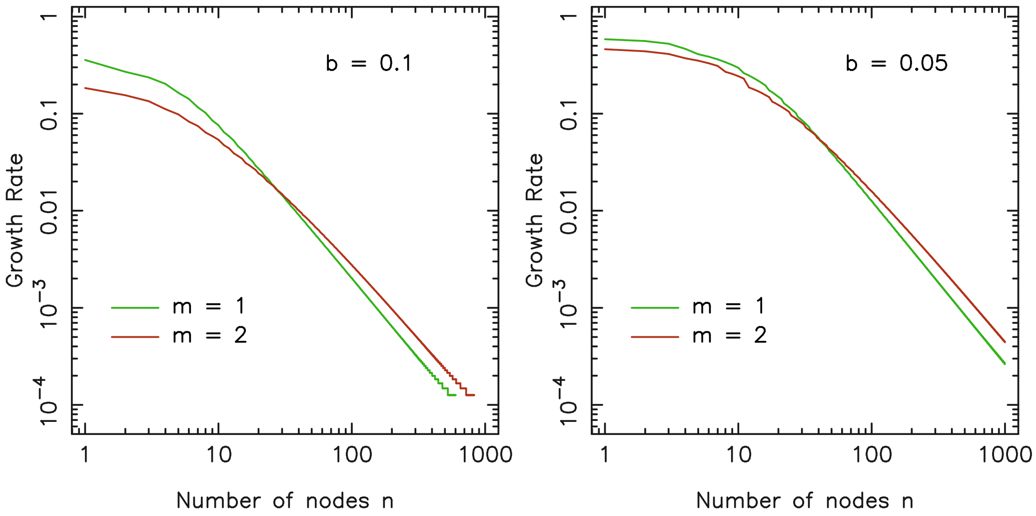

Figure 4.6: Growth rate ($\sqrt{-\omega^2}$) vs number of nodes for $\eta = 1/2$ and model II for σ_R. Appropriate labeling on the panels is done for the values of b and m.

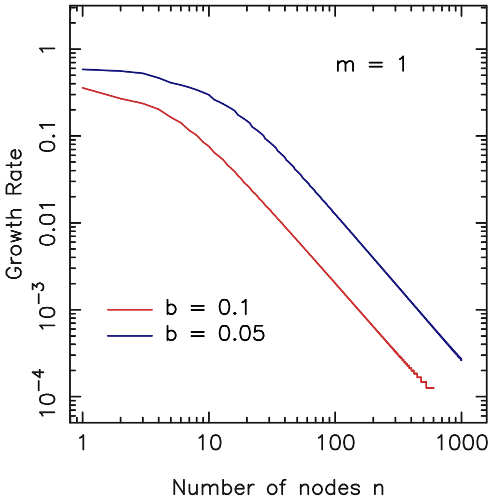

Figure 4.7: This plot shows the comparison between the eigenspectra for varying b and fixed m. Graphs are labeled for the values of b and m.

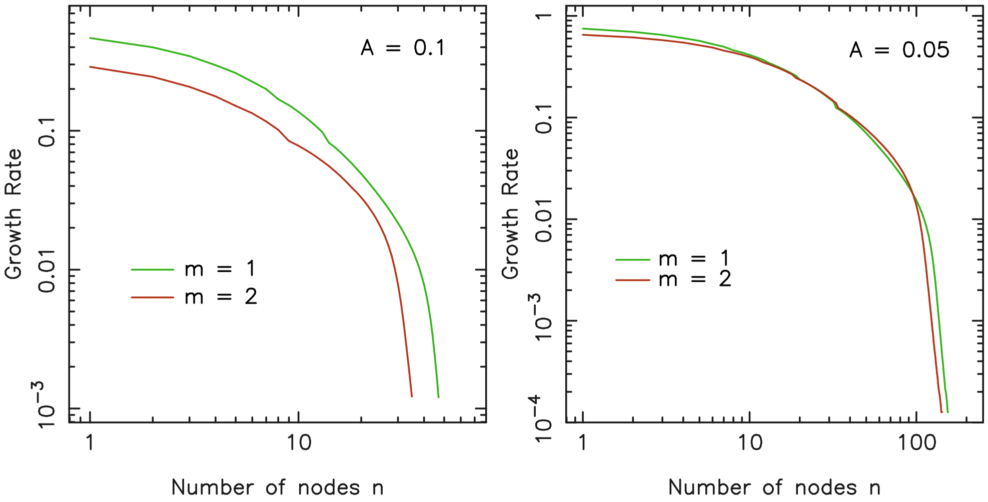

Figure 4.8: Growth rate vs number of nodes for $\eta = 1/2$, model I for σ_R. Values of A and m are mentioned as labels in the plot.

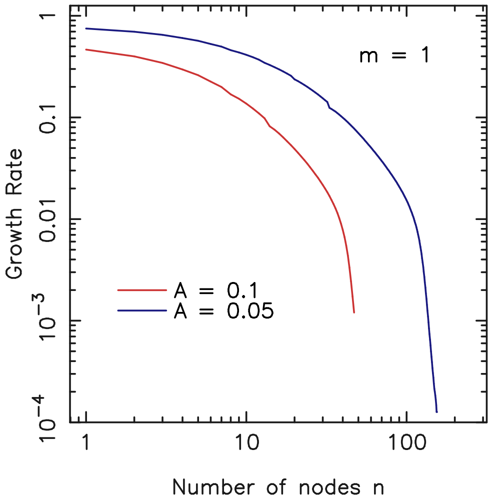

Figure 4.9: Comparison plot for growth rate vs number of nodes for $\eta = 1/2$, for different values of A for $m = 1$.

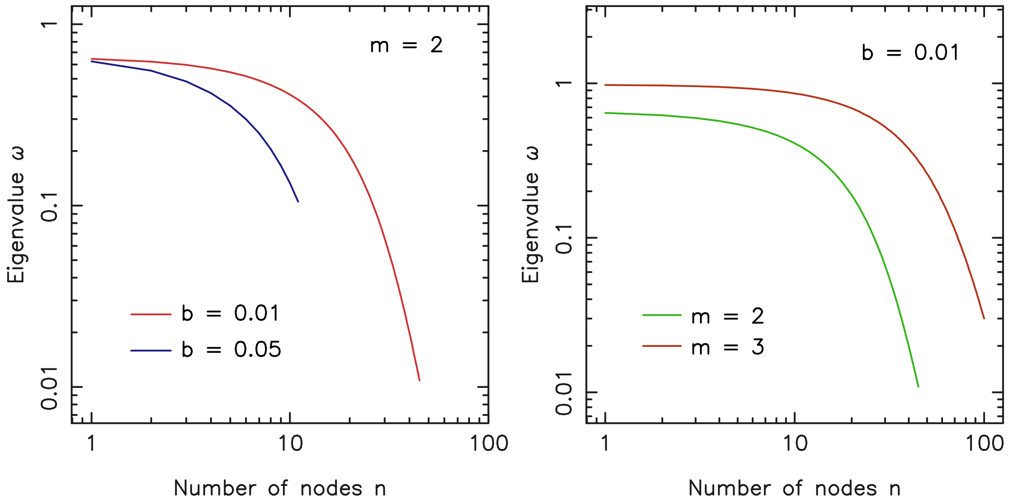

Figure 4.10: Spectrum for oscillatory modes for the case of equal counter–rotation using model II for velocity dispersion. Both the panels are labeled for b and m values.

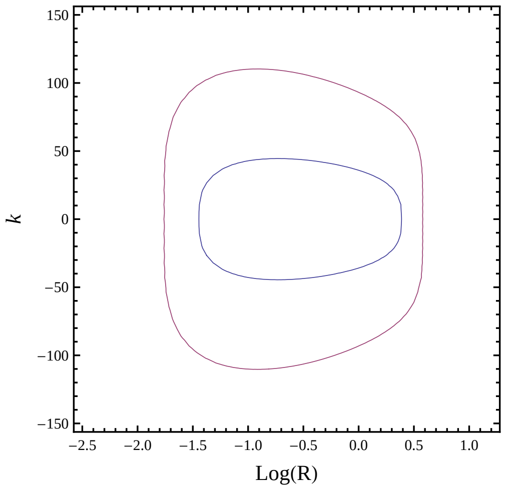

Figure 4.11: Closed contours for type I (real) eigenvalues for $\eta = 1/2$, σ_R used is model II, $b = 0.01$ and $\omega = 0.3$. Blue curve is for $m = 2$ & pink one is for $m = 3$.

Model I (for $A = 0.1$)		Model II (for $b = 0.1$)	
Local WKB solution for collisionless disc	Integral equation solution from Tremaine (2001)	Local WKB solution for collisionless disc	Integral equation solution from Gulati et al. (2012)
0.601	0.67	0.511	0.418
0.554	0.62	0.43	0.377
0.494	0.57	0.368	0.343
0.445	0.52	0.319	0.313
0.404	0.48	0.281	0.288

Table 4.1: Table for comparison of eigenvalues for $\eta = 0$ & $m = 1$ obtained from WKB-dispersion relation using both model I & II for σ_R(column 1 & 3) for $n = 1 - - - 5$. Column 2 gives the five highest eigenfrequencies obtained by solving the integral equation obtained and studied in Tremaine (2001). We read the numbers from the plots in Fig.-5 of Tremaine (2001). Column 4 are the integral equation solutions obtained (highest five frequencies) in the last chapter.

to compare both these approaches. Account of previous study of *slow* modes for softened-gravity disc in literature relevant to the present problem is in Tremaine (2001) and the previous chapter of this thesis. Both the studies treat softening in a different manner. In the first, softening length $b = \beta R$ is radius dependent where β is a constant, and in the other, softening length b is radius independent and is a constant. Consequences of both these are discussed in details in the last chapter. Softening length is thought to mimic epicyclic radius of star's orbit in nearly Keplerian disc, which is $\sim \sigma_R/\kappa$. Hence, model I used in this chapter corresponds to the softening used in Tremaine (2001), with $\beta = A$, and the model II correspond to softening used in the previous chapter. Comparisons with WKB solutions for both $\eta = 0$ and 1/2, with their respective solutions of softened-gravity integral eigenvalue problem relevant for model I and II are as follows:

1. $\boldsymbol{\eta = 0}$ **:** Comparison between the eigenvalues for $\eta = 0$ and $m = 1$ is presented in Table 4.1. First two columns are for model I for σ_R & $A = 0.1$ and next two are for model II for velocity dispersion and $b = 0.1$. First and third columns give the eigenvalues calculated from the local WKB dispersion relation in this chapter for $n = 1 - - - 5$ for both model I and II, respectively. First column is to be compared

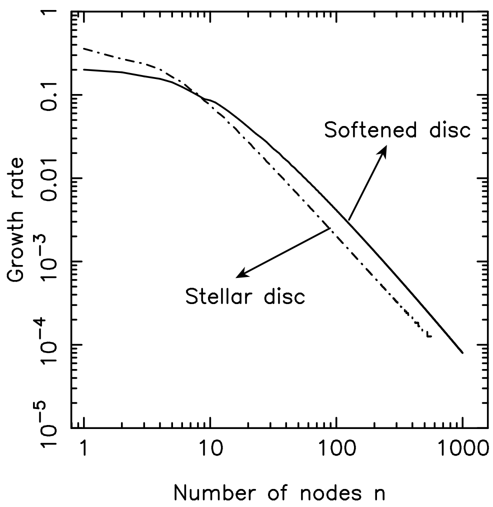

Figure 4.12: Comparison plot for growth rate vs number of nodes for $\eta = 1/2$, $m = 1$ & $b = 0.1$ between the spectrum calculated using the WKB dispersion relation for stellar disc and integral-equation solution for softened-gravity disc calculated in last chapter.

with the second column, which gives the highest five eigenfrequencies obtained from the integral-equation for softened-gravity disc given in Fig. 5 in Tremaine (2001). Corresponding eigenfrequencies for model II, obtained by solving integral-equation in the last chapter are given in the fourth column which is to be compared with the third column. Match between the local WKB solutions for stellar disc and eigenfrequencies from complete eigenvalue problem for softened-gravity disc is quite good (within few percent).

2. $\boldsymbol{\eta = 1/2}$ **:** Integral-equation solution for this case was studied in previous chapter. Figure 4.12 is a plot for growth rate versus number of nodes using, $m = 1$ & $b = 0.1$, for both local WKB solutions (dashed line) and integral equation solution (solid line). Spectrum matches pretty well.

4.6 Conclusions

In this chapter we have studied WKB-modes for general m for collisionless nearly Keplerian discs. We began by explaining the two-component unperturbed disc, which is a superposition of two co-planer discs rotating in opposite direction. Unperturbed orbits follow epicycles and its DF is given by Schwarzschild DF. Stability of both axisymmetric and non-axisymmetric modes is studied assuming that the velocity dispersion in both '±' discs is equal. Unlike zero pressure fluid discs, the stability of $m = 0$ modes does not imply the stability of $m \neq 0$ modes and hence the stability analysis is carried out separately. We have made some general comments regarding the nature of the modes for a given mass fraction η in the retrograde disc and solve the dispersion relation through the Bohr-Sommerfeld quantization condition numerically for $\eta = 0$ and $1/2$. We also made comparisons with the softened-gravity disc. Following conclusions about the properties of the modes and their implications have been made:

- Stability criterion for axisymmetric perturbations is simply the Toomre's stability criterion, that is $Q \equiv \sigma_R \kappa / 3.36 G \Sigma_{\rm d} > 1$.
- For $\eta = 0$, all the non-axisymmetric modes are stable. But when $\eta \neq 0$, non-axisymmetric perturbations are stable if they satisfy the condition given in Eq. (4.37). For epicyclic orbits this constraint is quite difficult to meet and hence modes are largely unstable.
- General trends in the eigenspectra for $\eta = 0$ are: (1) Number of nodes increases as ω decreases, (2) ω value decreases with increasing m, and (3) ω increases with decreasing velocity dispersion.
- For equal counter–rotation, the modes are either real or purely growing/damping. Growth rate for growing modes is in general independent of the m value and the growth rate is higher for lower velocity dispersion. Spectra of real eigenvalues obey the same pattern with the velocity dispersion but the trend reverses for the m variation. The trends of eigenvalues with different parameters can be explained using the contour plots in phase-space.
- A comparison of the WKB eigenvalues is made with the softened gravity disc considered in Tremaine (2001) and Ch. 3 of the present thesis. Match between the eigenvalues is quite reasonable despite the limitations of softened-gravity discs.

We have determined the eigenvalues for $\eta = 0$ & $1/2$. However we could not determine the eigenfunctions due to transcendental nature of the dispersion relation in k. In the next chapter we generalize WKB to include the non-local dependence of the self gravitational potential on the surface density. This allows us to explore both eigenvalues and eigenfunctions for arbitrary η.

Chapter 5

Non-Local WKB Theory for Eigenmodes of Axisymmetric Stellar Discs in the Epicyclic Approximation

5.1 Introduction

In the last two chapters we have formulated and studied the evolution of nearly Keplerian self-gravitating discs assuming;

1. The disc to be a zero pressure fluid disc, where disc particles interact via softened-gravity (Ch. 3).
2. The disc material was assumed to be collisionless, and we studied the properties of the disc locally using WKB approximation (Ch 4).

Although several properties of such systems could be studied in these chapters, there were following limitations (1) Softened-gravity disc mimics a collisionless disc, however we could study only $m = 1$ lopsided modes. They do not support modes for $m > 1$. The other m modes are also important, for instance, $m = 2$ mode supports bar formation. (2) While the local WKB analysis gives a rough idea of collisionless discs, it is difficult to say much about the eigenfunctions. The objective of this and the next chapter is to address these limitations.

To overcome the first limitation above, we consider a truly collisionless disc instead of considering a softened-gravity disc as done in Chapter 3. The WKB-dispersion relation is derived and analyzed for collisionless discs in the previous chapter, based on the following assumptions:

1. Radial wavenumber k times the radius R is much larger than the azimuthal wavenumber m, i.e. $|kR| \gg m$.
2. The epicyclic approximation in which the velocity dispersion σ_R is much less than the circular speed v_c. Also it is assumed that
$$\frac{\sigma_R}{v_c} \sim \frac{m}{|kR|} \ll 1\,.$$
3. The dominant contribution to the perturbed potential at a given point due to the perturbed surface density is local.
4. The Bohr-Sommerfeld quantization condition was used to determine eigenvalues.

One drawback of the above method is that eigenfunctions cannot be obtained as directly as in quantum mechanics because the dispersion relation is transcendental in k. We overcome this difficulty by dropping the assumption in item 3 above, of the locality of the relationship between perturbed self-gravity and surface density. Here we use standard WKB approximation without the assumption of local relationship between the perturbed potential & the perturbed surface density and epicyclic theory, together with the logarithmic-spiral decomposition of surface density and gravitational potential (Kalnajs, 1971). This results in an integral equation determining WKB eigenvalues and eigenfunctions.

In Section 5.2, we discuss the unperturbed disc. The integral equation is derived in Section 5.3. We solve the integral equation derived in § 5.3, to obtain the local WKB-dispersion relation in Section 5.4.

5.2 Unperturbed disc

Unperturbed disc is identical to the prograde disc in the previous chapter. Expressions for various quantities like near circular orbits of particles in the discs, distribution function for the unperturbed disc are given below for further reference in this chapter. The unperturbed stellar orbits are considered to be nearly circular, such orbits are called epicycles and are as given in Eq. (4.13) & (4.14):

$$\begin{aligned} R' &= R + \frac{\gamma\tilde{v}_\phi}{\kappa}\,(1-\cos(\tau)) + \frac{v_R}{\kappa}\sin(\tau)\,, \\ \phi' &= \phi + \frac{\Omega\tau}{\kappa} + \frac{\gamma\gamma'}{2\kappa}\tilde{v}_\phi\tau + \frac{\gamma}{R\kappa}\left[\gamma\tilde{v}_\phi\sin(\tau) - v_R\,(1-\cos(\tau))\right]\,, \end{aligned} \tag{5.1}$$

and

$$\begin{aligned} v_R' &= v_R\cos(\tau) + \gamma\tilde{v}_\phi\sin(\tau)\,, \\ \gamma\tilde{v}_\phi' &= \gamma\tilde{v}_\phi\cos(\tau) - v_R\sin(\tau)\,. \end{aligned} \tag{5.2}$$

where for time $t' = t$, phase-space coordinates $(\mathbf{r}', \mathbf{v}') = (\mathbf{r}, \mathbf{v})$. Also $\tilde{v}_\phi(R) = v_\phi(R) - v_c(R)$; $v_c(R) = R\,\Omega(R)$; $\gamma(R) = 2\Omega(R)/\kappa(R)$; $\tau = \kappa_g(t'-t)$; $\kappa_g = \kappa(R_g)$; and γ' is the derivative of γ w.r.t. R.

Disc is considered to be a collisionless systems. CBE is appropriate for studying the dynamical evolution of such systems. For the unperturbed axisymmetric stellar disc the solution of CBE under epicyclic approximation is given by the Schwarzschild DF, as used in the previous chapter:

$$f_0(R, v_R, \tilde{v}_\phi) = \frac{\gamma\Sigma_{\mathrm{d}}(R)}{2\pi\sigma_R^2}\exp\left(-\frac{v_R^2 + \gamma^2\tilde{v}_\phi^2}{2\sigma_R^2}\right)\,, \tag{5.3}$$

where $\Sigma_{\mathrm{d}}(R)$ is the unperturbed surface density profile.

5.3 Derivation of an integral equation for perturbations

A small–amplitude perturbation, f_1[1], is added to the distribution function f_0, i.e,

$$f(R, \phi, v_R, \tilde{v}_\phi, t) = f_0(R, v_R, \tilde{v}_\phi) + f_1(R, \phi, v_R, \tilde{v}_\phi, t)\,. \tag{5.4}$$

---

[1] All the perturbed quantities are denoted by subscript '1'

Perturbations in the surface density are related to the perturbed DF as

$$\Sigma_1(R,\phi,t) = \int f_1(R,\phi,v_R,\tilde{v}_\phi,t)\mathrm{d}^2\mathbf{v}\,, \tag{5.5}$$

where $\mathrm{d}^2\mathbf{v} = \mathrm{d}v_R\mathrm{d}\tilde{v}_\phi$. The corresponding perturbation in potential $\Phi_1(R,\phi,t)$ is related to perturbed surface density by the Poisson integral:

$$\Phi_1(R,\phi,t) \;= \Phi_1^{\mathrm{dt}}(R,\phi,t) + \Phi_1^{\mathrm{idt}}(R,\phi,t)\,, \tag{5.6}$$

where

$$\Phi_1^{\mathrm{dt}}(R,\phi,t) \;= -\,G\int_0^\infty\int_0^{2\pi}\frac{\Sigma_1(R',\phi',t)R'\mathrm{d}R'\mathrm{d}\phi'}{\sqrt{R^2+R'^2-2RR'\cos(\phi-\phi')}}\,, \tag{5.7}$$

and

$$\begin{aligned}\Phi_1^{\mathrm{idt}}(R,\phi,t) \;&= GR\int_0^\infty\int_0^{2\pi}\frac{\Sigma_1(R',\phi',t)\cos(\phi-\phi')\mathrm{d}R'\mathrm{d}\phi'}{R'}\,,\\ &= \pi GR(\delta_{m,1}+\delta_{m,-1})\exp[\mathrm{i}(\mathrm{m}\phi-\omega\mathrm{t})]\int_0^\infty\frac{\Sigma_a(R')}{R'}\mathrm{d}R'\,.\end{aligned} \tag{5.8}$$

To write the second equation from the first in above equation we have decomposed $\Sigma_1(R',\phi',t) = \Sigma_a(R')\exp[\mathrm{i}(m\phi'-\omega t)]$ and solved the integral over ϕ'. The term Φ_1^{dt} is called the direct term and is due to the gravitational interaction between the disc mass particles, and the term Φ_1^{idt} is the indirect term. The indirect term arises because the origin of the coordinate system considered here is located at the central mass position, which makes it a non–inertial frame. Note that the indirect term is present only if there is a central star around which the stellar disc rotate. In case of no central star the indirect term is identically equal to zero.

Linearized CBE is given by

$$\frac{\mathrm{d}f_1}{\mathrm{d}t} = -\left[f_0,\Phi_1\right]\,, \tag{5.9}$$

where the time derivative on the left hand side is taken along the unperturbed orbit, and the bracket $[*,*]$ on the right hand side is the Poisson Bracket. The solution of linearized CBE is given by

$$f_1(R,\phi,v_R,\tilde{v}_\phi,t) = -\int_{-\infty}^{t}\mathrm{d}t'\,[f_0,\Phi_1]_{\mathbf{x}',\mathbf{v}',t'}\,, \tag{5.10}$$

where $(\mathbf{x}', \mathbf{v}') = (R', \phi', v'_R, \tilde{v}'_\phi)$ are given by Eqs. (5.1) and (5.2).

We seek solutions of the perturbed quantities for which ϕ and t dependence of the perturbed quantities goes as $\exp[\mathrm{i}(m\phi - \omega t)]$ such that the perturbations vanish at $t \to -\infty$. This requires ω to have a non–zero positive imaginary part, however small it may be. Expansion of Poisson Bracket gives

$$[f_0, \Phi_1] = -\frac{\partial f_0}{\partial \mathbf{v}}.\nabla\Phi_1\,. \tag{5.11}$$

Using above and Eqs. (5.6) & (5.10) in Eqn. (5.5) we get

$$\Sigma_a(R) = \Sigma_a^{\mathrm{dt}}(R) + \Sigma_a^{\mathrm{idt}}(R)\,, \tag{5.12}$$

where

$$\Sigma_a^{\mathrm{dt}} = \exp[-\mathrm{i}(m\phi - \omega t)] \int_{-\infty}^{\infty}\int_{-\infty}^{\infty} \mathrm{d}v_R \mathrm{d}\tilde{v}_\phi \int_{-\infty}^{t} \mathrm{d}t' \left[\frac{\partial f_0}{\partial \mathbf{v}}.\nabla\Phi_1^{\mathrm{dt}}\right]_{\mathbf{x}',\mathbf{v}',t'}\,, \tag{5.13}$$

and

$$\Sigma_a^{\mathrm{idt}} = \exp[-\mathrm{i}(m\phi - \omega t)] \int_{-\infty}^{\infty}\int_{-\infty}^{\infty} \mathrm{d}v_R \mathrm{d}\tilde{v}_\phi \int_{-\infty}^{t} \mathrm{d}t' \left[\frac{\partial f_0}{\partial \mathbf{v}}.\nabla\Phi_1^{\mathrm{idt}}\right]_{\mathbf{x}',\mathbf{v}',t'}\,. \tag{5.14}$$

Rest of this section is dedicated to solving the above set of equations, by substituting for Φ_1^{dt} and Φ_1^{idt}, to get the final integral–equation for Σ_a.

5.3.1 Self consistency

We use the log-spiral expansion of surface density and potential (Kalnajs, 1971; Binney & Tremaine, 2008) to write Φ_1^{dt} in Eq. 5.13 in terms of Σ_a^{dt}:

$$\Phi_1^{dt}(R, \phi, t) = -\frac{G}{R^{1/2}} \int_{-\infty}^{\infty} \frac{\mathrm{d}\alpha}{2\pi} N(\alpha, m) A_m(\alpha) e^{\mathrm{i}(\alpha q + m\phi - \omega t)}\,, \tag{5.15}$$

where $q = \ln R$, and

$$A_m(\alpha) = \int_{-\infty}^{\infty} \mathrm{d}q' \, R'^{3/2} \Sigma_a(R') \mathrm{e}^{-\mathrm{i}\alpha q'} \,, \tag{5.16}$$

$$N(\alpha, m) = \pi \frac{\Gamma\left(\frac{m}{2} + \frac{1}{4} + \frac{\mathrm{i}\alpha}{2}\right) \Gamma\left(\frac{m}{2} + \frac{1}{4} - \frac{\mathrm{i}\alpha}{2}\right)}{\Gamma\left(\frac{m}{2} + \frac{3}{4} + \frac{\mathrm{i}\alpha}{2}\right) \Gamma\left(\frac{m}{2} + \frac{3}{4} - \frac{\mathrm{i}\alpha}{2}\right)} \,. \tag{5.17}$$

Note that $N(\alpha, m)$ is a real and even function of both m and α. Using this solution for $\Phi_1^{\mathrm{dt}}(R, \phi, t)$ and that of $f_0(R, v_R, \tilde{v}_\phi)$ given in Eq. (5.3) we get,

$$\begin{aligned} \left.\frac{\partial f_0}{\partial \mathbf{v}} . \nabla \Phi_1^{dt}\right|_{\mathbf{x}', \mathbf{v}', t'} &= \frac{G f_0}{R^{3/2} \sigma_R^2} \exp[\mathrm{i}(m\phi' - \omega t')] \int_{-\infty}^{\infty} \frac{\mathrm{d}\alpha}{2\pi} \times \\ &\times \left[\left(\mathrm{i}\alpha - \frac{1}{2}\right) v_R' + \mathrm{i}m\gamma^2 \tilde{v}_\phi'\right] N(\alpha, m) A_m(\alpha) \mathrm{e}^{\mathrm{i}\alpha q'} \,. \end{aligned} \tag{5.18}$$

Substituting the above in the expression for Σ_a^{dt} given by Eq. (5.13) we get

$$\begin{aligned} \Sigma_a^{\mathrm{dt}}(R) = &\frac{G}{R^{3/2} \sigma_R^2} \exp[-\mathrm{i}(m\phi - \omega t)] \int_{-\infty}^{\infty} \frac{\mathrm{d}\alpha}{2\pi} N(\alpha, m) A_m(\alpha) \times \\ &\times \int_{-\infty}^{\infty} \int_{-\infty}^{\infty} \mathrm{d}v_R \, \mathrm{d}\tilde{v}_\phi \, f_0 \int_{-\infty}^{t} \mathrm{d}t' \, \exp[\mathrm{i}(\alpha q' + m\phi' - \omega t')] \times \\ &\times \left[v_R' \left(\mathrm{i}\alpha - \frac{1}{2}\right) + \mathrm{i}m\gamma^2 \tilde{v}_\phi'\right] \,. \end{aligned} \tag{5.19}$$

In writing the above equation we have made the standard WKB approximations (see Appendix-K of Binney & Tremaine (2008)). These are

1. We have retained only up to first order terms in small parameter $|R' - R|$, which can have a maximum value of $2X$; X being the small epicyclic amplitude.

2. Also to a good approximation we can write $|R' - R| \ll R$, and hence any slowly varying function of R', like $\sigma_R(R')$, $\gamma(R')$, $\Sigma_d(R')$, can be replaced by their values at R and taken out of the integral.

3. Using equation (4.6), $(v_R^2 + \gamma^2 \tilde{v}_\phi^2)/(2\sigma_R^2) = \kappa^2 X^2 / 2\gamma^2 \sigma^2$. Since X is a constant for a given unperturbed orbit. The DF f_0 is independent of the trajectory followed by the unperturbed orbits, and hence can be taken out of integral over t'.

For the next step we use

4. We have $q' = \ln(R') = \ln(R + \delta R)$, where $\delta R \ll R$. Hence we can write $q' = q + (\delta R/R)$ and δR needs to be expressed in terms of v_R, $\tilde{v}_\phi$ and τ using Eq. (4.13).
5. We define $s = (\omega - m\Omega)/\kappa$, $u = v_R/\sigma_R$ and $v = \gamma\tilde{v}_\phi/\sigma_R$.
6. Henceforth we assume that $|\alpha| \gg m$ and we shall keep only leading order terms in α at each step. For large α, the leading order radial oscillations of phase are balanced by the (unperturbed) drift of ϕ at the rate Ω, while the epicyclic drift and oscillations of ϕ may be neglected. Also, in the linear term, i.e. the term outside the exponent, only $\mathrm{i}\alpha v'_R$ term contributes.

Inserting these and the values of v'_R, $\tilde{v}'_\phi$ and ϕ' from equations (4.13)–(4.14) in above the integral we find

$$\Sigma_a^{\mathrm{dt}}(R) = \frac{G\Sigma_d}{2\pi R^{3/2}\kappa\sigma_R}\int_{-\infty}^{\infty}\frac{\mathrm{d}\alpha}{2\pi}N(\alpha,m)A_m(\alpha)\,\mathrm{e}^{\mathrm{i}\alpha q}\int_{-\infty}^{0}\mathrm{d}\tau\,\exp\left[-\mathrm{i}s\tau\right]\mathscr{A}\,, \tag{5.20}$$

where, s' is the derivative of s w.r.t. the radius R. We have defined $\tau = \kappa_g(t' - t)$, and

$$\mathscr{A} = \int_{-\infty}^{\infty}\int_{-\infty}^{\infty}\mathrm{d}u\,\mathrm{d}v\,(au + bv)\exp\left[-\frac{u^2+v^2}{2} + \mathrm{i}(cu + dv)\right]\,; \tag{5.21}$$

$$a = \mathrm{i}\alpha\cos\tau\,,\quad b = \mathrm{i}\alpha\sin\tau\,,\quad c = \frac{\sigma_R}{R\kappa}\alpha\sin\tau\,,\quad \text{and}\quad d = \frac{\sigma_R}{R\kappa}\alpha(1-\cos\tau)\,. \tag{5.22}$$

Since v_R and $\tilde{v}_\phi$ are linear in small parameter 'X' and we are working only up to linear order in small parameters, we have replaced κ_g with $\kappa(R)$ in Eq. (5.20). Integrals in $\mathscr{A}$ can be solved to get

$$\mathscr{A} = 2\pi\mathrm{i}\,(ac + bd)\exp\left[-\frac{c^2+d^2}{2}\right]\,, \tag{5.23}$$

by using the standard integrals

$$\int_{-\infty}^{\infty}\mathrm{d}x\,\mathrm{e}^{-x^2/2}\,\mathrm{e}^{\mathrm{i}\mu x} = \sqrt{2\pi}\mathrm{e}^{-\mu^2/2}\ \text{and}\ \int_{-\infty}^{\infty}\mathrm{d}x\,x\,\mathrm{e}^{-x^2/2}\,\mathrm{e}^{\mathrm{i}\mu x} = \mathrm{i}\sqrt{2\pi}\,\mu\,\mathrm{e}^{-\mu^2/2}\,. \tag{5.24}$$

We evaluate c^2+d^2 and $ac+bd$ using Eq. (5.22);

$$c^2+d^2 = 2\chi\left(1-\cos\tau\right)\,, \quad \text{and} \quad ac+bd = \frac{\mathrm{i}\sigma_R\alpha^2}{R\kappa}\sin\tau\,,$$

where $\chi = \sigma_R^2\alpha^2/R^2\kappa^2$. Substituting these in Eq. (5.23) gives

$$\mathscr{A} = -\frac{2\pi\sigma_R}{R\kappa}\,\alpha^2\sin\tau\,\exp\left[-\chi(1-\cos(\tau))\right]\,. \tag{5.25}$$

Combining Eqs. (5.20) and (5.25), expression for $\Sigma_a^{\mathrm{dt}}(R)$ reduces to

$$\Sigma_a^{dt}(R) = -\frac{G\Sigma_d}{R^{5/2}\kappa^2}\int_{-\infty}^{\infty}\frac{\mathrm{d}\alpha}{2\pi}\,N(\alpha,m)A_m(\alpha)\,\alpha^2\,\mathrm{e}^{\mathrm{i}\alpha q}\mathscr{I}_1(s,\chi)\,, \tag{5.26}$$

where

$$\mathscr{I}_1(s,\chi) = \int_{-\infty}^{0}\mathrm{d}\tau\,\sin\tau\exp\left[-\mathrm{i}s\tau-\chi\left(1-\cos\tau\right)\right]\,, \tag{5.27}$$

The next step is to evaluate $\mathscr{I}_1$. First, using the transformation $\tau\to-\tau$ we get,

$$\mathscr{I}_1 = -\int_0^{\infty}\mathrm{d}\tau\,\sin\tau\exp\left[\mathrm{i}s\tau-\chi\left(1-\cos\tau\right)\right]\,,$$

We then divide the τ integral, which is from 0 to ∞, into a summation series of integrals from $\tau = 0$ to 2π, 2π to 4π and so on. And for each integral using the transformation $\tau\to\tau+2n\pi$ we get

$$\mathscr{I}_1 = -\sum_{n=0}^{\infty}\mathrm{e}^{2\pi\mathrm{i}ns}\int_0^{2\pi}\mathrm{d}\tau\,\sin\tau\exp\left[\mathrm{i}s\tau-\chi\left(1-\cos\tau\right)\right]\,.$$

Note that the τ integral is independent of n. And the summation series over n on the RHS of above expression is a geometric series of the form $\sum_{n=0}^{\infty}p^n$, where $|p| = |\exp(2\pi\mathrm{i}s)| = |\exp(-2\pi\mathrm{Im}(s))| < 1$, because $\mathrm{Im}(s) = \mathrm{Im}(\omega) > 0$ for the perturbations to vanish at $t\to-\infty$, as assumed earlier. This Implies that the series is convergent and the sum equals $1/(1-p)$. Hence we have

$$\mathscr{I}_1 = -\frac{1}{1-\mathrm{e}^{2\pi\mathrm{i}s}}\int_0^{2\pi}\mathrm{d}\tau\,\sin\tau\exp\left[\mathrm{i}s\tau-\chi\left(1-\cos\tau\right)\right]\,.$$

Using the transformation $\tau \to \tau + \pi$, above integral reduces to

$$\mathscr{I}_1 = \frac{\mathrm{e}^{\pi \mathrm{i} s}}{1 - \mathrm{e}^{2\pi \mathrm{i} s}} \int_{-\pi}^{\pi} \mathrm{d}\tau \, \sin\tau \exp\left[\mathrm{i} s\tau - \chi\left(1 + \cos\tau\right)\right] . \tag{5.28}$$

Note that $\sin\tau \, \mathrm{e}^{-\chi(1+\cos\tau)}$ is an odd function of τ and $\mathrm{e}^{\mathrm{i}x} - \mathrm{e}^{-\mathrm{i}x} = 2\mathrm{i}\sin x$, which when applied to $\mathscr{I}_1$ we get

$$\mathscr{I}_1 = \frac{-1}{\sin\pi s} \int_{0}^{\pi} \mathrm{d}\tau \, \sin\tau \sin(s\tau) \exp\left[-\chi\left(1 + \cos\tau\right)\right] .$$

Integrating by parts and using the identities $\mathrm{e}^{z\cos\theta} = \sum_{n=-\infty}^{\infty} I_n(z)\cos(n\theta)$ and $I_n(-z) = (-1)^n I_n(z)$, where $I_n(z)$ is the modified Bessel function of order n, where n is an integer, above integral reduces to

$$\mathscr{I}_1 = \frac{-1}{\chi}\left[1 - \frac{s\mathrm{e}^{-\chi}}{\sin(\pi s)} \sum_{n=-\infty}^{\infty} (-1)^n I_n(\chi) \int_{0}^{\pi} \mathrm{d}\tau \, \cos(s\tau)\cos(n\tau)\right] .$$

A little algebra gives $\int_0^{\pi} \mathrm{d}\tau \, \cos(s\tau)\cos(n\tau) = s(-1)^{n+1} \sin(\pi s)/(n^2 - s^2)$. Using this and the identities $\mathrm{e}^{z\cos\theta} = \sum_{n=-\infty}^{\infty} I_n(z)\cos(n\theta)$ for $\theta = 0$ & $I_{-n}(z) = I_n(z)$ in the above expression gives

$$\mathscr{I}_1 = -\frac{2\mathrm{e}^{-\chi}}{\chi} \sum_{n=1}^{\infty} \left(\frac{n^2}{n^2 - s^2}\right) I_n(\chi) \, . \tag{5.29}$$

Substituting for $\mathscr{I}_1$ from Eq. (5.29) in Eq. (5.26) and simplifying gives

$$\Sigma_a^{dt}(R) = \frac{2G\Sigma_d}{R^{5/2}\kappa^2} \sum_{n=1}^{\infty} \left(\frac{n^2}{n^2 - s^2}\right) \int_{-\infty}^{\infty} \frac{\mathrm{d}\alpha}{2\pi} \, N(\alpha, m) A_m(\alpha) \, \mathrm{e}^{\mathrm{i}\alpha q} \, B_n(\alpha, \chi) \, . \tag{5.30}$$

Here $B_n(\alpha, \chi)$ is defined as

$$B_n(\alpha, \chi) = \frac{\alpha^2}{\chi} \, \mathrm{e}^{-\chi} \, I_n(\chi) \, . \tag{5.31}$$

Note that

1. $B_n(\alpha, \chi)$ is an even function of α. This property will be useful while calculating the integral over α, as we shall see later.

2. To leading order in α, B_n is proportional to α^2.

Having expressed $\Sigma_a^{\rm dt}$ in the desired form Eqn. (5.30) we now turn to the calculation of $\Sigma_a^{\rm idt}$. Below we prove that, to leading order $\Sigma_a^{\rm idt} = 0$. $\Phi_1^{\rm idt}(R,\phi,t)$, as given in Eq. (5.8), can be rewritten as

$$\begin{aligned} \Phi_1^{\rm idt}(R,\phi,t) &= R\exp[{\rm i}(m\phi-\omega t)]\mathscr{I}_m\,, \\ \text{where,}\qquad \mathscr{I}_m &= \pi G(\delta_{m,1}+\delta_{m,-1})\int_0^\infty \frac{{\rm d}R'}{R'}\Sigma_a(R')\,, \end{aligned} \tag{5.32}$$

is a constant. Using this we can write

$$\left.\frac{\partial f_0}{\partial \mathbf{v}}.\nabla\Phi_1^{\rm idt}\right|_{\mathbf{x}',\mathbf{v}',t'} = -\frac{f_0}{\sigma_R^2}\exp[{\rm i}(m\phi'-\omega t')]\left(v_R'+{\rm i}m\gamma^2\tilde{v}_\phi'\right)\mathscr{I}_m\,. \tag{5.33}$$

Combining Eqs. (5.13) and (5.33) and defining s, τ, u and v as done before $\Sigma_a^{\rm idt}$ becomes

$$\Sigma_a^{\rm idt} = -\frac{\mathscr{I}_m\Sigma_d}{2\pi\kappa\sigma_R}\int_{-\infty}^0 {\rm d}\tau {\rm e}^{-{\rm i}s\tau}\mathscr{A}'\,, \tag{5.34}$$

where

$$\mathscr{A}' = \int_{-\infty}^\infty\int_{-\infty}^\infty {\rm d}u\,{\rm d}v\,(a'u+b'v)\exp\left[-\frac{u^2+v^2}{2}\right]\,, \tag{5.35}$$

$$\begin{aligned} a' &= \cos\tau - {\rm i}m\gamma\sin\tau\,, \\ b' &= \sin\tau + {\rm i}m\gamma\cos\tau\,. \end{aligned} \tag{5.36}$$

In writing the above integral we have neglected the oscillations in ϕ and the epicyclic drift term. Neglecting these terms involves same level of approximation as in calculating $\Sigma_a^{\rm dt}$. The integral in $\mathscr{A}'$ is exactly equal to zero since the integrand is an odd functions of u and v, which implies that

$$\Sigma_a^{\rm idt} = 0\,. \tag{5.37}$$

5.3.2 Integral equation

As given in Eq. (5.12), Σ_a is the sum of both Σ_a^{dt} and Σ_a^{idt}. Combining Eqs. (5.12), (5.16), (5.30), and (5.37) we get

$$\Sigma_a(R) = \frac{G\Sigma_d}{R^{5/2}\kappa^2}\int_{-\infty}^{\infty} \mathrm{d}q'\,\mathcal{G}_m(s,\chi,q-q')R'^{3/2}\Sigma_a(R')\,, \tag{5.38}$$

where

$$\mathcal{G}_m(s,\chi,q) = 2\sum_{n=1}^{\infty}\left(\frac{n^2}{n^2-s^2}\right)\int_{-\infty}^{\infty}\frac{\mathrm{d}\alpha}{2\pi}\,N(\alpha,m)\,B_n(\alpha,\chi)\,\mathrm{e}^{\mathrm{i}\alpha q}\,. \tag{5.39}$$

We have already discussed that both the functions $N(\alpha,m)$ and $B_n(\alpha,\chi)$ are even functions of α. Since 'sin' and 'cos' are odd and even functions respectively, only 'cos' term in the integral over α survives. Combining these, the integral equation reduces to,

$$\mathcal{S}(R) = \int_{-\infty}^{\infty}\mathrm{d}q'\,\left[\frac{\mathcal{C}(R)\mathcal{C}(R')}{\kappa(R)}\mathcal{G}_m(s,\chi,q-q')\right]\mathcal{S}(R')\,, \tag{5.40}$$

where

$$\mathcal{G}_m(s,\chi,q) = 4\sum_{n=1}^{\infty}\left(\frac{n^2}{n^2-s^2}\right)\int_{0}^{\infty}\frac{\mathrm{d}\alpha}{2\pi}\,N(\alpha,m)\,B_n(\alpha,\chi)\,\cos(\alpha q)\,. \tag{5.41}$$

and we have defined

$$\mathcal{S}(R) = \frac{R^{3/2}\Sigma_a(R)}{\mathcal{C}(R)} \qquad \text{and} \qquad \mathcal{C}(R) = \sqrt{\frac{G\Sigma_{\mathrm{d}}(R)}{R\kappa(R)}}\,. \tag{5.42}$$

Equation (5.40), together with the functions defined in Eq. (5.41) & (5.42) is the integral eigenvalue problem for tightly-wound linear modes of an axisymmetric disc in the epicyclic approximation. It is not restricted in application to Keplerian discs; it could be used to explore modes of a galactic disc, although we have not pursued the potential application in this thesis.

5.4 The local limit

Here we verify that a local approximation–valid when $|\alpha|$ is not just much larger than m, but is truly large–to the integral problem reduces it to the well-known WKB dispersion relation of (Toomre, 1964).

We first solve the integrals over 'q'' (in particular solve the q' integral in A_m, equation (5.16)) and 'α' in Σ_a (equation (5.39)) using the *stationary phase approximation.* This is a well known technique of asymptotic analysis that is useful in approximating oscillatory integrals. Underlying idea behind the approximation is that for an oscillatory integral with rapidly changing phase, most of the contribution to the integral cancels due to destructive superposition of oscillatory functions. Thus, the phase can be approximated by its Taylor expansion around the stationary phase point, that is the point at which phase change is zero. In addition, the non-oscillatory part of the integrand is simply replaced by its value at the stationary point. It simplifies the integrals considerably. This mathematical technique when applied to evaluate integrals gives an asymptotic solution to the integrals. For more details, refer to Lighthill (2001).

We begin by writing $\Sigma_a(R)$ as

$$\Sigma_a(R) = h(R)\exp\left[\mathrm{i}\int^R k(R'')\mathrm{d}R''\right] .$$

This essentially divides $\Sigma_a(R)$ into a slowly varying function $h(R)$ of R and a fast varying oscillatory function of R. Substituting this in equation (5.16) we get,

$$A_m(\alpha) = \int_{-\infty}^{\infty} \mathrm{d}q' R'^{3/2}\, h(R')\, \exp(\mathrm{i}\psi)\,, \tag{5.43}$$

where $\psi = \int^R k(R'')\mathrm{d}R'' - \alpha q'$, is the phase of the oscillatory part of the integral over q'. A point $R = R_*$ (or equivalently $q = q_*$) is called a stationary point if at $q = q_*$, $\mathrm{d}\psi/\mathrm{d}q = 0$, which when substituted for ψ gives the condition, $R_* k(R_*) = \alpha$. Since the phase is nearly constant at the stationary point (which in turn gives the leading contribution to the integral), we shall replace $\psi(R)$ with its Taylor expansion around R_*,

$$\psi(R) = \psi(R_*) + (q - q_*)^2 \varrho\,,$$

where, $\varrho = R_*^2(\mathrm{d}k/\mathrm{d}R|_{R_*} + \alpha/R_*^2)/2$. We retain terms up to second order in the Taylor expansion. Other parts of the integrand are replaced by their value at R_* and can be taken out of the integral. All this put together in the expression of A_m given in Eq. (5.43) gives,

$$\begin{aligned} A_m(\alpha) =& R_*^{3/2}\Sigma_a(R_*)\, \exp[-\mathrm{i}\alpha q_*] \int_{-\infty}^{\infty} \mathrm{d}q' \exp\left[\mathrm{i}(q'-q_*)^2\varrho\right] , \\ =& R_*^{3/2}\Sigma_a(R_*)\, \exp[-\mathrm{i}\alpha q_*] \left[\sqrt{\frac{\pi}{|\varrho|}} \exp\left[\mathrm{i}\,\mathrm{sgn}(\varrho)\frac{\pi}{4}\right]\right] . \end{aligned} \tag{5.44}$$

The second equality in the above equation uses the Gaussian integrals,

$$\int_{-\infty}^{\infty} \mathrm{d}x \exp\left[\pm\mathrm{i}\lambda x^2\right] = \sqrt{\frac{\pi}{|\lambda|}} \exp\left[\pm\mathrm{i}\,\mathrm{sgn}(\lambda)\frac{\pi}{4}\right] , \tag{5.45}$$

and $\mathrm{sgn}(\lambda)$ is the sign of λ. We next use this value of $A_m(\alpha)$ in the expression of Σ_a^{dt} given in equation (5.30) and the fact that $\Sigma_a = \Sigma_a^{\mathrm{dt}}$ (because the indirect term equals zero for the present formulation), to get

$$\begin{aligned} \Sigma_a(R) =& \frac{2G\Sigma_d}{R^{5/2}\kappa^2} \sum_{n=1}^{\infty} \left(\frac{n^2}{n^2-s^2}\right) \int_{-\infty}^{\infty} \frac{\mathrm{d}\alpha}{2\pi}\, N(\alpha,m)\, R_*^{3/2} h(R_*)\, \mathrm{e}^{-\chi} \times \\ & \times \left[B_n \sqrt{\frac{\pi}{|\varrho|}} \exp\left(\mathrm{i}\,\mathrm{sgn}(\varrho)\frac{\pi}{4}\right)\right] \exp[\mathrm{i}\varphi] , \end{aligned} \tag{5.46}$$

where the phase $\varphi = \int^{R_*} k(R'')\mathrm{d}R'' - \alpha(q_* - q)$. At the stationary phase point $\mathrm{d}\varphi/\mathrm{d}\alpha = 0$, which on substitution of φ, gives the stationary phase point as $q = q_*$ or $R = R_*$. Hence integral over α in above equation, on applying the stationary phase approximation, simplifies to

$$\begin{aligned} \Sigma_a(R) =& \frac{G\Sigma_d}{\pi R^{5/2}\kappa^2} \sum_{n=1}^{\infty} \left(\frac{n^2}{n^2-s^2}\right) N(kR,m)\, R^{3/2}\Sigma_a(R)\, B_n(\alpha,\chi) \times \\ & \times \sqrt{\frac{\pi}{|\varrho|}} \exp\left(\mathrm{i}\,\mathrm{sgn}(\varrho)\frac{\pi}{4}\right) \int_{-\infty}^{\infty} \mathrm{d}\alpha\; \mathrm{e}^{-\mathrm{i}\alpha^2\varsigma} , \\ =& \frac{2G\Sigma_d}{2R\kappa^2} \sum_{n=1}^{\infty} \left(\frac{n^2}{n^2-s^2}\right) N(kR,m)\, \Sigma_a(R)\, B_n(\alpha,\chi) \times \\ & \times \sqrt{\frac{1}{|\varrho\varsigma|}} \exp\left[\mathrm{i}\left(\mathrm{sgn}(\varrho)\frac{\pi}{4} - \mathrm{sgn}(\varsigma)\frac{\pi}{4}\right)\right] . \end{aligned} \tag{5.47}$$

Here ς is defined as $(1/2R_*)(\mathrm{d}R_*/\mathrm{d}\alpha)$ and equation (5.45) is used to write the second equality. A few points to be noted regarding ϱ and ς are:

1. $\varrho\varsigma = \frac{1}{4}$, and
2. $\mathrm{sgn}(\varrho) = \mathrm{sgn}(\varsigma)$.

Both can be derived using the relation $\alpha = R_* k(R_*)$, which was derived earlier. As we know, the basic constraint to be imposed for the present study is $|kR| \gg m$. Also note that $kR = \alpha$ at the stationary phase point. This gives an equivalent condition for WKB as $|\alpha| \gg m$. The asymptotic form of $N(\alpha, m)$ for $\alpha \gg m$ is

$$N(\alpha, m) \sim \frac{2\pi}{(\alpha^2 + m^2)^{1/2}} \sim \frac{2\pi}{|\alpha|}\,. \tag{5.48}$$

All these used together reduces equation (5.47) to

$$\Sigma_a(R) = \frac{2\pi G \Sigma_{\mathrm{d}} |k|}{\kappa^2} \sum_{n=1}^{\infty} \left(\frac{n^2}{n^2 - s^2} \right) \frac{2}{\chi} \mathrm{e}^{-\chi} I_n(\chi) \Sigma_a(R)\,, \tag{5.49}$$

which implies

$$\kappa^2 - (\omega - m\Omega)^2 = 2\pi G \Sigma_{\mathrm{d}} |k| \mathcal{F}(s, \chi)\,, \tag{5.50}$$

where

$$\mathcal{F}(s, \chi) \;=\; \frac{2}{\chi}\,(1 - s^2)\, e^{-\chi} \sum_{n=1}^{\infty} \frac{I_n(\chi)}{1 - s^2/n^2}\,. \tag{5.51}$$

Hence we have verified that the local limit of the integral eigenvalue problem (5.40) reduces to the well-known WKB dispersion relation (Toomre, 1964; Binney & Tremaine, 2008). In the next chapter we visit the integral eigenvalue problem in the limit of slow modes for a Keplerian disc.

Chapter 6

Eigenmodes of a Keplerian Stellar disc in the Tight-Winding Approximation

6.1 Introduction

In the previous chapter we derived an integral equation (5.40) to (5.42) for the eigenmodes of general axisymmetric stellar discs in the epicyclic and tight-winding approximation. In this chapter we solve the integral equation numerically and determine the slow $m = 1$ & $m = 2$ eigenvalues and eigenfunctions for a Keplerian stellar disc with a Schwarzschild distribution function. Basic questions that we try to address in this chapter are:

1. Are the modes generated stable or unstable?
2. What is the effect of varying velocity dispersion on the spectra?
3. How does the eigen-frequency spectra vary with m?
4. What do wavefunctions look like?
5. How do eigenfrequencies and eigenfunctions vary with the unperturbed surface density profile?

We take the *slow mode* limit of the integral equation derived in previous chapter (§ 5.3) and write an eigenvalue problem for the same in Section 6.2. In Section 6.3 we describe the numerical method adopted to solve the eigenvalue problem. Section 6.4 gives an account of solutions obtained for two unperturbed surface density profiles: (1) JT annular disc, (2) Kuzmin disc. Basic properties of the disc profiles will be explained in Section 6.4. We conclude this chapter in Section 6.5.

6.2 The integral equation in the slow mode limit

We begin with the general integral equation derived in previous chapter–Eqs. (5.40) – (5.42)–reproduced below for reference:

$$\mathcal{S}(R) = \int_{-\infty}^{\infty} \mathrm{d}q' \left[\frac{\mathcal{C}(R)\mathcal{C}(R')}{\kappa(R)}\mathcal{G}_m(s,\chi,q-q')\right]\mathcal{S}(R')\,, \tag{6.1}$$

where

$$\mathcal{G}_m(s,\chi,q) = 4\sum_{n=1}^{\infty}\left(\frac{n^2}{n^2-s^2}\right)\int_0^{\infty}\frac{\mathrm{d}\alpha}{2\pi}\,N(\alpha,m)\,B_n(\alpha,\chi)\,\cos(\alpha q)\,. \tag{6.2}$$

and we have defined

$$\mathcal{S}(R) = \frac{R^{3/2}\Sigma_a(R)}{\mathcal{C}(R)}, \quad \mathcal{C}(R) = \sqrt{\frac{G\Sigma_{\rm d}(R)}{R\kappa(R)}}\,, \tag{6.3}$$

$$s(R) = \frac{\omega - m\Omega(R)}{\kappa(R)}, \quad \text{and} \quad \chi(R) = \left(\frac{\sigma_R(R)\alpha}{R\kappa(R)}\right)^2. \tag{6.4}$$

$$B_n(\alpha,\chi) = \frac{\alpha^2}{\chi}\,\mathrm{e}^{-\chi}\,I_n(\chi)\,, \tag{6.5}$$

$$N(\alpha,m) = \pi\frac{\Gamma\left(\frac{m}{2}+\frac{1}{4}+\frac{\mathrm{i}\alpha}{2}\right)\Gamma\left(\frac{m}{2}+\frac{1}{4}-\frac{\mathrm{i}\alpha}{2}\right)}{\Gamma\left(\frac{m}{2}+\frac{3}{4}+\frac{\mathrm{i}\alpha}{2}\right)\Gamma\left(\frac{m}{2}+\frac{3}{4}-\frac{\mathrm{i}\alpha}{2}\right)}\,, \tag{6.6}$$

here $\Sigma_{\rm d}, \Omega, \kappa,$ and σ_R are the unperturbed surface density, azimuthal frequency, radial frequency and radial velocity dispersion, respectively. For a nearly Keplerian disc, $\Omega(R) \simeq \kappa(R) + O(\varepsilon)$. This property of the orbits enables the existence of slow mode with $|\omega| \ll |\Omega|$. This gives $s \simeq -m$, $\gamma \simeq 2$ to leading order and

$$m^2 - s^2 = \frac{2m(\omega - m\dot{\varpi})}{\kappa}\,. \tag{6.7}$$

Hence, in the summation over n from 1 to ∞ in Eq. (5.41), $n = m$ term dominates due to the presence of the factor $1/(n^2 - s^2)$.

Velocity Dispersion Profile: We take $\sigma_R(R) = \sigma R\kappa(R)$, where σ is a dimensionless constant less than unity. Using such a profile means that the radial profile of σ_R is same as $R\kappa(R) \simeq R\Omega(R) = v_c(R)$. Merits of using this profile are that: (1) It satisfies the epicyclic approximation with $\sigma < 1$, which is one of the basic assumptions used in building this theory. (2) As mentioned in the previous chapter, Jalali & Tremaine (2012) have studied a similar problem. Authors have given this as the radial profile of σ_R. Apart from being a reasonable model for velocity dispersion, as shown by them, this also helps us in making direct comparison of our results with theirs.

Since we have assumed σ to be constant, χ is also a constant, leading to considerable simplification. Using all these in Eqs. (6.1)–(6.6) we get

$$\omega\,\mathcal{S}(R) = m\dot{\varpi}(R)\mathcal{S}(R) + \int_{-\infty}^{\infty} \mathrm{d}q'\,\mathcal{H}_m(\sigma, q, q')\,\mathcal{S}(R')\,, \tag{6.8}$$

where the kernel

$$\mathcal{H}_m(\sigma, q, q') = 2m\,\mathcal{C}(R)\mathcal{C}(R')\int_0^{\infty} \frac{\mathrm{d}\alpha}{2\pi}\,N(\alpha, m)\,B_m(\alpha, \chi)\,\cos(\alpha(q - q'))\,. \tag{6.9}$$

This is the integral eigenvalue problem for slow modes in a nearly Keplerian collisionless disc. Note that the kernel of the integral equation is symmetric in R and R' (or q and q'). Hence the integral operator on the RHS can be regarded as a linear Hermitian operator. Properties of Hermitian operators imply that the eigenvalues ω are all real, *thus all slow modes are stable.* Also, the eigenfunctions $\mathcal{S}(R)$ can be assumed to be real.

We define a characteristic disc scale length 'a' such that R/a is the dimensionless radius, M_d/a^2 is the characteristic surface density and $\Omega^* = \sqrt{GM/a^3}$ is the characteristic value of orbital frequency. Using these all the physical quantities are casted into a dimensionless form. The overall effect is that the eigenfrequencies ω are scaled by a factor $\Omega^* a^3/GM_\mathrm{d}$. We shall keep using the same notations for quantities like R, Σ_d, ω, Ω and $\mathcal{C}(R)$ etc as used earlier, though these will represent dimensionless quantities in the rest of the chapter.

6.3 Numerical method

In this section we address the following issues:

1. How to evaluate each component of the integral equation?
2. Discretizing and converting the integral-equation to a matrix equation.
3. How the matrix entries are evaluated and the matrix is inverted?

Let us begin by addressing these issues one by one. First task at hand is to evaluate $\mathcal{H}_m$ defined in Eq. (6.9). Calculation of $\mathcal{H}_m$ basically involves the calculation of the integral over α, and evaluating functions like $N(\alpha, m)$ and $B_m(\alpha, \chi)$. The functional form of $B_m(\alpha, \chi)$ contains the combination $\mathrm{e}^{-\chi} I_m(\chi)$ and we shall calculate this numerically, instead of I_m itself, because I_m increases exponentially for large value of its argument, as explained earlier in § 4.5.

Next we explain the steps used to evaluate $N(\alpha, m)$. As defined in Eq. (6.6):

$$N(\alpha, m) = \pi \frac{\Gamma(z)\Gamma(z^*)}{\Gamma(z+\frac{1}{2})\Gamma(z^*+\frac{1}{2})}\,, \tag{6.10}$$

where

$$z = \frac{m}{2} + \frac{1}{4} + \mathrm{i}\frac{\alpha}{2}\,. \tag{6.11}$$

Using the identities $\Gamma(z^*) = \Gamma(z)^*$ and $zz^* = |z|^2$, expression for $N(\alpha, m)$ becomes

$$N(\alpha, m) = \pi \left| \frac{\Gamma(z)}{\Gamma(z+\frac{1}{2})} \right|^2 . \tag{6.12}$$

We then use the following identity to calculate $|\Gamma(x + \mathrm{i}y)|$:

$$|\Gamma(x+\mathrm{i}y)| = |\Gamma(x)| \prod_{n=0}^{\infty} \left[\frac{(x+n)^2 + y^2}{(x+n)^2} \right]^{-1/2} . \tag{6.13}$$

We take 'log' of both sides which converts the product series into a summation series. Convergence of summation series over n is achieved iteratively till the accuracy of 10^{-8} is attained, and then we exponentiate to get back $\Gamma(x+\mathrm{i}y)$. Also $|\Gamma(x+\mathrm{i}y)|$ is a decreasing function of y and we need to evaluate $|\Gamma(x+\mathrm{i}y)/\Gamma(x+\mathrm{i}y+1/2)|$ as a function of y. Hence when the minimum of machine precision is reached, $N(\alpha,m)$ indeterminant due to numerical underflow of the numerator and the denominator. This can be avoided by using its asymptotic form of this function given in Eq. (5.48).

Let us define K_m such that

$$\mathcal{H}_m(\sigma,q,q') = 2m\,\mathcal{C}(R)\mathcal{C}(R')K_m(\sigma,q-q')\,, \tag{6.14}$$

where

$$K_m(\sigma,q) = \int_0^\infty \frac{\mathrm{d}\alpha}{2\pi}\,N(\alpha,m)\,B_m(\alpha,\chi)\,\cos(\alpha q)\,. \tag{6.15}$$

Next we evaluate K_m as a function of q for a given σ. To evaluate the integral over 'α' we use a grid in $\log(\alpha)$ obtained using Gaussian quadrature rule. Though the integrand becomes quite small for large values of α, but due to the presence of oscillatory function, 'cos', the tail of the integrand becomes important. In principle the integral is to be taken upto infinity, which ensures complete cancellation due to oscillatory functions. Since we evaluate the integral numerically, with finite grid in α, we get small spurious contributions from the tail. To avoid these spurious contributions due to numerical integration we take α range to be quite high with very fine griding. For typical values of maximum value of α, $\alpha_{\max} = \mathrm{e}^{25-27}$, and number of grid points in $\log(\alpha)$ scale $N_\alpha = 10^7$, K_m converges till sixth or seventh decimal place. We tabulate the values of K_m vs q for given values of σ and m, we shall discuss next how do we choose the values for q.

For both 'q' and 'q'', the range covered in our numerical calculation is $[-6\,,6]$, divided in $n_q = 4000$ points each. We choose the lower range of q to avoid numerical singularities for $q \to -\infty$. Also, the upper range is chosen as the surface density decreases substantially beyond $q = 6$. Since each of 'q' and 'q'' range from -6 to 6, and these values enter K_m in a combination $q-q'$ which will vary from -12 to 12 with the presently chosen range, we calculate K_m from -14 to 14 with grid size of 10^5. The range is extended from $[-12,12]$ to $[-14,14]$ just to make sure that tail effects are minimized. As we have discussed earlier there is noise in the tail of the integrand over α due to the presence of oscillatory functions. Hence we do a box smoothening for K_m to reduce the noise further, which works fine precisely due to presence of these oscillatory functions. In Fig. 6.1 we display a plot of K_m as a function of q. Left panel is the plot of smoothened K_m and the right panel is zoom-in of y-axis from -1.5×10^{-4} to 1.5×10^{-4}. Green curve is

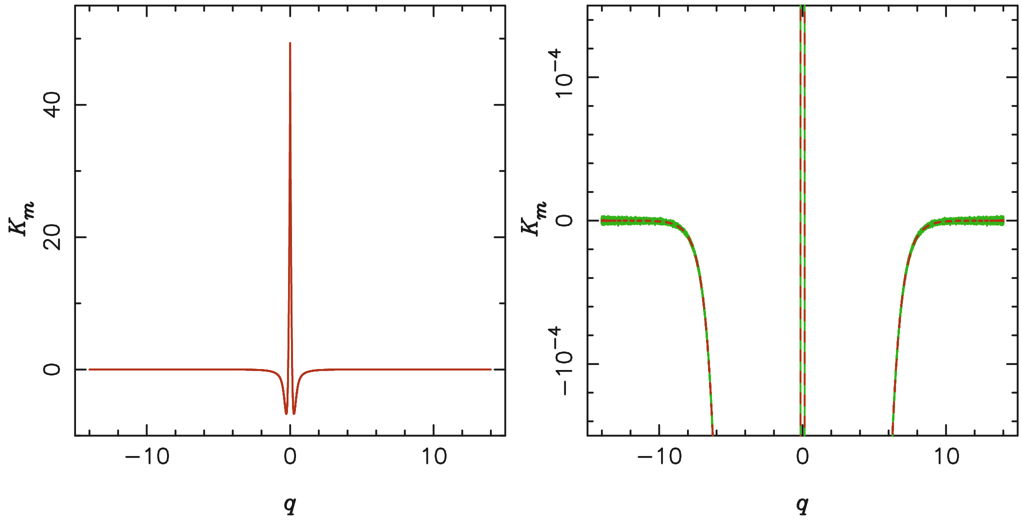

Figure 6.1: Plot of K_m vs q for $m = 1$, $\sigma = \sigma_R/R\kappa(R) = 0.1$. Left panel is the plot of smoothened K_m and the right panel displays the zoom of y-axis for a window of -1.5×10^{-4} to 1.5×10^{-4}. Green one is the original curve whereas red one is after doing a box-smoothening.

the unsmoothened curve whereas the red one is the smoothened curve. Clear effect of smoothening in reducing the noise can be seen. Once we have tabulated K_m as a function of q for a given m and σ as discussed above, we divide $-6 \le q$ (and q') ≤ 6 in a grid of n_q points and interpolate to calculate actual matrix entries.

Further, the discretization of the integral over q' in Eq. (6.8) follows the scheme as explained in § 3.9, Eq. (3.57). Using this, discretized integral-equation can be written as:

$$\mathbf{A}\mathcal{S} = \omega\mathcal{S}, \tag{6.16}$$

where $\mathbf{A}$ is a $n_q \times n_q$ matrix defined as

$$\mathbf{A} = \Big[w_{q_j}\mathcal{H}_m(\sigma, q_i, q_j) + m\dot{\varpi}_i\delta_{ij}\Big]. \tag{6.17}$$

Row and column indices are i and j, respectively. Note that no summation is implied over repeated indices. We divide q (and q') on a grid of n_q points using the Gaussian quadrature rule, where w_{q_j} are the weights. Since the weights are unequal, discretization does not allow the symmetry property of the kernel $\mathcal{H}_m$ to be carried forward in to $\mathbf{A}$.

We shall use the method discussed and used in § 3.9 to restore the symmetry.

We have now reduced our problem to a n_q dimensional matrix eigenvalue problem with ω as eigenvalue and the column vector $\mathcal{S}$ being the eigenvector. We next use the linear algebra package LAPACK (Anderson et al., 1999) to invert the matrix to calculate eigenvalues and eigenvectors. Most of the eigenvalues (out of the n_q values) we get are singular van Kampen modes, which are part of the continuum spectrum, along with the discrete spectrum of eigenvalues.

6.4 Numerical results

In this section we shall discuss the numerical results obtained after solving the matrix eigenvalue equation. We first discuss some general properties of K_m as a function of σ. Its general profile, that is the shape of K_m vs q plot, remains same as that in Fig. 6.1. But the peak values, width of the sinusoidal, and the errors on the each entry vary with σ. In Table 6.1, we have given various parameters of K_m vs q plot for different values of σ and $m = 1$. We note the following general trends:

- Both positive and negative peak, $p1$ (column 3) and $p2$ (column 4), respectively, vary as $1/\sigma^2$. This can be seen from the expression of K_m (more precisely B_m), which is proportional to $\alpha^2/\chi^2 = 1/\sigma^2$.
- Width of the sinusoid varies as σ.
- Although the absolute error, $\triangle$ (column 2), differ for each σ, with $\triangle$ increasing with decreasing σ, the relative error remains similar for almost all of them (column 5 and 6).

These trends persist for other m values. For the calculation of the eigenvalues we need an unperturbed surface density ($\Sigma_{\rm d}$) profile as an input. We shall use two profiles for it:

- **JT annular disc**: This is an annular disc model around the central massive object obtained by subtracting two Toomre (1963) discs. We shall call this profile as JT annular disc because it is used by Jalali & Tremaine (2012) earlier. The radial profile (dimensionless form) is given by

$$\Sigma_{\rm d}^{\rm JT}(R) = \frac{3}{4\pi}\left[\frac{1}{(1+R^2)^{3/2}} - \frac{1}{(1+R^2)^{5/2}}\right] = \frac{3R^2}{4\pi(1+R^2)^{5/2}}\,, \tag{6.18}$$

And the corresponding precession rate for nearly circular orbits is

$$\dot{\varpi}^{\mathrm{JT}}(R) = \frac{3(1-4R^2)}{4\Omega(R)(1+R^2)^{7/2}}\,. \tag{6.19}$$

Note that $\Omega(R)$ used here is the dimensionless azimuthal frequency. $\dot{\varpi}^{\mathrm{JT}}(R) > 0$ for $0 < R < 1/2$, zero at $R = 1/2$ and negative thereafter. Positive and negative maxima are 0.05861 and -0.2078, respectively. Both $\Sigma_{\mathrm{d}}^{\mathrm{JT}}(R)$ and $\dot{\varpi}^{\mathrm{JT}}(R)$ are plotted in the left pannel of Fig. 6.2.

- **Kuzmin disc:** We have used the Kuzmin disc model in this thesis earlier, but for the sake of completeness we give expressions for the surface density and the precession frequency for a Kuzmin disc

$$\Sigma_{\mathrm{d}}^{\mathrm{Kz}}(R) = \frac{1}{2\pi(1+R^2)^{3/2}}\,, \tag{6.20}$$

$$\dot{\varpi}^{\mathrm{Kz}}(R) = \frac{-3}{2\Omega(R)(1+R^2)^{5/2}}\,. \tag{6.21}$$

Both the quantities are in dimensionless units. Note that $\dot{\varpi}^{\mathrm{Kz}} \leq 0$ for all values of R. We plot both $\Sigma_{\mathrm{d}}^{\mathrm{Kz}}(R)$ and $\dot{\varpi}^{\mathrm{Kz}}(R)$ in the right pannel of Fig. 6.2.

Both these profiles differ from each other physically, and hence can give us a good idea regarding the effects of change in surface density on the eigenmodes. Surface density for Kuzmin disc is centrally concentrated whereas for JT annular disc is concentrated around $R = 1$. Precession frequency is negative throughout the radius range for Kuzmin disc, and for JT annular disc it starts from zero, attains a positive maxima, becomes negative, reaches a minima and then goes to zero. We give and compare the results from both these profiles next.

6.4.1 JT annular Disc

Here we present the numerical results for JT annular disc profile. We choose $m = 1$ & 2, and $\sigma = 0.1$, 0.2, 0.3 & 0.4. The plot of non-singular eigenvalues for JT annular disc is given in Fig. 6.3. The X-axis is the dimensionless pattern speed, $\Omega_p = \omega/m\omega_0$, where $\omega_0 = 0.05861$ is positive maxima value of precession frequency. Note that all frequencies are measured in units of '$\varepsilon\sqrt{GM/a^3}$', the natural slow mode frequency. The Y-axis is

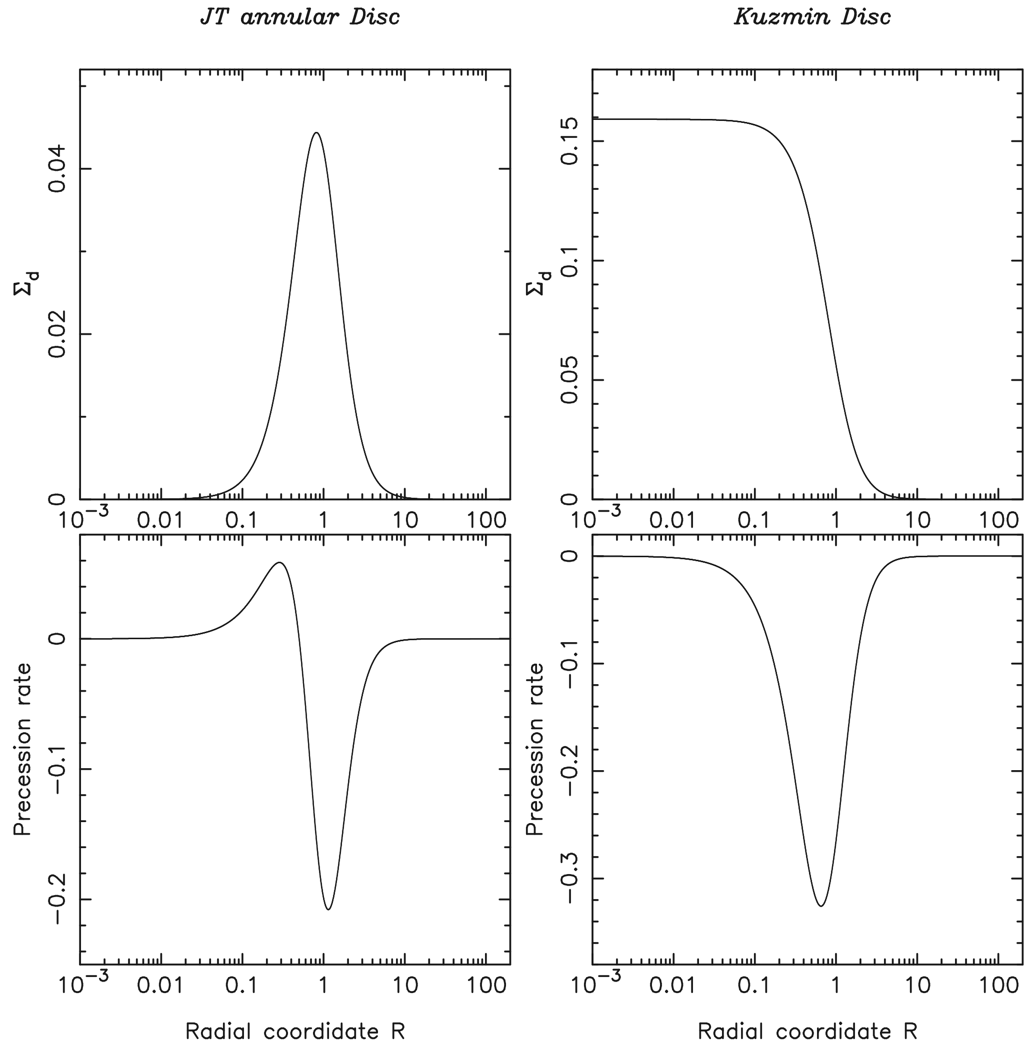

Figure 6.2: Surface density and precession frequency profiles for JT annular disc and Kuzmin disc are displayed. Panels on the left correspond to JT annular disc and those on the right give the profiles for Kuzmin disc. Top panels display the surface density, $\Sigma_{\rm d}$, and the bottom one's are plots for the precession rate $\dot{\varpi}$.

σ	$\triangle$	$p1$	$p2$	$\lvert\triangle/p1\rvert$	$\lvert\triangle/p2\rvert$
0.01	$\sim 10^{-4}$	5000 at $q = 0$	~ -650 at $\lvert q\rvert = 0.027$	$\sim 2 \times 10^{-8}$	$\sim 2 \times 10^{-7}$
0.1	$\sim 5 \times 10^{-7}$	~ 50 at $q = 0$	~ -6.7 at $\lvert q\rvert = 0.27$	$\sim 10^{-8}$	10^{-8}
0.2	$\sim 2 \times 10^{-7}$	~ 12 at $q = 0$	$\sim= -1.8$ at $\lvert q\rvert = 0.53$	$\sim 2 \times 10^{-8}$	$\sim 10^{-7}$
0.3	$\sim 10^{-7}$	~ 5.25 at $q = 0$	$\sim= -0.82$ at $\lvert q\rvert = 0.768$	$\sim 2 \times 10^{-8}$	$\sim 10^{-7}$

Table 6.1: This table is a comparison table for the calculation of matrix entries for different σ values and $m = 1$. First column is for σ values. Second one is for absolute value of maximum error (noise) in the smoothened K_m values. Next one gives the positive peak values, $p1$ of K_m and their respective q values where the curves peak, whereas forth column gives the negative peak values, $p2$ and their respective q values. Fifth and sixth column give the relative error for $p1$ and $p2$, respectively.

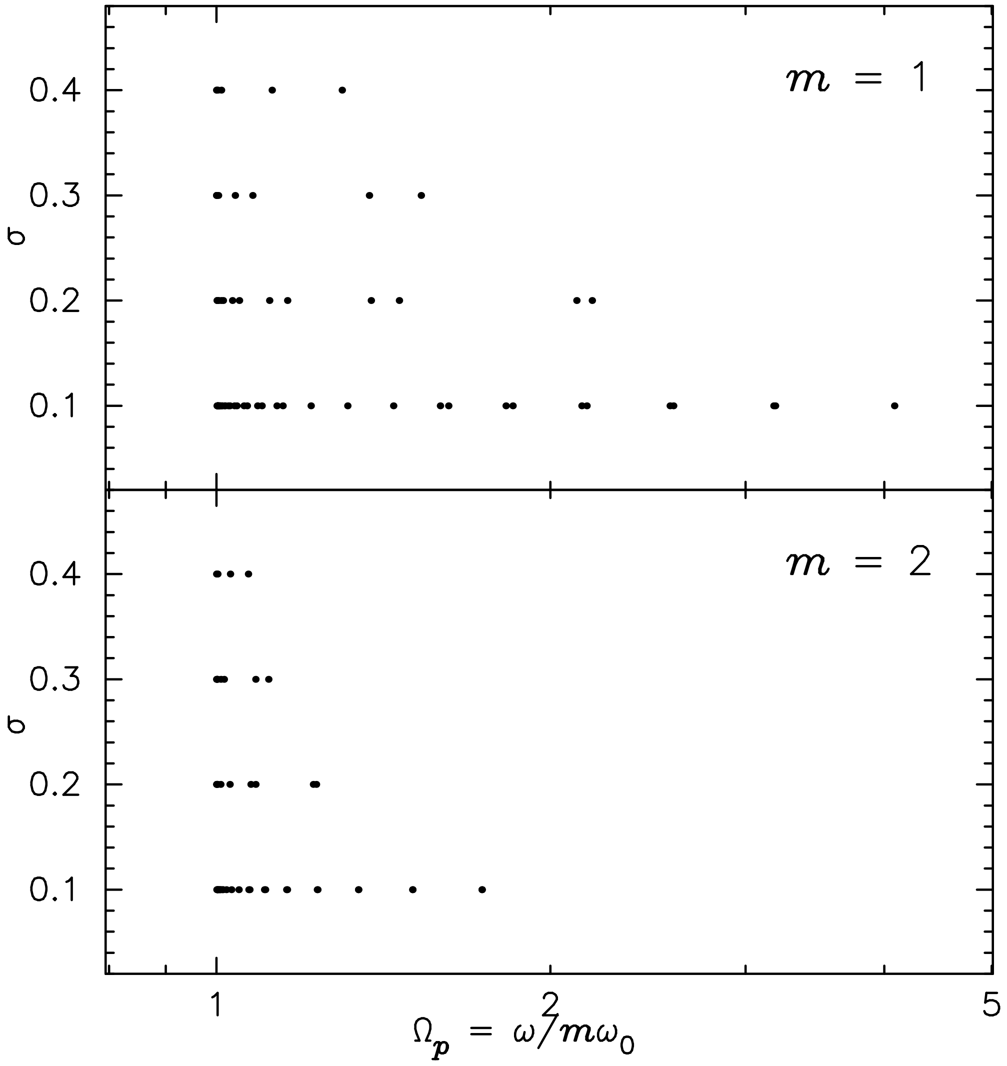

Figure 6.3: Non-singular eigenfrequencies for JT annular disc profile for $m = 1$ & 2 and $\sigma = 0.1, 0.2, 0.3$ and 0.4. Eigenvalues are all real and prograde. X-axis is $\Omega_p = \omega/m\omega_0$, where ω_0 is the positive maxima of precession rate and Y-axis is the σ value. Plots are labeled for their respective m values.

σ, which is a dimensionless measure of the heat in the disc. We note the following trends from Fig. 6.3 for $m = 1$ and $m = 2$ modes:

1. The modes are all stable with prograde pattern speeds $\Omega_p > 1$.
2. For given (σ, m), the pattern speed belongs to a discrete spectrum. Let $\Omega_{\max}(\sigma, m)$ be the largest eigenvalue of this spectrum. Then
   (a) At fixed m, $\Omega_{\max}$ is a decreasing function of σ.
   (b) At fixed σ, $\Omega_{\max}(\sigma, 1) > \Omega_{\max}(\sigma, 2)$.

Plot for $m = 1$ is to be compared with Fig. 4 of Jalali & Tremaine (2012). Mean eccentricity used by the authors is linearly proportional to σ used in the present work. Apart from the last property of the eigenspectra mentioned above (about which nothing has been said by the authors), our conclusions are consistent with their results. Eigenvalues match within a few percent which Jalali & Tremaine get by solving collisionless Boltzmann equation, and even better with the eigenvalues obtained after solving the local WKB dispersion relation. All the eigenvalues with $\Omega_p \leq 1$ that we get are singular for all the values of σ.

The variation of Ω_p with m follows the same trend as we get from solving the local WKB-dispersion relation in Chapter 4. Note that we have not used JT annular disc in calculating the eigenvalues in Ch. 4 hence we can not compare the numbers but still the general properties of the spectra can be compared.

Figure 6.4 and 6.6 show the radial profile of $\Sigma_a(R)$ for $m = 1$ and 2, respectively. Functions are normalized such that $\int \mathrm{d}q\, \Sigma_a^2(R) = 1$. We plot the eigenfunctions for the first two eigenvalues for all the values of σ. Panels are labeled for the values σ and Ω_p. Number of nodes increase as the Ω_p value decreases. In Fig. 6.5 and 6.7 we plot the image of oscillatory patterns of the positive part of $\Sigma_a(R)\cos(m\phi)$ for $m = 1$ and 2, respectively, which is essentially the positive component of the real part of $\Sigma_1(R, \phi, t)$ at $t = 0$. Plots for the highest values of Ω_p are displayed and their respective σ values are given in the panels. Surface density is normalized to unity in all the panels. Contours range from 0 to 1, and the corresponding colors are shown in a wedge on the right side. Wavepackets are more radially compact for lower values of σ.

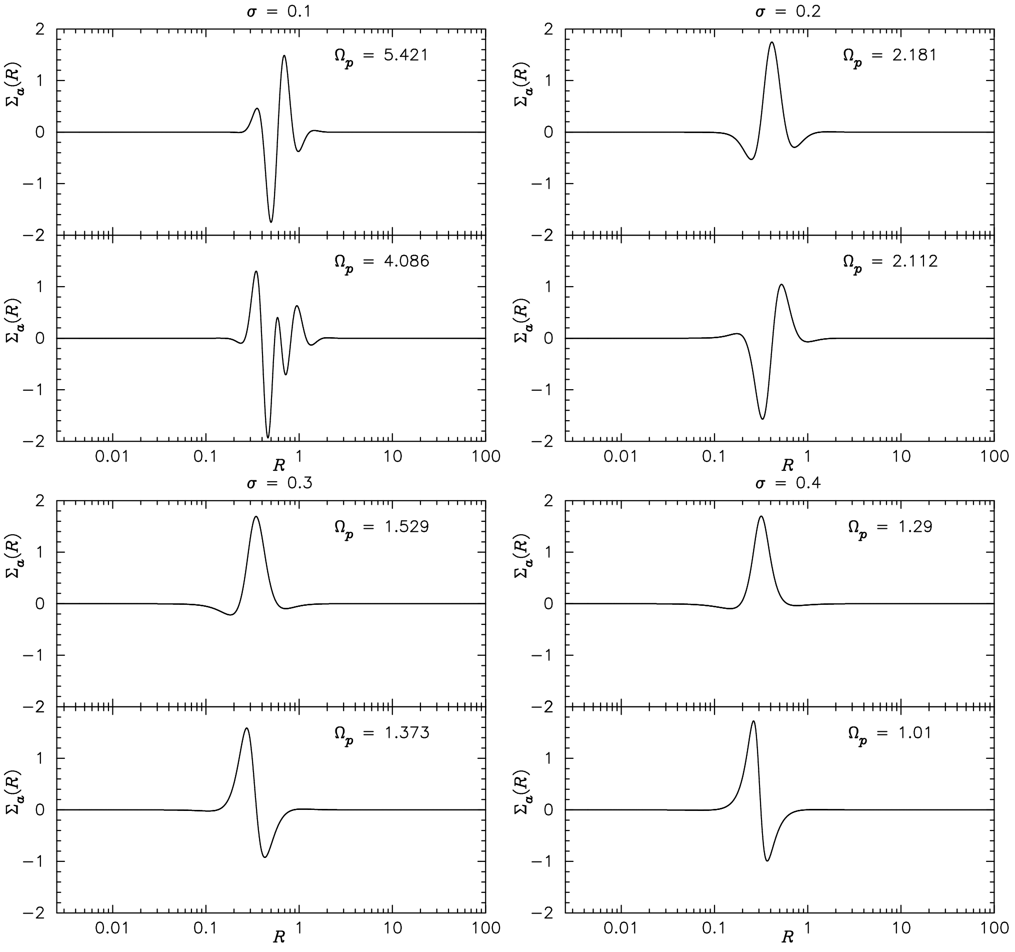

Figure 6.4: Plot of perturbed surface density, $\Sigma_a(R)$ as a function of R for $m = 1$ and JT annular disc profile. Eigenfunctions for first two eigenvalues for each value of σ are displayed. Panels are labeled for the values of σ and Ω_p. Functions are normalized such that $\int \mathrm{d}q\, \Sigma_a^2(R) = 1$.

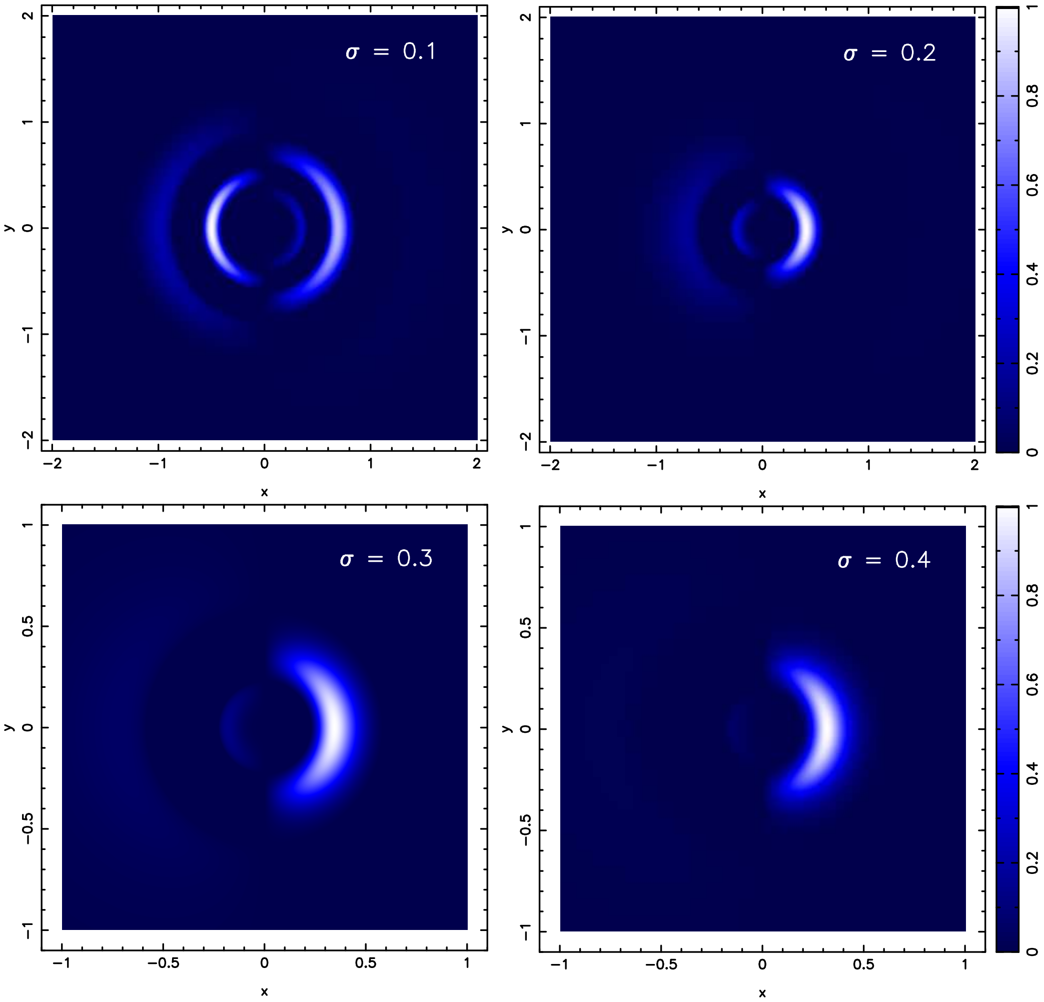

Figure 6.5: Patterns of oscillatory waves for JT annular disc. We have displayed the positive component of Real part of $\Sigma_1(R, \phi, t)$ at $t = 0$, for $m = 1$. Plots are for highest value of Ω_p for each value of σ and the panels are labeled for its respective σ values. The surface density is normalized to unity in all panels and the color scheme for contours from 0 to 1 is plotted in a wedge on right side of the image.

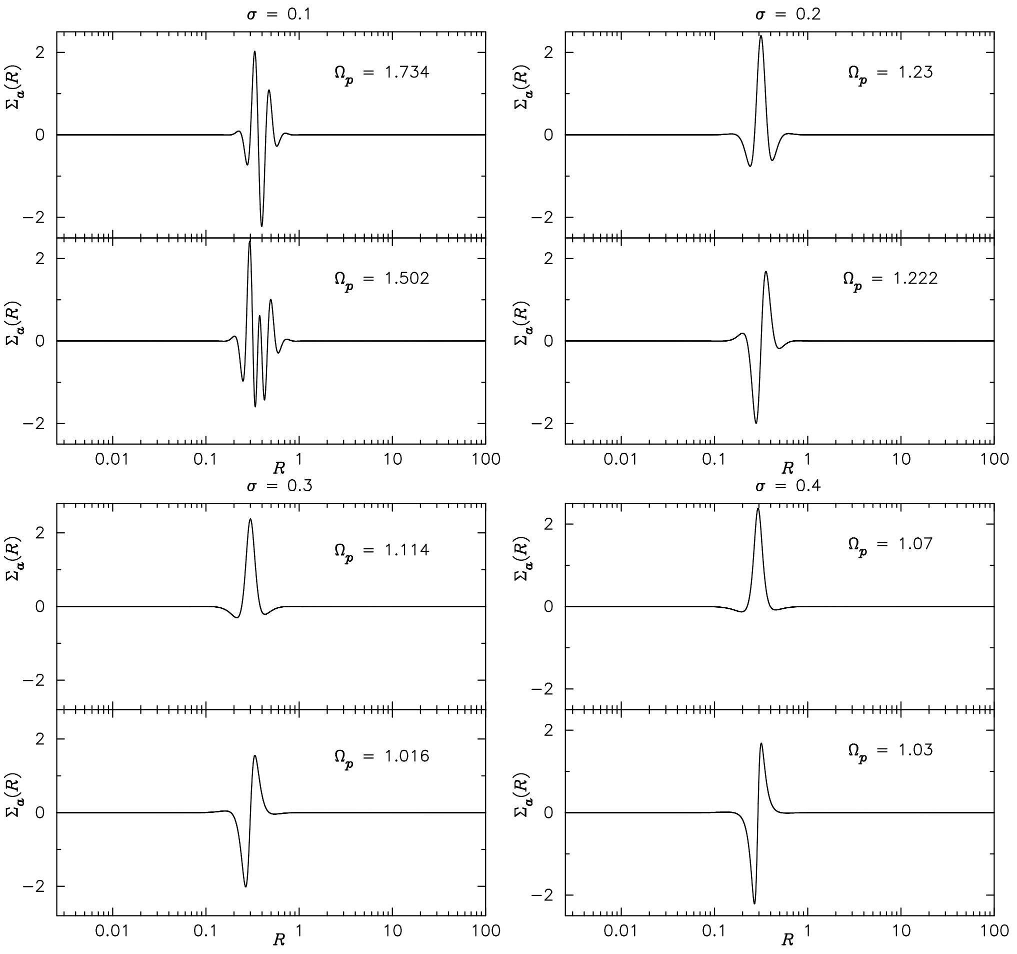

Figure 6.6: $\Sigma_a(R)$ vs R plot for $m = 2$ for two eigenmodes with least number of nodes, using $\Sigma_{\rm d}^{\rm JT}$ as the unperturbed disc. Panels are labeled for their respective σ and Ω_p values.

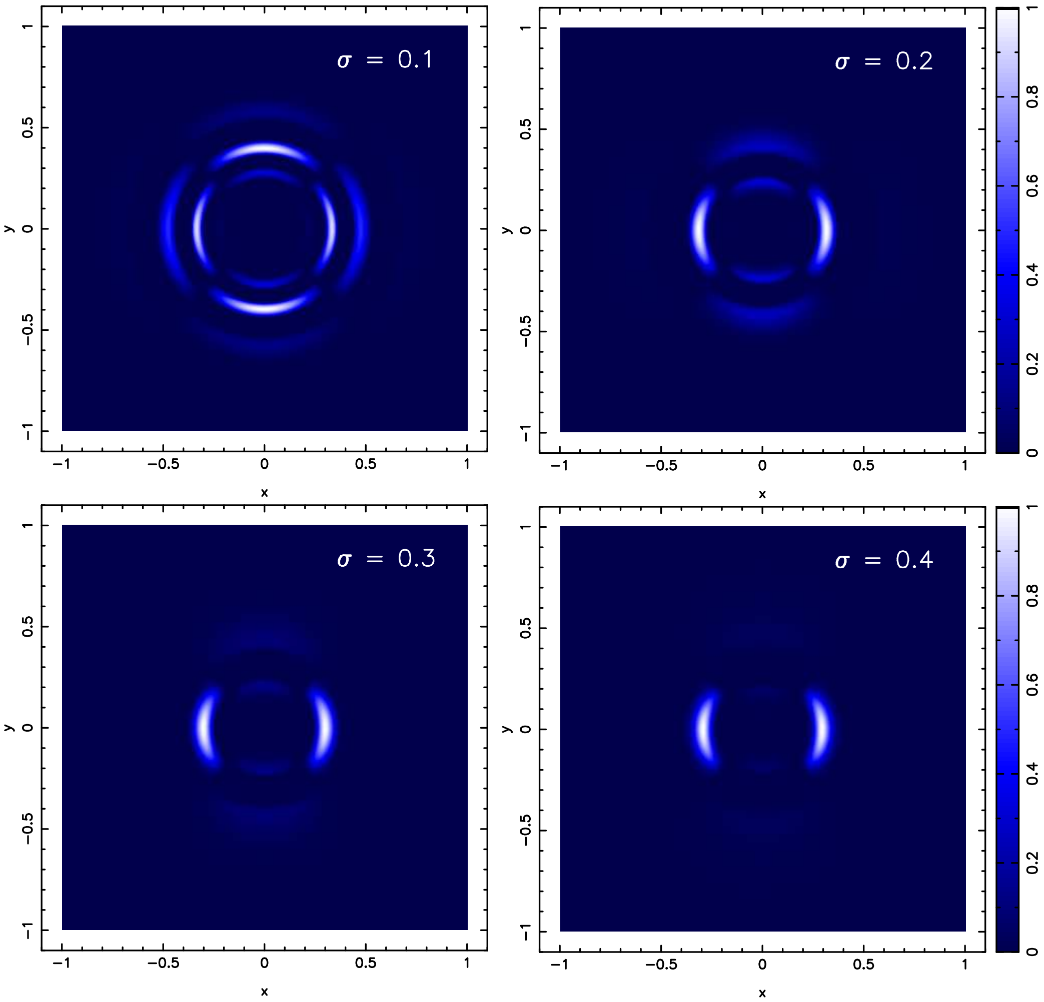

Figure 6.7: Image of positive component of Real part of $\Sigma_1(R,\phi,t)$ at $t=0$ for the same set of parameters as in figure 6.6. Plots of the largest Ω_p for each σ value are displayed.

6.4.2 Kuzmin disc

In this subsection we present the results for Kuzmin disc profile. Figure 6.8 gives the plot of non-singular eigenvalues for the Kuzmin disc. We have plotted for $m = 1$ & 2 and $\sigma = 0.1, 0.2, 0.3$ and 0.4. Horizontal axis is $\Omega_p = \omega/m\omega_0$, where ω_0 is the maxima of $|\dot{\varpi}|$ rather than positive maxima (as used for the JT disc) because for Kuzmin disc $\dot{\varpi}(R) \leq 0$. We note the following trends in the eigenspectrum for $m = 1$ and $m = 2$:

1. Eigenmodes are stable with prograde pattern speeds $\Omega_p > 0$, in contrast to JT disc where $\Omega_p > 1$.

2. For a given value of m, $\Omega_{\max}$ is a decreasing function of σ and $\Omega_{\max}(\sigma, 1) > \Omega_{\max}(\sigma, 2)$. Variation of $\Omega_{\max}$ with σ and m is similar to the JT disc.

In the Chapter 4 of the present thesis we calculated the eigenvalues by solving the local WKB-dispersion relation for the Kuzmin disc model. The present velocity dispersion is same as model I used there. In Fig. 6.9 we compare the solution of local WKB dispersion relation and the eigenmodes calculated in this section for $\sigma = 0.1$ (and $A = 0.1$ as used in Ch. 4). Top panel gives the integral equation solution and the lower panel gives eigenvalues obtained from local WKB dispersion relation. The eigenvalues differ from each other by about 20%, but qualitative trends are the same; for example, as we increase the value of m, the Ω_p value decreases, and Ω_p values increases with decreasing σ. Second one can be seen by comparing the plots for other σ values.

Figure 6.10, 6.11 and 6.12 are the plots of the perturbed surface density of the Kuzmin disc profile. In Fig. 6.10 we the plot $\Sigma_a(R)$ as a function R for $m = 1$. Plots are labeled for their σ and Ω_p values. $\Sigma_a(R)$ is normalized such that $\int \mathrm{d}q \Sigma_a^2(R) = 1$. Figure 6.11 give images of density enhancement region, real part of $\Sigma_1(R, \phi, t)$, at $t = 0$ for the highest eigenvalue for each σ value used in Fig. 6.10. Color scheme and normalization used is same as that used in Fig. 6.5. Radial profile of square normalized wave functions $\Sigma_a(R)$ for $m = 2$ are given in Fig. 6.12. Apart from the exact forms of Σ_a for all cases, overall properties of the eigenfunctions are same as that we get using JT annular disc; (1) Number of nodes increase with decreasing Ω_p value, (2) Wavefunctions are more radially compact for lower values of σ.

Next we compare the eigenvalues we get by solving the integral equation for the Kuzmin disc in this section with the solution of local WKB dispersion relation that are studied in Chapter 4 and the integral-equation solution for softened-gravity disc studied

Solution for local WKB dispersion relation	Integral equation solution for softened gravity disc	Integral equation solution for collisionless disc
0.601	0.67	0.767
0.554	0.62	0.657
0.494	0.57	0.569
0.445	0.52	0.496
0.404	0.48	0.436

Table 6.2: Table of comparison between the solution of local WKB dispersion relation for Kuzmin disc (obtained in Ch. 4), Integral equation solution for softened-gravity disc (Tremaine, 2001) and Integral equation solution studied in the present chapter for Kuzmin disc. Values are for $\sigma = 0.1$.

in Tremaine (2001). Note that although we have studied softened gravity disc in great detail in Ch 3 of this thesis, as discussed in Ch 3 and 4, softening considered in Ch. 3 of this thesis and Tremaine (2001) are different both qualitatively and quantitatively. The model for velocity dispersion used in this chapter directly corresponds to the one used by Tremaine (2001). In Table 6.2 we give the first five non-degenerate eigenvalues for all the three studies for $\sigma = 0.1$ and $m = 1$ ($A = 0.1$ in case of solution of local WKB dispersion relation as used in Ch. 4 and softening length $\beta = 0.1$ as used by Tremaine (2001)). First column is the local WKB-solution, second and third columns are for integral equation solution for softened-gravity disc and the collisionless discs, respectively. The eigenvalues match within $\sim 10\%$ and the match is within few percent for higher number of nodes.

6.5 Conclusions

In Ch. 5 and 6 we have studied eigenmodes for an axisymmetric stellar disc. We began with linearized CBE and formulated an integral eigenvalue problem under the tight winding approximation. We go one step beyond the usual WKB dispersion relation in the sense that the relation between the perturbed potential and surface density in not local anymore. This non-local formalism allows us to determine eigenfunctions, without the difficulties faced by the local WKB dispersion relation.

In Ch. 5 we derived the integral eigenvalue equation. Next in Ch. 6 we solved the

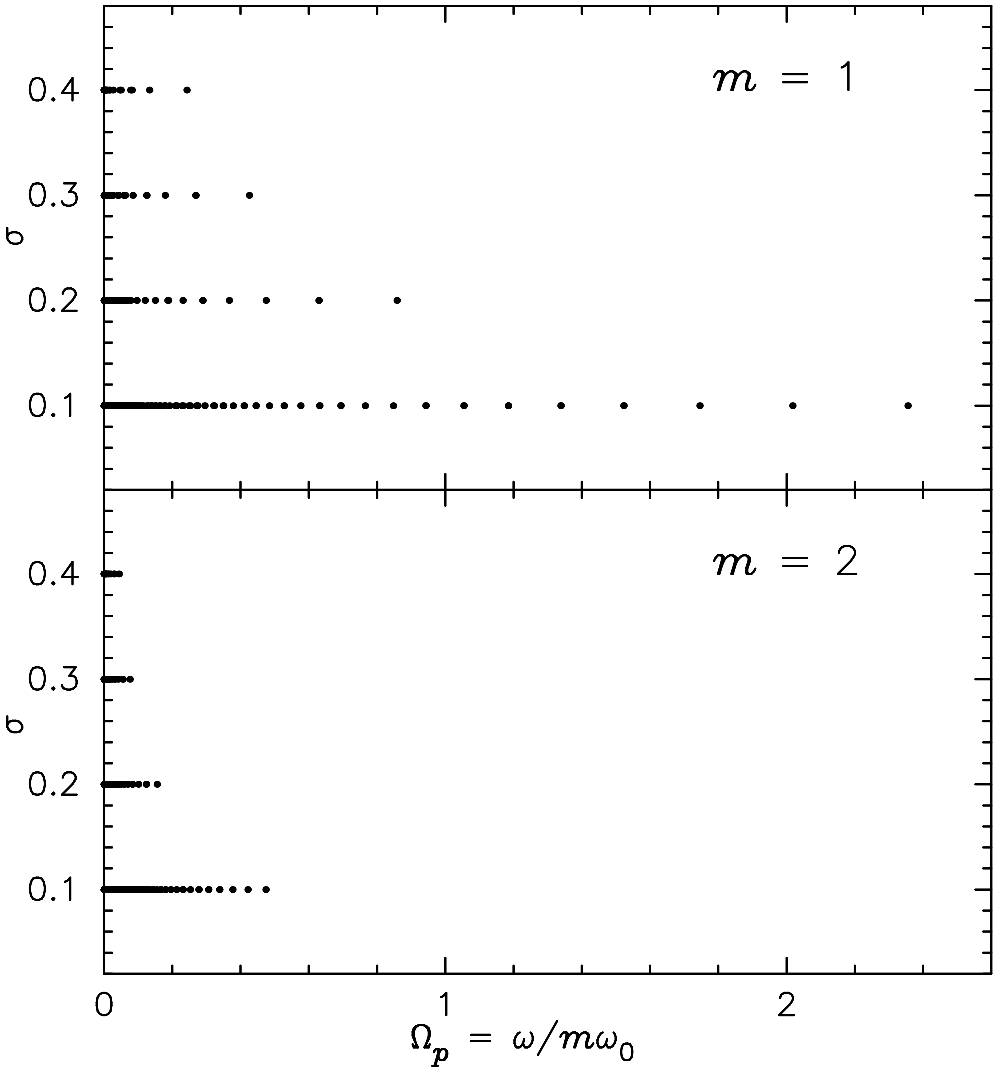

Figure 6.8: Plot of eigenvalues for Kuzmin disc profile. Horizontal axis is the pattern speed $\Omega_p = \omega/m\omega_0$, where ω_0 is the maximum of $|\dot{\varpi}|$ and the vertical axis is the σ value. Panels are labeled for their respective m values.

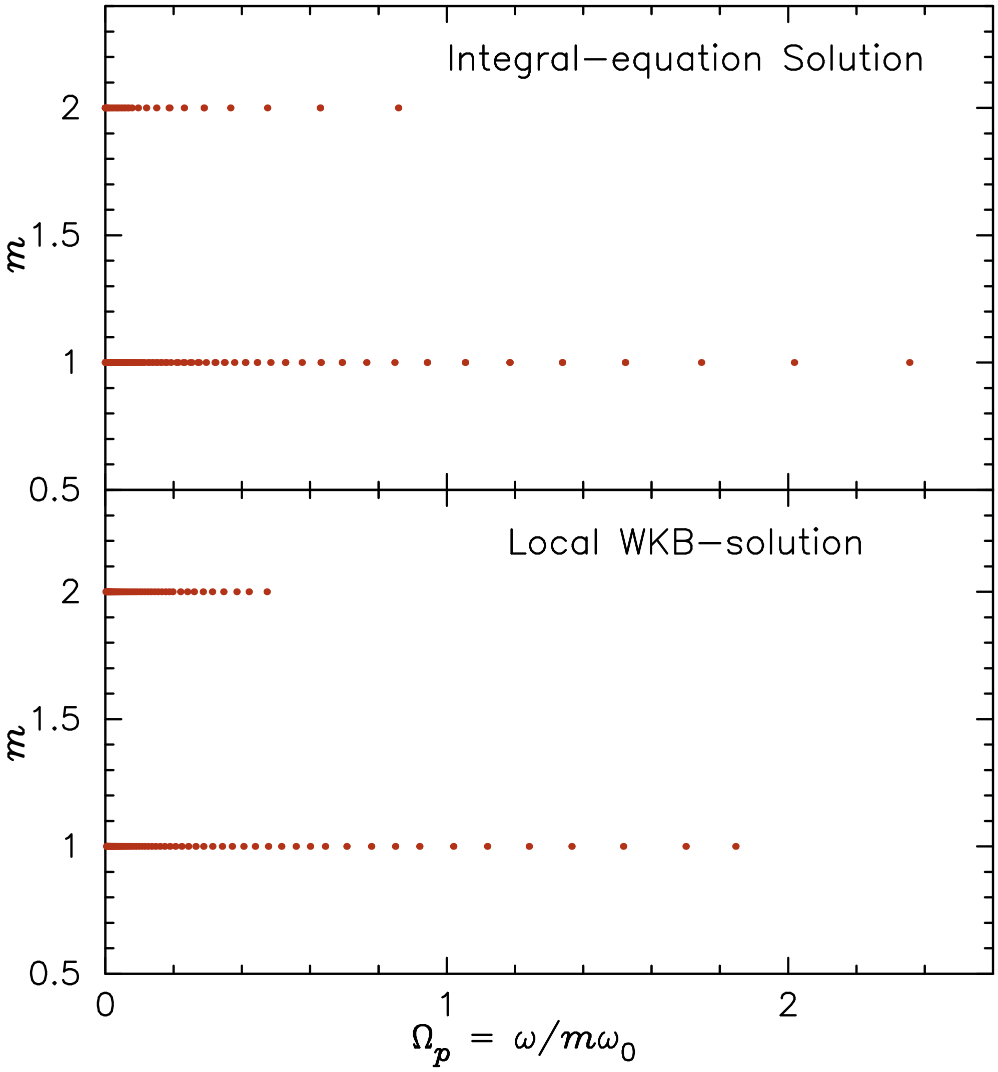

Figure 6.9: Comparison between the eigenvalues obtained by solving the local WKB dispersion relation and the eigenvalues calculated using the integral-equation for Kuzmin disc, with $\sigma = 0.1$. Horizontal and vertical axis are eigenvalue, Ω_p and m, respectively.

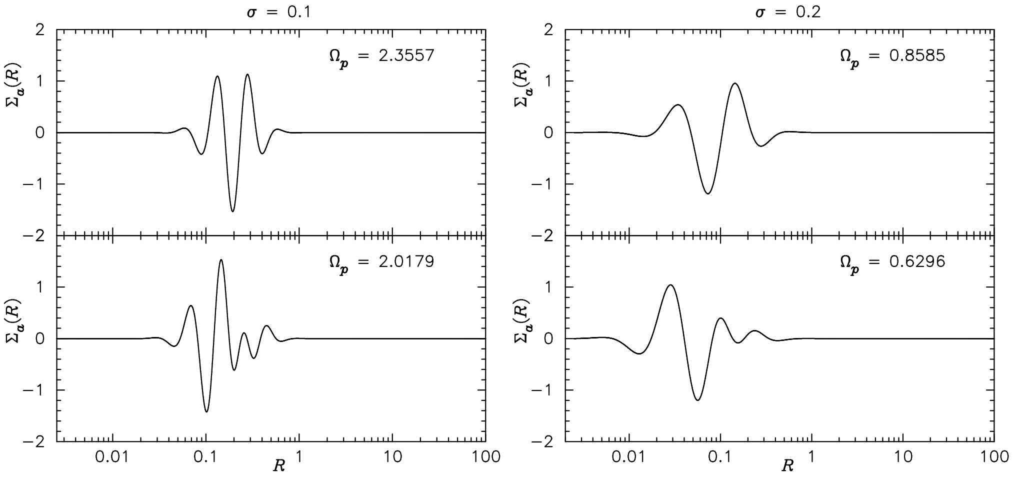

Figure 6.10: $\Sigma_a(R)$ vs R plot for $m = 1$, with $\Sigma_{\rm d}^{\rm Kz}$ as the unperturbed density. Panels are labeled for the relevant σ and Ω_p values. Normalization for $\Sigma_a(R)$ is same as used for JT annular disc.

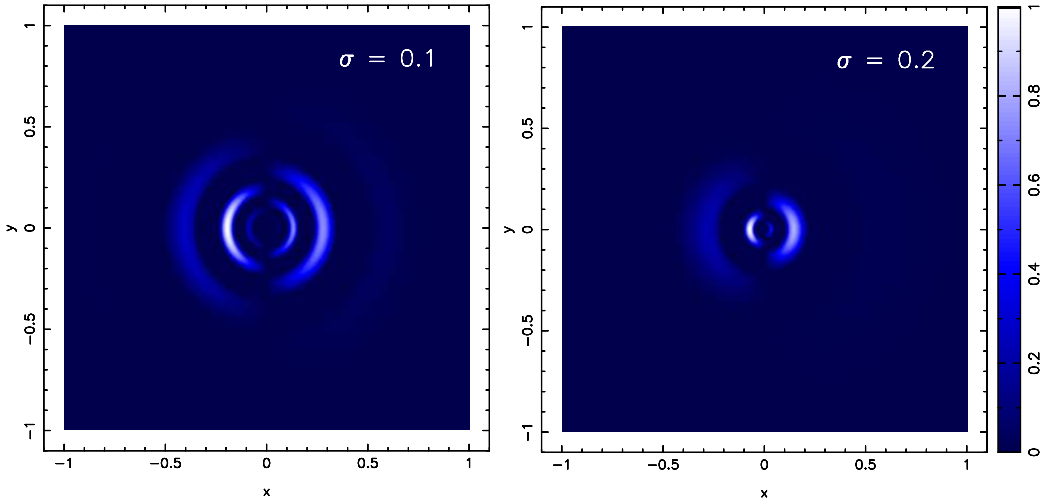

Figure 6.11: Image of positive part of the real component of $\Sigma_1(R, \phi, t)$ at $t = 0$, for highest eigenvalue for each σ value for the plots displayed in Fig. 6.10.

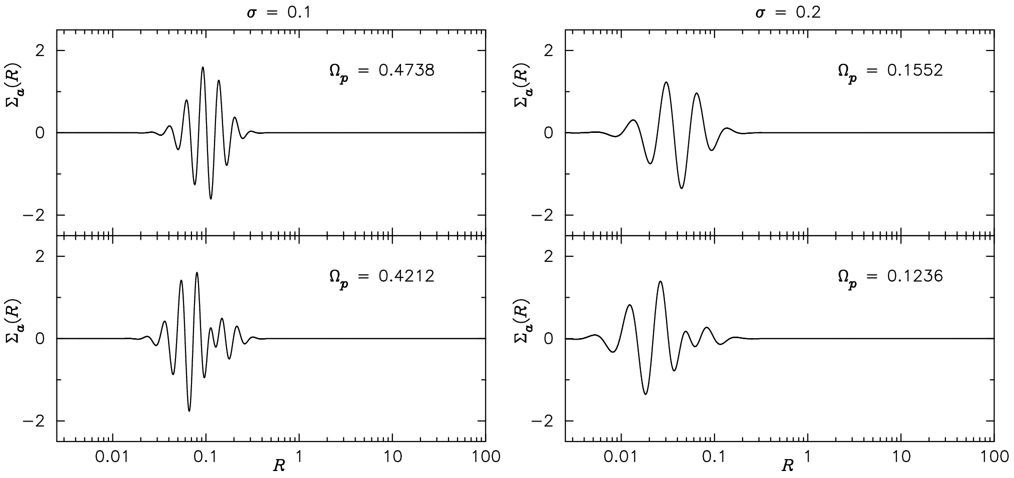

Figure 6.12: Square normalized eigenfunction $\Sigma_a(R)$ vs R plot for $m = 2$ for Kuzmin disc profile. Relevant labeling for σ and ω value is given in the plot.

full integral equation for slow modes, numerically. Numerical solution for two different unperturbed surface density profiles are calculated namely: (1) JT annular disc, (2) Kuzmin disc. Radial profile of velocity dispersion is assumed to be $\sigma_R(R) = \sigma R\kappa(R)$, where $\sigma < 1$ is a constant. This is a reasonable model for velocity dispersion as is shown by Jalali & Tremaine (2012). We began Ch. 6 by asking a few questions, which we tried to answer during the course of the analysis. A brief account of answers to those queries are as follows:

1. Are the modes generated stable or unstable?

   The kernel of slow mode integral-eigenvalue problem is symmetric and hence all the eigenvalues are real. Moreover all the non-singular eigenvalues that we get are prograde, $\Omega_p > 0$.

2. What is the effect of varying velocity dispersion on the spectra?

   Major trends seen with varying the σ value are: (a) Largest eigenfrequency is a decreasing function of σ. (b) Also, the number of non-singular eigenvalues increases as σ decreases.

3. How does the eigen-frequency spectra vary with m?

$\Omega_{\max}(\sigma, m)$ value decreases as we go from $m = 1$ to 2. In addition, for a given Ω_p value, number of nodes for $m = 1$ are larger than that for $m = 2$. In other words eigenfunctions are more radially compact for $m = 1$.

4. What do wavefunctions look like?

   Wavefunctions for various cases are displayed in § 6.4.1 and 6.4.2. General behaviour of the eigenfuntions is such that: (1) The wavelength of oscillations decreases with decreasing pattern speed, (2) Also the number of nodes increase with decreasing Ω_p values, (3) Wavepackets are more radially compact for lower values of σ.

5. How do eigenfrequencies and eigenfunctions vary with the unperturbed surface density profile?

   Largely the behaviour of the eigenfrequencies and the eigenfunctions is independent of the unperturbed surface density chosen for the two cases that we study. But there are quantitative differences like values of pattern speeds. In case of Kuzmin discs, all $\Omega_p > 0$ are non-singular though there is a continuum of eigenvalues close to $\Omega_p = 0$ whereas in case of JT annular discs the eigenvalues with $\Omega_p \leq 1$ are all singular modes.

All the conclusions offered here are largely consistent with the work presented in earlier chapter in this thesis and also by various authors like Tremaine (2001); Jalali & Tremaine (2012). Since the slow modes are stable, the excitation mechanism for such modes becomes important. Close encounter due to an object passing by can act as a perturber (external). Jalali & Tremaine (2012) have considered such a phenomenon in detail and conclude that external perturber largely acts as a good source for excitation of slow modes.

Slow modes exists with arbitrary azimuthal wavenumber m but the modes with lower m values are large scale and hence are most prominent in the observations. Also lower m modes are easy to excite, for example by an external perturber (Jalali & Tremaine, 2012). As noted by Jalali & Tremaine (2012), galactic discs surrounding a suppermassive BH and debris disc around stars are similar in the sense that dynamics of both the discs are influenced by the central object (star/suppermassive BH) and the self-gravity of the disc. Hence the analysis done in present chapter is also applicable to debris disc. Jalali & Tremaine (2012) also proposed that most of the non-axisymmetric features in the debris disc, galactic nuclei as discussed in § 1.2 may be due to slow modes. There are other hypothesis like a presence of massive planet in debris discs, which can also cause these asymmetries in the discs. These can be distinguished from slow modes if the structures are observed for long enough time or with higher resolutions. Features due to slow modes will rotate much slower as compared to the angular speed whereas structures due to planets in the discs will rotate at a speed comparable to the angular speed.

As discussed in Ch. 1, double peak stellar distribution is observed in two galaxies: M31 and NGC4486B. Distribution in both these galaxies differ from each other, for instance, both the peaks in NGC4486B are symmetric w.r.t. the photocenter in contrast to the peaks in M31. Double peak stellar distribution in NGC4486B is more likely to be due to $m = 2$ modes rather than $m = 1$ eccentric modes for M31. Both these galaxies being different morphologically can excite different m-modes predominantly. These eccentric modes may also play an important role in feeding the central BH in galaxies.

In future we would like to generalize this formalism to counter-rotating discs. This might give us some idea regarding a possible explanation for some of the unanswered questions left while studying the softened-gravity counter-rotating discs. We would also like to extend the study of slow modes to thick discs which resemble more realistic galactic discs.

Chapter 7

Summary and Outlook

Compact massive objects in the universe are often surrounded by matter in the form of gas, planets or stars. Of interest to the studies in this thesis, these could be: planets and debris discs around stars; gaseous accretion discs around stars, compact stellar remnants and stellar mass black holes; clusters of stars around massive black holes in galactic nuclei. Flattened, disc–like configurations are commonly observed in these, and we focus attention on idealized two dimensional, flat, razor–thin discs. When the central object is much more massive than the disc, the gravitational force of the central body is the main contributor to disc dynamics, and we speak of a *Keplerian disc*. Orbits of fluid elements or of stars can be thought of as slowly precessing Keplerian ellipses. The precession can be due to pressure gradients in thin accretion discs, or due to the disc self–gravity in stellar discs around massive black holes; in either case the precession time is much longer than Kepler orbital times. Keplerian discs such as these support stable non–axisymmetric *slow modes*. Two counter–rotating discs of stars around a central massive black hole are prone to non–axisymmetric linear instabilities. These are the topics of investigation in this theses, as explained in greater detail below:

- In Ch. 2 we studied slow $m = 1$ modes in thin accretion discs around a compact central mass. A WKB analysis suggested that the modes have wavelengths comparable to the disc size. These modes, being large scale, can dominate the over-all appearance of the disc. To study these modes better, we formulated the eigenvalue equation for the slow modes, which turned out to be in the Sturm-Liouville form; all the eigenvalues were thus found to be real. Real eigenvalues imply that the disc is stable to these perturbations. In the case of accretion discs, we have very uncertain knowledge of the surface density profile for the disc. We calculated the eigenvalues numerically for three test disc profiles: (1) The Shakura-Sunyaev disc, (2) the Kuzmin disc, and (3) a power law disc. For most cases the eigenvalues were negative. In the case of a power law disc, for certain combination of barotropic index Γ, and power law index β, we get positive eigenvalues. But these parameters regimes were unphysical. We also discussed the possible excitation mechanisms for these modes; for instance, excitation due to the stream of matter from secondary star that feeds the accretion disc, or through the action of viscous forces.

- Next we studied slow modes in counter-rotating, softened-gravity continuous discs. Slow modes are enabled in such systems due to the self gravity of the disc, which dominates the gas pressure in the disc. Counter-rotating streams of matters are well known to be unstable under eccentric perturbations. The earlier studies of these modes Tremaine (2001); Touma (2002); Tremaine (2005); Polyachenko et al. (2008); Sridhar & Saini (2010) had limitations, which we discussed in detail at relevant places in the thesis. These modes give rise to asymmetries in the disc that have been observed in self-gravitating systems like debris discs, and discs in galactic nuclei. In Ch. 3 we studied both the WKB-dispersion relation and the integral eigenvalue problem for coplanar counter-rotating discs. We now note the general conclusions obtained by us.
  - The system is stable for $m = 1$ perturbations in the case of no-counter rotation. This conclusion is consistent with the result of Tremaine (2001).
  - For other values of mass fraction η, the eigenvalues are imaginary and the discs are unstable. For $\eta = 1/2$, we get purely growing modes; whereas for other values of η, the eigenvalues are, in general, complex.
  - The pattern speed appears to be non-negative for all values of η, with the growth (or damping) rate being larger for larger values of the pattern speed.
  - Perturbed surface density profile is generally lopsided, with an over all rotation of the pattern as they evolve in time, with the pattern speed given by real part of the eigenvalue.
- Although softened gravity is known to serve as a surrogate to collisionless discs for $m = 1$ modes, both the systems are physically different for other m-modes. For softened gravity discs slow modes do not exist for $m > 1$, whereas collisionless

discs support all m-modes. This conclusion is motivated by the discussions given in the Appendix of Jalali & Tremaine (2012), which we also prove in § 4.3. Higher m-modes also form an important class of density waves and hence important to study. In Ch. 4 we studied slow modes in counter-rotating, nearly Keplerian, collisionless discs. Analysis in Ch. 4 to 6 is applicable to self gravitating systems like galactic nuclei and debris disc. The unperturbed orbits are assumed to follow epicyclic orbits and the DF of the prograde and the retrograde disc is given by the Schwarzschild DF. We first formulate the WKB dispersion relation for a given mass fraction η in retrograde disc and then apply slow mode approximation to it. For the no counter-rotation case, the above mentioned dispersion relation reduces to the one discussed in Toomre (1964); Binney & Tremaine (2008); Jalali & Tremaine (2012).

One of the important applications of the dispersion relation derived in this chapter is the stability analysis of the modes. For fluid discs, the stability of $m = 0$ modes guarantees the stability of higher m modes; and the stability criterion for such discs is the well known Toomre's stability criterion (Toomre, 1964; Tremaine, 2001; Binney & Tremaine, 2008). However, this is not the case for collisionless discs. Even if the discs are stable for axisymmetric modes, they can still be unstable for non-axisymmetric modes. Axisymmetric perturbations were found to be stable in our analysis, and the stability criterion turned out to be the Toomre's stability criterion. We studied the stability of non-axisymmetric modes separately for counter–rotating discs in Ch. 4. The non-axisymmetric perturbations were found to be unstable if the mass in the retrograde component of the disc is non-zero.

We next solved the dispersion relation using the Bohr-Sommerfeld quantization condition to obtain the eigen–spectrum for a given unperturbed surface density profile and velocity dispersion. We could obtain only the eigenvalues for no counter–rotation and equal counter–rotation. All the eigenvalues obtained were real for no counter–rotation; and purely growing/damping for equal counter–rotation. We also make a detailed comparison between the eigenvalues for $m = 1$ modes that we obtain with those obtained after solving the integral eigenvalue problem for the softened gravity discs considered in Tremaine (2001) (for no counter–rotation) and Ch. 3 of this thesis (for equal counter–rotation). The match between the eigenvalues is quite good, confirming the assertion that softened gravity disc serves as surrogate to collisionless disc.

- One of the drawbacks of the usual WKB analysis of tightly–wound disc modes is that it is not easy to determine the eigenfunctions. This is because the dispersion relation is transcendental in the wavenumber. In Ch. 5 we overcome this problem by relaxing the assumption of locality between the perturbed surface density and the perturbed potential. We considered an unperturbed axisymmetric stellar disc with a Schwarzschild DF, and derived an integral eigenvalue problem for tightly-wound modes of arbitrary m. This integral equation is not restricted in application to Keplerian discs: for instance, it could be used to explore modes of a galactic disc, although we do not do so in this thesis. After deriving the integral equation, we verify that, in the local approximation, the usual WKB-dispersion relation (Toomre, 1964; Binney & Tremaine, 2008; Jalali & Tremaine, 2012) is recovered.
- In Ch. 6 we apply the slow mode approximation to the integral equation and show that its kernel is symmetric, implying that the eigenvalues are all real and hence the disc is stable. We consider two unperturbed disc profiles, the Jalali–Tremaine annular discs, and the Kuzmin disc. We determine eigenvalues and eigenfunctions for both $m = 1$ and $m = 2$ slow modes, and discuss their properties. Two general statements we highlight here are: (i) All the non-singular eigenmodes have positive pattern speeds; (ii) The fastest pattern speed is a decreasing function of the heat in the disc.

In the future we would also like to extend the formulation of the integral equation for collisionless discs to counter-rotating discs. In this thesis we have studied slow modes for a gas disc and particle disc separately. But in most of the astrophysical discs both gas and particle discs exist together and are coupled to each other. A natural question to ask at this point is: What is the nature of slow modes if both gas and particle discs are coupled together and are bound to each other gravitationally? Also, we have studied slow modes in accretion discs where viscous forces are assumed to balance the radial inflow of the matter and do not have any effect on the nature of slow modes. However, as discussed in Ch. 2, there is a possibility that the slow modes in accretion discs could be excited due to viscous forces, but this would require reformulation of the eigenvalue problem including the effect of viscous forces.

Appendix A

Perturbed potential for softened gravity discs

Consider a two component counter-rotating coplanar disc whose origin coincides with the position of the central object as shown in Fig A.1. We want to calculate the perturbed potential due to a two component perturbed disc at point 'A'. As assumed in § 3.2, disc particle interact gravitationally via softened gravity (discussed in § 1.6) whereas central mass and disc particles interact via unsoftened Newtonian gravity. Perturbed potential $\delta\Phi_a$ at point 'A' due to mass δm_B at point 'B' contributed by both perturbed prograde and retrograde discs is given by

$$\delta\Phi_a = -\,G\delta m_B \left(\frac{1}{\sqrt{|\mathbf{R}^2 - \mathbf{R}'^2|^2 + b^2}} - \frac{\mathbf{R}\,.\,\mathbf{R}'}{R'^3} \right) , \tag{A.1}$$

and $\delta m_B = R'\,\mathrm{d}R'\,\mathrm{d}\phi'\,(\Sigma_a^+(R',\phi') + \Sigma_a^-(R',\phi'))$ where Σ_a^+ and Σ_a^- are perturbed surface densities of ± discs. We have used the discussion in § 6.2 of Murray & Dermott (1999) to write the above expression which is modified to include softened gravity. First term is called *direct term* whereas the second term is the *indirect term* which would not appear if origin coincides with the center of mass. Fourier analyzing the perturbation in ϕ-space that is perturbed quantity $X_a(R,\phi) = X_a^m(R)\exp(\mathrm{i}m\phi)$ we get

$$\begin{aligned}\delta\Phi_a^m =& -\,GR'\,\mathrm{d}R'\,\mathrm{d}\phi'\,(\Sigma_a^{m+}(R') + \Sigma_a^{m-}(R'))\exp(\mathrm{i}m\phi' - \phi)\times \\ &\times \left(\frac{1}{\sqrt{|\mathbf{R}^2 - \mathbf{R}'^2|^2 + b^2}} - \frac{\mathbf{R}\,.\,\mathbf{R}'}{R'^3} \right) .\end{aligned} \tag{A.2}$$

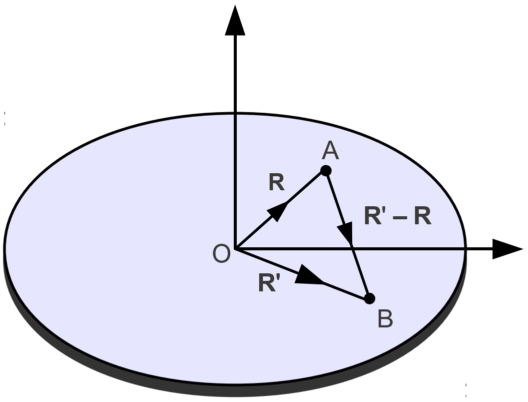

Figure A.1: Coplanar counter–rotating discs with its center at origin. The disc is marked for point masses A & B and their respective position vectors.

Integrating Eq. A.2 over ϕ' from 0 to 2π and R' from 0 to ∞ gives $\Phi_a^m(R)$:

$$\begin{aligned}\Phi_a^m(R) =& -G\int_0^\infty\int_0^{2\pi} R'\,\mathrm{d}R'\,\mathrm{d}\theta\,(\Sigma_a^{m+}(R')+\Sigma_a^{m-}(R'))\exp(\mathrm{i}m\theta)\times\\ &\times\left(\frac{1}{\sqrt{|\mathbf{R}^2-\mathbf{R}'^2|^2+b^2}}-\frac{\mathbf{R}\,.\,\mathbf{R}'}{R'^3}\right),\\ =&\int_0^\infty \mathrm{d}R'\,R' P_m(R,R')(\Sigma_a^{m+}(R')+\Sigma_a^{m-}(R'))\,,\end{aligned} \tag{A.3}$$

where we have used $\theta = \phi' - \phi$ which is the angle between $\mathbf{R}$ & $\mathbf{R}'$ and kernel P_m is defined as

$$P_m(R,R') = -\underbrace{G\int_0^{2\pi}\mathrm{d}\theta\,\frac{\exp(\mathrm{i}m\theta)}{\sqrt{|\mathbf{R}^2-\mathbf{R}'^2|^2+b^2}}}_{\mathrm{I}} + \underbrace{G\int_0^{2\pi}\mathrm{d}\theta\,\frac{\mathbf{R}\,.\,\mathbf{R}'\,\exp(\mathrm{i}m\theta)}{R'^3}}_{\mathrm{II}}\,. \tag{A.4}$$

Solving integral I gives us

$$\mathrm{I} = \frac{-2G}{R_>}\int_0^\pi \mathrm{d}\theta\,\frac{\cos m\theta}{(1-2\alpha\cos\theta+\alpha^2+\beta^2)^{s/2}}\,,$$

here $R_< = \min(R, R')$, $R_> = \max(R, R')$, $\alpha = R_</R_>$ and $\beta = b/R_>$. Evaluating II we get

$$\mathrm{II} = \frac{\pi G R}{R'^2}(\delta_{m,1} + \delta_{m,-1}),$$

δ_{ij} is the Kronecker's delta function. Combining all we get

$$P_m(R, R') \;=\; -\frac{\pi G}{R_>} B_1^{(m)}(\alpha, \beta) \;+\; \frac{\pi G R}{R'^2}(\delta_{m,1} + \delta_{m,-1})\,. \tag{A.5}$$

where

$$B_s^{(m)}(\alpha, \beta) \;= \frac{2}{\pi} \int_0^\pi \mathrm{d}\theta \, \frac{\cos m\theta}{(1 - 2\alpha\cos\theta + \alpha^2 + \beta^2)^{s/2}}\,, \tag{A.6}$$

are "softened Laplace coefficients", which was first used by Touma (2002).

Appendix B

Expressing softened Laplace coefficients in terms of (unsoftened) Laplace coefficients

Softened Laplace coefficients were defined in Touma (2002) as,

$$B_s^m(\alpha, \beta) \;=\; \frac{2}{\pi}\int_0^\pi \mathrm{d}\theta\, \frac{\cos m\theta}{\Delta^{s/2}} \tag{B.1}$$

where

$$\Delta \;=\; 1 + \alpha^2 + \beta^2 - 2\alpha\cos\theta \tag{B.2}$$

We now write

$$\Delta \;=\; \gamma^2 + \delta^2 - 2\gamma\delta\cos\theta \tag{B.3}$$

One solution for γ and δ is,

$$\begin{aligned} \gamma \;&=\; \left[\frac{1+\alpha^2+\beta^2}{2} \;+\; \frac{1}{2}\sqrt{(1+\alpha^2+\beta^2)^2 \;-\; 4\alpha^2}\right]^{1/2} \\ \delta \;&=\; \frac{\alpha}{\gamma} \end{aligned} \tag{B.4}$$

Therefore

$$B_s^m(\alpha,\beta) \;=\; \gamma^{-s}\, b_{s/2}^m\,(\delta/\gamma) \tag{B.5}$$

where

$$b_{s/2}^m(\alpha) \;=\; \frac{2}{\pi}\int_0^\pi \mathrm{d}\theta\,\frac{\cos m\theta}{(1+\alpha^2-2\alpha\cos\theta)^{s/2}}\,; \qquad \alpha < 1 \tag{B.6}$$

are the familiar (unsoftened) Laplace coefficients (Murray & Dermott, 1999). From Eqn. (B.5), we must have $(\delta/\gamma) < 1$. That this is indeed true can be proved using Eqns. (B.4): γ is a monotonically increasing function of β^2, hence $\gamma \geq 1$, and $(\delta/\gamma) = (\alpha/\gamma^2) < 1$.

Bibliography

Anderson E. et al., 1999, LAPACK Users' Guide, 3rd Ed., Society for Industrial and Applied Mathematics, Philadelphia, PA

Araki S., 1987, AJ, 94, 99

Bacon R. et al., 2001, A&A, 371, 409

Binney J., and Tremaine S., 2008, Galactic Dynamics: 2nd Ed., Princeton University Press

Brown C. K., and Magorrian J., 2013, MNRAS, 431, 80

Choudhuri A. R., 1998, The physics of fluids and plasmas : an introduction for astrophysicists, Cambridge University Press

Clampin M. et al., 2003, AJ, 126, 385

Ferrarese L., and Merritt D., 2000, ApJ, 539, L9

Feynman R., Leighton R. B., and Sands M. L., 1964-66, The Feynman Lectures on Physics, Addison-Wesley, 3 volumes

Frank J., King A., and Raine D. J., 2002, Accretion Power in Astrophysics, 3rd Edition, Cambridge University Press

Gebhardt K. et al., 2000, ApJ, 539, L13

Gebhardt K. et al., 1996, AJ, 112, 105

Goldreich P., and Tremaine S., 1979, ApJ, 233, 857

Gulati M., Saini T. D., and Sridhar S., 2012, MNRAS, 424, 348

Häring N., and Rix H.-W., 2004, ApJ, 604, L89

Heap S. R. et al., 2000, ApJ, 539, 435

Jalali M. A., and Tremaine S., 2012, MNRAS, 421, 2368

Kalnajs A. J., 1971, ApJ, 166, 275

Kato S., 1983, PASJ, 35, 249

Kazandjian M. V., and Touma J. R., 2013, MNRAS, 430, 2732

Landau L. D., and Lifshitz E. M., 1994, Quantum mechanics : non-relativistic theory, Pergamon Press, Oxford

Lauer T. R. et al., 1998, AJ, 116, 2263

Lee E., and Goodman J., 1999, MNRAS, 308, 984

Lighthill J., 2001, Waves in Fluids, Cambridge University Press

Lin C. C., and Shu F. H., 1964, ApJ, 140, 646

Lovelace R. V. E., Jore K. P., and Haynes M. P., 1997, ApJ, 475, 83

Marsh K. A. et al., 2006, ApJ, 646, L77

Mason E. et al., 2000, MNRAS, 318, 440

Merritt D., and Stiavelli M., 1990, ApJ, 358, 399

Miller R. H., 1971, Ap&SS, 14, 73

Murray C. D., and Dermott S. F., 1999, Solar system dynamics, Cambridge University Press

Narayan R., and Yi I., 1994, ApJ, 428, L13

Nixon C., King A., Price D., and Frank J., 2012, ApJ, 757, L24

Paczyńsky B., and Wiita P. J., 1980, A&A, 88, 23

Palmer P. L., and Papaloizou J., 1990, MNRAS, 243, 263

Peiris H. V., and Tremaine S., 2003, ApJ, 599, 237

Polyachenko E. V., Polyachenko V. L., and Shukhman I. G., 2008, MNRAS, 386, 1966

Press W. H., Teukolsky S. A., Vetterling W. T., Flannery B. P., 1992, Numerical recipes in Fortran (2nd Ed.): the art of scientific computing, Cambridge University Press, New York, NY, USA

Rauch K. P., and Tremaine S., 1996, New A, 1, 149

Reichard T. A. et al., 2009, ApJ, 691, 1005

Safronov V. S., 1960, Annales d'Astrophysique, 23, 979

Salow R. M., and Statler T. S., 2001, ApJ, 551, L49

Sambhus N., and Sridhar S., 2002, A&A, 388, 766

Sawamura M., 1988, PASJ, 40, 279

Sellwood J. A., and Merritt D., 1994, ApJ, 425, 530

Shakura N. I., and Sunyaev R. A., 1973, A&A, 24, 337

Sridhar S., and Saini T. D., 2010, MNRAS, 404, 527

Sridhar S., Syer D., Touma J., 1999, in Astronomical Society of the Pacific Conference Series, Vol. 160, Astrophysical Discs - an EC Summer School, Sellwood J. A., Goodman J., eds., p. 307

Sridhar S., and Touma J., 1999, MNRAS, 303, 483

Telesco C. M. et al., 2000, ApJ, 530, 329

Toomre A., 1963, ApJ, 138, 385

Toomre A., 1964, ApJ, 139, 1217

Touma J. R., 2002, MNRAS, 333, 583

Touma J. R., Tremaine S., and Kazandjian M. V., 2009, MNRAS, 394, 1085

Tremaine S., 1995, AJ, 110, 628

Tremaine S., 2001, AJ, 121, 1776

Tremaine S., 2005, ApJ, 625, 143

Tsang D., and Lai D., 2009, MNRAS, 396, 589

Zang T. A., and Hohl F., 1978, ApJ, 226, 521

Zhang L., and Lovelace R. V. E., 2005, Ap&SS, 300, 395